Dosimetry for 177Lu and 90Y radionuclide therapies through imaging and Monte Carlo simulations

Laure Vergnaud

▶ **To cite this version:**

Laure Vergnaud. Dosimetry for 177Lu and 90Y radionuclide therapies through imaging and Monte Carlo simulations. Medical Imaging. INSA de Lyon, 2023. English. NNT : 2023ISAL0068 . tel-04427153

HAL Id: tel-04427153
https://theses.hal.science/tel-04427153v1

Submitted on 30 Jan 2024

HAL is a multi-disciplinary open access archive for the deposit and dissemination of scientific research documents, whether they are published or not. The documents may come from teaching and research institutions in France or abroad, or from public or private research centers.

L'archive ouverte pluridisciplinaire **HAL**, est destinée au dépôt et à la diffusion de documents scientifiques de niveau recherche, publiés ou non, émanant des établissements d'enseignement et de recherche français ou étrangers, des laboratoires publics ou privés.

N°d'ordre NNT : 2023ISAL0068

THESE de DOCTORAT DE L'INSA LYON,
membre de l'Université de Lyon

Ecole Doctorale N° 160
(ELECTRONIQUE, ELECTROTECHNIQUE, AUTOMATIQUE)

Spécialité/ discipline de doctorat :

Traitement du Signal et de l'Image

Soutenue publiquement le 06/10/2023, par :
Laure Vergnaud

Dosimetry for ^{177}Lu and ^{90}Y radionuclide therapies through imaging and Monte Carlo simulations

---

Devant le jury composé de :

Dewaraja, Yuni	Professeure des universités, University of Michigan, Ann Arbor	Rapporteure
Dickson, John	Professeur des universités, University College London, London	Rapporteur
Strigari, Lidia	Professeure associée, University of Bologna, Bologna	Examinatrice
Cachin, Florent	Professeur des universités / Médecin nucléaire, Université Clermont Auvergne , Centre Jean Perrin, Clermont-Ferrand	Examinateur
Sarrut, David	Directeur de recherche, CNRS, Lyon	Directeur de thèse
Badel, Jean-Nöel	Physicien Médical, Ph.D, Centre Léon Bérard, Lyon	Co-directeur de thèse
Giraudet, Anne-Laure	Médecin Nucléaire, Ph.D., Centre Léon Bérard, Lyon	Invitée

Cette thèse est accessible à l'adresse : https://theses.insa-lyon.fr/publication/2023ISAL0068/these.pdf
© [L. Vergnaud], [2023], INSA Lyon, tous droits réservés

Département FEDORA – INSA Lyon - Ecoles Doctorales

SIGLE	ECOLE DOCTORALE	NOM ET COORDONNEES DU RESPONSABLE
CHIMIE	**CHIMIE DE LYON** **https://www.edchimie-lyon.fr** Sec. : Renée EL MELHEM Bât. Blaise PASCAL, 3e étage secretariat@edchimie-lyon.fr	**M. Stéphane DANIELE** C2P2-CPE LYON-UMR 5265 Bâtiment F308, BP 2077 43 Boulevard du 11 novembre 1918 69616 Villeurbanne **directeur@edchimie-lyon.fr**
E.E.A.	**ÉLECTRONIQUE, ÉLECTROTECHNIQUE, AUTOMATIQUE** **https://edeea.universite-lyon.fr** Sec. : Stéphanie CAUVIN Bâtiment Direction INSA Lyon Tél : 04.72.43.71.70 secretariat.edeea@insa-lyon.fr	**M. Philippe DELACHARTRE** INSA LYON Laboratoire CREATIS Bâtiment Blaise Pascal, 7 avenue Jean Capelle 69621 Villeurbanne CEDEX Tél : 04.72.43.88.63 **philippe.delachartre@insa-lyon.fr**
E2M2	**ÉVOLUTION, ÉCOSYSTÈME, MICROBIOLOGIE, MODÉLISATION** **http://e2m2.universite-lyon.fr** Sec. : Bénédicte LANZA Bât. Atrium, UCB Lyon 1 Tél : 04.72.44.83.62 secretariat.e2m2@univ-lyon1.fr	**Mme Sandrine CHARLES** Université Claude Bernard Lyon 1 UFR Biosciences Bâtiment Mendel 43, boulevard du 11 Novembre 1918 69622 Villeurbanne CEDEX **sandrine.charles@univ-lyon1.fr**
EDISS	**INTERDISCIPLINAIRE SCIENCES-SANTÉ** **http://ediss.universite-lyon.fr** Sec. : Bénédicte LANZA Bât. Atrium, UCB Lyon 1 Tél : 04.72.44.83.62 secretariat.ediss@univ-lyon1.fr	**Mme Sylvie RICARD-BLUM** Institut de Chimie et Biochimie Moléculaires et Supramoléculaires (ICBMS) - UMR 5246 CNRS - Université Lyon 1 Bâtiment Raulin - 2ème étage Nord 43 Boulevard du 11 novembre 1918 69622 Villeurbanne Cedex Tél : +33(0)4 72 44 82 32 **sylvie.ricard-blum@univ-lyon1.fr**
INFOMATHS	**INFORMATIQUE ET MATHÉMATIQUES** **http://edinfomaths.universite-lyon.fr** Sec. : Renée EL MELHEM Bât. Blaise PASCAL, 3e étage Tél : 04.72.43.80.46 infomaths@univ-lyon1.fr	**M. Hamamache KHEDDOUCI** Université Claude Bernard Lyon 1 Bât. Nautibus 43, Boulevard du 11 novembre 1918 69 622 Villeurbanne Cedex France Tél : 04.72.44.83.69 **hamamache.kheddouci@univ-lyon1.fr**
Matériaux	**MATÉRIAUX DE LYON** **http://ed34.universite-lyon.fr** Sec. : Yann DE ORDENANA Tél : 04.72.18.62.44 yann.de-ordenana@ec-lyon.fr	**M. Stéphane BENAYOUN** Ecole Centrale de Lyon Laboratoire LTDS 36 avenue Guy de Collongue 69134 Ecully CEDEX Tél : 04.72.18.64.37 **stephane.benayoun@ec-lyon.fr**
MEGA	**MÉCANIQUE, ÉNERGÉTIQUE, GÉNIE CIVIL, ACOUSTIQUE** **http://edmega.universite-lyon.fr** Sec. : Stéphanie CAUVIN Tél : 04.72.43.71.70 Bâtiment Direction INSA Lyon mega@insa-lyon.fr	**M. Jocelyn BONJOUR** INSA Lyon Laboratoire CETHIL Bâtiment Sadi-Carnot 9, rue de la Physique 69621 Villeurbanne CEDEX **jocelyn.bonjour@insa-lyon.fr**
ScSo	**ScSo*** **https://edsciencessociales.universite-lyon.fr** Sec. : Mélina FAVETON INSA : J.Y. TOUSSAINT Tél : 04.78.69.77.79 melina.faveton@univ-lyon2.fr	**M. Bruno MILLY** Université Lumière Lyon 2 86 Rue Pasteur 69365 Lyon CEDEX 07 **bruno.milly@univ-lyon2.fr**

*ScSo : Histoire, Géographie, Aménagement, Urbanisme, Archéologie, Science politique, Sociologie, Anthropologie

Cette thèse est accessible à l'adresse : https://theses.insa-lyon.fr/publication/2023ISAL0068/these.pdf
© [L. Vergnaud], [2023], INSA Lyon, tous droits réservés

Abstract

In nuclear medicine, targeted radionuclide therapy (TRT) involves intravenous injection of a radiopharmaceutical (radioactive drug) that specifically binds to tumour cells through a selected vector based on the type of receptors overexpressed. The radiopharmaceutical is internalised by the tumour cells, leading to their destruction. This treatment has proven effective for neuroendocrine tumours (NETs) and metastatic castration-resistant prostate cancer (mCRPC). However, treatment plans are standardised despite studies showing variations in absorbed doses (energy absorbed per unit mass) among different patients' organs at risk and tumours. To personalise these treatments, it is necessary to estimate absorbed doses and compare them with treatment toxicities and efficacy.

During the radioactive decay of certain radioisotopes such as ^{177}Lu, gamma photons are emitted and can be detected using a gamma camera. A Single Photon Emission Computed Tomography (SPECT) acquisition is typically performed to determine the 3D biodistribution of the radiopharmaceutical at a given time point, which is necessary for estimating absorbed doses in the regions of interest. In this thesis, we focused on the quantitative and dosimetric aspects of ^{177}Lu and ^{90}Y therapies using acquired SPECT images.

In TRT, dosimetry for ^{177}Lu requires monitoring the biodistribution of the radiopharmaceutical over time, which involves multiple post-injection SPECT acquisitions. However, clinical constraints often limit the availability of desired acquisition times and numbers. Therefore, the primary objective of the first contribution was to provide a dosimetric workflow that can adapt to the available number of acquisitions for ^{177}Lu-DOTATATE therapies in NETs. Several simplified dosimetry methods were proposed and evaluated against a reference method based on three post-injection acquisitions.

Selective Internal Radiation Therapy (SIRT) is a local treatment for liver lesions where ^{90}Y microspheres are injected into the intrahepatic artery, blocking the vessels that supply the tumours and destroying them. This treatment is simulated using an injection of ^{99m}Tc combined with albumin macroaggregates. A SPECT acquisition is then performed, and the image is reconstructed to predict absorbed doses and adjust the activity to be injected for therapy. During the SPECT acquisition, respiratory motion can impact the acquisition but is not necessarily corrected during reconstruction. The second contribution assessed the dosimetric impact of correcting for respiratory motion by comparing dose and activity estimates for injection with and without motion correction in the reconstruction.

Finally, more recently, CZT gamma cameras have allowed for reduced acquisition times while maintaining image quality. However, they do not always enable the acquisition of high-energy photons (>200 keV) and therefore, the recommended energy peak for ^{177}Lu dosimetry. In a third contribution, a feasibility study of quantification with ^{177}Lu (energy peak at 113 keV) was conducted using phantoms, and optimal reconstruction parameters were provided. These parameters were then used in a preliminary dosimetric study on patients treated with ^{177}Lu-PSMA.

Cette thèse est accessible à l'adresse : https://theses.insa-lyon.fr/publication/2023ISAL0068/these.pdf
© [L. Vergnaud], [2023], INSA Lyon, tous droits réservés

Cette thèse est accessible à l'adresse : https://theses.insa-lyon.fr/publication/2023ISAL0068/these.pdf
© [L. Vergnaud], [2023], INSA Lyon, tous droits réservés

Résumé

En médecine nucléaire, la radiothérapie interne vectorisée (RIV) consiste à injecter par intraveineuse un radiopharmaceutique (médicament radioactif) qui va venir se fixer aux cellules tumorales grâce à un vecteur sélectionné selon le type de récepteurs sur-exprimés par ces dernières, être internalisé et les détruire. Ce traitement a démontré son efficacité pour les tumeurs neuroendocrines (TNE) et pour les cancers de la prostate métastatiques résistants à la castration (PC). Cependant, les plans de traitement sont standardisés alors que des études ont montrées que les doses absorbées (énergie absorbée par unité de masse) par les organes à risque et les tumeurs diffèrent d'un patient à un autre. Afin de pouvoir les personnaliser, il est donc nécessaire d'estimer les doses absorbées et de les mettre en regard avec les toxicités et l'efficacité du traitement.

Lors de la désintégration radioactive de certains radioisotopes tels que le ^{177}Lu, des photons gamma sont émis et peuvent être détectés à l'aide d'une gamma caméra. Une acquisition TEMP (Tomographie d'Emission MonoPhotonique) est généralement réalisée afin de connaître la biodistribution 3D du radiopharmaceutique à un instant donné qui est nécessaire pour l'estimation des doses absorbées par les régions d'intérêt. Dans cette thèse, nous nous sommes intéressés aux aspects quantitatifs et dosimétriques des thérapies au ^{177}Lu et à l'^{90}Y à partir des images SPECT acquises.

En RIV, la dosimétrie au ^{177}Lu requière un suivi de la biodistribution du radiopharmaceutique au cours du temps et donc, des acquisitions TEMP post-injection multiples. Cependant, les contraintes cliniques ne permettent pas toujours de disposer des temps et du nombre d'acquisitions que l'on souhaiterait. C'est pourquoi, la première contribution a eu pour objectif de fournir un workflow dosimétrique s'adaptant au nombre d'acquisitions disponibles pour les thérapies au ^{177}Lu-DOTATATE (TNE). Plusieurs méthodes de dosimétrie simplifiées ont été proposées et évaluées par rapport à une méthode de référence s'appuyant sur trois acquisitions post-injection.

La radiothérapie interne sélective (RIS) est un traitement local des lésions hépatiques dans lequel des microsphères d'^{90}Y sont injectées dans l'artère intra-hépatique, vont venir se bloquer dans les vaisseaux irrigant les tumeurs et les détruire. Ce traitement est simulé à l'aide d'une injection de 99mTc associé à des macroaggrégats d'albumine. Une acquisition TEMP est ensuite réalisée puis l'image est reconstruite afin de prédire les doses absorbées et d'adapter l'activité à injecter pour la thérapie. Pendant l'acquisition TEMP, les mouvements respiratoires peuvent impacter l'acquisition mais ne sont pas forcément corrigés au cours de la reconstruction. La seconde contribution a permis d'évaluer l'impact dosimétrique de la correction du mouvement respiratoire en comparant les estimations de doses et d'activité à injecter avec et sans correction du mouvement dans la reconstruction.

Enfin, plus récemment, les gamma caméras CZT ont permis de réduire les durées d'acquisition tout en conservant la qualité de l'image. Cependant, elles ne permettent pas toujours d'acquérir les photons de hautes énergies (>200 keV) et donc, le pic

Cette thèse est accessible à l'adresse : https://theses.insa-lyon.fr/publication/2023ISAL0068/these.pdf
© [L. Vergnaud], [2023], INSA Lyon, tous droits réservés

énergétique recommadé pour la dosimétrie au ^{177}Lu. Dans une troisième contribution, une étude de faisabilité de la quantification au ^{177}Lu (pic énergétique à 113 keV) a été réalisée à l'aide de fantômes et des paramètres de reconstruction optimaux ont été fournis. Ces paramètres ont ensuite été utilisés lors d'une étude dosimétrique préliminaire sur patients traités au ^{177}Lu-PSMA.

Cette thèse est accessible à l'adresse : https://theses.insa-lyon.fr/publication/2023ISAL0068/these.pdf
© [L. Vergnaud], [2023], INSA Lyon, tous droits réservés

Acknowledgements

Ça y est ! Mes trois années de thèse sont maintenant terminées !
Trois années de travail, de découvertes et de rencontres !
Trois années intenses dans le monde de la recherche académique qui n'auraient pas été ce qu'elles ont été sans de nombreuses personnes que je tenais à remercier.

Pour commencer, mes directeurs de thèse, David SARRUT et Jean-Noël BADEL, qui furent en premier lieu les encadrants de mon projet de fin d'études (Et oui, ça remonte !) et qui m'ont, par la suite, permis de continuer l'aventure avec eux en thèse. Leurs enseignements respectifs ont coloré ma formation de chercheuse : d'un côté, la découverte de la dosimétrie, des calculs associés et des simulations Monte Carlo avec David, et de l'autre, la thérapie en médecine nucléaire, la préparation de fantômes et les acquisitions avec Jean-Noël. Je garde bien sûr en tête "qu'il faut toujours remettre au lendemain ce que tu aurais dû faire la veille" [David Sarrut] et qu'il est totalement possible d'associer médecine nucléaire et science fiction (ex : Star Wars) ou encore, médecine nucléaire et sport pour l'homogénéisation des fantômes, n'est-ce pas JN. Merci également de m'avoir permis de participer à de nombreux congrès et séminaires à l'international (Montpellier, Barcelone, Dublin, Viennes) afin de présenter régulièrement les travaux en cours et de m'avoir aider à les publier (David, pour les prochains doctorants, limite peut-être le vert même s'il est symbole d'espoir ;)). Merci mille fois !!!

Mes remerciements vont également aux membres de mon jury de thèse (Yuni DEWARAJA et John DICKSON en tant que rapporteurs et Lidia STRIGARI et Florent CACHIN en tant qu'examinateurs) qui m'ont fait l'honneur d'accepter d'évaluer mon travail bien que leurs emplois du temps soient chargés et d'avoir assister en présentiel à ma soutenance de thèse malgré la distance (Etats-Unis, Italie, Royaume-Uni et France). Je souhaite également remercier Anne-Laure GIRAUDET d'avoir accepté d'être membre invitée de mon jury, d'avoir été présente lors de la soutenance et de favoriser au quotidien l'obtention de données d'imagerie pour la recherche : c'est un élément primordial pour mener à bien ce type d'étude ! Merci !!!

Je tenais également à remercier tous mes collègues de travail du CLB toujours présents quand il y a besoin et surtout, toujours de bonne humeur ! Ce sont des personnes géniales avec qui j'ai pu passer de très bons moments (repas, pots de thèse, escapes game, cuisine, partage de bureau, voyage et j'en passe !). Pour ne pas faire très original, je vais citer ces personnes dans l'ordre alphabétique : Albert, Anaïs, Ane, Antoine, Aurélien, Camelea, David B., Eduardo, Estelle, Fériel, Francesca, Hoa, Joey, Lise-Marie, Madalina, Nelly, Maxime, Mélanie, Morritz, Théo, Thomas. Mention spéciale pour Madalina et Francesca avec qui je suis partie en congrès à Dublin et avec qui nous avons passé une semaine absolument incroyable ! Mention spéciale également pour Thomas, pour son aide précieuse que ce soit dans la récupération des données cliniques, la résolution de problèmes informatiques ou encore la préparation de la salle de soutenance ! Jean-Michel, merci pour ton

Cette thèse est accessible à l'adresse : https://theses.insa-lyon.fr/publication/2023ISAL0068/these.pdf
© [L. Vergnaud], [2023], INSA Lyon, tous droits réservés

temps et tes précieux conseils quel que soit le domaine (article, thé, emploi). Merci !!!

Du côté de la clinique, je souhaitais remercier Aurélie MOREAU pour tout le temps qu'elle a consacré à la relecture de mon travail (article, chapitre de thèse), pour tous ses conseils, toutes ses explications et sa bienveillance ! Merci également aux internes, Mina et Loris, avec qui j'ai pu beaucoup échanger lors des longues heures passées dans leur bureau afin de reconstruire toutes les images des patients avec les paramètres optimaux. Merci aux médecins, physiciens, radiopharmaciens et manips pour leur aide lorsqu'il y en a eu besoin (préparations de fantômes, discussion des travaux en cours). Merci !!!

Tout au long de ces années, j'ai pu rencontrer de nombreux physiciens/chercheurs qui m'ont beaucoup apporté et que je souhaitais également remercier. Merci pour tous vos conseils et vos enseignements !!!

Cette thèse n'aurait jamais été possible sans le financement du LYriCAN. Cela m'a permis de publier mes travaux et de pouvoir les présenter lors de congrès internationaux ! Merci à toutes les personnes qui ont rendu cela possible !!!

Enfin, mes derniers remerciements vont à ma famille et mes amis qui ont tous à leur façon contribué à la réussite de cette thèse ! Merci à mes parents de m'avoir soutenu tout au long de mes études mais promis, je m'arrête ici, 8 années c'est déjà bien ! Enfin, on verra ce que l'avenir me réserve ! Merci à la team Strasbourgeoise qui se reconnaîtra ! Merci pour leur amitié sans faille depuis le début de nos études en école d'ingénieurs ! Merci aux teams boxe et jujitsu avec qui j'ai passé de très bons moments et qui m'ont permis de garder un bon équilibre pendant cette thèse ! Merci à toutes et tous !!!

Je conclurais ces remerciements en disant que "tout est possible lorsque l'on est motivé, même faire une thèse en physique médicale sans master de physique médicale !"

Merci !!!!!!!!!!!!!!!!!!!!!!!!!!!!

Cette thèse est accessible à l'adresse : https://theses.insa-lyon.fr/publication/2023ISAL0068/these.pdf
© [L. Vergnaud], [2023], INSA Lyon, tous droits réservés

Contents

Cette thèse est accessible à l'adresse : https://theses.insa-lyon.fr/publication/2023ISAL0068/these.pdf
© [L. Vergnaud], [2023], INSA Lyon, tous droits réservés

Cette thèse est accessible à l'adresse : https://theses.insa-lyon.fr/publication/2023ISAL0068/these.pdf
© [L. Vergnaud], [2023], INSA Lyon, tous droits réservés

Cette thèse est accessible à l'adresse : https://theses.insa-lyon.fr/publication/2023ISAL0068/these.pdf
© [L. Vergnaud], [2023], INSA Lyon, tous droits réservés

Cette thèse est accessible à l'adresse : https://theses.insa-lyon.fr/publication/2023ISAL0068/these.pdf
© [L. Vergnaud], [2023], INSA Lyon, tous droits réservés

List of Figures

Cette thèse est accessible à l'adresse : https://theses.insa-lyon.fr/publication/2023ISAL0068/these.pdf
© [L. Vergnaud], [2023], INSA Lyon, tous droits réservés

Cette thèse est accessible à l'adresse : https://theses.insa-lyon.fr/publication/2023ISAL0068/these.pdf
© [L. Vergnaud], [2023], INSA Lyon, tous droits réservés

Cette thèse est accessible à l'adresse : https://theses.insa-lyon.fr/publication/2023ISAL0068/these.pdf
© [L. Vergnaud], [2023], INSA Lyon, tous droits réservés

Cette thèse est accessible à l'adresse : https://theses.insa-lyon.fr/publication/2023ISAL0068/these.pdf
© [L. Vergnaud], [2023], INSA Lyon, tous droits réservés

Cette thèse est accessible à l'adresse : https://theses.insa-lyon.fr/publication/2023ISAL0068/these.pdf
© [L. Vergnaud], [2023], INSA Lyon, tous droits réservés

Cette thèse est accessible à l'adresse : https://theses.insa-lyon.fr/publication/2023ISAL0068/these.pdf
© [L. Vergnaud], [2023], INSA Lyon, tous droits réservés

List of Tables

Cette thèse est accessible à l'adresse : https://theses.insa-lyon.fr/publication/2023ISAL0068/these.pdf
© [L. Vergnaud], [2023], INSA Lyon, tous droits réservés

Cette thèse est accessible à l'adresse : https://theses.insa-lyon.fr/publication/2023ISAL0068/these.pdf
© [L. Vergnaud], [2023], INSA Lyon, tous droits réservés

Cette thèse est accessible à l'adresse : https://theses.insa-lyon.fr/publication/2023ISAL0068/these.pdf
© [L. Vergnaud], [2023], INSA Lyon, tous droits réservés

Cette thèse est accessible à l'adresse : https://theses.insa-lyon.fr/publication/2023ISAL0068/these.pdf
© [L. Vergnaud], [2023], INSA Lyon, tous droits réservés

Acronyms

BED	Biologically Effective Dose
BSA	Body Surface Area
BP	Bed Position
CT	Computed Tomography
EBRT	External Beam Radiation Therapy
EQD2	Equivalent Dose in 2 Gy fraction
EUD	Equivalent Uniform Dose
GFR	Glomerular Filtration Rate
HCC	Hepatocellular Carcinoma
ICC	Intrahepatic Cholangiocarcinoma
LET	Linear Energy Transfer
LO	Limiting Organ
MAA	Macroaggregated Albumin
mCRC	metastases of Colorectal Cancer
MEGP	Medium Energy General Purpose
MTD	Maximum Tolerated Dose
NET	Neuroendocrine Tumor
NLMM	Non-Linear Mixed Model
OAR	Organ at Risk
OS	Overall Survival
PBPK	Physiologically-based pharmacokinetic
PET	Positron Emission Tomography
PRRT	Peptide Receptor Radionuclide Therapy
PSMA	Prostate-Specific Membrane Antigen
ROI	Region of Interest
RPT	Radiopharmaceutical Therapy

Cette thèse est accessible à l'adresse : https://theses.insa-lyon.fr/publication/2023ISAL0068/these.pdf
© [L. Vergnaud], [2023], INSA Lyon, tous droits réservés

SIRT Selective Internal Radiation Therapy

SPECT Single Photon Emission Computed Tomography

SSTR Somatostatin Receptor

STP Single Time Point

TAC Time Activity Curve

TDRC Time Dose-Rate Curve

VOI Volume of Interest

Cette thèse est accessible à l'adresse : https://theses.insa-lyon.fr/publication/2023ISAL0068/these.pdf
© [L. Vergnaud], [2023], INSA Lyon, tous droits réservés

Introduction

Cancer is a disease characterised by the uncontrolled multiplication and proliferation of abnormal cells, which evade regulatory mechanisms (*Definition* 2023). In France, in 2018, 382,000 new cases were diagnosed and, this figure is expected to rise in the future due to the aging population, advancement in diagnoses and an increase in risky behaviour (*Cancer figures* 2023). Personalised patient management is undertaken to determine the most suitable treatment options, including surgery, radiotherapy, chemotherapy, hormone therapy, immunotherapy or even targeted therapies (*Cancer treatments* 2023). More recently, Selective Internal Radiation Therapy (SIRT) and Targeted Radionuclide Therapy (TRT) have been included to this list.

These therapies, which are offered in nuclear medicine departments, tend to be tailored to each patient, similar to the approach used in external beam radiation therapy (EBRT). This is already the case with SIRT, which is a localised liver treatment. Prior to SIRT, a planning stage with ^{99m}Tc-MAA (macroaggregated albumin) is conducted to determine the appropriate ^{90}Y activity to be injected. This process aims to enhance the treatment response (Garin et al., 2021). However, in TRT with ^{177}Lu, treatments are standardised for all patients: they are injected with the same activity. Nevertheless, since 2018 in France, the public health code, specifically article R1333-62, stipulates that the radiation exposure to tissues must be "assessed and planned on an individual basis". The goal is to maximise exposure to tumours while minimising exposure to organs at risk (OAR).

The radiation exposure can be measured by estimating the energy deposited per unit of mass in each tissue, also known as the *absorbed dose*. It relies on factors such as the radioisotope used, its activity, its proximity to the target tissue, and the duration of exposure. Consequently, it is crucial to monitor the biodistribution of the radioisotope over time to enable dosimetry. This is especially important in the case of treatments involving^{177}Lu, as radiopharmaceuticals can either bind to tumours or OARs, or they can be eliminated through urination.

^{177}Lu offers the advantage of enabling both therapy and imaging, allowing for the assessment of its biodistribution. As it undergoes disintegration, it emits β^- particles that can be used for treating lesions. Additionally, the emitted gamma photons can be detected to visualise the treated areas. Detection of these photons is typically performed using a gamma camera, commonly an Anger-type camera, during SPECT/CT acquisition. Recent advancements have led to the development of CZT gamma cameras, initially for cardiac applications (Imbert et al., 2012) and subsequently for various other applications in nuclear medicine (Desmonts et al., 2020; Song et al., 2023). Solid-state cameras are gaining interest due to their superior energy resolution and detection efficiency compared to Anger cameras (Wernick and Aarsvold, 2004; Guérin et al., 2008), potentially enabling high-quality images with reduced acquisition time (3D whole-body acquisitions).

Dosimetry studies for ^{177}Lu therapies are currently the subject of extensive research (Hänscheid et al., 2017; Delker et al., 2016; Jackson et al., 2020a). However, standardisation and the establishment of a common methodology have not yet been

Cette thèse est accessible à l'adresse : https://theses.insa-lyon.fr/publication/2023ISAL0068/these.pdf
© [L. Vergnaud], [2023], INSA Lyon, tous droits réservés

achieved. One of the major challenges in the clinical implementation of these therapies lies in monitoring the biodistribution of ^{177}Lu over time. This task is particularly challenging due to the constraints associated with conducting multiple planar and/or SPECT acquisitions following each injection. Factors like the patient's health status, camera availability and scheduling, and the cost of examinations can restrict frequent acquisitions. Moreover, the acquired data are influence by physical phenomena that can be partially or entirely corrected during the reconstruction process, with parameters specific to each hospital.

This thesis focuses on the dosimetry and quantitative aspects of therapies using ^{90}Y (^{99m}Tc used for the pre-treatment planning) and ^{177}Lu. The primary objective is to establish clinical dosimetry protocols for ^{177}Lu therapies, considering practical limitations such as the available gamma camera types and the number of acquisitions feasible in a clinical setting. The second objective is to evaluate the impact of respiratory motion on predictive dosimetry, a crucial aspect in SIRT for tailoring the injected ^{90}Y activity to individual patients. The thesis is divided into two parts: *Part I* focuses on the current state of the art, while *Part II* presents original contributions.

The state of the art is structured into five chapters. Chapter 1 provides an overview of different types of radiation therapy, such as EBRT, SIRT, and TRT. A specific emphasis is placed on comparing EBRT and TRT to highlight the clinical challenges associated with TRT. Chapter 2 offers a concise review of the existing literature on ^{177}Lu TRT, with a focus on ^{177}Lu-DOTATATE and ^{177}Lu-PSMA. It includes a description of phase III trials, treatment regimens, adverse events, predictive and prognostic factors, as well as an overview of ongoing clinical trials. Chapter 3 provides a brief introduction to the radioisotopes used in this thesis, namely ^{177}Lu and ^{99m}Tc, along with an overview of Anger and CZT gamma cameras. Chapter 4 delves into the quantification and dosimetry aspects of TRT. It presents a non-exhaustive description of tomographic reconstructions, applied corrections, and dosimetric methods employed. Lastly, Chapter 5 comprises a literature review of available dosimetric workflows, with a specific focus on simplified methods involving only one or two acquisitions.

The subsequent four chapters concentrate on the contributions made throughout the three-year duration of the thesis. Chapter 6 encompasses the implementation of a dosimetric workflow tailored to the number of post-injection SPECT/CT acquisitions for patients undergoing treatment with ^{177}Lu-DOTATATE. In our centre, three acquisitions are typically conducted after the initial injection, followed by a single acquisition after each subsequent injection. However, this number may occasionally be reduced due to clinical limitations. The chapter introduces simplified methods and evaluates the resulting discrepancies compared to the reference method based on three acquisitions. This work has been published in EJNMMI Physics (Vergnaud et al., 2022). Chapter 7 focuses on assessing the impact of respiratory motion correction on dosimetry. This study employs ^{99m}Tc SPECT images of patients treated with SIRT, as the injected activity is concentrated in the liver, which is significantly affected by respiratory movement. This work has also been published in EJNMMI Physics (Vergnaud et al., 2023). In contrast to chapters 6 and 7, the final two chapters revolve around the utilisation of CZT gamma cameras in the context of ^{177}Lu dosimetry. Chapter 8 evaluates the performance of this novel camera type for ^{177}Lu dosimetry using phantoms. Chapter 9 complies preliminary dosimetric results obtained for the kidneys, liver, and spleen of thirteen patients treated with ^{177}Lu-PSMA. The work presented in Chapter 8 has been submitted to EJNMMI Physics and is currently undergoing the review process.

Cette thèse est accessible à l'adresse : https://theses.insa-lyon.fr/publication/2023ISAL0068/these.pdf
© [L. Vergnaud], [2023], INSA Lyon, tous droits réservés

Part I

State of the art

Cette thèse est accessible à l'adresse : https://theses.insa-lyon.fr/publication/2023ISAL0068/these.pdf
© [L. Vergnaud], [2023], INSA Lyon, tous droits réservés

Cette thèse est accessible à l'adresse : https://theses.insa-lyon.fr/publication/2023ISAL0068/these.pdf
© [L. Vergnaud], [2023], INSA Lyon, tous droits réservés

Chapter 1

External and internal radiation therapies

In this chapter, we briefly review several types of radiation-based cancer therapies in order to situate radionuclide-based treatments that will be further studied in the following chapters.

Radiotherapy is a type of cancer treatment developed more than one century ago (Gianfaldoni et al., 2017). Today, external beam radiotherapy (EBRT) is the most common, recommended for the treatment of well-differentiated solid tumours. Before treatment in itself, a personalised treatment plan is defined for each patient in order to maximise its effectiveness while limiting possible toxicities. More recently, internal radiotherapy has appeared in various forms (with sealed or unsealed sources, radioisotope associated with a ligand or not) and is aimed at other types of tumours (inoperable or inaccessible such as diffuse metastatic lesions). In this chapter, a non-exhaustive description of external radiotherapy is proposed (Section 1.1) followed by the presentation of the different types of internal radiotherapy (Section 1.2) with a focus on selective internal radiation therapy (SIRT) and targeted radionuclide therapy (TRT). Section 1.3 is devoted to the comparison of EBRT and TRT before concluding by highlighting the clinical challenges of TRT in Section 1.4).

1.1 External Beam Radiation Therapy (EBRT)

1.1.1 Principle

External radiotherapy consists of focusing an ionising beam (photons, electrons, or proton, ions for hadrontherapy) from different angles on a target volume to be treated. The dose of radiation to be delivered is prescribed and a treatment plan is drawn up to define the beam ballistic, the number of sessions, the dose per session and the frequency to optimise the irradiation (*Radiothérapie externe* 2023). A schematic diagram of the operation of external radiotherapy is shown in Figure 1.1.

There are different types of external radiotherapy (3-D conformal radiation therapy, Intensity-modulated radiation therapy, Volumetric Modulated Arc Therapy (VMAT), Tomotherapy, Stereotactic radiosurgery, Stereotactic body radiation therapy) which will not be described in this chapter (Yorke et al., 2011; *External Beam Radiation Therapy for Cancer* 2023).

1.1.2 Effects of ionising radiation on cells

Ionizing radiation will damage and/or fragment the DNA strands of cells (single-strand or double-strand breaks) by direct or indirect interaction following the

Cette thèse est accessible à l'adresse : https://theses.insa-lyon.fr/publication/2023ISAL0068/these.pdf
© [L. Vergnaud], [2023], INSA Lyon, tous droits réservés

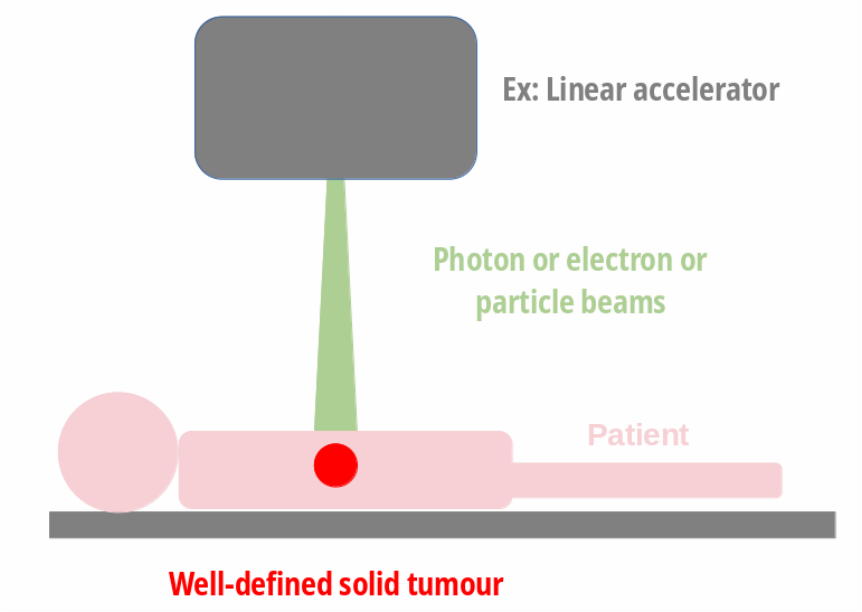

FIGURE 1.1 – Schematic diagram of external radiotherapy

creation of free radicals (hydroxyl) during the radiolysis of water [1] (Kassis and Adelstein, 2005). The nature of the damage caused impacts the fate of the cells. Indeed, a double-strand break leads irremediably to cell death, whereas single-strand breaks are potentially repairable unless other interactions damage the second strand (Dale and Carabe-Fernandez, 2005). The repair can be "faithful", that is to say consistent with the initial DNA: the cell survives normally. If this is not the case, the mutations can lead to cell death (programmed or elimination by the immune system), cancer or an abnormality in the DNA (*Arbre des évolutions possibles de la cellule* 2023). Each type of tissue has its own repair capacity of the order of 0.5h-3h which implies that all of the repairs can take place between two external radiotherapy sessions: there is therefore no cumulative effect on the cells (Dale and Carabe-Fernandez, 2005). Moreover, biological responses (bystander effects) as well as the involvement of the immune system could also be involved in the damage to tumor cells (Pouget et al., 2022).

1.1.3 Absorbed Doses

Absorbed doses (D) corresponds to the energy (E) provided by the radiation and absorbed in a mass of tissue, divided by the mass (M) of this tissue as expressed in the equation (1.1). It is expressed in J/kg or more generally in Grays (Gy).

$$D[Gy] = \frac{E[J]}{M[kg]} \tag{1.1}$$

It is also possible to estimate the biologically effective dose (BED) which takes into account the physical absorbed dose but also the radiobiological parameters. It is also expressed in Gy. These quantities are important when setting up the treatment plan because the tumours must receive the prescribed dose and the doses to healthy tissues must not exceed certain thresholds. In this thesis, only the physical absorbed doses were considered.

1. Chemical decomposition of water by interaction with ionizing radiation which gives rise to hydrogen and hydroxyl radicals (Saffre, 2011).

Cette thèse est accessible à l'adresse : https://theses.insa-lyon.fr/publication/2023ISAL0068/these.pdf
© [L. Vergnaud], [2023], INSA Lyon, tous droits réservés

1.1.4 Organs at Risk (OAR)

Ionizing radiation beams pass through healthy tissues before reaching their target for which it is essential to estimate absorbed doses. Some organs can be damaged if the doses they receive exceed a given threshold set by recommendations (Milano et al., 2007): these are organs at risk (OAR). These thresholds depend on the volumes considered and are used when planning the treatment: reaching the dose prescribed to the tumour while sparing the surrounding healthy tissue as much as possible.

1.2 Internal Radiation Therapy

1.2.1 Iratherapy

Iratherapy or radioiodine 131 therapy is used to treat hyperthyroidism (Kaplan et al., 1998) and thyroid cancers (Sweeney and Johnston, 1995). This therapy consists of administering radioactive iodine 131 to the patient orally or by injection, as thyroid cells naturally take it up as well as well-differentiated cancer cells. During its decay, the 131 iodine (^{131}I, $t_{\frac{1}{2}}$ = 8.2 days) will emit β particles (192 keV) that will damage healthy and tumour thyroid cells as well as gamma photons (essentially 365 keV) that will allow the control of the treatment by acquiring scintigraphic images. In the case of cancers, this treatment is generally offered after surgical removal of the thyroid to destroy the remaining tumour cells and/or distant metastases or to remove the thyroid if it is not operable.

1.2.2 Internal radiation therapy for painful bone metastases

As with thyroid treatment, internal radiation therapy can be used to treat pain associated with bone metastases of prostrate or breast cancers for example. Indeed, some radionuclides (^{89}Sr, ^{223}Ra, ^{32}P) are absorbed by bones by behaving biologically like calcium. Liepe and Kotzerke, 2011 have proposed a review of the radionuclides available for this type of treatment, emphasising that this therapy is effective because it allows high doses to be delivered to metastatic lesions while preserving healthy tissue.

1.2.3 Brachytherapy

Brachytherapy involves positioning a sealed radioactive source close to or inside the tumour, either temporarily or permanently. This technique allows the lesion to be strongly irradiated while preserving the surrounding healthy tissue. It is characterised by the radionuclide chosen (^{226}Ra,^{137}Cs, ^{60}Co, ^{182}Ta, ^{192}Ir, ^{125}I, ^{198}Au, ^{32}P, ^{90}Sr, ^{90}Y, ^{106}Ru (*La Brachythérapie ou Curithérapie* 2023)), the location (interstitial, intracavity, intraluminal, surface, intraoperative (Odei et al., 2016)), the duration of irradiation and the dose rate (from ultra low to high) as described by Skowronek, 2017. It can be used for skin, breast and prostate cancers for example (non-exhaustive list) (Tanderup et al., 2017).

Cette thèse est accessible à l'adresse : https://theses.insa-lyon.fr/publication/2023ISAL0068/these.pdf
© [L. Vergnaud], [2023], INSA Lyon, tous droits réservés

1.2.4 Selective Internal Radiation Therapy (SIRT)

1.2.4.1 Description of the treatment

Selective Internal radiation therapy or radioembolisation is a local treatment for inoperable hepatic tumours. It is indicated and reimbursed in France in cases of hepatocellular carcinoma (HCC), intrahepatic cholangiocarcinoma (ICC) or metastases of colorectal cancer (mCRC). In the literature, it is also used in breast cancer metastases (Barakat et al., 2022,Cheng et al., 2021), neuroendocrine tumours (King et al., 2008), uveal melanoma (Gonsalves et al., 2019) and metastases of pancreatic cancer (Helmberger et al., 2021). This treatment consists to bring microspheres of ^{90}Y as close as possible to the lesion, via the hepatic artery using a microcatheter, during an interventional radiology procedure. The disintegration of ^{90}Y atoms will generate β^- emissions whose average distance and energy are of the order of 3 mm and 0.93 MeV (Rathke et al., 2019) and which will damage the tumour cells (1.2).

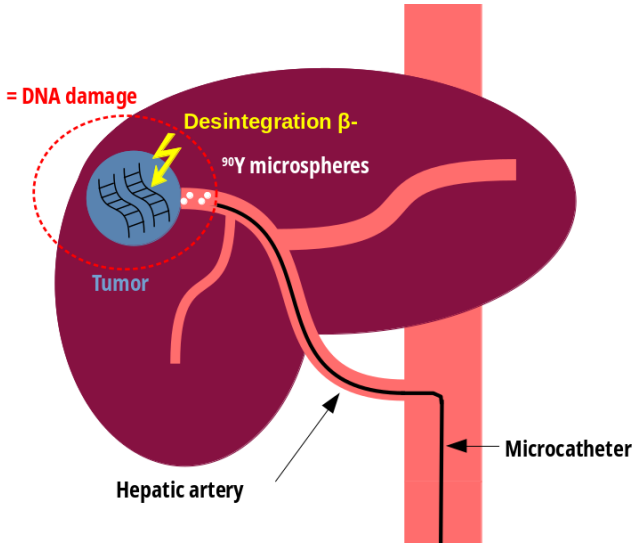

FIGURE 1.2 – Schematic diagram of radioembolisation treatment

1.2.4.2 Types of ^{90}Y microspheres

In France, two types of ^{90}Y microspheres are available: resin spheres (SIR-Sphere®, Sirtex Medical Limited Australia, Sidney, Australia) and glass spheres (TheraSphere®, Boston Scientic Corporation, Marlborough, MA, USA) (Garin et al., 2020). Their specific characteristics (activity, diameters) can be for example found in the thesis of Joey Labour (Labour, 2021) and impact the biodistribution and homogeneity of the activity in the tissues. This explains why the recommended absorbed doses to tumours and healthy tissues (Weber et al., 2022) are specific to each type of spheres. Thus, for each patient, a type of microsphere is selected as well as an activity to offer the best personalised treatment. For example, Garin et al., 2021 have shown that personalising the treatment improves response rate compared to standard treatment for HCC.

1.2.4.3 Pre-treatment SIRT planning

Before treating the patient, an angiography and a ^{99m}Tc macroaggregated albumin (MAA) scintigraphy are performed to verify the safety of the treatment for the

Cette thèse est accessible à l'adresse : https://theses.insa-lyon.fr/publication/2023ISAL0068/these.pdf
© [L. Vergnaud], [2023], INSA Lyon, tous droits réservés

patient (inclusion criteria) as well as to personalise the activity to be injected.

Angiography Its aim is to know the vascularisation of the liver in order to avoid extra-hepatic shunts (pulmonary and gastrointestinal) which could occur during the injection of the microspheres, to know where to position the catheter and the blood flow. Indeed, microspheres must be as close as possible to the tumours while protecting the healthy tissue (risk of radiation pneumonitis Kim et al., 2019 for example).

Scintigraphy After the angiography stage, ^{99m}Tc-MAA (between 75 and 150 MBq, Giammarile et al., 2011) is injected to simulate the biodistribution of the microspheres in the liver. A SPECT/CT acquisition is then performed to check for the presence or absence of a shunt, to personalise the activity to be injected using predictive dosimetry and, to estimate the dose absorbed by the lungs. It could be a contraindication if it is too high compared to the maximum recommended tolerated dose. The use of ^{99m}Tc-MAA as a substitute for ^{90}Y microspheres is discussed as good correlations have been demonstrated between the absorbed tumour doses estimated with the two radionuclides (^{99m}Tc and ^{90}Y) for HCC but not for hepatic metastases (Jadoul et al., 2020; Garin et al., 2016). It should be noted that the ^{99m}Tc and the MAA can disassociate over time (free ^{99m}Tc) and that the dimensions of the MAA are not strictly the same as those of the microspheres (Garin et al., 2019).

^{166}Ho More recently, ^{166}Ho microspheres named QuiremSpheres TM (Quirem BV, Deventer, the Netherlands) have begun to be tested and used for radioembolisation (Stella et al., 2022). It has the advantage that it can be used for pre-treatment imaging (81 keV gamma photon emissions for SPECT/CT acquisition or paramagnetic properties for MRI) and for treatment (1.85 MeV β^- emissions at maximum). This allows a better prediction of the biodistribution of ^{166}Ho microspheres than if ^{99m}Tc-MAA had been used (Elschot et al., 2014).

Once the distribution of the ^{90}Y microspheres has been estimated, dosimetric methods described in section 4.5 are used to calculate the absorbed doses to healthy tissue and tumours as a function of the injected activity. The latter is modulated so that the absorbed doses follow international recommendations for tolerance limits for the type of spheres used.

1.2.4.4 PET post-treatment imaging

Once the ^{90}Y microspheres have been injected, their biodistribution is checked using PET/CT acquisition. Indeed, the ^{90}Y decay scheme leads to e^-/e^+ pairs production (32 per million decays) whose positron annihilation gives rise to two photons of 511 keV. Finally, coincidence detection will allow us to trace the location of the decay and thus the actual biodistribution of the microspheres. A dosimetric estimate can also be made to ensure that the absorbed doses correspond to the planned doses. SPECT/CT acquisition of bremsstrahlung radiation (Dewaraja et al., 2017; Siman et al., 2016) is also possible but more rarely used as the photon spectrum is continuous and the photons can be of high energy causing septal penetration and scatter as described by Rong et al., 2012.

Cette thèse est accessible à l'adresse : https://theses.insa-lyon.fr/publication/2023ISAL0068/these.pdf
© [L. Vergnaud], [2023], INSA Lyon, tous droits réservés

1.2.4.5 Limitations

The use of ^{99m}Tc-MAA biodistribution as a surrogate for ^{90}Y is still debated. Indeed, in the case of HCC, a good correlation has been demonstrated between the absorbed dose computed before and after radioembolisation while that obtained for metastatic disease is low (Jadoul et al., 2020; Garin et al., 2016). During these comparisons, the contours made on the SPECT/CT image are registered to the PET/CT image. The impact of this registration compared to a new manual contouring was evaluated by Della Gala et al., 2022 and showed that these registrations should be taken with care because the dose thresholds to the tumour to be reached can be different: between 85 and 110 Gy. Finally, it is important to stress that the position of the catheter must be the same between planning and treatment at the risk of having different biodistributions (Kim et al., 2019) and therefore different dosimetries. It is under these conditions that Richetta et al., 2019 showed a good correlation between dosimetry for patients treated for HCC with resin microspheres.

1.2.5 Targeted Radionuclide Therapy (TRT)

Targeted Radionuclide Therapy (TRT) is a treatment option for inoperable, unreachable tumours and metastases over-expressing a certain type of receptor. For example, well-differentiated or moderately differentiated grade 1 and 2 neuroendocrine tumours (NET) over-express somatostatin receptors 2 (SSTR2) (Smit Duijzentkunst et al., 2017) while they are prostate-specific membrane antigens (PSMA) in the case of cancers of the prostate. This property is exploited to reach the lesions and to treat them. Radiopharmaceuticals (radioactive drugs) specific to each pathology have been developed. They consist of a radioisotope which is the source of radiation for the treatment, a molecular vector which allows the radioisotope to be internalised in the tumour cell, and a chelator which binds the radioisotope to the vector as described in Figure 1.4. They are injected intravenously, will move through the bloodstream (Figure 1.3), and bind to the tumour receptors. It will then be internalised by the cells before disintegrating by emitting photons and/or particles (Figure 1.5). These will interact with their environment causing DNA damage and the cellular effects described in Section 1.1.2. It is important to note that internalisation depends on the vector. For instance, somatostatin antagonist analogs do not internalise and remain on the surface of tumour cells, unlike agonist analogs, which undergo internalisation (Bournaud et al., 2019).

The vector, also called ligand, can be of different natures depending on the receptors over-expressed by the tumour to achieve selective binding of the radiopharmaceutical: a peptide [2] (Cremonesi et al., 2018), an antigen (Jackson et al., 2022) or an antibody (Forrer et al., 2009b) and be associated with various radioisotopes (^{177}Lu, ^{90}Y, ^{111}In, ^{131}I, ^{225}Ac for example). It should be noted that some receptors over-expressed by the tumour may also be found in healthy organs: there may therefore be physiological uptake by certain organs which must be taken into account so as not to damage them (Demirci et al., 2016).

Currently, alpha therapies are under investigation as they may provide more effective treatment of lesions while reducing the risks of toxicity, such as hematological toxicity, commonly found in ^{177}Lu-PSMA therapies. ^{225}Ac was suggested for patient retreatment following two cycles of ^{177}Lu-PSMA in the article authored by Kratochwil et al., 2016a.

2. This is known as Peptide Receptor Radionuclide Therapy (PRRT).

Cette thèse est accessible à l'adresse : https://theses.insa-lyon.fr/publication/2023ISAL0068/these.pdf
© [L. Vergnaud], [2023], INSA Lyon, tous droits réservés

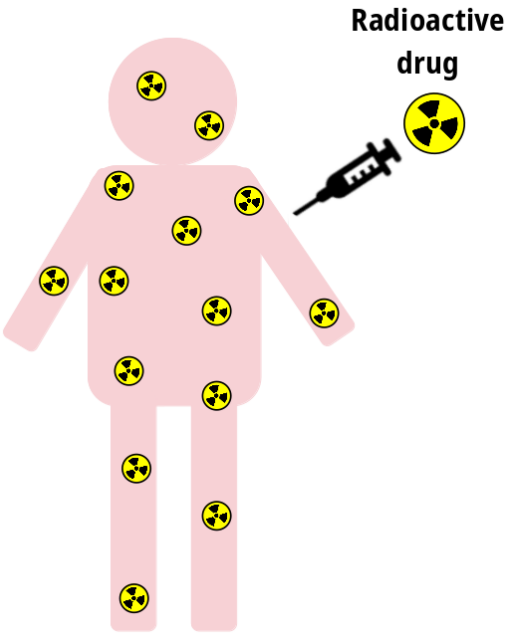

FIGURE 1.3 – Schematic diagram of how targeted radionuclide therapy works. Once the radiopharmaceutical has been injected, it moves through the bloodstream before being either internalised by the tumour cells or eliminated.

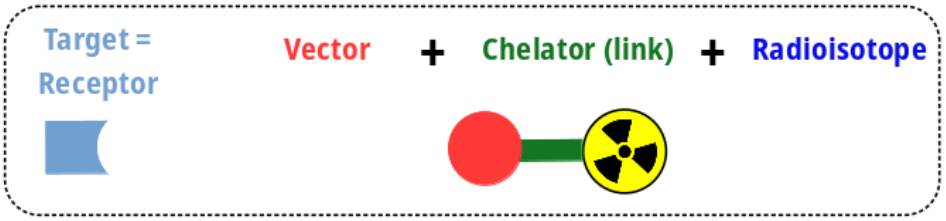

FIGURE 1.4 – Scheme of the structure of a radiopharmaceutical

In this thesis, we focus on two radiopharmaceutical therapies using ^{177}Lu: ^{177}Lu-DOTATATE and ^{177}Lu-PSMA. The first is indicated for the treatment of advanced, progressive, somatostatin receptor-positive midgut neuroendocrine tumours while the second is recommended for castration-resistant metastatic prostate cancer. A description of these therapies and the management of patients will be given in Chapter 2. This ^{177}Lu radioisotope is particularly interesting because it allows both the treatment of lesions and the viewing of what has been treated through the emission of gamma photons from the patient (Chapter 3).

1.3 Comparison between EBRT and TRT

Although the radiobiological principles used to treat tumours are the same, the cellular responses differ between EBRT and TRT (Dale and Carabe-Fernandez, 2005). The properties specific to each of them are given in Table 1.1.

External radiotherapy is a planned treatment that optimises the delivery of the prescribed dose to the tumour in order to spare healthy tissue as much as possible. The ionising beam delivers a homogeneous or heterogeneous dose to the irradiated

Cette thèse est accessible à l'adresse : https://theses.insa-lyon.fr/publication/2023ISAL0068/these.pdf
© [L. Vergnaud], [2023], INSA Lyon, tous droits réservés

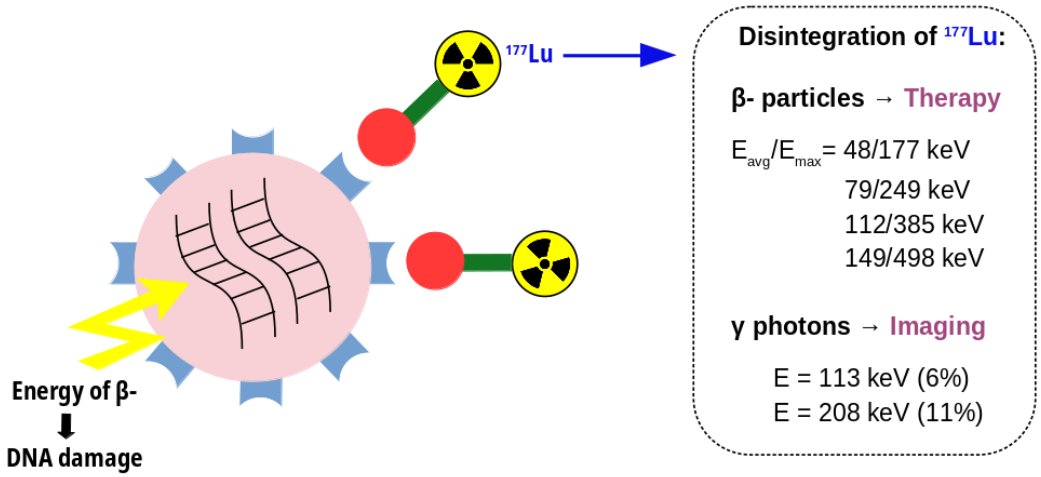

FIGURE 1.5 – Schematic diagram of targeted radionuclide therapy. The radiopharmaceutical binds to receptors on the surface of tumour cells, is internalised and the disintegration of the radioisotope causes DNA damage.

	EBRT	TRT
Type of treatment	Personalised	Standardised
Dosimetry required	Yes	No
Location of OARs	On the path of the beam	Organs expressing the same receptors as the lesions
Target volumes	Well-defined solid tumour	Inoperable or unreachable tumour and metastases
Dose-rates	High (1-2 Gy/min) Homogeneous Stable over time	Low (<0.5 Gy/h) Heterogeneous Variable over time
Irradiation time	≈ 1 minute	Continuous over several days
LET	Around 4 keV/µm	Radioisotope dependent β^-: 0.2 keV/µm α: 80-100 keV/µm

TABLE 1.1 – Comparison of properties specific to EBRT and TRT extracted from articles of Morris et al., 2021; Pouget et al., 2021; Dale and Carabe-Fernandez, 2005; Sadeghi et al., 2010; Kassis and Adelstein, 2005 and website *LET* 2023

volume and to the tissues it passes through over a very short period of time. For TRT, the treatment is systemic, which means that the distribution of the radiopharmaceutical depends on its binding to the receptors, whose distribution is not necessarily homogeneous (within a volume and between volumes). Part of the radiopharmaceutical is eliminated biologically (urination) and the other part physically (radioactive decay): there is therefore continuous irradiation of tissues by the radiopharmaceutical with a spatially and temporally variable dose-rate. The prescribed activity is the same for all patients, but the doses absorbed are not. Personalised treatment implementation is more complex for TRT than for EBRT because the characteristics of the radiation source are not known in time, nor are the duration of tissue exposure and the corresponding dose rates. Dose estimates can be made after treatment, as explained in Chapters 4, 5, 6 and 9. Radiobiological concepts have been developed

Cette thèse est accessible à l'adresse : https://theses.insa-lyon.fr/publication/2023ISAL0068/these.pdf
© [L. Vergnaud], [2023], INSA Lyon, tous droits réservés

to enable the comparison of absorbed doses delivered even when dose-rates and/or distributions differ. The biological effective dose (BED) allows for the consideration of the radiobiological effects of radiations on cells. The equivalent uniform dose (EUD) concept holds that two dose distributions are considered equivalent when they result in identical biological effects (Kalogianni et al., 2007). The equivalent dose in 2 Gy fraction (EQD2) involves the conversion of the total dose into an equivalent dose administered in 2 Gy fractions to compare treatment plans.

Finally, TRT requires special radiation protection measures, as the patient is slightly radioactive after the radiopharmaceutical has been injected (recovery of radioactive waste, hospitalisation of the patient for 24 hours, for example).

1.4 Clinical challenges

TRT has already proved its efficacy and therapeutic value in phase III clinical trials (Chapter 2), leading to its routine clinical use. However, a number of challenges remain.

1. Improving patient selection. Patient selection is essential to avoid unnecessary treatments and the adverse effects that can accompany them. A pre-treatment scintigraphic imaging, as ^{68}Ga-PSMA PET for ^{177}Lu-PSMA treatments, has to perform to check for the presence of receptors on the surface of tumour cells. If the number of receptors is insufficient, treatment will not be recommended for the patient. However, more criteria are needed to effectively detect patients who will have a good response to treatment. Studies are underway to find factors that predict response and improve selection (Chapter 2, Section 2.7).

2. Personalising treatment. In other treatments such as SIRT, personalisation of the injected activity has shown a significant improvement in the response rate (Garin et al., 2021) for advanced hepatocellular carcinoma treated with resin and glass microspheres. In TRT, the injected activities are standardised, although the effects differ from one patient to another. Dosimetry could be correlated with treatment response to fine-tune the injected activity and enhance the treatment outcome. Initial results, based on the maximum dose limit tolerated in the kidneys, have been proposed by Del Prete et al., 2019 and have shown an increase in the dose absorbed by tumours (Chapter 2, Section 2.3.2). Establishing dose-effect and dose-toxicity relationships is a major challenge in personalising TRT.

3. Adaptation to clinical constraints. TRT requires PET acquisitions for patient inclusion and SPECT/CT acquisitions for dosimetry. This means an increase in camera occupancy over very short periods of time (e.g. 3 SPECT/CT acquisitions in one week for one patient), as well as an increase in the activity of nuclear medicine departments with a growing proportion of therapy. Numerous clinical indications are currently being evaluated and will potentially be added (Chapter 2, Section 2.8). It therefore becomes difficult to set up dosimetry for all patients, to multiply SPECT acquisitions after each cycle and to bring back patients who live far from the hospital. The development of dosimetric workflows adapting to the number of acquisitions available and requiring only a small number then becomes essential. This is also the subject of Chapter 6 in the context of ^{177}Lu-DOTATATE therapies which will also be applied in Chapter 9 for ^{177}Lu-PSMA therapies.

Cette thèse est accessible à l'adresse : https://theses.insa-lyon.fr/publication/2023ISAL0068/these.pdf
© [L. Vergnaud], [2023], INSA Lyon, tous droits réservés

4. Securing the supply of radiopharmaceuticals. The supply of certain radiopharmaceuticals such as ^{177}Lu-PSMA-617 is under pressure following the halt in production at certain sites and the increase in demand as explained by Czernin and Calais, 2023. This leads to delays that can impact patient care and cause loss of opportunity.

1.5 Conclusion

Radiotherapy has diversified with the arrival of new types of therapy for which many challenges have to be met. In this chapter we wanted to provide a brief overview of the different type of radiation-based therapies. In the following sections, we will focus on the implementation of dosimetry by adapting to clinical constraints in the context of ^{177}Lu-DOTATATE and ^{177}Lu-PSMA therapies.

Cette thèse est accessible à l'adresse : https://theses.insa-lyon.fr/publication/2023ISAL0068/these.pdf
© [L. Vergnaud], [2023], INSA Lyon, tous droits réservés

Chapter 2

Targeted Radionuclide Therapy (TRT) with ^{177}Lu

This chapter is a short review of the literature on ^{177}Lu-DOTATATE and ^{177}Lu-PSMA radiopharmaceuticals used in therapy and is aimed at providing the clinical elements needed to understand the thesis. They have been proven to be of therapeutic benefit to patients in international, open-label, randomised phase III studies. A description of the different stages of patient management is proposed: pre-treatment imaging, treatment planning, adverse events, post-treatment imaging, response assessment, prognostic factors, and ongoing clinical trials.

2.1 Phase III clinical trials

2.1.1 NETTER-1 Clinical trial

The efficacy and safety of ^{177}Lu-DOTATATE in treating patients with advanced, progressive, somatostatin receptor-positive midgut neuroendocrine tumours (NET) was evaluated in the NETTER-1 phase III study (Strosberg et al., 2017b; Strosberg et al., 2021). Two hundred twenty-nine patients were included and divided into two groups: 116 patients received octreotide long-acting repeatable and ^{177}Lu-DOTATATE treatment which consists of four injections of 7.4 GBq apart of 8 weeks (treated group) and 113 patients received only octreotide long-acting repeatable (control group). The two treatments were compared on three aspects: progression-free survival, overall survival, and objective tumour response. The results of the first two end-points are shown in Figure 2.1.

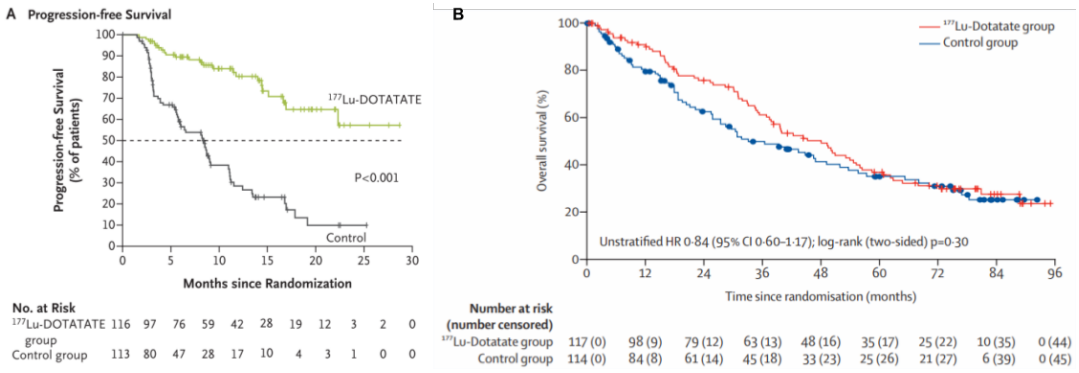

FIGURE 2.1 – Progression-free survival (left, Strosberg et al., 2017b) and overall survival (right, Strosberg et al., 2021) between the ^{177}Lu-DOTATATE group and the control group.

Cette thèse est accessible à l'adresse : https://theses.insa-lyon.fr/publication/2023ISAL0068/these.pdf
© [L. Vergnaud], [2023], INSA Lyon, tous droits réservés

In Figure 2.1, the progression-free survival (median: 30 months vs 14 months) and the overall survival (median: 48.0 months vs 36.3 months) are higher in the treated group compared to the control group. The number of deaths is lower with ^{177}Lu-DOTATATE until around 60 months, after which the results of the two treatments become comparable. Studies concerning the retreatment of patients are described in Section 2.3.3. Concerning the objective tumour response, one complete response was observed in the treatment group versus none in the control group, and 17 partial responses versus 3.

This study demonstrated the value of using ^{177}Lu-DOTATATE therapy as an adjunct to standard management compared to standard management alone. In particular, it established the potential adverse events and their frequency. These are detailed in Table 2.1.

2.1.2 VISION Clinical trial

The VISION clinical trial (Sartor et al., 2021) evaluated the therapeutic value of the ^{177}Lu-PSMA for patients with metastatic castration-resistant prostate cancer. Eight hundred and thirty-one patients meeting the inclusion criteria were divided into two groups: 581 received standard therapy plus ^{177}Lu-PSMA-617 (treated group) and 280 received standard therapy only (control group). For patients receiving ^{177}Lu-PSMA, 4 to 6 injections were given at 6-week intervals. As in the NETTER-1 trial, progression-free survival, overall survival, objective response, disease control, and adverse events were compared.

Figure 2.2 shows the increase in progression-free survival and overall survival when the patient receives ^{177}Lu-PSMA injections. More grade 3 or higher adverse events were observed for patients treated with ^{177}Lu-PSMA.

2.2 Pre-treatment imaging

^{68}Ga pre-treatment acquisitions are used to verify patient eligibility for treatment. Indeed, the therapy concept is based on the over-expression of certain types of receptors (somatostatin receptors or PSMA) on the surface of tumour cells. If the radiopharmaceutical does not bind sufficiently to the lesions, the treatment is ineffective. They, therefore, offer better patient selectivity to avoid unnecessary treatments. Hence, image-based diagnostic companion test have been developed to visualize and quantify the biodistribution of the vector in the patient, before the treatment.

2.2.1 ^{68}Ga PET/CT acquisition

^{68}Ga-SSTR PET (e.g. ^{68}Ga-DOTATATE in Stenvall et al., 2022) or PSMA is used to qualitatively verify whether or not receptor expression is sufficient for treatment, i.e. whether the uptake of a given lesion is greater than the uptake of the liver (Hope et al., 2020; Sartor et al., 2021). Generally, PET acquisition takes place one hour after the injection so that the radiopharmaceutical has time to bind to tumour cells and enough radioactivity remains to obtain a good quality image (half-life time: 68 min).

2.2.1.1 ^{68}Ga-SSTR (Somatostatin Receptor)

The relationship between pre-treatment and treatment was assessed quantitatively. Only two significant correlations were found between the uptake activity

Cette thèse est accessible à l'adresse : https://theses.insa-lyon.fr/publication/2023ISAL0068/these.pdf
© [L. Vergnaud], [2023], INSA Lyon, tous droits réservés

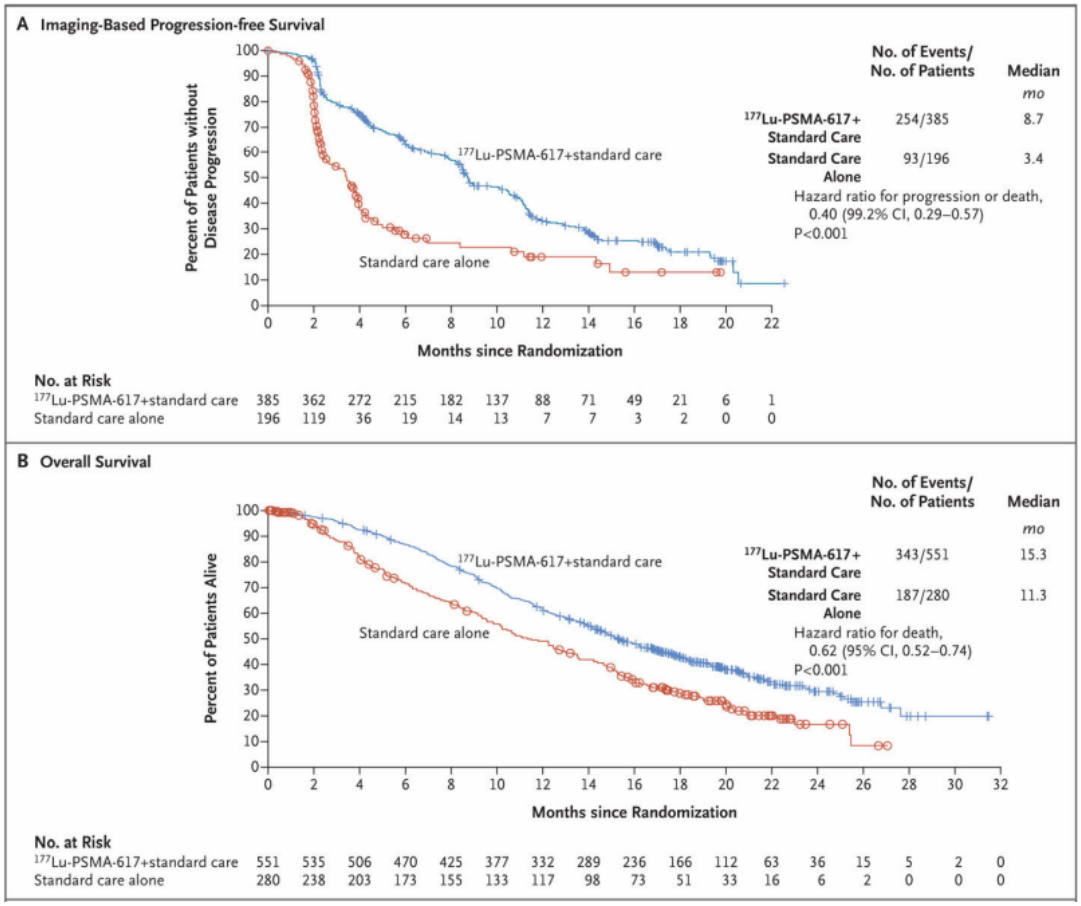

FIGURE 2.2 – Progression-free survival (top) and overall survival (bottom) between the ^{177}Lu-PSMA-617 + standard care group and the control group with the standard care alone (Sartor et al., 2021).

concentration of the ^{68}Ga-DOTATATE PET scan and the absorbed dose of ^{177}Lu-DOTATATE (spleen and tumours) although when there are high uptakes on the PET scan, there are also high doses on the SPECT (Stenvall et al., 2022). Moreover, a difference in kinetics between absorption and internalisation was highlighted by Wong et al., 2022 by comparing the ratios of SUV tumours on normal organs between PET and ^{177}Lu-DOTATATE SPECT acquired at 4h and 24h whereas ^{68}Ga-DOTATATE PET is used for the inclusion of patients.

Finally, other radiopharmaceuticals such as ^{68}Ga-DOTATOC or ^{68}Ga-DOTANOC can also be used for pre-treatment imaging. Velikyan et al., 2014 have shown that it does not influence on disease staging assessment and patient inclusion. The EANM practical guidelines consider that the detection rates of radiotracers are equivalent (Hope et al., 2023). However, ^{68}Ga-DOTATATE is still recommended as the biodistributions of activity in normal organs in the patient are not quite the same for all ^{68}Ga-SSTR tracers (e.g. different binding affinity).

2.2.1.2 ^{68}Ga-PSMA

Several studies have demonstrated the relationship between the uptake observed on pre-treatment ^{68}Ga PET and the dose absorbed during ^{177}Lu-PSMA therapy estimated from post-treatment acquisitions. For example, Violet et al., 2019 performed

Cette thèse est accessible à l'adresse : https://theses.insa-lyon.fr/publication/2023ISAL0068/these.pdf
© [L. Vergnaud], [2023], INSA Lyon, tous droits réservés

3D dosimetry based on SPECT acquisitions of 30 patients treated with ^{177}Lu-PSMA-617 and found significant correlations between absorbed doses (tumours and normal tissue) and the pre-treatment imaging with ^{68}Ga-PSMA-11. In the Wang et al., 2019 study, only 9 patients were included, 4 treated with ^{177}Lu-EB-PSMA-617 and 5 with ^{177}Lu-PSMA-617 for whom planar dosimetry was performed and correlated with ^{68}Ga-PSMA-617 PET. Several PET radiotracers have been developed to perform pre-treatment imaging for ^{177}Lu-PSMA therapy. These include ^{68}Ga-PSMA-11, ^{68}Ga-PSMA-617 and ^{68}Ga-PSMA-I&T. They were compared in a retrospective study conducted by Gühne et al., 2022 based on their biodistribution and tumour detection rates. They showed statistically significantly different biodistributions while they are described as being similar by Fendler et al., 2023. These differences could be explained by the fact that the comparison was inter-patient and not intra-patient. Despite this, there was no evidence that the tumour detection rate was better for either of them. This was partly observed in comparisons of ^{68}Ga-PSMA-11 with ^{68}Ga-PSMA-I&T where the detection rates were comparable for Berliner et al., 2017 and slightly higher for ^{68}Ga-PSMA-11 for McCarthy et al., 2017.

2.2.2 ^{18}F-FDG PET/CT acquisition

^{18}F-FDG PET imaging is a complementary imaging to ^{68}Ga imaging (Seifert et al., 2023a) by providing prognostic value (tumour heterogeneity, Hofman et al., 2015) and information regarding the aggressiveness of the lesion (Severi et al., 2013). Indeed, it allows the localisation of metabolically active regions where tumour development is likely to be rapid. Generally, acquisition also takes place within one hour as its half-life is 109.77 min. However, this acquisition is not compulsory, but is strongly recommended. In general, it is potential mismatches with ^{68}Ga-PET that are looked for.

2.2.3 Conclusion

In conclusion, pre-treatment ^{68}Ga PET imaging makes it possible to select patients who will respond best to treatment. ^{18}F-FDG PET imaging provides additional, but not mandatory, information. Significant correlations between pre-treatment imaging and absorbed doses have not always been demonstrated (e.g. Stenvall et al., 2022).

2.3 Treatment planning

2.3.1 Standardised treatment planning

Currently, in France, ^{177}Lu therapies are standardised, i.e. each patient receives a defined number of injections of 7.4 GBq. For the treatment of NETs, they receive 4 injections (approximately) every 8 weeks. For metastatic castration-resistant prostate cancer, they receive between 4 and 6 injections at 6 week intervals. The last two injections can be given to patients who respond well to and tolerate the treatment. In both cases, treatment may be stopped after two injections if the cancer continues to progress despite the therapy. If undesirable effects occur, the injected activity may be reduced (Ladrière et al., 2023) or the treatment stopped. The treatment plans are shown in Figure 2.3.

Cette thèse est accessible à l'adresse : https://theses.insa-lyon.fr/publication/2023ISAL0068/these.pdf
© [L. Vergnaud], [2023], INSA Lyon, tous droits réservés

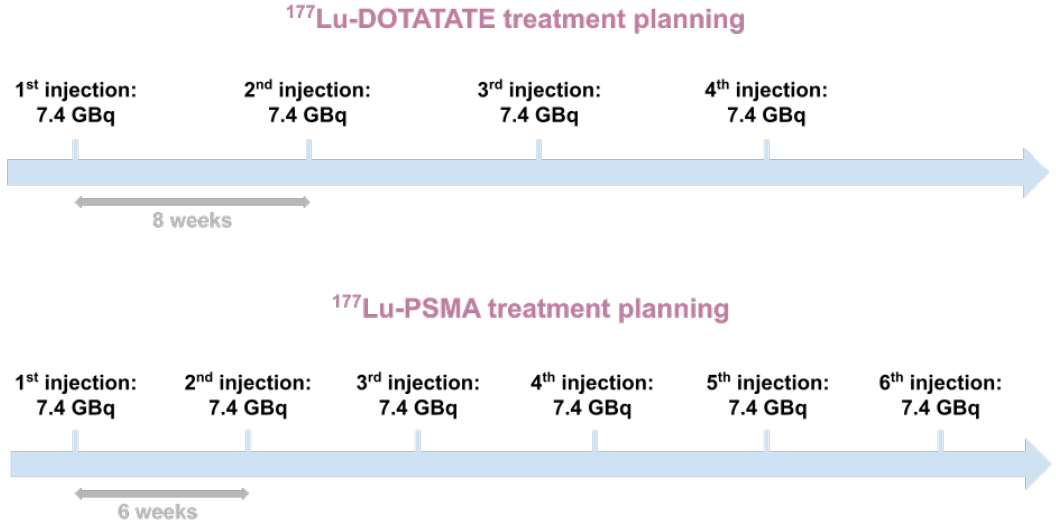

FIGURE 2.3 – Diagram showing standardised treatment plans for patients treated with ^{177}Lu-DOTATATE and ^{177}Lu-PSMA.

2.3.2 Personalised treatment planning

Although standardised therapies have been shown to be of therapeutic value, many studies have highlighted the differences in absorbed doses between patients (Sundlöv et al., 2017; Violet et al., 2019). This is why several authors have conducted phase II clinical trials to verify the feasibility, safety, and efficacy of personalised treatment for each patient (change in injected activity or number of injections). They aimed to increase the doses absorbed by the lesions while preserving the organs at risk like kidneys.

In the P-PRRT trial (Phase II clinical trial, NCT02754297), Del Prete et al., 2019 defined a maximum total absorbed dose for the kidneys to be distributed over the four injections, taking into account potential renal or haematological impairment. The adaptation of the treatment took into account the glomerular filtration rate (GFR) and the body surface area (BSA) for the first injection and then the absorbed dose per injected activity for the following injections. The first results suggested that personalisation was possible with an increase in the doses absorbed by the lesions without, however, impacting the tolerance of the treatment.

In the ILUMINET trial (Phase II clinical trial, NCT01456078), an activity of 7.4 GBq of ^{177}Lu-DOTATATE was injected at each cycle but the number of cycles was adapted to each patient according to the cumulative effective biological dose absorbed by the kidneys (27 Gy or 40 Gy). As with the P-PRRT study, the personalisation of the treatment allowed an increase in the response rate without, however, increasing the toxicities (Sundlöv et al., 2022). Similarly, Garske-Román et al., 2018 performed a prospective study on 200 patients with metastasized somatostatin receptor-positive neuroendocrine tumors whose cycle count of 7.4 GBq was matched to the dose absorbed by the kidneys (23 Gy). They showed that patients who reached 23 Gy to the kidneys, in 3 to 9 cycles, had a higher overall survival than thosewho received only 4 cycles (54 months vs 25 months).

The duration between cycles was also modified in the LUTHREE study (NCT03454763): 5 weeks for one group and 8-10 weeks for the other with a total of 5 cycles. Results are not available to our knowledge.

These phase II studies have shown the benefit of adapting ^{177}Lu-DOTATATE

Cette thèse est accessible à l'adresse : https://theses.insa-lyon.fr/publication/2023ISAL0068/these.pdf
© [L. Vergnaud], [2023], INSA Lyon, tous droits réservés

treatment to each patient to improve their efficacy by avoiding undertreatment and not increasing toxicities. To our knowledge, to date, no study has tested the personalisation of ^{177}Lu-PSMA treatments for each patient, either by modifying the activity per cycle, the number of cycles, or the time between two cycles.

Two types of doses can be distinguished: the maximum tolerated dose (the absorbed dose up to which healthy tissues are preserved) and the therapeutic dose absorbed by tumours. In previous studies, authors primarily relied on the maximum tolerated dose by the kidneys to prevent toxicities, but it would also have been possible to consider the therapeutic dose absorbed by the tumours. This second option is seldom chosen, probably because the scarcity of robust dose-effect relationship. Notable examples of such relationships can be found in the works of Ilan et al., 2015 and Violet et al., 2019, which demonstrated a correlation, while Jahn et al., 2021 did not demonstrate a statistically significant correlation between the cumulative injected activity and the morphological response of the lesions. Similarly, Jahn et al. Jahn et al., 2020 showed no correlation between tumour dose and all parameters relating to tumour shrinkage and biochemical response for small intestinal neuroendocrine metastases.

2.3.3 Retreatment

In the months following treatment with ^{177}Lu-DOTATATE, the disease may progress and lead to re-treatment of the patient. A retrospective study (NCT05816720) was initiated for 31 patients re-treated with one or more additional cycles, 6 months apart from the initial treatment. A follow-up of 11 years was carried out to know the progression-free survival, the overall survival, and the percentage of response to treatment. A phase II study (NCT05773274, RETREAT Trial) will start to compare the effects (PFS) of re-treatment with ^{177}Lu-DOTATATE and that with everolimus as well as toxicities and safety. The retreatment of relapsed intestinal NET patients with ^{177}Lu-DOTATATE (ReLUTH Phase II clinical trial NCT04954820) is being investigated to see if adding 4 cycles of 7.4 GBq instead of 2 is more effective without increasing toxicities (Deshayes et al., 2022). As with personalisation of treatment, re-treatment of patients with ^{177}Lu-PSMA does not yet appear to have been studied.

2.4 Side effects

These therapies can cause adverse effects whose toxicity seems to remain limited, mainly in grades 1 and 2. Grade 3 toxicities affected less than 10% of patients included in the NETTER-1 and VISION trials, except anemia for ^{177}Lu-PSMA (12.9%). A non-exhaustive list is given in Table 2.1. In the context of PRRT with ^{90}Y and ^{177}Lu, Bodei et al., 2015 proposed a retrospective study including 807 patients whose adverse effects were monitored for a median of 30 months. They attempted to identify the risk factors associated with renal and haematological toxicity(ies) and showed, for example, that hypertension and haematological toxicity were risk factors for nephrotoxicity.

Some organs are at greater risk of developing toxicities due to their high radiopharmaceutical uptake. For ^{177}Lu-DOTATATE therapy, the kidneys, liver, spleen, and bone marrow are considered as OARs (Marin et al., 2018) even if only kidneys and bone marrow are limiting organs (LO) (Sandström et al., 2013). For ^{177}Lu-PSMA

Cette thèse est accessible à l'adresse : https://theses.insa-lyon.fr/publication/2023ISAL0068/these.pdf
© [L. Vergnaud], [2023], INSA Lyon, tous droits réservés

Side Effects (All grades)	^{177}Lu-**DOTATATE**	^{177}Lu-**PSMA**
Xerostomia	X	33/50[1] ; 205/529[2]
Nausea	65/111[3] ; 48/97[4]	24/50[1] ; 187/529[2]
Constipation	5/97[4]	107/529[2]
Vomiting	52/111[3]	13/50[1] ; 100/529[2]
Pain	29/111[3] (abdominal) 32/111[3] (musculoskeletal) 18/97[4] (abdominal)	9/50[1] (bone) 124/529[2] (back)
Fatigue	44/111[3] ; 60/97[4]	19/50[1] ; 228/529[2]
Xerophthalmia	X	5/50[1]
Nephrotoxicity	1/97[3]	5/50[1]
Anemia	16/111[3] ; 51/97[4]	14/50[1] ; 168/529[2]
Leukopenia	11/111[3] ; 32/97[4]	66/529[2]
Thrombocytopenia	28/111[3] ; 58/97[4]	19/50[1] ; 91/529[2]
Neutropenia	6/111[3] ; 28/97[4]	15/50[1]
Lymphopenia	20/111[3]	75/529[2]
Lymphocytopenia	X	36/50[1]
Anorexia	X	8/50[1]
Weight loss	2/97[4]	4/50[1]
Arthralgia	X	118/529[2]
Loss of appetite	20/111[3]	112/529[2]
Diarrhea	32/111[3] ; 19/97[4]	100/529[2]
Flushing	7/97[4]	X

TABLE 2.1 – List of adverse events caused by ^{177}Lu-DOTATATE or ^{177}Lu-PSMA treatments. The duration of collection of extracted adverse events was 3 months after the end of treatment for Violet et al., 2020[1], up to 30 days after the end of treatment for Sartor et al., 2021[2], up to progression-free survival or up to 76 weeks after randomisation for Strosberg et al., 2017b[3] and up to 3 months after the end of ^{177}Lu-DOTATATE treatment when the BED of the kidneys reached 27 Gy for Sundlöv et al., 2022[4].

therapy, the lacrimal and salivary glands must be added as LO. High uptake was also observed in the duodenum and ileum on ^{68}Ga PET (Demirci et al., 2016).

Several methods have been developed to limit the uptake in these organs. For example, for renal protection, an intravenous injection of amino acids is given 30-60 min before treatment until 3-4 h to reduce the reabsorption of the radiopharmaceutical and thus, the damage to renal function. This injection has been shown to be effective for radiolabelled therapies with somatostatin analogs (Barone et al., 2004; Rolleman et al., 2003) but appears to be ineffective for ^{177}Lu-PSMA therapies (Yadav et al., 2017). It should be noted that PSMA receptors are found in the proximal tubules of the kidneys (Baccala et al., 2007) and therefore there is a physiological binding of the radiopharmaceutical. Mannitol infusion seemed to be a good candidate to protect the kidneys because a reduction in renal uptake was observed for ^{68}Ga PET (Matteucci et al., 2017) but was not confirmed for ^{177}Lu-PSMA therapy. Indeed, the dose differences observed with and without mannitol were not significantly different (Sarnelli et al., 2019). In several studies, external cooling was used to limit the uptake of ^{177}Lu-PSMA in the salivary glands (Fendler et al., 2017; Delker et al., 2016). However, Yilmaz et al., 2019 showed that it had no influence on uptake

Cette thèse est accessible à l'adresse : https://theses.insa-lyon.fr/publication/2023ISAL0068/these.pdf
© [L. Vergnaud], [2023], INSA Lyon, tous droits réservés

in the parotid glands. Sarnelli et al., 2019 evaluated the use of folic polyglutamate tablets to compete with ^{177}Lu-PSMA at the receptor level. This led to a significant decrease in the average dose absorbed by the parotid glands.

2.5 Post-treatment imaging

During treatment, the patient is monitored using biological analyses. It is possible, but not necessary, to add post-treatment post-treatment acquisitions to check whether the fixating lesions identified on the ^{68}Ga PET scan have been treated. Currently, post-treatment acquisitions after each injection are neither compulsory nor necessary for the administration of the treatment. However, they are essential for estimating doses absorbed by organs at risk and lesions and establishing potential correlations with toxicities and efficacy (Cremonesi et al., 2018). For example, the P-PRRT and ILUMINET clinical trials (described in Section 2.3.2) have based the personalisation of ^{177}Lu-DOTATATE therapy by considering the kidneys as OARs whose absorbed dose or effective biological dose must not exceed a certain threshold.

2.6 Response assessment

The assessment of the response can be made using biological data, imaging, patient quality of life, and/or the pain experienced. Indeed, the evolution of tumour markers such as PSA (Prostate-Specific Antigen) for prostate cancer (Lilja et al., 2008) or chromogranin A (CgA) for NETs (Belli et al., 2009) even if it is imperfect allows the progression of cancer to be followed. If the treatment is effective, these markers tend to decrease compared to the baseline over time. For ^{177}Lu-PSMA, a biological response is considered to be at least a 50% decrease in PSA (Turpin et al., 2019), whereas for ^{177}Lu-DOTATATE, the CgA level must decrease by at least 25% (Thapa et al., 2016). Response to treatment for metastatic prostate cancer is generally based on CT and bone scan (Prostate Cancer Clinical Trials Working Group 3 recommendations, Fendler et al., 2023). Metabolic (EORTC, PERCIST, and, RECIP 1.0) and anatomical (WHO and RECIST 1.1) response criteria for solid tumours based on PET/CT imaging are also used in clinical practice (Scarpa et al., 2017; Zhang et al., 2019; Fendler et al., 2017; Gafita et al., 2022; Fanti et al., 2021). They allow the classification of the patient's disease course following treatment by using PSMA PET/CT consensus statement (Fanti et al., 2021): progressive disease (PD), partial remission (PR), stable disease (SD), and mixed response (MR). Finally, several questionnaires can be completed to monitor the patient's quality of life and pain: the Functional Assessment of Cancer Therapy-Prostate (FACT-P, Esper et al., 1997) and the Brief Pain Inventory (BPI, Stanhope, 2016), respectively. Clinical response criteria are also available, such as the Visual Analogue Score (VAS) for pain, analgesia scoring and quality of life (Karnofsky Performance Status and ECOG performance status) (Yadav et al., 2020). The choice of measures included in the assessment of treatment response differs between studies. More recently, two frameworks (PROMISE and PROMISEV2) have been provided to improve the organisation of data in clinical studies and to define standards for reporting (disease localisation, distribution, WLPSM expression, response monitoring) (Seifert et al., 2023b; Eiber et al., 2018).

Cette thèse est accessible à l'adresse : https://theses.insa-lyon.fr/publication/2023ISAL0068/these.pdf
© [L. Vergnaud], [2023], INSA Lyon, tous droits réservés

2.7 Predictive and prognostic factors

To improve the selection of patients who can benefit from these treatments, many studies have focused on predicting responses based on pre-treatment imaging and biological analyses. A state-of-the-art of prognostic and predictive biomarkers for ^{177}Lu-PSMA treatments has been proposed by Heidegger et al., 2022. They identified clinical biomarkers such as age, the significant presence or absence of symptoms, the presence of visceral and/or hepatic metastases, bone invasion, biochemical progression after the first cures, previous treatments as well as the confrontation FDG and PSMA PET images. Other biomarkers could be extracted from the images (total tumour volume, uptake, and uptake compared to healthy liver, bone scan index) but no common methodology has been defined for volumes for example. Evaluations of blood biomarkers were also carried out (PSA, Lactate dehydrogenase, C-reactive protein, hemoglobin, platelets, alkaline phosphatase) and a summary of biomarkers associated with treatment response was given in Figure 3 of the article by Heidegger et al., 2022. Similarly, for ^{177}Lu-DOTATATE therapies, prognostic and predictive factors for response were obtained, e.g. number of bone metastases, NET subtypes, CgA level, and ascites for example (Swiha et al., 2022; Becx et al., 2022). Clinical trials are underway to assess whether information extracted from multiple imaging modalities (^{18}F-FDG and ^{68}Ga-octreotate PET/CT, apparent diffusion coefficients from MRI and estimated doses from SPECT/CT images for each cycle) can be predictive of individual tumour response (NCT01842165 ; LUMEN), to study the cellular response to radiation following ^{177}Lu-DOTATATE treatment for subsequent development of response biomarkers (NCT05513469; Radio-Marker) or to identify biomarkers of radio sensitivity (NCT03667092 ; GENEBIOLuNET). Today, nomograms have been developed from these factors and validated for patients treated with ^{177}Lu-PSMA (mCRPC). They allow the prediction of overall survival, progression-free survival of PSA, and a decrease of at least 50% in PSA for each individual (Gafita et al., 2021).

Finally, as with the personalisation of the treatment in SIRT, studies have looked at the relationship between the binding of the radiopharmaceutical in a given volume from the PET image and the absorbed dose corresponding estimated from SPECT images (Ezziddin et al., 2012; Bruvoll et al., 2023; Violet et al., 2019). Peters, 2022 proposed a dosimetric estimate from the PET image which they compared with that obtained from SPECT images. They showed that prediction was possible mainly for healthy organs of patients treated for hormone-sensitive prostate cancer. Akhavanallaf et al., 2023 were interested in predicting tumour dose using a machine learning algorithm to which they provided information extracted from the ^{68}Ga PET image as well as a series of clinical and pathological biomarkers. A comparable study was conducted by Peterson et al., 2023b for renal dosimetry using regression models.

2.8 Ongoing clinical trials

New uses for these radiopharmaceuticals are being investigated, whether for other diseases and/or different stages of the disease. A non-exhaustive list of clinical trials (ClinicalTrials.gov) is given for each disease.

The NETTER-1 study showed the therapeutic interest of ^{177}Lu-DOTATATE for midgut NETs and evaluations are underway for G2-G3 advanced GEP-NET (NETTER-2, NCT03972488), pancreatic NETs (NCT02230176), bronchial

Cette thèse est accessible à l'adresse : https://theses.insa-lyon.fr/publication/2023ISAL0068/these.pdf
© [L. Vergnaud], [2023], INSA Lyon, tous droits réservés

NETs (NCT04665739), paragangliomas and pheochromocytomas (NCT03206060), meningiomas (NCT05278208, NCT03971461, NCT04082520), neuroblastomas (NCT04903899, NCT03966651), glioblastomas (NCT05109728), Merkel cell carcinomas (combination of treatments: NCT05583708, NCT04261855), metastatic nasopharyngeal cancer (NCT05198479) and stage IV or recurrent breast cancer (NCT04529044) (Hope et al., 2020; Elajami et al., 2022). In the case of NET liver metastases, several evaluations of the modes of administration of ^{177}Lu-DOTATATE (intravenous vs. intrahepatic) are also performed to choose the one that will maximise the concentration of activity in the lesions while protecting healthy tissue (NCT03590119, NCT04837885).

Today, ^{177}Lu-PSMA-617 is mainly used for metastatic castration-resistant prostate cancers (NCT03511664, VISION) and more recently, for hormone-sensitive cancers (NCT04720157, PSMAddition). Trials are currently underway to assess the effectiveness of this radiopharmaceutical treatment combined with other treatments: a detailed description has been made by Ramnaraign and Sartor, 2023. Other applications are in the test phase, such as advanced salivary gland cancers (NCT04291300, LUPSA) or recurrent grade 3-4 gliomas (NCT05644080). Finally, ^{177}Lu-PSMA can be combined with another I&T ligand whose therapeutic interest for metastatic castration-resistant prostate cancers is currently being verified in a phase III study (NCT05204927).

2.9 Conclusion

The ^{177}Lu therapies presented are promising therapies that have shown their effectiveness compared to standard management during phase III studies and whose number of adverse effects remains low. They are currently being tested for other pathologies and other stages of the disease. To improve patient selection, prognostic and predictive biomarkers are being studied as well as personalisation of the treatment plan to increase the treatment efficiency for each patient. In this chapter, we were interested in ^{177}Lu which is a β^- emitter but it is possible to replace it with an α emitter as proposed by Kratochwil et al., 2016a (^{225}Ac-PSMA-617). It could make it possible to limit haematological toxicity due to the low range of alpha (50-100 µm) and which could be effective when there is radio resistance to β^- emitters. However, ^{225}Ac-PSMA-617 has drawbacks such as the risk of dissociation of the radioisotope and the ligand or even the disintegration scheme. Only one phase I study is currently underway (NCT04597411). In the following, this radiopharmaceutical will not be studied and we will focus on ^{177}Lu therapies.

Cette thèse est accessible à l'adresse : https://theses.insa-lyon.fr/publication/2023ISAL0068/these.pdf
© [L. Vergnaud], [2023], INSA Lyon, tous droits réservés

Chapter 3

Radioisotopes and Imaging systems

In nuclear medicine, radiopharmaceuticals are administered to patients for diagnostic and/or therapeutic purposes. Many are available on the market to meet different needs and a single radioisotope can be used for several purposes by associating it with different vectors. For example, ^{123}I can be used for neurology but also for cardiology with the ^{123}I-MIBG. Similarly, ^{99m}Tc is used for many assessments as myocardial perfusion, scintigraphic bone and to predict the distribution of ^{90}Y microspheres during radioembolisation (^{99m}Tc-MAA). For therapy, ^{131}I is used for the treatment of hyperthyroidism and thyroid cancers, ^{90}Y microspheres for liver cancers and hepatic metastases, ^{177}Lu-DOTATATE and ^{177}Lu-PSMA for neuroendocrine tumors and metastatic castration-resistant prostate cancers, respectively. More recently, studies have focused on alpha therapy, including the combination of ^{225}Ac with PSMA-617 in the treatment of PSMA-positive prostate cancer to evaluate its safety (Phase I, NCT04597411) or with PSMA-I&T to assess its efficacy for metastatic castration-resistant prostate cancer (TATCIST, Phase II, NCT05219500).

In this chapter, we will focus on two radioisotopes (^{99m}Tc and ^{177}Lu) whose biodistribution can be visualized with a gamma camera (Anger NaI(Tl) scintillation gamma camera and Semiconductor Cadmium Zinc Telluride (CZT)-based gamma camera) by planar and/or SPECT acquisition. Other imaging systems and other radioisotopes will not be described.

3.1 Radioisotopes description

3.1.1 ^{99m}Tc

Definition ^{99m}Tc is derived the decay of ^{99}Mo (β^- emission) and will itself decay into ^{99}Tc by emitting gamma photons (Equation 3.1) whose energy is approximately 140 keV (87.8%). It has a half-life of 6.01 hours, which implies that its production takes place in nuclear medicine centers by separation of ^{99}Mo and ^{99m}Tc, Figure3.1. A description of the different separation methods has been proposed by Dash et al., 2013.

$$^{99}_{42}\text{Mo} \rightarrow ^{99m}_{43}\text{Tc} \rightarrow ^{99}_{43}\text{Tc} \tag{3.1}$$

Interest for medical applications In practice, ^{99m}Tc is widely used in nuclear medicine for scans because it emits low-energy photons that can be detected with

Cette thèse est accessible à l'adresse : https://theses.insa-lyon.fr/publication/2023ISAL0068/these.pdf
© [L. Vergnaud], [2023], INSA Lyon, tous droits réservés

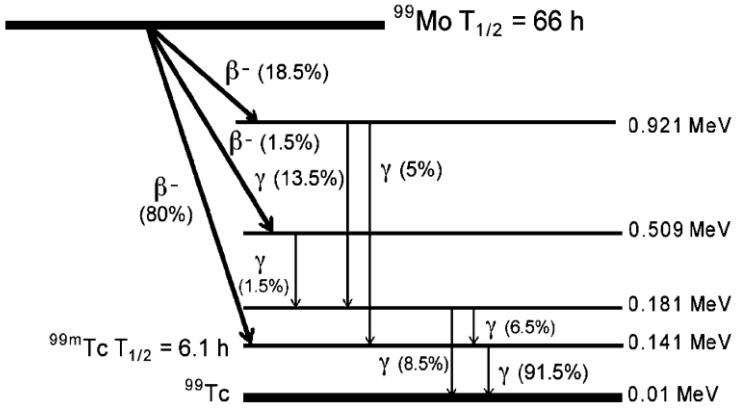

FIGURE 3.1 – Decay scheme of ^{99m}Tc extracted from Pillai et al., 2013

a gamma camera. The activity to be injected is therefore limited and allows the patient's irradiation to be reduced (many photons, little energy deposit). Its emission spectrum is shown in Figure 3.3.

3.1.2 ^{177}Lu

Definition ^{177}Lu is a radioisotope that decays to ^{177}Hf emitting β^- particles (E_{mean}/E_{Max}(%): 47.66/177.0 keV (11.61); 78.61/248.6 keV (0.006); 111.69/385.3 keV (9.0); 149.35/498.3 keV (79.4)) and gamma photons (112.95 keV (6.17%) and 208.37 keV (10.36%)) as shown in Figure 3.2. It has a half-life of 6.6463 d and can be obtained by two processes: neutron capture or neutron irradiation (Dash et al., 2015).

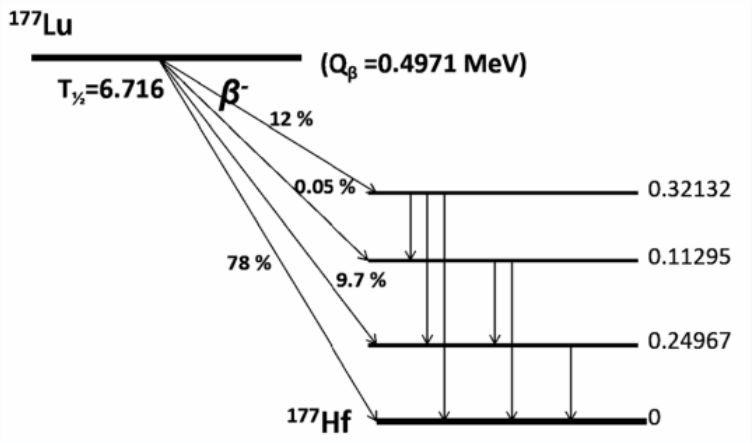

FIGURE 3.2 – Decay scheme of ^{177}Lu extracted from Dash et al., 2015

Interest for medical applications The ^{177}Lu allows both the treatment of the patient through the emission of β^- particles with an average displacement of 0.67 mm in soft tissue (Dash et al., 2015) (maximum displacement: 1.6 mm, Alsadi et al., 2022) and the visualization of the treatment by gamma photons collected with a gamma camera. Its energy spectrum is given in Figure 3.3 in which, the two main photopeaks (113 keV and 208 keV) are represented as well as the scattered windows that frame it. This radioisotope is associated with a vector (DOTATATE or PSMA-617) as described in Chapter 2 for the targeted treatment of inoperable lesions and metastases.

Cette thèse est accessible à l'adresse : https://theses.insa-lyon.fr/publication/2023ISAL0068/these.pdf
© [L. Vergnaud], [2023], INSA Lyon, tous droits réservés

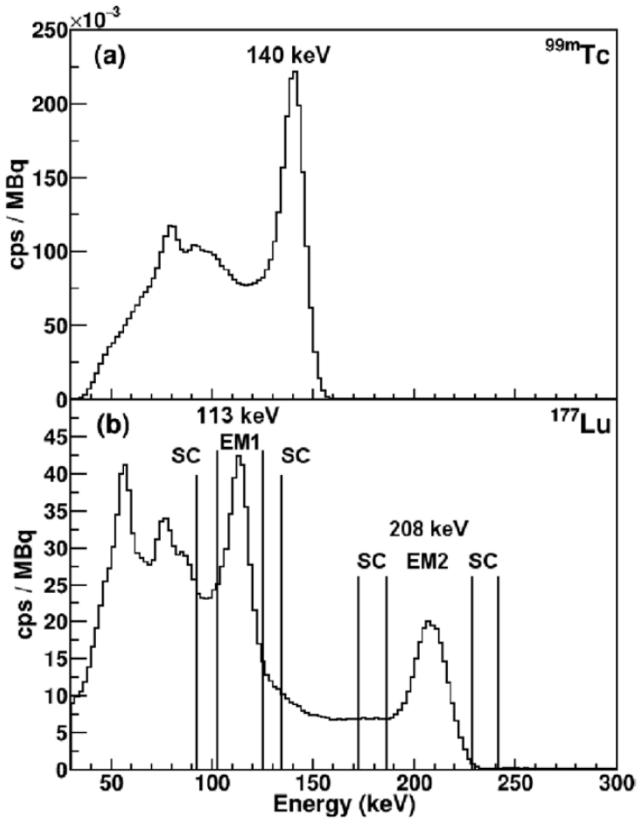

FIGURE 3.3 – SPECT-measured Emission spectrum of ^{99m}Tc (LEHR collimator) and ^{177}Lu (MEGP collimator), extracted from the article of Robinson et al., 2016.

3.2 Gamma camera acquisitions

Two acquisition modes are available to detect gamma photons: planar acquisitions and SPECT acquisitions.

3.2.1 Planar acquisition

Planar acquisition consists of multiple acquisitions by projection in the plane of the patient when the detectors are placed on either side of the patient (anterior and posterior). In the case of planar whole-body acquisition, the bed will move progressively between both heads (7-20 cm/min, Garkavij et al., 2010; Zhang et al., 2018; Sandström et al., 2010) from head to toe. This type of acquisition is common in clinic because it is fast and allows a large field of view to be acquired. However, the obtained images correspond to anterior-posterior projections of the biodistribution of the activity in the patient. This leads to an overlap of organs and lesions in the images which can be particularly annoying if one wants to study a specific region.

3.2.2 SPECT acquisition

During SPECT acquisitions, unlike planar acquisitions, the detector heads rotate around the patient and acquire projections of the biodistribution of the radiopharmaceutical in the field of view from different angles. At the end, a 3D image of the biodistribution can be reconstructed from the projections (see Chapter 4). This type of acquisition gives a more accurate information of the biodistribution of the

Cette thèse est accessible à l'adresse : https://theses.insa-lyon.fr/publication/2023ISAL0068/these.pdf
© [L. Vergnaud], [2023], INSA Lyon, tous droits réservés

activity than planar acquisitions because the correction of physical phenomena such as attenuation, scattering, dead time and many others can be directly included in the reconstruction. For gamma cameras associated with a scanner, a CT acquisition can generally be performed to provide anatomic information and correct the attenuation. There is no overlap of organs and lesions. However, the acquisition has a limited field of view: therefore, to perform a 3D whole-body SPECT acquisition, several SPECT acquisition positions are needed and consequently, it leads to a longer total acquisition time.

3.3 Gamma camera systems

Currently, two types of gamma cameras are available: Anger-type gamma cameras and solid-state gamma cameras.

3.3.1 Anger NaI(Tl) scintillation gamma camera

Anger type gamma cameras are composed of two to three detector heads as shown in Figure 3.4. Each head consists of a collimator, a scintillator crystal generally with sodium iodide activated with thallium, a light guide and photomultipliers. When the gamma photon leaves the patient, it must pass through the collimator which has been chosen according to the radioisotope (energy spectrum) and the best compromise between sensitivity and spatial resolution. For example, for ^{177}Lu, it is recommended to use a MEGP (Medium Energy General Purpose) collimator with the photopeak at 208 keV (De Nijs et al., 2014). It allows to select only the photons that arrive perpendicularly to the detector in order to localize their origin. Then, they interact with a scintillator crystal that will transform gamma photons into light photons and whose thickness has an impact on the sensitivity: for example, crystals 5"8 have a better sensitivity than crystals 3"8. Ljungberg et al., 2016 evokes 35% more photons detected in the 20% wide primary window. At the output, a light guide makes it possible to bring the light photons to the input of the photomultipliers. Photomultipliers ultimately transform light photons into an electrical signal.

The conversion of photons into an electrical signal is a so-called *indirect conversion* (transition of gamma photons into light photons then into an electrical signal). This can cause signal loss and add noise.

3.3.2 Semiconductor Cadmium Zinc Telluride (CZT)-based gamma camera

Solid-state detectors have made their way into the clinic in recent years. Initially, they were used for cardiac gamma cameras (D-SPECT, Spectrum Dynamics, Caesarea, Israël; Discovery NM 530c, GE Healthcare, Haïfa, Israël) whose geometry was redesigned to be closer to the myocardium and whose volume was reduced compared to an Anger-type gamma camera. In addition, it has been shown that its sensitivity is better, which has reduced acquisition times and/or injected activity for comparable diagnostic performance (Esteves et al., 2009; Duvall et al., 2011). Then, semiconductors replaced scintillator crystals and photomultipliers in gamma cameras with two heads (Discovery NM/CT 670 or 870 CZT, GE Healthcare, Haïfa, Israël) as well as in those with twelve detector heads and more degrees of freedom (VERITON-CT, Spectrum Dynamics, Caesarea, Israël; StarGuide, GE Healthcare,

Cette thèse est accessible à l'adresse : https://theses.insa-lyon.fr/publication/2023ISAL0068/these.pdf
© [L. Vergnaud], [2023], INSA Lyon, tous droits réservés

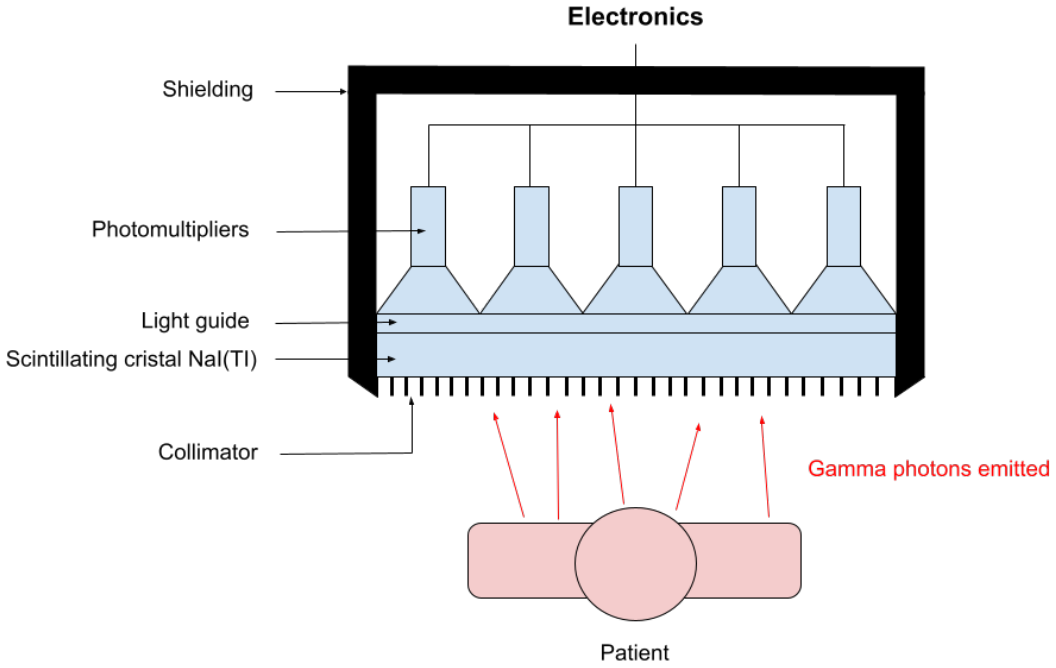

FIGURE 3.4 – Schematic diagram of one detector head of an Anger type gamma camera

Haïfa, Israël). In the following, only the description of non-cardiac gamma cameras with twelve detector heads will be available: the example of the VERITON-CT system.

3.3.2.1 Semiconductor detectors

Definition of semiconductors Semiconductors are materials that are neither conducting nor insulating. In conducting materials, the valence and conduction bands overlap, allowing electrons to pass easily from one band to the other. In contrast, insulators have a band gap (forbidden electronic states) that prevents electrons from passing. Semiconductors also have a band gap, but it is smaller than that of insulators (6 eV), which allows electrons receiving energy to pass (Figure 3.5).

Principle Initially, the semiconductor behaves like an insulator. When an incident photon reaches the detector, it will cross the collimator and transfer its energy to the semiconductor. This energy will allow several electrons from the valence band to move into the conduction band and thus create electron-hole pairs. The applied electric field deflects the holes towards the cathode and the electrons towards the anode, creating an electric signal whose intensity is proportional to the energy released by the incidence of the gamma photon (d'Aillon, 2005). This principle is described in Figure 3.6.

In practice, each pixel of detectors is like a PN junction: on one side, the semiconductor is N-doped (excess of electrons) and on the other, it is P-doped (deficit of electrons) (Szeles, 2004; Ben Bouallègue et al., 2015). At the junction, holes and electrons recombine to create pairs: this region is called the depletion zone. This region is reverse biased using a voltage generator to minimize the current flowing through. Thus, when gamma photons create electron-hole pairs in the depletion zone, the measured current is proportional to the energy of the interacting photon.

Cette thèse est accessible à l'adresse : https://theses.insa-lyon.fr/publication/2023ISAL0068/these.pdf
© [L. Vergnaud], [2023], INSA Lyon, tous droits réservés

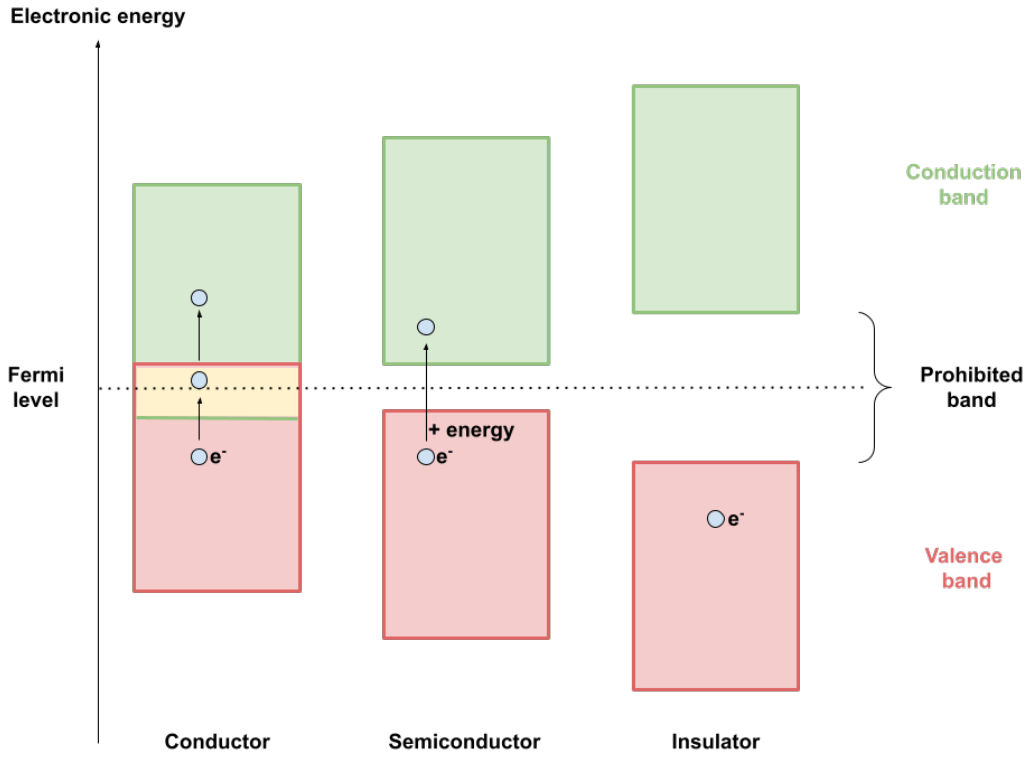

FIGURE 3.5 – Diagram illustrating the relative positions of the valence and conduction bands for conducting, semiconducting and insulating materials. The band gap corresponds to energy levels that cannot be reached by electrons. The Fermi level is in the middle of the band gap.

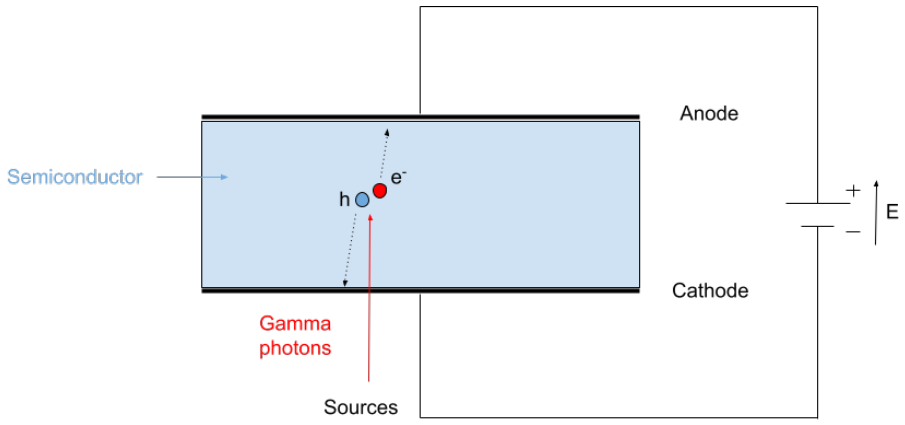

FIGURE 3.6 – Schematic diagram of how a CZT detector works when a photon is detected.

Semiconductor materials Initially, the main semiconductors used in detectors were silicon and germanium because they have good energy resolution (Darambara and Todd-Pokropek, 2002). However, under conditions of clinical use of nuclear medicine (room temperature), they do not work properly. Indeed, the band gap of these materials is small (1.12 eV for the silicon and 0.68 eV for the germanium Collings, 1980), so that in the absence of photons, the electrons of the valence

Cette thèse est accessible à l'adresse : https://theses.insa-lyon.fr/publication/2023ISAL0068/these.pdf
© [L. Vergnaud], [2023], INSA Lyon, tous droits réservés

band can pass in the conduction band thanks to thermal energy.

Semiconductor	Density (g/cm^3)	Atomic number	Band gap energy (eV) at 25°C
Silicon (Si)	2.33	14	1.12
Germanium (Ge)	5.33	32	0.68
Cadmium Telluride (CdTe)	6.20	48, 52	1.44
Cadmium Zinc Telluride (CdZnTe)	5.78	48, 30, 52	1.57

TABLE 3.1 – Physical properties (density, atomic number, band gap energy) of four common semiconductors: silicon, germanium, cadmium telluride and cadmium zinc telluride extracted from Del Sordo et al., 2009.

CZT is particularly interesting for gamma-ray detectors because, in addition to its good energy resolution, it can be used at room temperature thanks to its wide bandwidth (1.57 eV). It should be noted, however, that its operating temperature (21°C $\pm$ 2°C for the VERITON) must be respected so as not to impair its performance, lose detector homogeneity or cause irreversible damage if the temperature is too high. Moreover, its high atomic number allows it to have a better stopping power (Cherry et al., 2012) and therefore a better detection efficiency than Anger type gamma cameras. Furthermore, its density is higher than that of other common semiconductors used in detectors (Table 3.1), which favours photoelectric interaction. The counting rate is superior with CZT cameras, as for a 140 keV photon, 30,000 electron-hole pairs are generated compared to 1,500 in Anger cameras (Nichols et al., 2009). Finally, the thickness of the semiconductor has an impact on the efficiency of gamma radiation absorption, which also depends on the energy of the photons (Figure 3.7). These semiconductors thus have all the necessary characteristics to be used in a detector (Del Sordo et al., 2009).

3.3.2.2 Structure

The VERITON system differs from Anger-type gamma cameras in two respects: 1. the use of solid state detectors and 2. its geometry. It is composed of twelve independent detector heads attached to a ring that can make four successive rotational movements for a whole-body acquisition. Each head can move independently towards the patient by a translational movement and contains a 128x16 pixel solid-state detector which sweeps over 60 degrees to scan the field of view as shown in Figure 3.8.

The purpose of these successive movements and this geometry is to bring the detectors as close as possible to the patient and to use the entire detector surface to collect a maximum number of photons and improve the SPECT image.

Each detector head is equipped with a tungsten parallel hole collimator which cannot be changed unlike the Anger-type gamma camera. Without adaptation of the collimator, high energy photons can cross the septa and create downscatter. This phenomenon will be amplified by the rotation of the detector head since the collimators will not be constantly perpendicular to the patient.

The detection is made with a semiconductor material, the CZT. It allows the conversion of gamma photons into an electrical signal: this is called *direct conversion*. This feature, combined with the simultaneous acquisition of all twelve detectors

Cette thèse est accessible à l'adresse : https://theses.insa-lyon.fr/publication/2023ISAL0068/these.pdf
© [L. Vergnaud], [2023], INSA Lyon, tous droits réservés

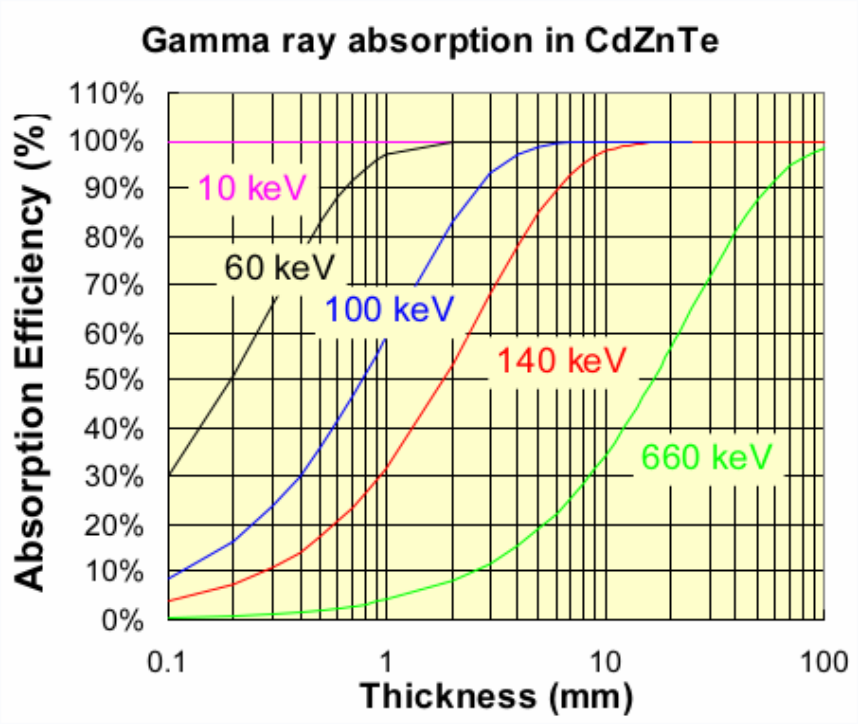

FIGURE 3.7 – Efficiency of gamma radiation absorption as a function of semiconductor thickness and gamma photon energy. This figure was extracted from Szeles, 2004.

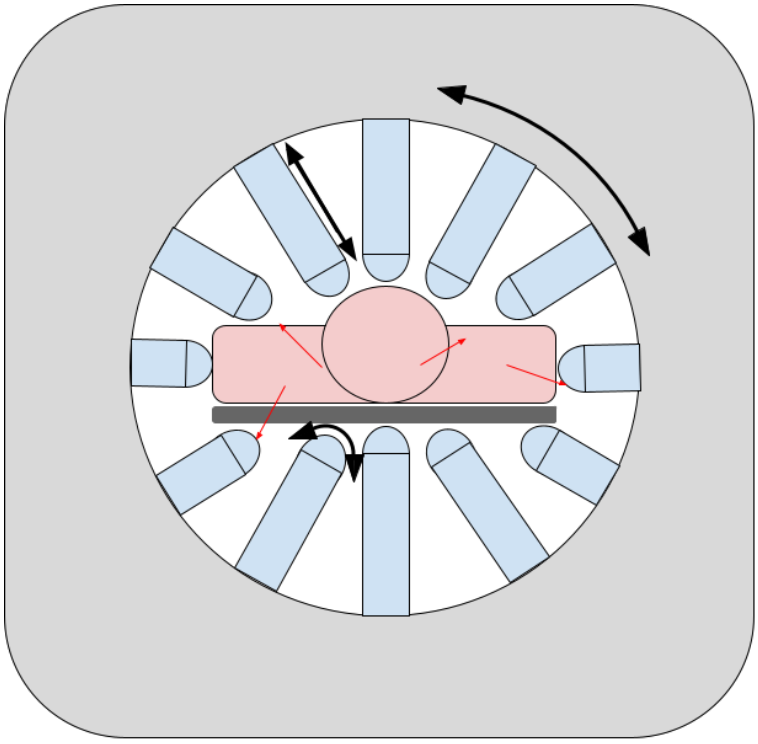

FIGURE 3.8 – Schematic diagram of the VERITON-CT system with the movements of their detector heads

from various angles, the proximity of detectors to the patient, the collimator, and

Cette thèse est accessible à l'adresse : https://theses.insa-lyon.fr/publication/2023ISAL0068/these.pdf
© [L. Vergnaud], [2023], INSA Lyon, tous droits réservés

the high energy resolution of the CZT, enhances the overall sensitivity of the imaging system.

A comparative table of the technical specifications of the VERITON-CT and StarGuide gamma cameras is available in the article of Serre et al., 2021.

3.3.2.3 Clinical applications

Several studies have tested the performance of the VERITON system for different clinical procedures from phantoms and/or patient's images: brain perfusion (Bordonne et al., 2020; Cassol et al., 2019), bone scintigraphy (Bahloul et al., 2021) and myocardial scintigraphy (Imbert et al., 2021b). They have shown improved sensitivity and contrast compared to Anger cameras which has led to improvements in image quality. These applications are the main uses of the VERITON system in a nuclear medicine department. For example, in Toulouse, France, 35% of the examinations are brain scans, 61% are myocardial scans, 3% are bone scans and 1% are MIBG scans (Blanc et al., 2021). These figures may differ according to the type of institution considered: in hospitals dedicated to cancer, brain scans are potentially less important. Conversely, for the ^{177}Lu-PSMA treatment (details in Chapters 1 and 2), the whole-body SPECT/CT acquisition can be necessary for treatment follow-up and calculation of absorbed doses without having too long acquisition times and would be a possible new application. For the moment, the quantitative performances of VERITON for the ^{177}Lu, of which only the photopeak at 113 keV can be used, have only been little studied (Meeting reports by Imbert et al., 2020 and Imbert et al., 2021a). We will study the use of VERITON with the ^{177}Lu radioisotope in Chapters 8 and 9.

3.3.3 Comparison of gamma camera detection systems

A non-exhaustive comparison of Anger and solid state gamma cameras is available in Table 3.2.

	Anger camera	**Solid state camera**
Detection principle	Indirect	Direct
Material	NaI(Tl)	CZT
Theoretical energy resolution (140 keV)[1]	5%	<0.5%
Energy resolution (140 keV)[2]	10.6%	<3.0%
Intrinsic spatial resolution[2]	3.5 mm	< 2.5 mm

TABLE 3.2 – Comparative table of performances of scintillation and semiconductor detectors. Data were extracted from Wernick and Aarsvold, 2004[1] and Guérin et al., 2008[2] articles.

Note that in clinical use, only CZT is used as semiconductor material and that the thicknesses of the detectors are not the same in the comparison proposed by Guérin et al., 2008. In the case of myocardial SPECT, a comparison of the performance of Anger and CZT cameras was performed by Imbert et al., 2012 and showed a clear superiority of the performance of CZT cameras over Anger cameras (sensitivity and spatial resolution). The same conclusions were obtained with the VERITON system used with ^{99m}Tc by Desmonts et al., 2020 (better sensitivity, energy resolution and image contrast). Although the use of solid-state cameras seems promising, Anger-type

Cette thèse est accessible à l'adresse : https://theses.insa-lyon.fr/publication/2023ISAL0068/these.pdf
© [L. Vergnaud], [2023], INSA Lyon, tous droits réservés

gamma cameras are still widely used in nuclear medicine departments (developed in the 1960s vs 2000 for solid state cameras) and remains financially more accessible.

Cette thèse est accessible à l'adresse : https://theses.insa-lyon.fr/publication/2023ISAL0068/these.pdf
© [L. Vergnaud], [2023], INSA Lyon, tous droits réservés

Chapter 4

SPECT quantification and Dosimetry

The absorbed doses in lesions and organs at risk are dependent on the spatial distribution of the radiopharmaceutical over time. In the case of ^{177}Lu treatments, the radiopharmaceutical gradually binds and is subsequently internalised, while a portion of its activity is eliminated through biological processes, such as urinary excretion, or physical decay. Gamma cameras are used to assess the biodistribution at different time-points (pharmacokinetics) by recovering the photons detected perpendicularly by the detector. As explained in the previous chapter, these acquisitions yield a series of projections that are used to reconstruct the three-dimansional distribution (Section 4.1), which necessitates correction for specific physical phenomena like attenuation and scattering (Section 4.2). Prior to using any of the dosimetry methods outlined in Section 4.4, a calibration factor must be determined to convert detected counts into activity (Section 4.3). Section 4.5 focuses on the application of physical corrections for predictive dosimetry in SIRT.

4.1 SPECT reconstruction

Once the SPECT acquisition has been performed, a reconstruction is required to obtain a 3D representation of the biodistribution of the radiopharmaceutical within the patient at a specific time. Various reconstruction algorithms are available on clinical imaging systems.

4.1.1 Radon transform

The set of two-dimensional projections taken at different θ angles corresponds to the mathematical model known as Radon transform of the three-dimensional density function (Groch and Erwin, 2000) that needs to be reconstructed. Reversing the Radon transform allows to obtain the density function. However, due to the finite number of available projections and the presence of noise in the projections (*Tomographic Reconstruction* 2023), there is no uniqueness in finding a solution. The inverse problem is ill-posed [1], and two main types of methods are used to solve it: analytical methods and iterative methods. In the following sections, we will focus on describing the most commonly used methods in clinical practice, although other methods and/or adaptations do exist.

1. A well-posed problem is such that 1) a solution exists, 2) the solution is unique, 3) the solution's behaviour changes continuously with the initial conditions.

Cette thèse est accessible à l'adresse : https://theses.insa-lyon.fr/publication/2023ISAL0068/these.pdf
© [L. Vergnaud], [2023], INSA Lyon, tous droits réservés

4.1.2 Filtered back projection

The filtered back-projection method is an analytical method that involves filtering the projections using a ramp filter to improve the quality of the 3D reconstruction obtain through back-projection. Additionally, a filter such as Gaussian or Butterworth can be applied to reduce noise while preserving the signal, thereby improving the image quality. Without this filtering step, the resulting 3D reconstruction may appear blurred (Groch and Erwin, 2000). This method is simple and fast but does not easily take into account physical phenomena (e.g. attenuation, scattering) and can be disturbed by noise.

4.1.3 Iterative reconstructions

4.1.3.1 Principle

Iterative reconstructions are increasingly used to take into account the physical phenomena impacting the projections. Figure 4.1 illustrates the working principle of the iterative algorithms. These methods aim to reconstruct an activity distribution based on measured projections. For this purpose, an initial estimate of the activity distribution is defined, which could be a uniform image. This distribution is then projected to obtain estimated projections, which are compared to the measured projections to determine a correction matrix. This matrix is subsequently applied to the estimated distribution, updating it for the next iteration.

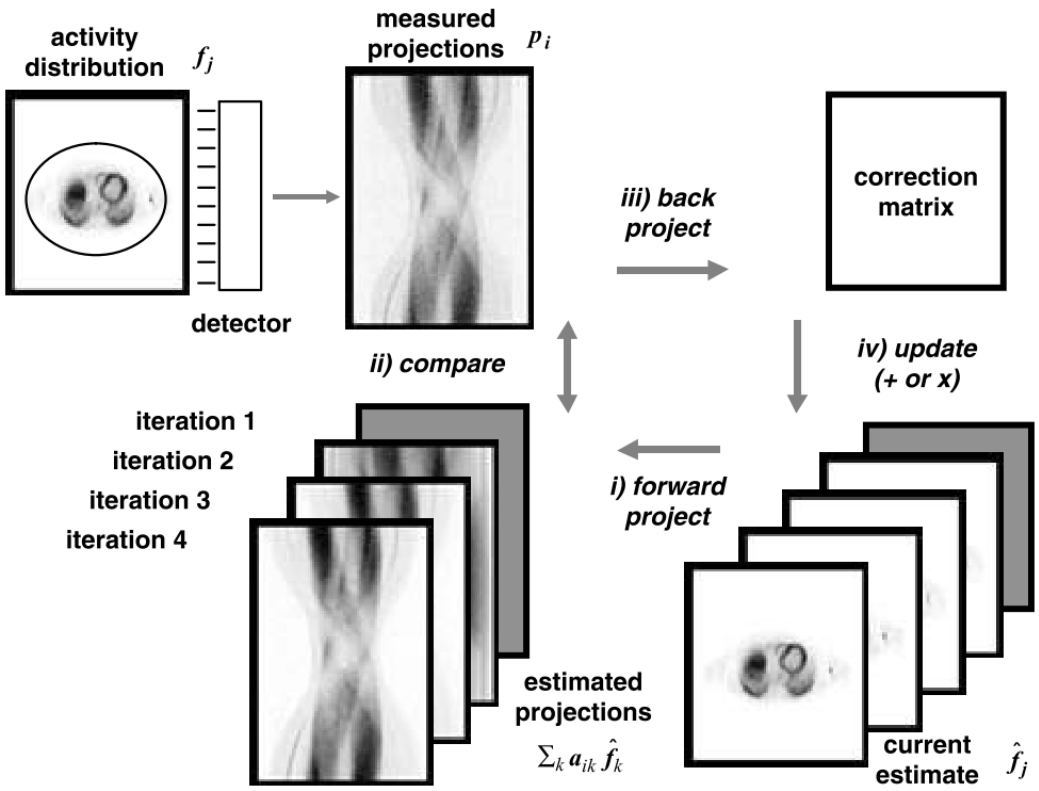

FIGURE 4.1 – Schematic diagram of iterative reconstruction methods from Hutton et al., 2006

There are two types of iterative methods: algebraic methods and statistical methods. The first type of method will not be discussed here. However, a comprehensive

Cette thèse est accessible à l'adresse : https://theses.insa-lyon.fr/publication/2023ISAL0068/these.pdf
© [L. Vergnaud], [2023], INSA Lyon, tous droits réservés

literature review on iterative reconstruction methods has been provided by Hutton et al., 2006.

4.1.3.2 ML-EM

The ML-EM (Maximum Likelihood Expectation Maximization) algorithm is a statistical iterative method used for tomographic reconstruction. It is based on the likelihood modelled with a Poisson statistic, which represents the probability of obtaining the measured activity distribution from the estimated activity distribution. The objective is to maximise the likelihood, and thus the probability that the measured and estimated projections are the same. The maximisation is achieved using an expectation maximisation algorithm which updates the estimated activity distribution at each iteration. This method converges in all cases and the assumption of a Poisson statistic ensures non-negativity (Hutton et al., 2006, Shepp and Vardi, 1982). It also allows for the correction of certain physical phenomena which will be described in the following section. The calculation times can be significant.

4.1.3.3 OS-EM

The OSEM algorithm (Ordered Subset Expectation Maximization) is an algorithm that reduces the calculation time compared to MLEM algorithms. Indeed, the updating of the projections is no longer done on all the projections but on one subset of projections. Frey et al., 2012 mentionned a possible time reduction of a factor of 8 to 30 without impacting the image quality by simply reducing the number of iterations. In addition, this algorithm offers more accurate quantification and better image quality than the filtered back-projection algorithm according to Dickson et al., 2010.

Nowdays in clinic, most of the indutstrially available reconstruction methods are based on OSEM.

4.1.3.4 Noise control

Increasing the number of iterations is necessary to converge on an accurate reconstruction of the SPECT image. However, this is accompanied by an increase in noise which can be controlled by the use of a post-reconstruction filter or by regularisation methods such as the penalized likelihood method (De Pierro, 1995; Webster Stayman and Fessler, 2000) directly included in the reconstruction.

4.1.4 Deep learning reconstruction

For several years, deep learning methods have been used to perform tomographic reconstructions in PET and SPECT. For example, Shao et al., 2021 compared the use of a deep neural network (DNN) for SPECT image reconstruction with the use of an OSEM algorithm. They showed better performance for the DNN: noise robustness, resolution and quantification accuracy. Note that the scatter correction was not applied. A literature review was proposed by Wang et al., 2020 on this subject while Visvikis et al., 2022 highlighted the applications of artificial intelligence in the fields of nuclear medicine and molecular imaging.

Cette thèse est accessible à l'adresse : https://theses.insa-lyon.fr/publication/2023ISAL0068/these.pdf
© [L. Vergnaud], [2023], INSA Lyon, tous droits réservés

4.2 Physic corrections

During the acquisition process, various physical phenomena have an impact on the detection and positioning of photons. It is essential to compensate for these effects during reconstruction to ensure accurate quantification of activity in the SPECT image. This section provides a description of these phenomena and presents a non-exhaustive list of correction methods.

4.2.1 Attenuation

4.2.1.1 Definition

Attenuation of primary gamma photons occurs when they interact with the tissue through which they pass. This can result in the total absorption of the photon through the photoelectric effect, or partial absorption and scattering through Compton scattering, or scattering only through coherent scattering. The linear attenuation coefficient, denoted as μ, and expressed in cm^{-1}, is used to characterise the probability of interaction between photons and the traversed tissue per unit length (Zaidi and Hasegawa, 2003). It depends on the energy of the photon and its location (Ritt et al., 2014). If we consider a photon flux of intensity I_0 passing through a material of linear attenuation coefficient μ and thickness dx, then the transmitted photon flux I is given by Eq. 4.1.

$$I = I_0 \exp(-\mu \times dx) \tag{4.1}$$

In the case of a patient, photons generally interact with multiple tissues that have varying linear attenuation coefficients (e.g. water, air, bone). Therefore, having knowledge of these values is crucial for ensuring accurate attenuation correction.

4.2.1.2 Correction methods

In 1978, Chang, 1978 proposed the use a single linear attenuation coefficient for the entire patient. However, this assumption may not hold true,especially when the field of view includes regions with heterogeneous properties. In clinical practice, an increasing number of gamma cameras are now equipped with a scanner to estimate attenuation maps that can be used for correction purposes (Fleming, 1989). Hounsfield units are associated with linear attenuation coefficients through conversion curves determined for each system and for different energies. Figure 4.2 provides an example of such conversion curves for three different photon energies.

In the case of SPECT/CT acquisition for brain perfusion, Ishii et al., 2012 showed that the CT-based method provides more accurate attenuation corrections compared to the Chang algorithm. However, the CT-based method can still be affected by uncertainties related to the registration between CT and SPECT images and patient movement it (further details in Section 4.5). Additionally, artefacts present in the CT images, such as prostheses, can impact attenuation correction (Ritt et al., 2014). Moreover, some clinically available gamma cameras do not have a CT scan option, making CT-based attenuation correction impossible. To address this, some authors have successfully estimated attenuation maps from SPECT data using deep convolutional neural networks, particularly for myocardial perfusion (Shi et al., 2020). They compared the synthetic CT images generated with the acquired CT images and their influence on the reconstructed SPECT image and observed consistent results. Others have used residual and UNet deep convolutional neural networks to directly

Cette thèse est accessible à l'adresse : https://theses.insa-lyon.fr/publication/2023ISAL0068/these.pdf
© [L. Vergnaud], [2023], INSA Lyon, tous droits réservés

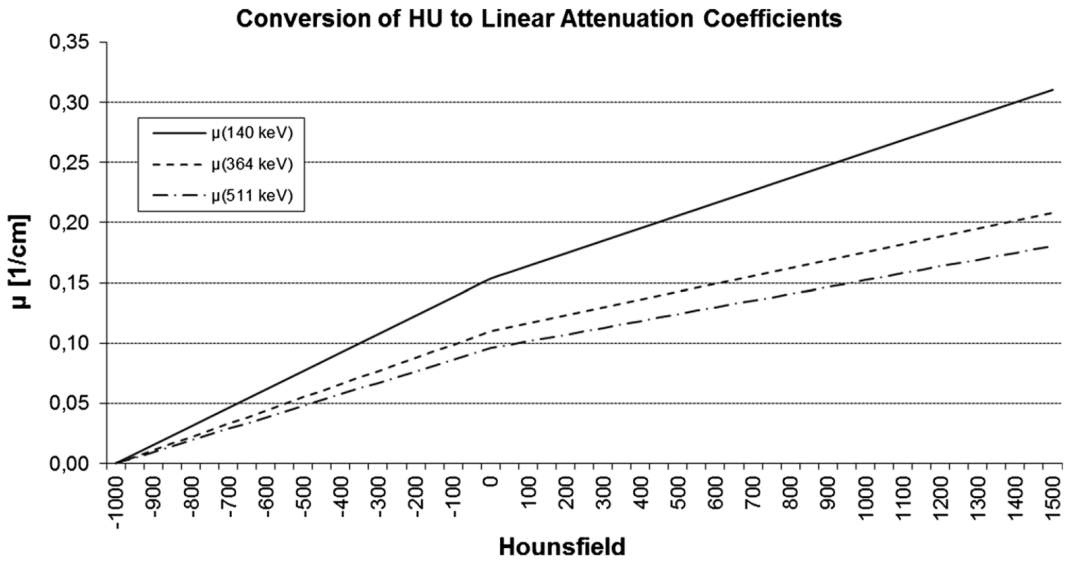

FIGURE 4.2 – Example of conversion curves for different energies of photon extracted from Ritt et al., 2014.

correct attenuation in SPECT images (Mostafapour et al., 2021) and showed that this method was better than the Chang's algorithm, which is the only available option in the absence of an attenuation map. This work has also been proposed by Sakaguchi et al., 2021 for SPECT images of brain perfusion using a convolutional neural network.

4.2.1.3 Questioning the use of CT for attenuation correction

When a scanner is combined with a gamma camera, CT-based attenuation correction is the gold standard. After the injection of the radiopharmaceutical, the patient continuously absorbs the dose from the radioactive decay to which it is necessary to add doses due to the X-radiation which go through the body during each CT acquisition. Today, some scanners available in clinics allow low-dose CT scans (around 2 mGy CTDI for VERITON CT) to be performed. However, these scans can be impacted by noise and artifacts and degrade the accuracy of the SPECT image attenuation correction. To avoid this, Gupta et al., 2017 attempted to reduce the absorbed doses for bone scintigraphy and demonstrated that image quality was better with the "low-dose" protocol (110 kVp and 40 mAs) compared to the standard protocol (130 kVp and 70 mAs), which was better for soft tissues. Another method would be to acquire only one CT and successively register it with each SPECT image in order to correct for attenuation during reconstruction, as used by Delker et al., 2016. For ^{177}Lu therapies, the absorbed dose from X-rays radiation is very low compared to the doses delivered to organs and lesions (on the order of Gy).

4.2.2 Scatter

4.2.2.1 Definition

The scatter corresponds to the modification of the direction of a photon by interaction with matter. The main effect is the Compton effect (*Compton effect* 2023) which occurs when the photon interacts with free or valence electrons layer. Part

Cette thèse est accessible à l'adresse : https://theses.insa-lyon.fr/publication/2023ISAL0068/these.pdf
© [L. Vergnaud], [2023], INSA Lyon, tous droits réservés

of the photon's energy is transmitted to the electron and the direction of the photon is changed. The second effect, which is less common and occurs with photons of lower energy (<100 keV, Cherry et al., 2012), is coherent scattering (*Coherent scattering* 2023). This time, the photon keeps its energy which is too low to release an electron and only changes direction. The scatter has both an impact on the quality of the SPECT image and on the quantification (Jaszczak et al., 1984). It occurs in the patient, in the collimator and in the crystal (De Nijs et al., 2014). s

4.2.2.2 Scatter correction methods

In this section, only the most commonly used and clinically available scatter correction methods are described. A detailed literature review has been proposed by Hutton et al., 2011. The two scatter correction methods presented are based on the energy distribution (Dewaraja et al., 2012).

Dual-Energy Window method (DEW) The use of the Dual-Energy Window method (Jaszczak et al., 1984) requires the acquisition of two energy windows of the same width: one for the main photopeak and a second for the scatter. It is assumed that the proportion of scattered photons in the main photopeak window corresponds to a fraction k of the counts in the scatter window (C_{Scat}). The number of counts in the main photopeak corrected for scatter (C_{Prim}) is given by the equation 4.2 where C_{Tot} is the number of counts in the main photopeak window before correction for scatter.

$$C_{Prim} = C_{Tot} - k \times C_{scat} \tag{4.2}$$

The value of k must be estimated either experimentally or by Monte Carlo simulation (Jaszczak et al., 1984). This value is generally considered to be equal to 0.5 for ^{177}Lu (De Nijs et al., 2014; Huh et al., 2023; Marin et al., 2017). Koral et al., 1990 applied this method directly on projection data.

Triple-energy window method (TEW) The Triple-Energy Window method was proposed by Ogawa et al., 1991. It consists of acquiring photons from the photopeak window as well as from the two windows adjacent to the photopeak window. An estimate of the number of photons scattered in the main window is made by considering a trapezoidal region at the base of the photopeak with the following dimensions: left and right heights equal to $\frac{C_{Left}}{W_{Left}}$ and $\frac{C_{Right}}{W_{Right}}$ respectively and base equal to W_{Base}. C_{Left} and C_{right} are the counts measured in adjacent windows while W_{Left}, W_{Right} and W_{Base} are the widths of the adjacent and main windows. The Eq. 4.3 is the estimation of scattered photons C_{Scat}.

$$C_{Scat} \approx (\frac{C_{Left}}{W_{Left}} + \frac{C_{Right}}{W_{Right}}) \times \frac{W_{Base}}{2} \tag{4.3}$$

Counts (C_{Tot}) acquired in the main window correspond to the sum of primary counts (C_{Prim}) and scattered counts (C_{Scat}). The number of primary counts in each pixel of each projection is obtained with the Eq. 4.4 as described in Ogawa et al., 1991.

$$C_{Prim} = C_{Tot} - C_{Scat} \tag{4.4}$$

Cette thèse est accessible à l'adresse : https://theses.insa-lyon.fr/publication/2023ISAL0068/these.pdf
© [L. Vergnaud], [2023], INSA Lyon, tous droits réservés

The width of adjacent windows has an influence on the quantification. Indeed, if these windows are small, they will be more sensitive to noise and a filter should be used, whereas if the windows are wider, the noise is less important but the scattering estimate is also less accurate (Dewaraja et al., 2012).

Other methods based on the energy distribution such as the downscatter correction, the combination of scatter and downscatter corrections or the dual-photopeak window method are presented and compared in the article by De Nijs et al., 2014. Accurate scatter estimation obtained by Monte Carlo simulation (Dewaraja et al., 2017) remains the reference method but it is generally not used in clinical practice because of the long computation times. Therefore, Xiang et al., 2020 proposed to use a deep learning (DL) approach and compared reconstructions performed with estimates obtained by DL and those obtained by MC simulation and showed similar results especially for contrast recovery. Today, scatter corrections can be directly included in the reconstruction algorithms.

4.2.2.3 Recommendations concerning scatter correction for ^{177}Lu

As seen in the previous chapter, ^{177}Lu decays into photons whose energies are mainly 113 keV and 208 keV. In clinical practice, only one of the two peaks is used and the choice of the scatter correction method depends on this. Indeed, a portion of the photons from the primary energy peak at 208 keV are scattered and end up in the low-energy window, while the primary energy peak at 113 keV is both scattered and contaminated by the scattered high-energy photons (downscatter). The TEW scatter correction method is recommended for the quantification of ^{177}Lu for the two photopeaks (Ljungberg et al., 2016) even if it causes signifcant incaccuracy in quantification when activity is low and/or background is present. In the second case, the overestimation of activity recovery can reach 30% (Robinson et al., 2016). According to De Nijs et al., 2014, the best scatter correction method for ^{177}Lu is the Effective Scatter Source Estimation (ESSE Frey and Tsui, 1996) whatever the chosen peak (Karimi Ghodoosi et al., 2018) but, to our knowledge, it is not available in clinic.

4.2.3 Partial volume effect correction

4.2.3.1 Definition

For each imaging system, it is possible to estimate its spatial resolution which characterises the size of the smallest feature that can be distinguished in the reconstructed images. It is composed of the intrinsic resolution of the detector and the collimator resolution which is spatially-variant. At about 10 cm, the depth of the organs, the spatial resolution of the system can be approximated by the spatial resolution of the collimator only (Cherry et al., 2012). Gamma cameras are known to have poor spatial resolution (at 10cm for ^{177}Lu, between 18 and 22 mm Full Width at Half Maximum = FWHM with a FBP reconstruction (Ryu et al., 2019)) which results in an underestimation of the activity concentration when the volumes of interest are less than 2/3 times the FWHM (Marquis et al., 2023). This is known as the partial volume effect. Cross-contamination is one of the main causes of PVE due to the Point-Spread Function of the system (PSF) (Erlandsson et al., 2012) even if there is a second phenomenon which contributes to it *tissue fraction effect* and which is related to the sampling of the image. Several factors relating to the characteristics of the system (spatial resolution and sampling of the image), the object (size, shape, surrounding tissues) and the method of measurement can affect the PVE (Soret et al., 2007). In practice, for a hot volume of interest placed in an equally hot environment,

Cette thèse est accessible à l'adresse : https://theses.insa-lyon.fr/publication/2023ISAL0068/these.pdf
© [L. Vergnaud], [2023], INSA Lyon, tous droits réservés

the activity of the volume is partly spilled into the environment ("spill-out") and likewise for part of the activity of the environment in the volume ("spill-in") (Srinivas et al., 2009).

4.2.3.2 PVE correction applied for ^{177}Lu

The PVE correction is essential for accurate ^{177}Lu dosimetry as shown by Marquis et al., 2023. They observed that the non-correction of this effect leads to a significant underestimation of absorbed doses in lesions. It can be explained by the size of lesions which are mainly smaller than spatial resolution of the system. Note that a 42% threshold segmentation was applied and could impact results because for ^{177}Lu therapy the uptake is heterogeneous and the volume of lesion segmented on CT scan could be different. The authors believe that this effect may be one of the reasons for the difficulty in establishing a dose-response relationship. Moreover, the PVE depends on the activity distribution which evolves over time (fixation and then radioactive and biological elimination), especially for lesions (Erlandsson et al., 2012). In clinical practice, two methods are mainly used and will be described in this section. For the others, they are detailed in the review of Erlandsson et al., 2012.

Method n°1: Inclusion of PSF in reconstruction This method consists of estimating the PSF using a point-source in the air acquired at different distances from the detector. For each acquisition, the FWHM can be estimated before modelling the PSF by a Gaussian. Deconvolving the PSF during the reconstruction would reduce the PVE but increases the noise and may create Gibbs artefacts.

Method n°2: Recovery coefficients This second method consists of post-reconstruction correction of the volumes of interest using experimentally estimated correction factors called Recovery Coefficients (RC). Typically, a phantom containing spheres of different sizes are filled with a known activity concentration. The same applies to the background. Srinivas et al., 2009 emphasised the importance of setting activity in the background in order to be as close as possible to the clinical reality. The calculation of these factors is usually done using the Eq. 4.5 (Finocchiaro et al., 2019), although variants can be found in the literature (e.g. Eq. 4.6 by Srinivas et al., 2009).

$$RC = \frac{Measured\ activity}{True\ activiy} \tag{4.5}$$

$$RC = \frac{Measured\ sphere\ activity - Measured\ bkg\ activity}{Known\ sphere\ activity - Known\ bkg\ activity} \tag{4.6}$$

4.2.4 Deadtime correction

4.2.4.1 Definition

The dead time is the minimum time needed between two successive photons for being both detected by the system. If the count rate is too high, the system will not be able to detect all the events, resulting in a loss of detected photons. The estimated count rate will be lower than the true count rate [Rapport SFPM n°28].

Cette thèse est accessible à l'adresse : https://theses.insa-lyon.fr/publication/2023ISAL0068/these.pdf
© [L. Vergnaud], [2023], INSA Lyon, tous droits réservés

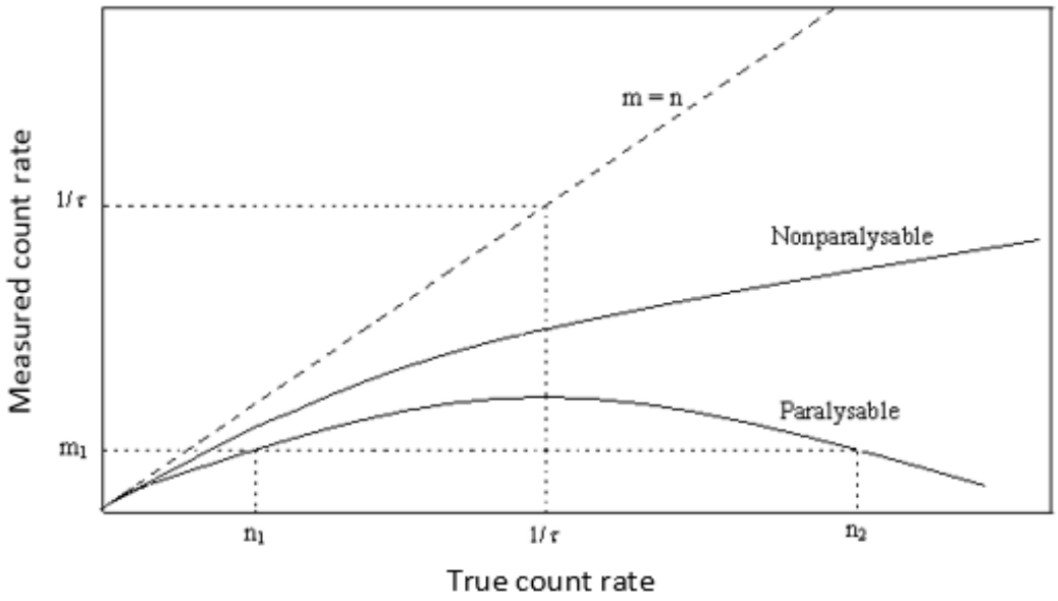

FIGURE 4.3 – Schematic diagram showing the behaviour of the paralysable and non-paralysable models. The measured count rate is estimated based on the true count rate. Extracted from Usman and Patil, 2018.

4.2.4.2 Models

The detectors can follow two ideal models of dead time behaviour: the paralyzable model and the non-paralyzable model. Typically, the detector response combines both (Yousaf et al., 2015), but sometimes one is supposed to be dominant over the other and one ideal model is considered. In the following, m is the measured count rate [count/s], n the true count rate [count/s] and τ the dead time [s].

Paralyzable model When a second photon arrives during the dead time created by the first, this second photon is not detected and the dead time it takes to detect a new event starts again from zero. The paralyzable model is described by equation 4.7 and represented in Figure 4.3.

$$m = n \times \exp\left(-n \times \tau\right) \tag{4.7}$$

Non paralyzable model With this second model, the second incident photon is also not detected, but unlike the stalled model, the dead time does not restart from the second event but only from the first. The non-paralyzable model is described in equation 4.8 and represented in Figure 4.3.

$$m = \frac{n}{1 + n \times \tau} \tag{4.8}$$

Hybrid model Combinations of the two previously models are also proposed in the literature. Lee and Gardner, 2000 developed a model which considers the two dead times (Eq. 4.9).

$$m = \frac{ne^{(-n\tau_P)}}{1 + n\tau_N} \tag{4.9}$$

Cette thèse est accessible à l'adresse : https://theses.insa-lyon.fr/publication/2023ISAL0068/these.pdf
© [L. Vergnaud], [2023], INSA Lyon, tous droits réservés

Where τ_P is the paralyzable dead time and τ_N the non-paralyzable. A disadvantage of this method is that the order of the dead times has an impact on the model (Yousaf et al., 2015) and there is no justification in the choice of this order. Patil and Usman, 2009 modified the model described by the Eq. 4.9 by replacing the paralysable and non-paralysable dead times with a single dead time and a paralysis factor (Eq. 4.10). When two events are detected successively, the dead time can be increased and this increase represents the paralysis factor.

$$m = \frac{ne^{-n\tau f}}{1 + n\tau(1-f)} \tag{4.10}$$

A comparison between the paralyzable, the non-paralyzable and the two hybrid models was performed by Yousaf et al., 2015. The authors showed the difficulty and necessity of choosing the dead time model as it is influenced by the operating conditions of the systems.

4.2.4.3 Dead Time estimation methods

In order to estimate the detector dead time, two main methods are available in the literature: the two-source method and the decaying source method. More recently, a third method has been proposed. These are described in the following.

Two-sources method The two-sources method (1 and 2) consists of performing three successive acquisitions with a first source (1), then adding the second (1+2) and removing the first (2). Their true count rates are noted R_1, R_{12} and R_2, respectively. R_{BG} is the background one (Gardner and Liu, 1997). It is important to have identical sources whose positions do not vary between acquisitions. The relationship between the count rates is given by Eq. 4.11 and allows the estimation of the dead time τ to be derived using one of the models described above (Section 4.2.4.2). The disadvantage of this method is that it requires a priori on the model to be used.

$$R_1 + R_2 = R_{12} + R_{BG} \tag{4.11}$$

Decaying source method In this method, a known source of activity is positioned as close as possible to the detector to allow for dead time and the count rate is recorded. Over time, the activity decreases and the count rate is read regularly. It is thus possible to plot the measured count rates against the actual count rates and to model the curve using one of the models presented in the section 4.2.4.2. One advantage of this method is that it is not necessary to have a priori on the model to use. However, it can be used only with short half-life except if the distance between the detector and the source is modified to change the count rates as suggested in Gardner and Liu, 1997. If the background counts is non-negligible, an adaptation of this method was proposed by Choi et al., 2023.

Radiation Absorption Law method (Akyurek, 2021) This method is based on the gamma attenuation law described in Eq. 4.12.

$$n_1 = n_0 e^{-(\frac{\mu}{\rho})\rho X} \tag{4.12}$$

Where n_0 and n_1 are the true numbers of incident and transmitted photons, $\frac{\mu}{\rho}$ the mass attenuation coefficient and the density of the material passed through.

Cette thèse est accessible à l'adresse : https://theses.insa-lyon.fr/publication/2023ISAL0068/these.pdf
© [L. Vergnaud], [2023], INSA Lyon, tous droits réservés

A radioactive source is placed in front of a detector and the number of gamma photons is measured (m_0). Then, a shielding material, assumed to be very thin, is placed between the two and the number of transmitted photons is measured (m_1). m_0 and m_1 are then expressed using one of the two models presented previously (Eq. 4.2.4.2 and 4.2.4.2). The ratio $\frac{m_0}{m_1}$ is used in order to extract the dead time τ. The assumption of a very thin material is important because it allows to consider a build up factor of 1, i.e. there are no scattered photons related to the interaction with matter.

4.2.4.4 Correction methods

Once the dead time has been evaluated, its correction can be applied either to the SPECT projections or to the reconstruction. This is also the subject of the article by Desy et al., 2022 which assesses the influence of this choice on dosimetry for ^{177}Lu radiopharmaceutical therapy. On the data of 12 patients, the differences in absorbed doses for the kidneys, the bone marrow and the lesions are overall less than 2% except in rare cases. They showed that in practice it is possible to correct dead time directly in reconstructions. However, if the dead time is important and/or there are asymmetries in the image, the precision of the quantification is better with a correction of the dead time directly in the projections (Cohalan et al., 2020).

4.2.4.5 Dosimetric impact in ^{177}Lu treatments

Dead time is one of the physical phenomena that can impact ^{177}Lu quantification. Desy et al., 2020 evaluated this impact for the renal dosimetry of 564 patients treated with ^{177}Lu-octreotate and activities greater than 7.4 GBq. They, therefore, set up simulations to compare the influence of the dead time correction at times D1 and D3 on the absorbed renal dose when 7.4 GBq are injected. They observed differences (%) of: [1.9 ; -0.54 ; -1.04 ; -2.60 ; -6.65] ([Minimum ; 1^{st} decile ; Median ; 9^{th} decile ; Maximum]). They recommend correcting for dead time to improve quantification, especially if PRRT is personalised. Solid-state cameras are not subject to loss of detected events because the charge collection time is very low. However, when two events occur successively, a single combined pulse is created instead of two: this is called the pile-up effect (Usman and Patil, 2018).

4.2.5 Filters

Intra- and/or post-reconstruction filters can be proposed to reduce noise in the reconstructions. They will have the effect of smoothing the images by reducing the high frequencies. However, the application of filters will modify the quantification in the images: this is why filters are not recommended for reconstructions that will be used for dosimetry (Dickson et al., 2022). In MIRD No.23 (Dewaraja et al., 2012), a post-filter is applied when the TEW method is used to correct the scatter but the scatter energy windows are narrow. Indeed, the latter are more likely to be noisy than the wider windows.

4.3 Calibration factor

Estimating the calibration factor is an essential step in dosimetry. Indeed, it allows to convert SPECT images, expressed in counts per mL, into activity (Bq). This

Cette thèse est accessible à l'adresse : https://theses.insa-lyon.fr/publication/2023ISAL0068/these.pdf
© [L. Vergnaud], [2023], INSA Lyon, tous droits réservés

conversion can be performed either with a calibration factor CF or a sensitivity factor SF (equations 4.13 and 4.14 respectively). In both cases, the latter must be determined for each imaging system, each radionuclide, each set of acquisition and reconstruction parameters.

$$CF[MBq/counts] = \frac{A[MBq]}{Counts} \tag{4.13}$$

$$SF[counts/s/MBq] = \frac{Counts}{T[s] \times A[MBq]} \tag{4.14}$$

With A the activity in the phantom, $Counts$ the number of counts reconstructed and T the acquisition time. Two main methods exist in the literature for estimating the calibration factor (Ljungberg et al., 2016; Dewaraja et al., 2012):

1) SPECT acquisition of a large uniform phantom of known activity with the same acquisition and reconstruction parameters as for patients (D'Arienzo et al., 2016)

2) Planar acquisition of a source point in air

Uribe et al., 2017 showed that the calibration factors they obtained with each of the methods are roughly the same. The first models better the patient and therefore the associated physical phenomena. However, the implementation of the calibration is more cumbersome (Zhao et al., 2018). The second method is easy to set up and can be repeated regularly to check the stability of the calibration factor (Frey et al., 2012) but requires that the corrections applied (attenuation, scatter) are perfect (Dewaraja et al., 2012). Other calibration phantoms based on these two methods have also been used in the literature. These are listed and compared in the paper by Zhao et al., 2018 and have shown that it is possible to use a point source and obtain sufficient accuracy provided the scatter is corrected.

This factor can be affected by the shape of the phantom, the collimator (De Nijs et al., 2014) but also different physical phenomena such as attenuation, scattering (Karimi Ghodoosi et al., 2018; De Nijs et al., 2014), partial volume effect and dead time.

Robinson et al., 2016 printed and used 3D phantoms of the same shape as the organs and showed that this improved quantification at the organ level while Ramonaheng et al., 2021 tested the influence of the shape of the calibration phantom on the recovery coefficients (RC) and quantification. They found that the quantification errors were approximately the same for the RCs regardless of shape when all corrections are applied. Mezzenga et al., 2017 attempted to determine the optimal geometry for performing the calibration by comparing the uniform Jaszczak phantom with a 16 mL sphere in a Jaszczak phantom. As a result of this study, they recommend using the uniform phantom and not the sphere. The large uniform phantom is also interesting because it avoids partial volume effects especially if the number of detected counts is evaluated in the whole field of view (Zhao et al., 2018). Despite this, the conditions for estimating the calibration factor do not match those of the VOIs in a patient: difficulties in contouring the VOIs, spill-in/spill-out effects and PVE. Indeed, the activity concentration around a volume of interest may vary between volumes of interest and patients and is not taken into account in the estimation of the calibration factor. The PVE tends to spread the activity that is in the volume outside the volume. This can lead to more or less important quantitative errors depending on the applied correction method and the choice of the segmentation method. Uribe et al., 2017 compared three segmentation methods: 40% thresholding, anatomical segmentation on the CT and the "IADT" method (Grimes et al., 2012)

Cette thèse est accessible à l'adresse : https://theses.insa-lyon.fr/publication/2023ISAL0068/these.pdf
© [L. Vergnaud], [2023], INSA Lyon, tous droits réservés

developed in their team and showed that the estimated activities were always underestimated when the inserts were in a background. Karimi Ghodoosi et al., 2018 recommend using small VOIs within the phantoms to limit the PVE knowing that they have shown that the volume of the chosen phantoms creates uncertainty in the estimation of the calibration factor. At present, there is no unanimous agreement on the ideal segmentation method for dosimetry.

Concerning the dead time, D'Arienzo et al., 2016 evaluated its impact on the absolute quantification and observed error less than 2% for an activity of 1.36 GBq. Similarly, for Mezzenga et al., 2017, they observed 0.5 % for the uniform phantom (704 MBq) and 1.2 % for the 16 mL sphere (484.8 MBq). Finally, Beauregard et al., 2011 evaluated the impact of dead time on patient quantification and showed deviations ranging from 6.6 % to 11.7 % when injected activities were between 8.3 GBq and 10.2 GBq (higher than the 7.4 GBq allowed in France).

More recently, Halty et al., 2018 proposed a new calibration method based entirely on patient images to obtain patient-specific calibration factors. This method assumes that all injected activity is in the patient at the time of the acquisitions (planar + SPECT) and that the biodistribution of the activity is not significantly changed between the two acquisitions. Although the factors obtained are patient-specific, this method has several drawbacks: 1. all injected activity must be in the patient which implies that all acquisitions are performed before micturition, 2. two acquisitions must be performed instead of a single SPECT and 3. this method was not validated for ^{177}Lu, only for ^{99m}Tc. The calibration factor is necessary for absolute quantification but not for relative quantification. Indeed, in the case of radioembolization treatment, all injected activity is assumed to be in the field of view. The biodistribution is obtained by normalising the SPECT image.

4.4 Dosimetric methods

Once the SPECT images are reconstructed and calibrated, the biodistribution of activity in the patient for each acquisition time is known. The volumes of interest (organs at risk and/or tumours) are then segmented on either the CT or SPECT image or both for each acquisition. To save time, the images are registered so that the contours are only made at the first time and then propagated to the following times. The activities in the volumes are estimated for each time and then the Time Activity Curve (TAC) is fitted using a model (trapezoidal, mono-exponential, bi-exponential, see Chapter 5). The integral of this curve corresponds to the cumulative activity of the volume. Finally, several dosimetric methods can be used to estimate the absorbed doses by the volumes. In the following sections, we briefly reviews the main methods. In the following, the region containing the activity will be referred to as the "source region" called h and the region in which the absorbed dose is looked at as the "target region" called k.

4.4.1 Local deposition method

The local deposition method assumes that all the energy from the decays of a source voxel is deposited in the same voxel that corresponds to the target voxel. The mean particle path must be sufficiently small for this assumption to be acceptable: the average range of β^- particles is 0.67 mm (maximum: 2.2 mm) (**Hennrich2022**). For instance, this assumption is incorrect for gamma photons that pass through and exit the patient's body.

Cette thèse est accessible à l'adresse : https://theses.insa-lyon.fr/publication/2023ISAL0068/these.pdf
© [L. Vergnaud], [2023], INSA Lyon, tous droits réservés

4.4.2 Organ-based S-value (MIRD)

This method is a conventional method (Furhang et al., 1997) based on pre-calculated S-values from digital phantoms for organs at risk (Chauvin et al., 2020) and lesions (Olguin et al., 2020). Using the MIRD formalism (Howell et al., 1999), the mean absorbed dose ($\bar{D}_k$) by a target volume k can be written as in Eq. 4.15.

$$\bar{D}_k = \sum_h \tilde{A}_h \times S_{k \leftarrow h} \tag{4.15}$$

Where $\tilde{A}_h$ is the cumulative activity in the source region h and $S_{k \leftarrow h}$ is the dose absorbed by k from the decays of h. The S-values are dependent on the radionuclide, the characteristics of the model (age, sex, mass, size) and the tissue of interest (Bardiès and Gear, 2021). The activity distributions are assumed to be homogeneous within the different tissues as well as the distribution of the dose deposited in the target (Giap et al., 1995). The tissue mass is used to scale the corresponding S-value in several studies to improve the accuracy of dosimetry as in the Santoro et al., 2018 study. The OpenDose collaboration provides access to a database of estimated S-values derived from anthropomorphic phantoms, aiming to facilitate the implementation of dosimetry in each hospital (Chauvin et al., 2020).

4.4.3 Dose Point Kernel method (DPK)

The DPK method consists of convolving a dose point kernel, usually estimated by Monte Carlo simulation, with an activity distribution map (Furhang et al., 1996) to obtain an absorbed dose map. The dose point kernels represent the energy deposited by a point-source at different distances in a uniform medium. They are determined for a specific radionuclide as computed by Graves et al., 2019 and a given medium assumed to be homogeneous and infinite, which can lead to inaccuracies in regions where there are several media (Giap et al., 1995).

4.4.4 Voxel S-value method (VSV)

The VSV method works on the same principle as the organ-based S-value method but at the voxel level. Each S-value represents the dose to the target voxel from the decays of one of the N voxels in the source volume. The resulting equation is the same as Eq. 4.4.2 except that the cumulative activities are also calculated at the voxel scale. The S-values are pre-calculated (Xin et al., 2023) and depend on the radionuclide, the size and the geometry of the voxels. Tissue heterogeneity is not taken into account as was the case for the DPK method (Bolch et al., 1999).

4.4.5 Monte Carlo simulations

Monte Carlo simulations are used to simulate the transport of particles (e.g. electrons, photons) through the different tissues of the human body and estimate energy deposits in space as a function of interactions between radiation and matter. Each tissue is characterised by an atomic number and density obtained from the CT scan, while the activity distribution of the radionuclide is extracted from the SPECT or PET images. As a result, a dose rate map at the voxel level is estimated. This is referred to as a patient-specific dosimetry method because it allows the characteristics of the patient (geometry, density, atomic number) and the source distribution to be taken into account (Furhang et al., 1996). One of the disadvantages of this method is that the calculation times can be long. In addition, Monte Carlo simulations can

Cette thèse est accessible à l'adresse : https://theses.insa-lyon.fr/publication/2023ISAL0068/these.pdf
© [L. Vergnaud], [2023], INSA Lyon, tous droits réservés

also be used in other dosimetric methods to estimate DPK or S-values (Sarrut et al., 2014). This approach will be further described in the next chapters.

4.4.6 Comparison of dosimetric methods

As mentioned earlier, several dosimetric methods exist, each with their own advantages and disadvantages. Monte Carlo simulations remain the reference method as they allow for the radionuclide, tissue heterogeneity and patient-specific activity distributions to be taken into account. However, it is not often used in clinical practice because of the long calculation times. The local deposition method relies on a strong assumption about the location of the energy deposition which is only valid for particles of low mean path. In the case of gamma (113 keV or 208 keV) photons, for example, this assumption is false because the energy deposits can be far from the source. The organ-based S-value method is often used because it is simple and fast to implement. However, it is not patient specific as the estimation of S-values is based on reference phantoms although the mass of the organs can be scaled. The distribution of activity within the same volume is also assumed to be homogeneous which is not the case for patients treated with ^{177}Lu. Finally, the DPK and VSV methods are also simple, fast, clinically usable and above all patient specific. However, the kernels and S-values are estimated assuming that the material is homogeneous and infinite, which does not correspond to what is found in a patient. For this reason, a density correction has been proposed and tested in several studies: Dieudonné et al., 2013 have shown that this correction has a small but significant impact on the calculation of absorbed dose in the abdomen while Brosch-Lenz et al., 2021 have highlighted the need to apply it for the estimation of absorbed dose for bone lesions (here, for patients treated with ^{177}Lu-PSMA). Kim et al., 2022 compared the heterogeneity-corrected VSV method with Monte Carlo simulations and highlighted its accuracy and speed in estimating absorbed dose.

4.4.7 AI methods for radionuclide therapy

Artificial intelligence methods are currently finding various applications in radionuclide therapy. They can be employed for dosimetry (Akhavanallaf et al., 2021; Lee et al., 2019) or to delineate organs at risk (Jackson et al., 2018). Monte Carlo simulations are considered the gold standard for dosimetry but can be time-consuming. Therefore, Li et al., 2022 used a convolutional neural network to learn the differences in dose rate maps obtained with voxel dose kernels and Monte Carlo simulations. Finally, machine learning algorithms were implemented to predict absorbed doses from pre-treatment images, radiomics, dosiomics (Plachouris et al., 2023), or pre-treatment biological samples (Xue et al., 2022). To complement this, Avanzo et al., 2021 provided a more detailed description of the clinical applications of AI methods and the associated challenges.

4.5 SIRT dosimetry

The personalisation of the treatment by radioembolization requires a dosimetric estimate based on the ^{99m}Tc-MAA SPECT image. The method of calculating the ^{90}Y activity to be injected depends on the type of spheres chosen: mono-compartmental (glass spheres) or compartmental (resin or glass spheres), also known as the "partition model" (Levillain et al., 2021; Weber et al., 2022). These methods are based on the MIRD formalism described in Section 4.4.2. They assume that the activity

Cette thèse est accessible à l'adresse : https://theses.insa-lyon.fr/publication/2023ISAL0068/these.pdf
© [L. Vergnaud], [2023], INSA Lyon, tous droits réservés

is homogeneously distributed within the volumes considered. Empirical methods also exist for resin microspheres using tumor involvement or body surface area (Giammarile et al., 2011). The pulmonary shunt is also assessed using the lung shunt fraction (LSF described in Bastiaannet et al., 2018) whose value should not be too high in order to avoid radiation pneumonitis.

International recommendations (Weber et al., 2022; Levillain et al., 2021) have been developed to establish maximum tolerated dose limits depending on the type of treatment and the calculation method used. They also suggest applying attenuation and scatter corrections to improve the visual quality and quantification of the SPECT image. Moreover, these corrections reduce the errors of estimation of LSF. There is no indication whether or not respiratory motion correction is used in SPECT, although this affects the estimate of mean hepatic dome volume in the lungs (Levillain et al., 2021).

SPECT acquisitions last for several minutes during which the patient may move voluntarily (e.g. movement of the arms or head) or involuntarily (respiratory movement, cardiac movement). These movements impact the quality of the acquired image and the resulting quantification (Frey et al., 2012). For this reason, methods have been proposed to estimate and correct the movement. Kyme and Fulton, 2021 have performed a literature review of all these methods in the case of SPECT but also PET and CT acquisitions. These include the use of additional external devices, the addition of a second imaging or markers in the field of view, or the extraction of the signal from the acquisitions themselves. In the case of radioembolization, respiratory motion may influence the estimated distribution of activity (contribution to the partial volume effect, Soret et al., 2007) present almost entirely in the liver and could impact pretreatment dosimetry.

A few studies have investigated the impact of respiratory motion correction on SPECT and PET images. Ausland et al., 2018 proposed a phantom study including 5 spheres of ^{90}Y of different volume with homogeneous or non-homogeneous activity. They showed an underestimation of the dose absorbed by the tumors and an overestimation of the dose in the normal liver. A similar study (Osborne et al., 2018) was performed on a patient equipped with a respiratory band to extract the respiratory signal. They also highlighted the underestimation of the dose to the tumor. For SPECT, Bastiaannet et al., 2017 showed a decrease in activity recovery and tumor/non-tumor (TN) ratios on phantoms. Santoro et al., 2022 tested their methodology of respiratory motion correction on phantoms and then applied it to 12 patients with only one lesion and highlighted the negative impact of breathing on quantification. Finally, Lu et al., 2022 assessed the impacts of the respiratory movement, the attenuation correction and the segmentation of volumes of interest on the LSF and the TN ratio. They observed that the greatest impact is due to poor contouring of VOIs. LSF and TN ratio estimates are best when respiratory motion correction, attenuation correction, and VOIs are applied and correct. Impact of respiratory motion will be further studied in Chapter 7.

Cette thèse est accessible à l'adresse : https://theses.insa-lyon.fr/publication/2023ISAL0068/these.pdf
© [L. Vergnaud], [2023], INSA Lyon, tous droits réservés

Chapter 5

^{177}Lu Dosimetric studies review

This chapter provides a literature review encompassing clinical and research dosimetric studies conducted thus far (as of spring 2023) for ^{177}Lu therapies. A wide range of dosimetric workflows have been implemented to evaluate the absorbed doses in patients, considering OARs areas and/or lesions, while considering the clinical constraints and available data (e.g. imaging, biology) specific to each medical centre. In a 2017 European survey conducted by Sjögreen Gleisner et al., 2017, encompassing 26 countries, clinical practices in molecular radiotherapy, including patient and treatment numbers, and the implementation of dosimetry, were reviewed. The survey revealed that ^{177}Lu radiolabelled with somatostatin analogues was used in 13 out of 26 countries, with systematic post-treatment imaging, but post-treatment dosimetry was performed in only 44% of cases. During the same period, ^{177}Lu-PSMA was used in only 2 countries, with systematic post-treatment dosimetry. Presently, ^{177}Lu therapies are becoming more prevalent, and clinical trials are underway to explore new applications (Chapter 5, Section 2.8). However, dosimetry is not consistently employed. In a study by Eberlein et al., 2017, the necessity of individual dosimetry for theranostic treatments, such as radioiodine therapy, PRRT with ^{177}Lu or ^{90}Y, was questioned. The study concluded that dosimetry is essential for treatment optimisation and predicting treatment responses.

5.1 Clinical constraints

Clinical constraints can pose challenges to the implementation of dosimetry. Factors such as the patient's health condition (including pain and fatigue), an increasing number of patients leading to longer camera occupancy time, and the need for multiple acquisitions after each injection can all hinder the process. Furthermore, additional human resources are required for tasks such as segmentation and calculations. To facilitate this process, commercial dosimetric software packages have become available in the market, as described by Capala et al., 2021. Several comparisons between different software packages have been conducted (Santoro et al., 2021, Huizing et al., 2020, Mora-Ramirez et al., 2020, Ramonaheng et al., 2022). However, the time required for dosimetry remains a challenge, particularly as it is not extensively used for personalised treatment. To address this issue, Dewaraja et al., 2022 proposed an almost fully automated dosimetry workflow with a total calculation time of 25 minutes. This workflow includes tasks such as OAR segmentation, SPECT registration for contour propagation, Monte Carlo simulations, and voxel-level fitting and integration. Subsequently, EANM guidelines (Gear et al., 2023) have been provided to enable the implementation of dosimetry while considering the resources available at each centre. These guidelines outline the roles of different

Cette thèse est accessible à l'adresse : https://theses.insa-lyon.fr/publication/2023ISAL0068/these.pdf
© [L. Vergnaud], [2023], INSA Lyon, tous droits réservés

actors, resource sharing, and examples of dosimetry protocols with their respective advantages and disavantages for various therapies.

5.2 Dosimetry methodology

Several methodologies have been developed for the dosimetry of ^{177}Lu therapies, and some of these have been discussed in recent literature reviews. Jackson et al., 2022 and Alsadi et al., 2022 provided information on imaging protocols and absorbed doses at the level of OARs and lesions; however, they did not describe the dosimetric workflow specifically for ^{177}Lu-PSMA therapies. Sjögreen Gleisner et al., 2022 presented both the dosimetric workflow and absorbed doses but only for salivary and lacrimal glands (^{177}Lu-PSMA) and for tumours (^{177}Lu-PSMA and ^{177}Lu-DOTATATE). Huizing et al., 2018 discussed the dosimetric workflow but did not provide absorbed doses for ^{177}Lu-DOTATATE. Lastly, Nautiyal et al., 2022 described the workflows and provided absorbed doses for ^{177}Lu-PSMA therapies. The objective of this section is to provide a detailed description of the dosimetric workflows and absorbed doses for ^{177}Lu therapies based on the existing literature reviews. Additionally, absorbed doses for previously unconsidered volumes have been included, along with the most recent dosimetric studies (Tables 5.2 and 5.3 for ^{177}Lu-SSRT and 5.4, 5.5, 5.6, 5.7 and 5.8 for ^{177}Lu-PSMA). This section aims to provide a comprehensive review specificaly for ^{177}Lu-PSMA therapy, while the discussion for ^{177}Lu-DOTATATE is not exhaustive. The calibration stage of the gamma camera will not be discussed here, as it has already been addressed in Section 4.3.

5.2.1 Planar or SPECT acquisition or both

The biodistribution of the radiopharmaceutical in the patient can be monitored using a set of planar or SPECT acquisitions (Section 3.2) or a combination of both, involving several planar acquisitions and a single SPECT acquisition. The estimation of absorbed doses relies on the type of acquisitions used. For instance, Willowson et al., 2018b compared the absorbed doses in the kidneys estimated from 2D planar images and 3D SPECT images and found that the doses obtained from planar images were three times higher (^{177}Lu-DOTATATE). Similarly, Rosar et al., 2021 conducted a study (3D vs hybrid vs planar) with ^{177}Lu-PSMA-RLT (TRT) for different volumes such as kidneys, liver, parotid, submandibular, and bone metastases. They observed that the dose estimates calculated using the hybrid method were more precise (closer to those obtained with the 3D SPECT method) compared to the planar 2D method. Generally, it is recommended to employ 3D SPECT images for accurate quantification of ^{177}Lu. In 2D planar images, organs are superimposed, leading to inaccuracies in attenuation correction and segmentation (Rosar et al., 2021). However, planar images allow for whole-body acquisitions in a short time, which becomes crucial when the number of acquisitions increases, making them commonly used. 3D SPECT/CT acquisitions require more time and involve acquiring multiple beds for whole-body reconstruction. These acquisitions offer several advantages: organs are not overlapping, anatomical contouring can be performed using CT images, and precise attenuation correction is available. Considering the time constraint as a potential obstacle to the implementation of dosimetry, several alternatives have been proposed:

— Use of hybrid dosimetry, which involves obtaining several whole-body planar 2D acquisitions (metastatic patients) along with a SPECT acquisition, resulting

Cette thèse est accessible à l'adresse : https://theses.insa-lyon.fr/publication/2023ISAL0068/these.pdf
© [L. Vergnaud], [2023], INSA Lyon, tous droits réservés

in dosimetry comparable to 3D dosimetry (only SPECT acquisitions).

— Use of CZT gamma cameras that enable whole-body 3D SPECT acquisitions (as described in Section 5.2.2)

— Reduction of the number of time-points for SPECT acquisitions (as described in Section 5.2.3)

For ^{177}Lu-SSTR therapies, typically, the tumours and OARs are located within one or two FOV(s) of the Anger-type gamma camera. Hence, it is feasible to perform SPECT acquisitions for each time-point. However, in the case of ^{177}Lu-PSMA-RTL therapies, patients have bone metastases spread throughout the body and additional OARs (such as salivary and lacrimal glands). Consequently, whole-body acquisition becomes necessary, but it can be challenging to achieved 3D imaging using a conventional gamma camera. Therefore, hybrid dosimetry is commonly employed. In the Tables dedicated to dosimetric workflows for ^{177}Lu-PSMA therapies, only 6 out of 27 studies use multiple 3D SPECT acquisitions.

5.2.2 Type of gamma camera for dosimetry

Recently, the introduction of CZT gamma cameras equipped with twelve detection heads has resulted in faster acquisition times for whole-body 3D SPECT imaging. Currently, there are two commercially available cameras: StarGuide (General Electric Healthcare, Haifa, Israel) and VERITON (Spectrum Dynamics, Caesarea, Israel). A study conducted by Song et al., 2023 compared the performance of the StarGuide camera to an Anger type gamma camera (GE Discovery 670 Pro) for ^{177}Lu therapy. The results showed comparable detection rates between the two cameras, while the acquisition time was three times shorter for the CZT camera (12 min vs 32 min). Similarly, a study (Desmonts et al., 2020) evaluated VERITON with a Symbia camera (3/8") for four different radioelements (^{99m}Tc, ^{123}I, ^{201}Tl and ^{111}In) and demonstrated the potential to reduce the acquisition time by a factor of 2 to 3 for the VERITON camera while maintaining the same image quality. It is worth noting that these studies did not specifically evaluate the quantification of ^{177}Lu, which is addressed in Chapter 8. Furthermore, a clinical trial (NCT04467567, EVADOVE177Lu) is currently in progress to compare the dosimetry from an Anger-type gamma camera and that from a CZT gamma camera.

5.2.3 Single or multiple post-treatment acquisitions

Increasing the number of SPECT acquisitions can pose challenges in implementating dosimetry. This is particularly true for patients experiencing bone pain, as they may have difficulty remaining under the camera for extended periods. In France, for instance, patients are typically hospitalised for only 24 hours following the injection, necessitating their return to the hospital for late acquisitions. Notably, not all patients reside in close proximity to the hospital, further complicating matters. Moreover, the availability of cameras is limited, considering the escalating number of patients benefiting from this type of therapy. Consequently, several studies have focused on reducing the number of acquisitions by carefully selecting the most relevant time-points.

Cette thèse est accessible à l'adresse : https://theses.insa-lyon.fr/publication/2023ISAL0068/these.pdf
© [L. Vergnaud], [2023], INSA Lyon, tous droits réservés

Time-point reduction and selection To begin with, Chicheportiche et al., 2020 aimed to retain only two out of the three time-points (24h, 96h and 168h) acquired following the initial injection of ^{177}Lu-DOTATATE. They compared the calculated dose values using two time-points with those derived from three time-points. The smallest differences in cumulative activity were observed with the 24h and 168h time-points. It is worth noting that a mono-exponential curve fit was employed. The choice of fitting model (mono- or bi-exponential) and the reduction in the number of time-points for ^{177}Lu-PSMA-I&T therapies were specifically discussed by Resch et al., 2023. The optimal compromise for kidney and lesion dosimetry (BED) was found to be a mono-exponential fit using three time-points at 1, 3, and 7 days. The same acquisition time-points were selected for ^{177}Lu-DOTATATE in estimating dosimetry for organs and tumours (Freedman et al., 2020).

Single time-point methods When the aim is to minimise acquisitions to a single acquisition, prior information (such as patient or population pharmacokinetic parameters) or simplifications become necessary. Various methodologies and models for ^{177}Lu described in the literature are complied in Table 5.1.

Simplified workflow comparison Comparisons of simplified methodologies have been conducted to streamline the dosimetric process. Hänscheid et al., 2018 and Madsen et al., 2019 proposed STP methods that involve fitting the TAC with a mono-exponential function. The effective half-life in these methods is estimated through theoretical approximation or using population-based data, respectively. Hou et al., 2021 compared these two methods and found that the errors caused could be very large (except for ^{177}Lu-DOTATATE) compared to the reference method using three time-points. They recommended using a 72-hour post-injection acquisition along with the patient's effective half-life determined from a previous cycle. Gustafsson and Taprogge, 2022 highlighted the risk of underestimating the cumulative activity when relying on these simplified methods. The method proposed by Madsen et al., 2019 was further evaluated by Zhao et al., 2019, who compared it with other simplified approaches (mono-exponential function and 2 time-points). The study revealed that the highest kidney absorbed dose occured between 23 hours and infinity, and using the effective half-life time of a patient population resulted in a 10% error for the kidney dose when the selected time was 1.5 times the effective half-life. Sundlöv et al., 2018 compared ten dosimetric methods based on image type, time-points, and their number. They found that the most accurate and resource-efficient approach involved a single SPECT/CT acquisition at 96h after each cycle. In the context of ^{177}Lu-PSMA therapies, Brosch-Lenz et al., 2023 evaluated the methodologies of Hänscheid et al., 2018 and Garske et al., 2012 (with different STPs) for kidneys and tumours using SPECT/CT acquisitions at either 48h or 72h. The majority of deviations fell within the range of $\pm$20%.

Various simple mathematical functions, such as trapezoidal, linear, mono-exponential, bi-exponential, or tri-exponential functions are commonly employed to fit time activity curves (TAC). However, it is important to consider that some effects are common across all patients (known as fixed effects), while others are specific to each individual (known as random effects). These effects can be effectively described using non-linear mixed models (NLMM). In a study conducted by Devasia et al., 2020, the cumulative kidney activities estimated from a single time-point were compared using NLMM and the mathematical models proposed by Hänscheid et al., 2018 and Madsen et al., 2019. The results demonstrated that, on average, the

Cette thèse est accessible à l'adresse : https://theses.insa-lyon.fr/publication/2023ISAL0068/these.pdf
© [L. Vergnaud], [2023], INSA Lyon, tous droits réservés

NLMM approach exhibited lower bias and fewer outliers compared to the mathematical models.

Furthermore, it is worth considering the inclusion of a physiologically-based pharmacokinetic (PBPK) model to incorporate the patient's physiology factors into the analysis (Hardiansyah et al., 2022). In order to assess the effectiveness of the two workflows, namely employing only the NLMM or integrating both NLMM and PBPK model, a comparison was conducted using a single acquisition at different time-points. The results demonstrated that the cumulative activity estimates for kidneys and tumours were similar between the two workflows. Moreover, the differences in dose estimations were not found to statistically significant. Notably, acquiring images at approximately 47h post-injection yielded the lowest error in both cases (Hardiansyah et al., 2022).

To minimize the overall number of acquisitions, Mix et al., 2022 introduced a method to estimate the cumulative dose in the kidneys based solely on the dose estimated in the first treatment cycle. This approach appears feasible; however, its applicability is limited to a maximum of four cycles. This method was also examined for other organs such as spleen, liver, bone marrow, and lesions, and was compared with another simplified approach that used data from cycles 1 and 4, as proposed by (Pirozzi Palmese et al., 2023). They demonstrated an overestimation of the cumulative dose when only cycle 1 was considered, with differences of less than $\pm 10\%$ when cycles 1 and 4 were included.

Cette thèse est accessible à l'adresse : https://theses.insa-lyon.fr/publication/2023ISAL0068/these.pdf
© [L. Vergnaud], [2023], INSA Lyon, tous droits réservés

Authors	N° patients	Volumes	Curve fit	Hypothesis	Methods
Hänscheid et al., 2017*	29	K, NET, L, S	Mono- or Bi-exp	Fixed tissue specific effective half-lives	Mono-exp with empirical effective half-lives K: 50h, L and S: 67h, NET: 77h If bi-exp, approximation mono-exp
Hänscheid et al., 2018*	29	K, NET, L, S	Mono- or Bi-exp	Theoretical approach of T_{eff}	Approximation of the integral (cumulative activity) from a time-point at 4d
Jackson et al., 2020a**	30	T, K, PG	Tri-exp	Homogeneity of pharmaco-kinetic parameters	Use of average pharmacokinetic parameters in a patient population (scaling)
Garske et al., 2012**	30	K, L, S	Mono-exp	Unchanged effective half-life	Reuse effective half-life from cycle 1 for other cycles
Hardiansyah et al., 2022*	8	T, K, L, S and WB	PBPK model + Non-linear mixed model (NLMM)	Prior knowledge about patients	PBPK model + NLMM + Acquisition at 47h
Devasia et al., 2020**	10 (250 virtual)	K	Non-linear mixed model	Prior knowledge about patients	Artificial reduction of the number of time-points (1 or 2) + use time-points of others patients
Madsen et al., 2019**	NA (^{90}Y)	K	Mono-exp or Bi-exp	Population averages of kinetic parameters	Use of population kinetic parameters as prior knowledge
Brosch-Lenz et al., 2023**	20	K and T	Mono-exp	Same effective half-life between cycles	Reuse effective half-life of cycle 1
Chicheportiche et al., 2021**	32	K, BM, L, S and T	Mono-exp	Mainly self-dose for all except BM	Trained multiple linear regression model + 1 SPECT 168h after cycle 1 and 24h after other cycles

TABLE 5.1 – Methodologies for estimating absorbed doses in kidneys (K), liver (L), spleen (S) , parotid glands (PG), red marrow (RM), tumours (T) and neuroendocrine tumours (NET) during ^{177}Lu therapies based on a single acquisition. The symbol * indicates studies conducted for ^{177}Lu-SSTR, while ** denoted studies conducted for ^{177}Lu-PSMA-RTL.

Cette thèse est accessible à l'adresse : https://theses.insa-lyon.fr/publication/2023ISAL0068/these.pdf
© [L. Vergnaud], [2023], INSA Lyon, tous droits réservés

Acquisition time-points Acquisition time-points play a crucial role in the accuracy of the dosimetric estimates. The limited number of available time-points necessitates careful selection. Sandström et al., 2020 evaluated dosimetric methods using one or two time-points in comparison to three time-points for kidneys, and they recommend a minimum of two time-points, ideally one early and one late. Peterson et al., 2023a also examined methods employing one, two, or three acquisitions and proposed optimal time choices for different volumes of interest (kidneys, liver, spleen and tumours) and for each method. They advise staying close to the optimal time-point to minimise errors, though the optimal times vary depending on the specific volumes considered (STP method of Hänscheid et al., 2018: kidneys: 63h, liver: 97h, spleen: 70h and, tumours: 133h). However, adhering to these recommendations for all volumes of interest can be challenging in practice. Sometimes, the selection of the optimum time-point must be made in consideration of clinical constraints. For instance, Hänscheid et al., 2018 developed an STP method based on a single acquisition at 96h, whereas in Germany, Hänscheid et al., 2017 specify a hospital stay of only 2 to 3 days post-injection for patients. As a results, they devised a new STP method based on a fixed effective half-life for each relevant organ, with an acquisition time of 2 or 3 days. In conclusion, a late acquisition time-point appears necessary to minimise dose estimation errors, especially for the kidneys in ^{177}Lu-DOTATATE (Larsson et al., 2012) and ^{177}Lu-PSMA-I&T (Rinscheid et al., 2020), or for the lacrimal glands in ^{177}Lu-DKFZ-PSMA-617 (Hohberg et al., 2016).

Limitations Several simplified methods have been developed and evaluated to facilitate access to dosimetry. However, it is important to note some limitations. Firstly, a large number of studies only focus on evaluating and/or comparing kidneys, while in practical settings, other OARs and tumours would also need to be considered. Secondly, not all studies follow the same reference protocols, such as using the same imaging type, the same number of time-points, or the same specific time-points. It means that the estimated optimal time-point may only be optimal compared to the available time-points. To address this, some authors have proposed comparative studies of simplified dosimetric methods using a standardised frame of reference. Additionally, not all methods are evaluated for all radiopharmaceuticals, and the results cannot be directly applied across different biodistributions. Thirdly, when estimating dosimetry, effective half-life times are often approximated theoretically, assumed to be invariant during treatment cycles for the same patient, or taken as the average from a population of patients. However, there is inter-patient variability, particularly in the kinetics of lesions (Peters et al., 2022), which can impact the results. If a patient's pharmacokinetics differ greatly from the cohort used, errors in dosimetry can be significant. Furthermore, this approach requires a cohort of patients who have undergone multiple post-treatment acquisitions, representing the diversity of patients treated. The reuse of an effective half-life time from a previous cycle may be affected by potential inter-cycle variations due to treatment efficacy or tumour progression. Unfortunately, this method has not been extensively compared in the literature. Fourthly, while acquiring a late-time measurement has often been recommended to minimise errors (Hou et al., 2021; Hänscheid et al., 2018), it may not always be practical in clinical setting, especially when patients are discharged from the hospital within 24 hours. Finally, each hospital establishes its own guidelines for the number of post-treatment acquisitions, which may not always be feasible due to patient health, technical limitations, or logistical reasons. These challenges led us, in Chapter 6, to propose a dosimetric workflow that adapts based on the available number of acquisitions.

Cette thèse est accessible à l'adresse : https://theses.insa-lyon.fr/publication/2023ISAL0068/these.pdf
© [L. Vergnaud], [2023], INSA Lyon, tous droits réservés

5.2.4 Voxel- or organ-based dosimetry

The dosimetry assessments of ^{177}Lu therapies presented in Tables 5.2, 5.3, 5.4, 5.5, 5.6, 5.7 and 5.8 have primarily been conducted at the organ level rather than the voxel level, although the latter approach is starting to emerge (Dewaraja et al., 2022; Violet et al., 2019; Akhavanallaf et al., 2021; Jackson et al., 2013; Sarrut et al., 2017b). In Section 5.3.1, we will explore how the uptake of ^{177}Lu radiopharmaceuticals in tissues, such as kidneys, exhibits heterogeneity. Voxel-level dosimetry accounts for these fluctuations, whereas they are averaged out at the organ level. However, voxel-based dosimetry is influenced by factors such as the accuracy of registration between CT scans acquired at different times, noise, and the limited spatial resolution of gamma cameras, which leads to the partial volume effect, as described by Carter et al., 2021. These challenges are considered and corrected in organ-level dosimetry. Furthermore, it is important to note that the range of beta particles' radiation is smaller than the dimensions of a voxel, which means that variations in deposited dose cannot be accurately captured (Chiesa et al., 2019). Finally, the relationship between absorbed doses and treatment responses has been demonstrated both at the voxel scale (Violet et al., 2019) and the organ scale (Alipour et al., 2023).

5.2.5 Importance of regions-of-interest delineation

Once the acquisitions and the scale for dosimetry have been determined, it is necessary to contour the OARs and the tumours. Typically, CT images are used for segmenting OARs as they provide anatomical information. To streamline the contouring process, the deep learning-based automatic organ segmentation extension ('TotalSegmentator') of the 3D Slicer software or other deep learning approaches, as employed by Dewaraja et al., 2022, can be used. However, contouring small volumes like the lacrimal and salivary glands can pose challenges, and an alternative approach using SPECT images may be considered, particularly for tumours. Details contouring methodologies for each VOI are provided in Sections 5.3.1, 5.3.2, 5.3.3, 5.3.4, and 5.4. It is important to consider the partial volume effects caused by the low spatial resolution of gamma cameras.These effects are not accounted for when using CT contours unless they are corrected in the SPECT images. However, for SPECT image-based tumour segmentation methods, as assessed by Gustafsson et al., 2017, the contours will depend on the applied corrections during reconstruction and the presence of noise, especially when thresholding based on a maximum value. For instance, the application of resolution compensation underestimates tumour volumes in methods such as Otsu and Fourier surface. In Chapter 8, a comparison of various dosimetric methods in the context of estimating activity concentration recovery coefficients is presented, along with their impact on the results.

5.2.6 Influence of the Time Activity Curve fitting method

The curve fitting step is crucial for modelling the biokinetics of ^{177}Lu radiopharmaceuticals, which involves a binding phase followed by an elimination phase, further divided into biological elimination (urine) and radioactive elimination (Jackson et al., 2013). The choice of the modelling approach depending on the number of available time-points and clinical constraints. Guerriero et al., 2013 highlighted the impact of curve fitting on kidney dose estimation when time-points are lacking up to twice the effective half-life time. Typically, simple mathematical models such as trapezoidal, linear, mono-exponential, bi-exponential, or tri-exponential models

Cette thèse est accessible à l'adresse : https://theses.insa-lyon.fr/publication/2023ISAL0068/these.pdf
© [L. Vergnaud], [2023], INSA Lyon, tous droits réservés

(Jackson et al., 2020b) are employed, particularly when the number of time-points is limited (refer to Table 5.1). The selection of the appropriate model depends on the specific tissue under consideration and can even be adapted for the voxel-level analysis. The study of Sarrut et al., 2017b used the Akaike criterion to determine the best-fit model, which was further incorporated into the dosimetric workflow proposed by Dewaraja et al., 2022. Once of the dosimetric method described in Chapter 4 is selected, it is applied accordingly.

5.2.7 Uncertainties of dosimetric workflow

The literature encompasses numerous dosimetric workflows with varying levels of uncertainties. At each stage, uncertainties are introduced, such as calibration, segmentation, and curve fitting. While the EANM practical guidance (Gear et al., 2018) offers a framework for evaluating the overall uncertainty of dosimetric workflows, it is seldom reported in the literature. Gustafsson et al., 2023 emphasise the importance of providing comprehensive details about methodological choices, especially when calculating averages for voxels or distinct regions, to mitigate comparison errors.

5.3 Organs at risk

5.3.1 Kidneys

The kidneys filter the blood containing the administered radiopharmaceuticals and are considered OARs in both ^{177}Lu therapies. The risk of reabsorption exists for ^{177}Lu-SSTR, while the presence of PSMA receptors in the kidneys is a consideration for ^{177}Lu-PSMA. Following injection, the distribution of the radiopharmaceutical in kidneys is heterogeneous, as demonstrated by Konijnenberg et al., 2007 through ex-vivo autoradiography of healthy kidney tissue. The absorbed dose is typically assessed and compared to the maximum tolerated dose used in EBRT, which is 23 Gy (Section 5.5), to minimise the risk of renal toxicity. Various contouring methods have been proposed, including manual segmentation of the entire kidney (M1) (Sandström et al., 2010; Heikkonen et al., 2016) and placement of small spheres of 2cm^3 (Del Prete et al., 2019) or 4cm^3 (Sandström et al., 2010; Heikkonen et al., 2016) in the region of maximum activity (M2). The M1 method considers anatomical information but averages the heterogeneous distribution of activity, whereas the M2 method relies on the region of maximum activity. There is a risk of overestimating the dose absorbed by the kidneys with the M2 method. Heikkonen et al., 2016 compared the absorbed doses using the M1 and M2 methods for the kidneys and estimated doses for the cortex and medulla. They observed a factor of 1.7 between M1 and M2 and observed differences between kidney regions: 0.41 ± 0.22 Gy/GBq for the cortex and 0.62 ± 0.27 Gy/GBq for the medulla. Renal dosimetry is essential as the kidneys are often the dose-limiting organs (197 out of 200 patients) according to Sandström et al., 2010 and are commonly used to personalise the injected activities. Renal toxicity remains very low (Table 2.1), and Heikkonen et al., 2016 reported no renal toxicity observed within two years of treatment initiation. Several studies have investigated dose-toxicity correlations for the kidneys, as described by Cremonesi et al., 2018.

Cette thèse est accessible à l'adresse : https://theses.insa-lyon.fr/publication/2023ISAL0068/these.pdf
© [L. Vergnaud], [2023], INSA Lyon, tous droits réservés

5.3.2 Bone marrow

Bone marrow, located within the bones, is an organ comprised of two main types: red marrow and yellow marrow (Figure 5.1). Red marrow, also known as active bone marrow, is responsible for the production of blood cells, including red blood cells, white blood cells, and platelets. On the other hand, yellow marrow generates the body's connective tissues (*The Anatomy of Bone Marrow* 2023). The distribution and proportion of each type of bone marrow vary based on the patient's age and sex (Dooms et al., 1985). Hindorf et al., 2010 provide the distribution of active marrow proportions in different regions of the skeleton in healthy adults. For instance, while the arms and legs have minimal active marrow, the vertebrae, coccyx, and ribs have higher proportions. In the subsequent discussion, the term "bone marrow" will specifically refer to the active bone marrow (BM).

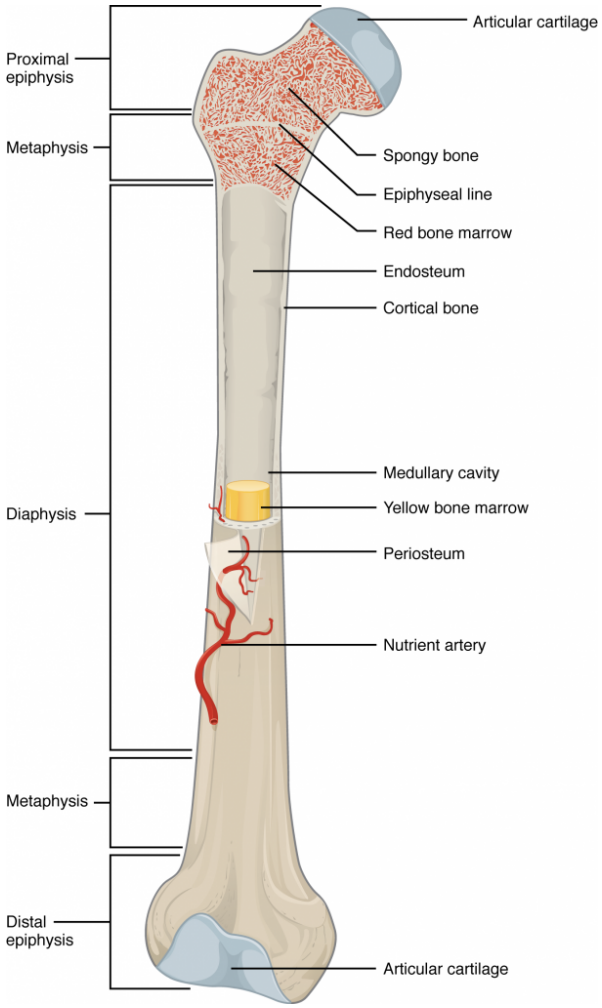

FIGURE 5.1 – Anatomy of a Long Bone depicting the location of active red bone marrow, yellow bone marrow, and spongy bone. This diagram is sourced from the *The Anatomy of Bone Marrow* 2023 website.

The BM receives absorbed dose from the activity present within the BM itself (self-dose), as well as in the blood and the rest of the body (cross-dose). Estimating the dose accurately is challenging due to the patient-specific distribution of BM, leading to the implementation of various methods. Firstly, biopsy is used to determine the activity present in the BM, enabling the calculation of self-dose alone.

Cette thèse est accessible à l'adresse : https://theses.insa-lyon.fr/publication/2023ISAL0068/these.pdf
© [L. Vergnaud], [2023], INSA Lyon, tous droits réservés

However, this approach is invasive for the patient (Sgouros, 1993). Secondly, assuming no binding of the radiopharmaceutical in these regions, the concentration of activity in the blood is considered to be the same as in the BM. Cumulative activity is estimated based on the activity concentration, BM mass, and the red marrow-to-blood ratio (RMBLR), which has been compared by Ferrer et al., 2010 (RMBLR = 0.36 vs patient-dependent). Additionally, cumulative activity in the rest of the body is estimated to account for the cross-dose. Thirdly, dose estimation can be derived from imaging. A specific region of the BM is selected as a surrogate for the entire BM, typically in proximity to organs with high uptake where the dose is likely to be highest. Vertebrae are often chosen for this purpose (Hagmarker et al., 2019). This method calculates the total absorbed dose, encompassing both self-dose and cross-dose, which is not negligible for this organ (Forrer et al., 2009a)). However, since BM is contained within the spongy bone (Figure 5.1), dose estimations from a surrogate not only correspond to the absorbed dose by active bone marrow but also that absorbed by the spongy bone. Precise localization of BM and the implementation of voxel-scale dosimetry could enhance the accuracy of these results. Importantly, this approach relies solely on imaging, without the need for blood or BM samples, which are already required for dosimetric estimates of the other OARs. Moreover, Hemmingsson et al., 2023 demonstrated that blood-based dosimetry methods may underestimate the absorbed dose by not considering the prolonged elimination of specific uptake.

Similar to the kidneys, the objective of BM dosimetry is to compare it with haematological toxicity. In the case of radioimmunotherapy, Ferrer et al., 2010 demonstrated that image-based dosimetric methods were better predictors of toxicity compared to blood-based methods. For ^{177}Lu-DOTATATE therapy, Hagmarker et al., 2019 established correlations between doses estimated from vertebrae and platelets. However, the presence of bone metastases can compromise the use of imaging-based dosimetry. This is because the metastases can replace the BM in the vertebrae of interest, rendering them unsuitable as substitutes. Moreover, if the metastases are in the close proximity to the BM and exhibit high uptake, they can cause significant irradiation of the BM (Kind et al., 2022). Additionally, preceding treatments prior to RPT with ^{177}Lu may have already damage a portion of the patient's BM. Therefore, it is crucial to estimate the remaining localisation of the patient's BM to accurately assess the dose received by this organ. Consequently, several authors have explored methods to determine the location of active bone marrow such as using, [^{18}F]FLT (McGuire et al., 2011) or even ^{99m}Tc-anti-granulocyte antibody (Gosewisch et al., 2019).

5.3.3 Salivary glands

The salivary glands (Figure 5.2) are OARs during ^{177}Lu-PSMA therapies due to the presence of PSMA receptors on which the radiopharmaceutical binds. Various strategies have been investigated to reduce the absorbed dose in these glands. For instance, co-administration of polyglutamate tablets (Paganelli et al., 2020) or external cooling (Junqueira et al., 2021) have been tested. Reviews summarizing the mechanisms underlying salivary gland toxicity and protective strategies have been compiled by Heynickx et al., 2021 and Mahajan et al., 2022. A recent study by Siebinga et al., 2023 demonstrated that the salivary glands could reach saturation as the injected activity increased, unlike tumours. This finding could have implications for treatment personalisation. Segmentation of the salivary gland volumes is typically perfored through direct contouring on the CT images or by incorporating a margin

Cette thèse est accessible à l'adresse : https://theses.insa-lyon.fr/publication/2023ISAL0068/these.pdf
© [L. Vergnaud], [2023], INSA Lyon, tous droits réservés

of 1 or 2 cm to account for the partial volume effect, as proposed by Violet et al., 2019.

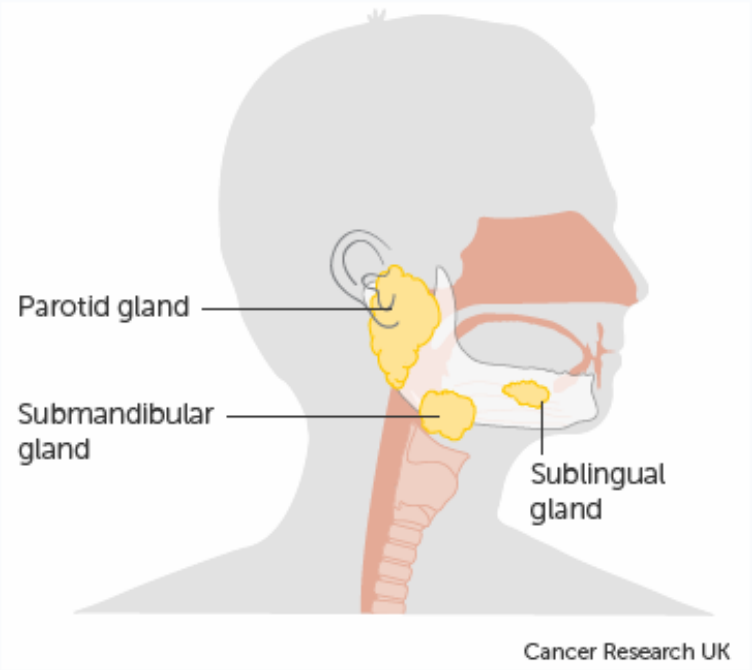

FIGURE 5.2 – Diagram of the salivary glands extracted from the Cancer Research UK website (*Salivary glands* 2023).

5.3.4 Lacrimal glands

The lacrimal glands (Figure 5.3) are relatively small organs that are considered dose-limiting (Hohberg et al., 2016), which can pose challenges in their segmentation. Contouring methods for the lacrimal glands are similar to those used for the salivary glands.

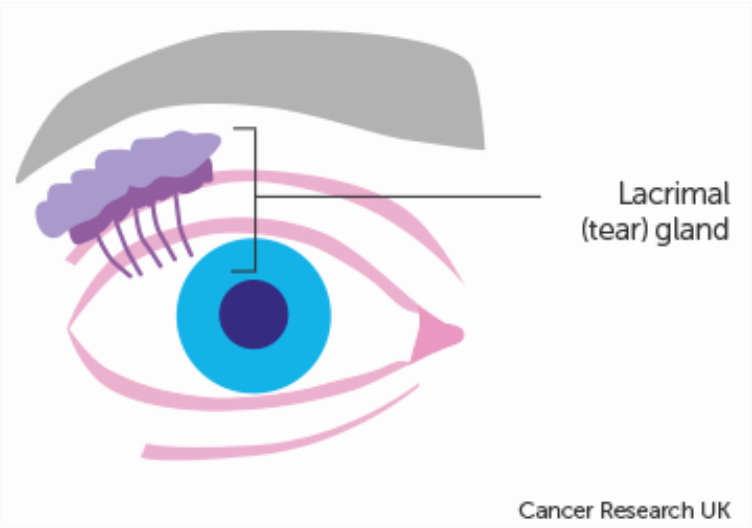

FIGURE 5.3 – Diagram of the lacrimal glands extracted from the Cancer Research UK website (*Lacrimal glands* 2023).

Cette thèse est accessible à l'adresse : https://theses.insa-lyon.fr/publication/2023ISAL0068/these.pdf
© [L. Vergnaud], [2023], INSA Lyon, tous droits réservés

5.4 Tumour

5.4.1 Dosimetry

Tumour dosimetry is conducted to establish a relationship between the absorbed dose and the response of the tumour (Alipour et al., 2023). This allows for the determination of response thresholds in patients, similar to radioembolisation. The precision of tumour dosimetry is essential, considering the heterogeneity of receptors on the surface of tumour cells, which can influence the relationship between absorbed dose and number of double strand breaks per cell (response) (Tamborino et al., 2022). A review of technical and biological factors affecting the relationship dose-response in RPT, along with unresolved questions, was provided by Sgouros et al., 2021. In the literature, two strategies are commonly employed: individual lesion dosimetry (Delker et al., 2016; Okamoto et al., 2017; Feuerecker et al., 2022) or total tumour volume dosimetry (Violet et al., 2019). In the case of individual lesion dosimetry, only visible and contoured tumours, which may not represent the full extent of the patient's disease, are considered. This approach cannot be combined with biological indicators of disease progression, such as PSA levels, as they depend on the entire tumour burden. On the other hand, the second method allows for such integration, but it is more challenging to implement, often involving thresholding of functional images. Regardless of the chosen strategy, Völter et al., 2021 showed that estimated doses had a similar correlation with patient response in the context of ^{177}Lu-PSMA therapies. In Section Roth et al., 2022, STP methods were presented to reduce imaging burden in clinical practice. However, when considering individual lesions, it is important to account for the decrease in absorbed dose over treatment cycles, especially for grade 2 NETs, in ^{177}Lu-DOTATATE therapies.

5.4.2 Tumour sink effect

The tumour sink effect refers to increased uptake of the radiopharmaceutical by tumours, with a corresponding decrease in uptake in healthy tissue. A retrospective study including 33 patients demonstrated this effect in the salivary glands, spleen and, potentially the liver (Burgard et al., 2023). Similarly, Filss et al., 2018 observed lower absorbed doses in the salivary glands and kidneys when there was a higher tumour burden. Understanding this effect is essential for personalising treatments, especially in cases of extensive disease (Jackson et al., 2022), as it would allow preserving healthy tissues while increasing the doses to tumours. Hence, Tuncel et al., 2021 tried to identify factors predictive of tumour sink effect and identified three factors: total lesion index uptake on the ^{68}Ga-PSMA PET scan, pre-treatment PSA level, and the rate of change of PSA. They also found that this effect was present in only around a quarter of their patients (17/65).

5.5 Maximum Tolerated Dose (MTD)

Generally, the maximum tolerated dose (MTD) thresholds used in external radiotherapy (Milano et al., 2007) are typically applied to targeted radionuclide therapy. However, the type of irradiation differs between the two therapies, as discussed in Chapter 1. In fact, the dose-rates are lower with heterogeneous and continuous irradiation, and LET are also different (around 4 keV/µm for EBRT vs 0.2 keV/µm for Beta emitters). For instance, in EBRT, the dose limit for the kidney is set at 23 Gy, and for the BM, it is 2 Gy. The validity of these thresholds has been questioned by

Cette thèse est accessible à l'adresse : https://theses.insa-lyon.fr/publication/2023ISAL0068/these.pdf
© [L. Vergnaud], [2023], INSA Lyon, tous droits réservés

Bergsma et al., 2016a and Bergsma et al., 2016b in the context of PRRT with ^{177}Lu-DOTATATE. Furthermore, treatment fractionation could allow these thresholds to be exceeded (Eberlein et al., 2017) by increasing the dose from 23 Gy to 35 Gy for 4 cycles.

5.6 Dose estimation from the PET image

Some authors have explored the possibility of predicting absorbed doses based on the ^{68}Ga PET image, which is commonly used to include patients and identify the lesions to be treated. One method, proposed by Peters et al., 2022, involved establishing the absorbed dose ratio between PET and SPECT. They found ratios close to 1 for the liver, parotid glands and, submandibular glands. However, for the kidneys, this factor had to be adjusted to equal 1, and there was a large variability observed for the tumours. As explained in Section 2.7, Peterson et al., 2023b and Akhavanallaf et al., 2023 have attempted to predict absorbed doses for kidneys and tumours using regression and machine learning models, respectively. Machine learning techniques were also used to predict doses to OARs using either imaging and biological data (Xue et al., 2022) or radiomics and dosimic features extracted from images (study in progress in the Patras team, Greece).

5.7 Conclusion

In this chapter, a literature review of available dosimetric workflows has been proposed, along with a detailed description of STP methods. Currently, practices for dosimetry vary among different centers where it is performed. Initiatives have been implemented to standardise them (Tran-Gia et al., 2021). In addition, recommendations have been issued to improve dosimetry in multicenter studies (Taprogge et al., 2021), and acquisitions of anthropomorphic ^{177}Lu phantoms have been made available to enable the comparison of dosimetric workflows and associated uncertainties (Robinson et al., 2023).

Cette thèse est accessible à l'adresse : https://theses.insa-lyon.fr/publication/2023ISAL0068/these.pdf
© [L. Vergnaud], [2023], INSA Lyon, tous droits réservés

Authors	N° Patients	Imaging	Time-points	Curve fitting	Dosimetry	VOI	Dose per IA (Gy/GBq)
Pirozzi Palmese et al., 2023	30	SPECT/CT Discovery NM/CT 670 (GE)	3h, 20h and 90/120h	Mono-exp or trapezoidal (OAR and T) Bi-exp (RM)	MIRD formalism OLINDA/ EXM®v1.0	Kidney Spleen Liver Red Marrow Tumours	0.54 ± 0.15 0.64 ± 0.32 0.67 ± 0.81 0.016 ± 0.006 4.5 ± 2.9
Sundlöv et al., 2017	51	Hybrid NA	WB: 1h, 24h, 48h or 96h and 168h + 1 SPECT 24h	Trapezoidal 1h to 24h + Mono-exp from 24h	LundADose software	Kidneys	0.61 (Median)
Del Prete et al., 2019	52	SPECT/CT Symbia T6	4h, 24h and 72h	Constant (0-4h) Linear (4-24h) Mono-exp	OLINDA/ EXM 1.0	Kidney Bone marrow Tumour	0.56 0.031 4.8
Del Prete et al., 2017	36	SPECT/CT Symbia T6 (Siemens)	4h, 24h and 72h	Trapezoidal (0-24h) + Mono-exp	OLINDA software	Kidney Bone marrow Tumour	0.55 ± 0.19 0.045 ± 0.025 4.0 ± 2.2
Heikkonen et al., 2016	24	SPECT/CT Symbia T2	24h, 72h and 168h	Mono-exp	OLINDA software	Whole kidney Small volume	0.44 ± 0.15 0.74 ± 0.28
Sandström et al., 2010	24	***SPECT Large VOI*** Hawkeye Millennium (GE) ***SPECT Small VOI***	1h, 24h, 96h and 168h	Mono-exp	OLINDA software	R Kidney L Kidney Liver Spleen R Kidney L Kidney Liver Spleen	5.5 ± 2.1 5.0 ± 1.6 4.5 ± 3.6 5.8 ± 2.9 5.3 ± 2.3 4.4 ± 1.3 3.1 ± 1.8 5.7 ± 2.7
		Planar	1h, 24h, 96h and 168h			R Kidney L Kidney Liver Spleen	6.7 ± 3.5 7.8 ± 6.8 4.4 ± 3.2 5.7 ± 3.2
Guerriero et al., 2013	28	SPECT/CT Symbia T2 (Siemens	2h, 6h, 20h, 44h and 67h	Best fit visually selected	OLINDA/ EXM	Kidneys	1.0 ± 0.2

TABLE 5.2 – Dosimetric workflows available in the literature for ^{177}Lu-DOTATATE therapies. For Heikkonen et al., 2016, two methods of calculating the dose to the kidneys are available: whole kidney contouring (whole kidney) and a 4cm^3 sphere in the kidney (small volume). For Sandström et al., 2010, doses in Gy are given.

Cette thèse est accessible à l'adresse : https://theses.insa-lyon.fr/publication/2023ISAL0068/these.pdf
© [L. Vergnaud], [2023], INSA Lyon, tous droits réservés

Authors	N° Patients	Imaging	Time-points	Curve fitting	Dosimetry	VOI	Dose per IA (Gy/GBq)
Wehrmann et al., 2007	69	Planar SPIRIT DH-V (Mediso)	3h, 20h, 44h and 68h	Mono-exp or Bi-exp	OLINDA/ EXM	Whole-body	0.05 ± 0.02
						Kindeys	0.9 ± 0.3
						Spleen	1.2 ± 0.5
						Metastases	9.7 ± 12.4
						Liver metastases	12.4 ± 15.1
						Lymph node metastases	8.0 ± 8.4
						Bone metastases	5.4 ± 4.4
						Pancreas metastases	3.0 ± 2.9
						Soft tissue metastases	5.8 ± 4.0
Sandström et al., 2013	200	Planar and SPECT	24h, 96h and 168h	Mono-exp or Bi-exp	OLINDA/ EXM	Right kidney	4.69
						Left kidney	4.39
						Liver	2.80
						Spleen	5.35
Garkavij et al., 2010	21	***SPECT/CT*** Discovery VH ***Planar***	24h and/or 96h 0.5h, 24h, 96h and 168h Cycles 1-2 24h and 96h other	Trapezoidal + Mono-exp	Local deposition MIRD formalism + mass-scaled	Kidneys (M1A)	0.97 ± 0.24
						Kidneys (M1B)	1.15 ± 0.29
						Kidneys (M2)	0.81 ± 0.21
						Kidneys (M3)	0.90 ± 0.21
Santoro et al., 2018	12	SPECT/CT Discovery 670 NM/CT GE	4h, 24h, 72h and/ or 192h	Mono-exp	OLINDA/ EXM v1.0	Liver	0.54 ± 0.58
						Kidneys	0.43 ± 0.13
						Spleen	0.61 ± 0.13
						Red marrow	0.04 ± 0.02
Marin et al., 2018	47	SPECT/CT Symbia TruePoint (Siemens)	4h, 24h and 168h	Bi-exp	OLINDA/ EXM v1.0	Kidneys	0.78 ± 0.35
						Spleen	1.07 ± 0.58
						Red marrow	0.028 ± 0.010
Santoro et al., 2021	21	SPECT/CT Discovery 670 NM/CT	4h, 24h, 72h and 192h	Mono-exp	PLANET Dose	Liver	0.45 ± 0.50
						Kidneys	0.45 ± 0.13
						Spleen	0.62 ± 0.17

TABLE 5.3 – Dosimetric workflows available in the literature for ^{177}Lu-DOTATATE therapies. For Sandström et al., 2013, doses in Gy are given.

Cette thèse est accessible à l'adresse : https://theses.insa-lyon.fr/publication/2023ISAL0068/these.pdf
© [L. Vergnaud], [2023], INSA Lyon, tous droits réservés

Authors	N° Patients	Imaging	Time-points	Curve fitting	Dosimetry	VOI	Dose per IA (Gy/GBq)
Delker et al., 2016*	5	Hybrid Symbia T2 (Siemens)	1h, 24h, 48h and 72h	Linear and mono-exp for K, L, S and selected T	S-value + organ mass SG from planar images	Kidneys	0.6 ± 0.18
						Salivary glands	1.4 ± 0.53
						Liver	0.11 ± 0.06
						Spleen	0.10 ± 0.03
						Bone marrow	0.012 ± 0.005
						Bone lesions	5.3 ± 3.7
						Lymph metastases	4.2 ± 5.3
						ST metastases	2.1 ± 0.8
Fendler et al., 2017**	15	Hybrid SPECT patients' head	1h, 24h, 48h and 72h	Linear and mono-exp for K, L, S and selected T	S-value + organ mass	Salivary glands	1.0 ± 0.6
						Right kidney	0.6 ± 0.2
						Left kidney	0.5 ± 0.3
						Tumour	6.1 ± 4.9
						Liver	0.1 ± 0.1
						Spleen	0.1 ± 0.1
						Bone marrow	0.002 ± 0.005
Yadav et al., 2017*	26	Planar Symbia (Siemens)	0.5h, 3.5h, 24h, 48h, 72h, 96h, 120h, 144h and 168h	Mono-exp or Bi-exp	OLINDA/EXM 1.0	Liver	0.36 ± 0.11
						Kidneys	0.99 ± 0.31
						Salivary glands	1.24 ± 0.27
						Red marrow	0.048 ± 0.059
						Bladder + contents	0.23 ± 0.092
						Tumours	10.94 ± 18.01
						Whole-body	0.016 ± 0.003
Violet et al., 2019**	30	2-3 SPECT/CT Symbia T6 or Intevo 16 (Siemens)	4h, 24h and 96h	Tri-exp	OLINDA	Parotid glands	0.58 ± 0.43
						Submandibular glands	0.44 ± 0.36
						Lacrimal glands	0.36 ± 0.18
						Kidneys	0.39 ± 0.15
						Spleen	0.08 ± 0.06
						Liver	0.10 ± 0.05
						Bone marrow	0.11 ± 0.10
						Bone metastases	5.28 ± 2.46
						Node	3.91 ± 3.93
Kabasakal et al., 2015**	7	Planar Symbia T16 (Siemens)	4h, 24h, 48h and 120h	Bi-exp	OLINDA 1.1	Parotid glands	1.17 ± 0.31
						Kidneys	0.88 ± 0.40
						Bone marrow	0.034 ± 0.014
						Liver	0.28 ± 0.09
						Whole-body	0.061 ± 0.026

TABLE 5.4 – Dosimetric workflows available in the literature for ^{177}Lu-PSMA therapies (*^{177}Lu-DKFZ-PSMA-617; **^{177}Lu-PSMA-617; ***^{177}Lu-PSMA-I&T). ST: Soft Tissue

Cette thèse est accessible à l'adresse : https://theses.insa-lyon.fr/publication/2023ISAL0068/these.pdf
© [L. Vergnaud], [2023], INSA Lyon, tous droits réservés

Authors	N° Patients	Imaging	Time-points	Curve fitting	Dosimetry	VOI	Dose per IA (Gy/GBq)
Okamoto et al., 2017***	18	Planar Symbia T6 (Siemens)	30-120 min, 24h and 6-8d	Mono-exp or Bi-exp	OLINDA/ EXM	Kidneys	0.72 ± 0.21
						Liver	0.12 ± 0.06
						Parotid glands	0.55 ± 0.14
						Lacrimal glands	3.8 ± 1.4
						Submandibular glands	0.64 ± 0.40
						Tumours	3.2 ± 2.6
						Lymph node metastases	3.2 ± 2.2
						Bone metastases	3.4 ± 2.7
						Liver metastases	1.2 ± 0.67
						Lung metastases	1.75 ± 0.92
Feuerecker et al., 2022***	6	Planar Symbia T6 (Siemens)	1h, 4h, 24h, 48h and 7d	Mono-exp or Bi-exp	OLINDA/ EXM	Bone marrow (L2-L4)	0.22 ± 0.21
						Bone marrow (thigh)	0.30 ± 0.27
						Kidneys	0.73 ± 0.18
						Liver	0.07 ± 0.03
						Parotid glands	0.80 ± 0.41
						Lacrimal glands	1.92 ± 0.80
						Submandibular glands	0.67 ± 0.31
						Tumour	2.64 ± 2.24
						Bone metastases	1.70 ± 1.13
						Lymph node metastases	4.51 ± 2.69
Scarpa et al., 2017**	10	Hybrid Symbia (Siemens)	0.5h, 4h, 24h, 72h and 96h +24h (SPECT)	Mean of two or three exp decay functions	OLINDA/ EXM	Red marrow	0.042 ± 0.028
						Lacrimal glands	1.0 ± 0.69
						Parotid glands	0.56 ± 0.25
						Submandibular glands	0.50 ± 0.15
						Kidneys	0.60 ± 0.36
						Spleen	0.12 ± 0.09
						Liver	0.12 ± 0.06
						Skeletal metastases	3.4 ± 1.9
						Lymph node metastases	2.6 ± 0.4
						Visceral metastases	2.4 ± 0.78
Peters et al., 2022**	10	SPECT/CT Symbia T16 (Siemens)	1h, 24h, 48h, 72h and 168h	Trapezoidal + Mono-exp or Bi-exp or Tri-exp + extrapolation	Hermes HybridViever	Salivary glands	0.39 ± 0.17
						Kidneys	0.49 ± 0.11
						Lesions	3.25 ± 3.19
						Liver	0.09 ± 0.01
						Bone marrow	0.017 ± 0.008

TABLE 5.5 – Dosimetric workflows available in the literature for ^{177}Lu-PSMA therapies (*^{177}Lu-DKFZ-PSMA-617; **^{177}Lu-PSMA-617; ***^{177}Lu-PSMA-I&T).

Cette thèse est accessible à l'adresse : https://theses.insa-lyon.fr/publication/2023ISAL0068/these.pdf
© [L. Vergnaud], [2023], INSA Lyon, tous droits réservés

Authors	N° Patients	Imaging	Time-points	Curve fitting	Dosimetry	VOI	Dose per IA (Gy/GBq)
Zhang et al., 2019**	16	Hybrid SPIRIT DH-V (Mediso)	5 WB between 0.5h-118h + 1 SPECT between 45h-118h	Bi-exp	OLINDA / EXM	Kidneys	0.81 ± 0.32
						Whole-body	0.058 ± 0.027
						Tumour	13.75 ± 31.59
Kabasakal et al., 2017**	6	Hybrid Symbia T16 (Siemens)	WB: 4h, 24h, 48h and 120h + 1 SPECT 24h	NA for OAR Bi-exp for blood	OLINDA 1.1	Parotid glands	1.90 ± 1.19
						Kidneys	0.82 ± 0.25
						Bone marrow	0.030 ± 0.008
						Liver	0.17 ± 0.09
Sarnelli et al., 2019**	9	Planar Discovery NM/CT 670 (GE)	1h, 16-24h, 36-48h and 120h	Mono-exp or Bi-exp	OLINDA / EXM 1.1	Parotid glands	0.81 ± 0.74
						Kidneys	0.67 ± 0.27
						Red marrow	0.044 ± 0.017
						Whole-body	0.049 ± 0.031
						Liver	0.16 ± 0.15
Rosar et al., 2021**	24	SPECT/CT Philips BrightView XCT (Philips)	24h, 48h and ≥ 96h	Constant + Trapezoidal + Trapezoidal + Mono-exp	IDAC 2.1 software	Kidneys	0.54 ± 0.28
						Liver	0.10 ± 0.05
						Parotid glands	0.81 ± 0.34
						Submandibular glands	0.72 ± 0.39
						Bone metastases	1.68 ± 1.32
Paganelli et al., 2020**	13	Hybrid Discovery NM/CT 670 (GE)	WB: 0.5-1h, 16-24h, 36-48h and 120h + 1 SPECT/CT 16-24h	Mono-exp (L), Bi-exp (PG, K, RM, WB, T) and Tri-exp (T)	OLINDA / EXM 1.0	Parotid glands	1.04 ± 0.82
						Kidneys	0.41 ± 0.19
						Liver	0.18 ± 0.14
						Submandibular glands	0.67 ± 0.36
						Lacrimal glands	2.06 ± 1.24
						Red marrow	0.042 ± 0.017
						Whole-body	0.053 ± 0.037
						Bone lesions	4.70 (mean only)
						Lymph node lesions	3.64 (mean only)
Kratochwil et al., 2016b**	4	Hybrid GE Hawkeye Millennium	WB: 0.5h, 3h, 20h, 44h and 5-8d SPECT: 20h	Three phases: linear + mono- or bi-exp + mono- or Bi-exp	OLINDA / EXM	Kidneys	0.75 ± 0.19
						Red marrow	0.03 ± 0.01
						Parotid glands	1.28 ± 0.40
						Submandibular glands	1.48 ± 0.37
						Metastases	6-22
Baum et al., 2016†	30	Hybrid SPIRIT DH-V (Mediso)	5 WB between 0.5h-118h + 1 SPECT between 45h-118h	Mono-exp or Bi-exp	OLINDA / EXM	Whole-body	0.02 ± 0.01
						Kidneys	0.8 ± 0.4
						Parotid glands	1.3 ± 2.3
						Tumours	3.3 ± 14
						Bone metastases	3.0 ± 10
						Lymph node metastases	4.0 ± 20

TABLE 5.6 – Dosimetric workflows available in the literature for ^{177}Lu-PSMA therapies (*^{177}Lu-DKFZ-PSMA-617; **^{177}Lu-PSMA-617; ***^{177}Lu-PSMA-I&T). For Kratochwil et al., 2016b, a trapezoidal model was used to fit the salivary glands and tumours. † median±std

Cette thèse est accessible à l'adresse : https://theses.insa-lyon.fr/publication/2023ISAL0068/these.pdf
© [L. Vergnaud], [2023], INSA Lyon, tous droits réservés

Authors	N° Patients	Imaging	Time-points	Curve fitting	Dosimetry	VOI	Dose per IA (Gy/GBq)
Hohberg et al., 2016*	9	Planar ECAM (Siemens)	0.5h, 24h, 48h, 72h and 168h	Bi-exp	OLINDA/ EXM 1.1	Lacrimal glands	2.82 ± 0.76
						Salivary glands	0.72 ± 0.14
						Kidneys	0.53 ± 0.17
						Nasal mucous membrane	0.42 ± 0.12
						Whole-body	0.063 ± 0.023
Mix et al., 2022**	59	SPECT/CT BrightView XCT	1h, 24h, 48h, 72h and 6-9d	Trapezoidal + exponential tail	STRATOS	Kidneys	0.67 ± 0.24
Privé et al., 2021**	10	SPECT/CT Symbia T16 or Intevo Bold	1h, 24h, 48h, 72h and 168h	NA	MIRD	Salivary glands	0.39 ± 0.17
						Kidneys	0.49 ± 0.11
						Liver	0.09 ± 0.01
						Bone marrow	0.02 ± 0.00
						Tumour (Cycle 1)	2.51 ± 2.43
						Tumour (Cycle 2)	1.78 ± 1.24
Völter et al., 2021**	30	SPECT (CT 24h) Symbia T2 (Siemens)	24h, 48h, and 72h	Mono-exp	Mass-scaled sphere S-value	Tumour	5.7 ± 6.4
						Lymph node metastases	7.7 ± 9.7
						Bone metastases	4.7 ± 3.9
Barna et al., 2020***	22	Planar GE Discovery VH GE Millennium VG Siemens E.CAM	0.5h, 4h, 18h, 24h, 48h, 72h and/or 96h	Linear + Mono-exp (PG) or Bi-exp (Other)	IDAC-Dose 2.1	Kidneys	0.71
						Liver	0.27
						Red marrow	0.040
						Tumours (bone)	4.4
						Tumour (Lymph node)	5.5
						Tumour (Liver)	4.9
						Parotid glands	0.77
Maffey-Steffan et al., 2020**	32	Planar Symbia (Siemens)	0.5h, 4h, 24h, 72h and 96h	Tri-exp decay or Bi-exp for WB-remainder	OLINDA/ EXM	Bone metastases	4.3 ± 3.0
						Lymph node metastases	3.3 ± 2.2
						Visceral lesions	3.0 ± 1.4
						Red marrow	0.039 ± 0.028
						Lacrimal glands	0.85 ± 0.51
						Parotid glands	0.53 ± 0.22
						Submandibular glands	0.46 ± 0.17
						Kidneys	0.77 ± 0.56
						Liver	0.13 ± 0.08

TABLE 5.7 – Dosimetric workflows available in the literature for ^{177}Lu-PSMA therapies (*^{177}Lu-DKFZ-PSMA-617; **^{177}Lu-PSMA-617; ***^{177}Lu-PSMA-I&T).

Cette thèse est accessible à l'adresse : https://theses.insa-lyon.fr/publication/2023ISAL0068/these.pdf
© [L. Vergnaud], [2023], INSA Lyon, tous droits réservés

Authors	N° Patients	Imaging	Time-points	Curve fitting	Dosimetry	VOI	Dose per IA (Gy/GBq)
Schuchardt et al., 2022	138	Planar SPIRIT DH-V (Mediso) Symbia T (Siemens)	5 WB between 0.5h to 68h 1 SPECT at 24h, 48h or 72h	Mono-exp or Bi-exp	OLINDA 2.0	Kidneys	0.77** / 0.92***
						Whole-body	0.04/0.03
						Parotid glands	0.5/0.5
						Lacrimal glands	5.1/3.7
						Tumour	5.9/5.8
						Bone metastases	6.0/5.9
						Lymph node metastases	7.1/6.9
Özkan et al., 2020***	10	Planar JETStream (Philips) or Intevo 6 (Siemens)	4h, 24h, 48h, 72h, 120h and 168h	Exponential curves	OLINDA / EXM 1.1	Kidneys	0.70 ± 0.24
						Parotid glands	1.34 ± 0.78
						Submandibular glands	0.94 ± 0.45
						Lacrimal glands	2.28 ± 1.29
Kamaldeep et al., 2021**	30	Planar Symbia E (Siemens)	0.5h, 2h, 12h, 24h, 72/96h	Bi-exp	OLINDA 2.0	Kidneys	0.49 ± 0.17
						Liver	0.07 ± 0.04
						Salivary glands	0.53 ± 0.25
						Lacrimal glands	1.23 ± 0.70
						Bone marrow	0.03 ± 0.02
						Spleen	0.16 ± 0.08
						Bone lesions	6.03 ± 8.34
						Lymph nodes	15.71 ± 14.72
						Primary site	3.29 ± 2.76
						Liver lesions	9.92 ± 3.02
						Lung lesions	5.30 ± 8.22
						Soft tissue deposit	4.68 ± 4.81
Xue et al., 2022***	23	Hybrid	WB: 30-150 min 24h and 6-8d	NA	OLINDA / EXM	WB	0.031 ± 0.017
						Kidneys	0.648 ± 0.165
						Liver	0.067 ± 0.035
						Salivary glands	0.565 ± 0.389
						Spleen	0.306 ± 0.227
Chatachot et al., 2021***	8	Planar Discovery NM/CT 670 (GE)	4h and 24h	Mono-exp	OLINDA / EXM v. 2.0	Kidneys	0.81 ± 0.24
						Bone marrow	0.02 ± 0.01
						Liver	0.13 ± 0.10
						Urinary bladder	0.27 ± 0.25
						Spleen	0.16 ± 0.07
						Lacrimal glands	3.62 ± 1.78
						Parotid glands	0.21 ± 0.14
						Submandibular glands	0.09 ± 0.07

TABLE 5.8 – Dosimetric workflows available in the literature for ^{177}Lu-PSMA therapies (*^{177}Lu-DKFZ-PSMA-617; **^{177}Lu-PSMA-617; ***^{177}Lu-PSMA-I&T). For Schuchardt et al., 2022, amean doses are given for ^{177}Lu-PSMA-617 (left) and ^{177}Lu-PSMA-I&T (right).

Cette thèse est accessible à l'adresse : https://theses.insa-lyon.fr/publication/2023ISAL0068/these.pdf
© [L. Vergnaud], [2023], INSA Lyon, tous droits réservés

Cette thèse est accessible à l'adresse : https://theses.insa-lyon.fr/publication/2023ISAL0068/these.pdf
© [L. Vergnaud], [2023], INSA Lyon, tous droits réservés

Part II

Contributions

Cette thèse est accessible à l'adresse : https://theses.insa-lyon.fr/publication/2023ISAL0068/these.pdf
© [L. Vergnaud], [2023], INSA Lyon, tous droits réservés

Cette thèse est accessible à l'adresse : https://theses.insa-lyon.fr/publication/2023ISAL0068/these.pdf
© [L. Vergnaud], [2023], INSA Lyon, tous droits réservés

Chapter 6

Adaptive dosimetric workflow for ^{177}Lu-DOTATATE treatments

In this chapter, a clinically usable dosimetric workflow adapting to limited numbers of SPECT/CT acquisitions has been implemented for the ^{177}Lu-DOTATATE treatments. This work was adapted from the article entitled "Patient-specific dosimetry adapted to variable number of SPECT/CT time-points per cycle for ^{177}Lu-DOTATATE therapy" (Vergnaud et al., 2022) which was published in EJNMMI Physics.

6.1 Introduction

Peptide receptor radionuclide therapy is a cancer treatment option (Strosberg et al., 2017a) for patients suffering from unresectable neuroendocrine tumours that express somatostatin receptors (Mansi et al., 2020) as described in Chapter 2. The treatment consists to intravenously inject somatostatin analogue radiolabelled with ^{177}Lu (^{177}Lu-DOTATATE). The treatment efficacy was demonstrated in the NETTER study (Strosberg et al., 2017a) and its use was approved by the FDA in 2018 (Bhardwaj et al., 2019). Currently, the treatment is standardised: 4 injections of 7.4 GBq spaced about 8 weeks apart. However, it has been shown that the absorbed dose distribution is variable between patients (Sandström et al., 2013) and the biodistribution of the radiopharmaceutical evolves over time after injection due to physiological mechanisms like the number of receptors or the blood flow in an organ (Hardiansyah et al., 2020). This is why today the implementation of patient-specific image-based dosimetry is a challenge (Chapter 1). Indeed, it can help to guide the treatment, to evaluate the dose-toxicity and dose-response relationships (Ljungberg and Sjögreen Gleisner, 2016; Ljungberg and Sjogreen Gleisner, 2018; Del Prete et al., 2017; Strigari et al., 2014; Ilan et al., 2015).

The accuracy of dosimetric estimates depends on the number of SPECT/CT acquisitions available after each injection. Ideally, several time-points would be required to build a time activity curve (TAC) in the organs of interest (Hänscheid and Lassmann, 2020; Bardiès and Buvat, 2011). However, post-processing acquisitions are not mandatory and their number and frequency are institutionally dependent. Furthermore, in clinical practice, acquiring multiple time-points can be difficult due to patient health, technical or logistical reasons. At the Léon Bérard Centre, for example, the standard procedure is to acquire three time-points after the first injection (1H, 24H and 96H/144H) and then a single one for each other cycle (24H). One of the current issues is to set up workflows requiring only a small number of SPECT/CT acquisitions in order to facilitate the implementation of dosimetry in clinical practice.

Cette thèse est accessible à l'adresse : https://theses.insa-lyon.fr/publication/2023ISAL0068/these.pdf
© [L. Vergnaud], [2023], INSA Lyon, tous droits réservés

In the literature, several articles propose dosimetric workflows requiring only a few acquisitions after each cycle. On the one hand, some works try to reduce the number of acquisitions by selecting the appropriate time-points and/or the type of acquisition (planar and/or SPECT/CT) so that the error from the original workflow is as small as possible (Sundlöv et al., 2018; Chicheportiche et al., 2020). Others proposed workflows reduced to a single SPECT/CT acquisition from the second cycle (Willowson et al., 2018a; Madsen et al., 2019; Hänscheid et al., 2018; Sandström et al., 2020; Zhao et al., 2019; Devasia et al., 2020), based on an approximation of the time-integrated activity or a priori information: use of pharmacokinetics obtained in a previous cycle (Garske et al., 2012) or from other patients (Jackson et al., 2020a). In most published studies, the TAC is modeled with mono-exponential function that considers only one global decrease phase and not the three physiological phases: one uptake phase and two clearance phases (rapid- and long-term). Recently, Jackson et al. (Jackson et al., 2020a) developed a method based on a tri-exponential model to estimate the absorbed doses from a single activity time-point by using pre-calculated factors. These factors were obtained from selected time-activity curves of other patients and were time-dependant but not patient-specific. The method was validated for ^{177}Lu-PSMA-617 therapy for different organs (kidneys, liver, spleen) and tumours but not for bone marrow. Moreover, in many articles, absorbed doses are computed using the MIRD formalism (Howell et al., 1999) based on pre-calculated S-values on digital phantoms (Chauvin et al., 2020). However, cross-doses impact vary from patient to patient and it is not easy to get S-values for tumours (Olguin et al., 2020). Overall, the proposed workflows are not fully patient-specific as they are based on pre-calculated S-values, the patient-specific pharmacokinetics are not respected or simplified by a mono-exponential function. Moreover, they are not validated for all organs at risk (OAR) and alternative methods were not necessarily proposed if acquisitions were missing from their standard procedures as it could be the case in clinical practice.

In this work, we propose an image-based patient-specific dosimetric workflow with a reduced number of acquisitions in ^{177}Lu-DOTATATE therapy for neuroendocrine tumours applicable in clinic. Alternative methods were implemented and assessed in order to use the workflow even if some acquisitions are missing. The proposed method is based on Monte Carlo simulations to compute patient-specific dose rates. Time Dose-Rate Curves are fitted with tri-exponential functions and take into account patient-specific pharmacokinetics computed at one cycle with several time-points to estimate time-integrated absorbed dose for the other cycles with a single time-point. Also, several ways to evaluate dose in bone marrow, one of the two main OAR with kidneys(Sandström et al., 2010), are proposed and compared.

6.2 Material and methods

6.2.1 Patients

In this study, two cohorts of patients were included. The first cohort (*patient cohort*, Section 6.2.1.1) was used to perform dosimetric calculations and to validate alternative methods requiring few SPECT/CT acquisitions. The second cohort was used for validation only (*validation cohort*, Section 6.2.1.2).

Cette thèse est accessible à l'adresse : https://theses.insa-lyon.fr/publication/2023ISAL0068/these.pdf
© [L. Vergnaud], [2023], INSA Lyon, tous droits réservés

6.2.1.1 Patient cohort

This cohort was composed of thirteen patients, 8 women and 5 men, with neuroendocrine tumours (NET) treated by peptide receptor radionuclide therapy with ^{177}Lu-DOTATATE (LUTATHERA®), between November 2018 and March 2021 at the Léon Berard Center (Lyon, France). They were treated with four cycles of 6832 ± 158 MBq injections with about 8 weeks between two cycles, except for patient 1 with 28 weeks between cycles 3 and 4 and patient 10 with 24 weeks between cycles 2 and 3 and an injected activity equal to 3428 MBq for cycle 3.

6.2.1.2 Validation cohort

The second cohort included seven additional patients (2 women and 5 men) treated at the ICANS (Strasbourg, France) with ^{177}Lu-DOTATATE. They received 7222 ± 113 MBq at cycles 1 and 4 between July 2020 and September 2021.

6.2.2 Image acquisition

For the *patient cohort*, three tomographic SPECT/CT acquisitions were planned at 1H, 24H and 96H or 144H post-injection after the first injection. The last time-point, 96H or 144H, varies according to the weekend constraints. For the other cycles, only one acquisition at 24H was planned. However, some acquisitions cannot be performed for clinical or technical reasons or due to the COVID pandemic. The table 6.1 summarizes the available images. A total of 63 images were considered. For patient P10, additional images were acquired at cycles 3 and 4.

		P1	**P2**	**P3**	**P4**	**P5**	**P6**	**P7**	**P8**	**P9**	**P10**	**P11**	**P12**	**P13**
Cycle 1	1H	X	X	X	X	X	X	NA	X	X	X	NA	X	NA
	24H	X	X	X	X	X	X	X	X	NA	NA	X	X	X
	96H	X	X	X	X	NA	X	NA	X	X	NA	X	NA	NA
	144H													
Cycle 2	24H	X	X	X	X	NA	NA	X	X	X	X	X	NA	X
Cycle 3	1H										X			
	24H	X	X	NA		NA	NA	X	X	X	X	X	X	X
	96H										X			
Cycle 4	1H								X	X	X			
	24H	X	X	NA		X	X	X			X	X	X	X
	96H										X			

TABLE 6.1 – SPECT/CT acquisition time-points for all patients of the patient cohort, all cycles. NA: planned but not available, X: available.

For the *validation cohort*, three SPECT/CT acquisitions were performed and are available at 6H, at 24H and at 7 days after cycles 1 and 4. Cycles 2 and 3 were not considered because they were only followed by SPECT/CT acquisition at 24H which would not have allowed the validation of alternative dosimetric methods.

Cette thèse est accessible à l'adresse : https://theses.insa-lyon.fr/publication/2023ISAL0068/these.pdf
© [L. Vergnaud], [2023], INSA Lyon, tous droits réservés

6.2.3 Quantitative tomographic SPECT/CT acquisitions

6.2.3.1 Acquisition parameters

Image acquisitions were performed with a GE Discovery NM CT 670 for the *patient cohort* and with a GE Discovery NM CT 870 DR for the *validation cohort*. Imaging system are composed of two detectors at 180° equipped with MEGP (Medium Energy General Purpose) collimators. The acquisition parameters for each system are given in Table 6.2.

Acquisition parameters	GE Discovery NM CT 670	GE Discovery NM CT 870 DR
Thick crystal	3"8	5"8
Number of projections	60	30
Time per projection (s)	15	40 (80 at 7 days)
Photopeak energy window (keV)	208	208
Energy window width	15%	20%
Scatter photopeak energy window (keV)	176.8	176.8
Scatter correction window	17.6%	10%

TABLE 6.2 – Acquisitions parameters used for SPECT images of the *patient cohort* with the GE Discovery NM CT 670 and those of the *validation cohort* with the GE Discovery NM CT 870 DR.

6.2.3.2 Reconstruction parameters

For both cohorts, images were reconstructed in Xeleris 3.0 software with OSEM 3D algorithm (8 iterations and 8 subsets) with PSF correction ("resolution recovery"). Attenuation was corrected with the CT images. Scatter correction was performed with the Dual Energy Window method (as the TEW method was not available in the software).

6.2.3.3 Calibration

Pixel's values in the reconstructed images, initially expressed in number of detected counts, were converted to quantitative activity in MBq/mL by using an experimentally determined sensitivity factor (Equation 4.14 of Section 4.13). A Jaszczak phantom was filled with a known activity of ^{177}Lu before being acquired with the same protocol as for patients (Dewaraja et al., 2012; Ljungberg et al., 2016). This method is recommended by MIRD No. 23 and allows the partial volume effect to be ignored.

The sensitivity factors in tomographic mode (i.e. taking into account both detector heads) were 7.6 cps/MBq and 18 cps/MBq for the Discovery NM CT 670 and 870DR cameras, respectively. This difference of sensitivity factor can probably be explained by the crystal thickness and energy window.

Cette thèse est accessible à l'adresse : https://theses.insa-lyon.fr/publication/2023ISAL0068/these.pdf
© [L. Vergnaud], [2023], INSA Lyon, tous droits réservés

6.2.3.4 Dead time

For the early acquisition, approximately one hour after the injection, images from the patient cohort were corrected for dead time according to a variation of the decaying source method. Indeed, some are performed before micturition and a majority of the injected activity may be in the field of view and cause dead time. For later acquisition, dead time was considered as negligible (Desy et al., 2020) and not accounted for.

Dead time estimation To be able to measure it, a 39.7 MBq vial filled of ^{177}Lu was positioned in front of the detector crystal and was considered as a point source (Figure 6.1). Then, the source was gradually moved away from the detector (34 cm to 2.37 m) to vary the count rate as proposed by Gardner and Liu, 1997 and Usman and Patil, 2018. For each position, the acquisition was performed three times and the count rates were averaged to limit variability. In addition, background noise was estimated by performing a source-free acquisition and was removed from all count rates evaluated. Finally, a paralyzable model (Section 4.2.4.2) was used to determine the value of the dead time.

FIGURE 6.1 – Measurement set up to estimate the dead time of the GE Discovery NM/CT 670 gamma camera using the decaying source method. The source is located in a vial attached to a support which is itself attached to a mobile trolley allowing the distance between the source and the detector to be varied.

Dead time correction The dead time was corrected in the projections of the 1H SPECT acquisitions based on wide-energy spectrum count rate. They were then reconstructed with the same reconstruction parameters as presented in Section 6.2.3.2.

Cette thèse est accessible à l'adresse : https://theses.insa-lyon.fr/publication/2023ISAL0068/these.pdf
© [L. Vergnaud], [2023], INSA Lyon, tous droits réservés

Evaluation of the impact of the dead time correction For each patient in the *patient cohort* having cycles with three SPECT/CT acquisitions, the 1H SPECT acquisitions were reconstructed with and without dead time correction. Dosimetry of kidney, liver, spleen and bone marrow were performed with each and compared.

In the following calculations, the exact time duration between the end of injection and the acquisition was determined according to the acquisition hours stored in the DICOM header of the images and was used for calculations.

6.2.4 Adaptive organ-based dosimetric workflow

After acquiring and reconstructing the SPECT images, the volumes of interest should be segmented. This is the case for the kidneys, liver including intra-hepatic lesions, spleen and bone marrow. In the following, a section will be specifically devoted to bone marrow dosimetry because it shows a much lower uptake than the other organs.

6.2.4.1 Volumes of Interest (VOI)

All the four volumes of interest (VOI), left and right kidneys, liver and spleen (LK, RK, L, S), were manually segmented on the first acquired CT image. For liver, if tumours were present, they were included in the segmented volume. This method preserves the anatomical contours of organs, which is not the case with SPECT images, which can be degraded by factors such as limited spatial resolution (partial volume effect). Obtained 3D contours were then propagated to all other time-points CT images thanks to deformable vector fields obtained from deformable image registration (Delmon et al., 2013), as described in Sarrut et al., 2017a. Final contours were visually evaluated and manually corrected if necessary.

6.2.4.2 General approach

Monte Carlo simulations description Monte Carlo simulations with GATE (Sarrut et al., 2014) were used to estimate dose rate distributions (Sarrut et al., 2017a). To that end, SPECT images were used as a 3D source of emitted gamma. CT images were resampled at the same pixel spacing than the SPECT images (4.4 mm side). SPECT voxels are considered as an isotropic source of decaying ^{177}Lu with activity proportional to the count value in the voxel. The Monte Carlo engine takes care of simulating all daughter particles, including electrons and photons. The recommended `emstandard_opt4` (Sarrut et al., 2014) physics list was used. The production cuts were set to 0.1 mm for all particles. Absorbed dose distributions were stored in a 3D matrix of voxels having the same spacing as the initial SPECT image. Simulations were performed to obtain a statistical uncertainty around 1% in each VOI with a high uptake (LK, RK, L, S). In practice, it means that 1×10^6 (1 MBq) primary particles (decaying ions) were simulated. The final dose rate distribution was then scaled to the total activity estimated from the SPECT images by summing all voxels values multiplied by the sensitivity factor corresponding. This computation was performed for all available SPECT time-points (1H, 24H, 96H or 144H). This approach allows us to take into account both self and cross-dose in the MIRD terminology (Dewaraja et al., 2012).

Cette thèse est accessible à l'adresse : https://theses.insa-lyon.fr/publication/2023ISAL0068/these.pdf
© [L. Vergnaud], [2023], INSA Lyon, tous droits réservés

Contribution of the cross-dose to the total dose The cross-dose is the dose deposited in the volume of interest but whose decays have taken place in another volume. The latter could have an impact in the case of a lesion with a high uptake and close to a VOI. To evaluate the contribution of the cross-dose to the total dose, patient P5 of the *patient cohort* was selected as he has a large lesion close to all other segmented VOIs. The cross-dose proportion was calculated using simulations with or without removing the activity in the lesion on the SPECT image as shown in Figure 6.2. The absorbed doses were then estimated in all VOIs and compared. If the differences are small then the proportion of the cross-dose will have had little impact on the absorbed doses for that patient.

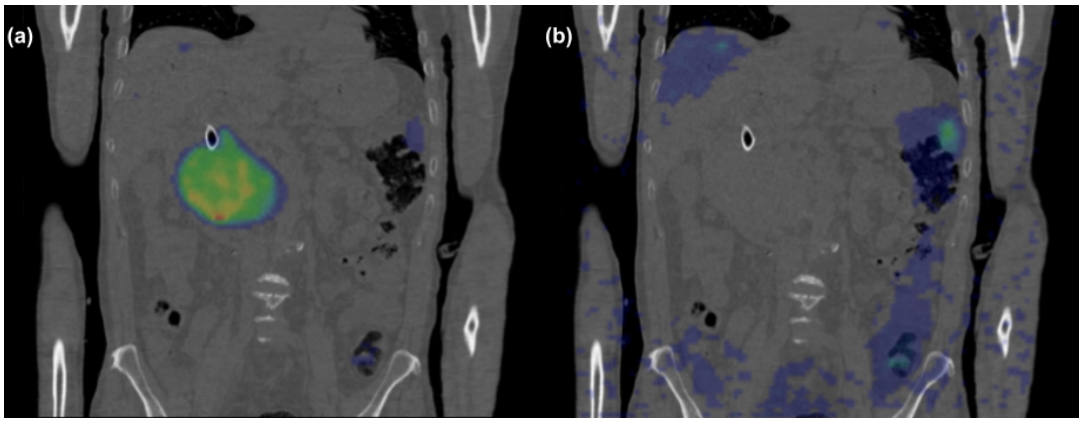

FIGURE 6.2 – Superposition of the 24H SPECT image of cycle 1 including lesion and CT (a) and the 24H SPECT image of cycle 1 without lesion and CT (b) for patient 5 of the *patient cohort*.

Dose estimates were made using the Single Time-Point Inter-patient method, which will be presented in Section 6.2.4.5, as three SPECT/CT acquisitions were not available for the first cycle.

6.2.4.3 Tri-exponential fit for Time Dose-Rate Curve

For all VOI and all time-points, the organ dose rate (ODR) was computed by averaging dose rate values of all voxels belonging to the VOI. Note that dose rate distribution maps were upsampled to the same pixel spacing than VOI drawn on CT images. This step leads to a Time Dose-Rate Curve (TDRC) for all injections, similar to the conventional Time-Activity Curve (TAC) except that it is determined with dose-rate and not the activity, thus already integrating the cross-dose. In order to compute the total absorbed dose corresponding to the time integral of those curves, the analytical method proposed by Jackson et al. (Jackson et al., 2020b; Jackson et al., 2013) based on tri-exponential function was used by replacing activity (A) with dose rate (Ω), see Equation (6.1).

$$TDRC(t)\ [Gy/s] = -\Omega_1 e^{-(\lambda+k_1)t} + \Omega_2 e^{-(\lambda+k_2)t} + \Omega_3 e^{-(\lambda+k_3)t} \tag{6.1}$$

where λ is the radioactive decay constant of ^{177}Lu, Ω_i and k_i are the amplitudes and decay rates of three phases: an uptake phase followed by a rapid wash-out and a long-term clearance. An example is available at the top left corner of figure 6.3. Tri-exponential parameters were computed with the same algorithm described in Jackson et al., 2020b therefore all Ω_i were decay-corrected before fitting TDRC and the correction was reversed during integration. ODR were assumed to be equal to zero

Cette thèse est accessible à l'adresse : https://theses.insa-lyon.fr/publication/2023ISAL0068/these.pdf
© [L. Vergnaud], [2023], INSA Lyon, tous droits réservés

just before the treatment and 600H after the injection. The parameter k_1 was set to -1.3 s^{-1} in the article by Jackson et al. (Jackson et al., 2020b). Here, we are dealing with TDRC and not TAC so this value cannot be used. Instead, the value of k_1 was optimized by gradient descend in order to obtain a difference between the ODR value of the first acquisition and the fitted model lower to 0.00001 mGy/s (i.e. 1000 times lower than the ODR value). At the end, the time-integration of TDRC corresponds to the absorbed dose by organ, see Equation (6.2).

$$Dose\ by\ organ\ [Gy] = \frac{-\Omega_1}{(\lambda + k_1)} + \frac{\Omega_2}{(\lambda + k_2)} + \frac{\Omega_3}{(\lambda + k_3)} \tag{6.2}$$

6.2.4.4 Particular case: acquisition at 24H was missing in the cycle 1

The tri-exponential function can be used if three ODR are available as planned in cycle 1. However, the ODR at 24H was missing for some patients. In that case, the missing ODR was substituted with the ODR of another cycle at 24H for the same patient (the closest in time) and its exact time duration was used for the TDRC fitting. Since the injected activities vary from cycle to cycle, the substituted ODR was scaled to the cycle activity. This method assumes that the difference between the missing ODR and the substituted ODR is small therefore the closest cycle has been used. This method is named the Missing Time-Point method (M1) and is shown in figure 6.3.

The variability of ODR was assessed for each patient and each VOI at 24H (ex: ODR of left kidney at 24H of cycles 1, 2, 3 and 4). For this, ODR were scaled to the first injected activity and a variation coefficient (%) was computed.

To estimate the error associated with the Missing Time-Point method (M1), we calculated absorbed doses by organs with two methods for patients who had three ODR: 1) from the three initial ODR (reference method) and 2) from two initial ODR and a substituted ODR at 24h (Missing Time-point method M1). The percentage of dose difference between both methods were computed for the patient and the validation cohorts.

6.2.4.5 Absorbed dose estimation for cycles with a single acquisition

At cycles 2, 3 and 4, one single ODR at 24H was generally available. Absorbed dose estimation was performed by exploiting tri-exponential-fitted TDRC from the first cycle, assuming similar pharmacokinetics after assessing the variability of the ODR for each time point and each patient. The TDRC was scaled to the single ODR value as illustrated figure 6.3. Time-integrated absorbed dose was computed from the scaled TDRC. This method is named the STP-Intra method for Single Time-Point Intra-patient method (M2). A similar approach was proposed by Garske et al. (Garske et al., 2012) with a mono-exponential function where they assumed that effective half-life was unchanged between cycles.

For eight patients, three time-points were available for several cycles: one from the patient cohort (cycles 3 and 4) and seven from the validation cohort (cycles 1 and 4). In these cases, the STP-Intra method (M2) was compared to the tri-exponential method (reference method) using three time-points. Percentages of dose difference were computed.

In the rare cases when cycle 1 has not enough time-points, tri-exponential fit cannot be used and absorbed dose were estimated by using the average TDRC of other patients, scaled to the available ODR, like in Jackson et al., 2020a, and illustrated

Cette thèse est accessible à l'adresse : https://theses.insa-lyon.fr/publication/2023ISAL0068/these.pdf
© [L. Vergnaud], [2023], INSA Lyon, tous droits réservés

in figure 6.3. This method assumes that the pharmacokinetics of TDRC are homogeneous from one patient to another. This second alternative method is named the STP-Inter method for Single Time-Point Inter-patient method (M3).

The errors associated with this approach were estimated for cycle 1 in the patient cohort and for cycles 1 and 4 for the validation cohort by leave-one-out, comparing tri-exponential to STP-Inter dose estimation and computing the percentage of dose difference. The leave-one-out method was applied independently to each cohort.

6.2.4.6 Dosimetric workflow for bone marrow

As discussed in Chapter 5, the bone marrow is a tissue divided into red bone marrow (production of blood components) and yellow bone marrow (fat storage). The proportion and distribution of each depends on the patient and changes over time. There are currently no recommendations regarding bone marrow segmentation for this therapy. The workflow was similar except that three different VOI types were delineated to estimate doses absorbed for tests, according to various proposal in the literature: 1) the trabecular part of vertebrae between L2 and L4, 2) between L1 and L5 and 3) between T9 and L5. Note that patients in both cohorts did not have bone marrow lesions. In the presence of such lesions, bone marrow substitutes cannot really be used. As explained in Hindorf et al., 2010, VOI should contain bone marrow (thoracic vertebrae: 16.1% of total bone marrow and lumbar vertebrae: 12.3% in adults) and be in the vicinity of organs with a high uptake because those volumes will mainly absorb the dose (cross-dose). L2 to L4 VOI was used in Santoro et al., 2018; Ferrer et al., 2010 and was related hematological toxicity. L1 to L5 and T9 to L5 were used by Hagmarker et al. Hagmarker et al., 2019 to establish dose/toxicity relationship. For thoracic vertebrae, only vertebrea visible in the field of view of all patients were selected for this study. Dosimetry in all VOI were compared. Moreover, the visible part of the humerus (upper part) was also delineated to have a reference for the background noise because it is the only region where there is no tumour or organ with a high uptake but that contains bone marrow (2.3% Hindorf et al., 2010). Note that for three patients in the validation cohort, the T9 vertebrae was not or not totally in the field of view.

Cette thèse est accessible à l'adresse : https://theses.insa-lyon.fr/publication/2023ISAL0068/these.pdf
© [L. Vergnaud], [2023], INSA Lyon, tous droits réservés

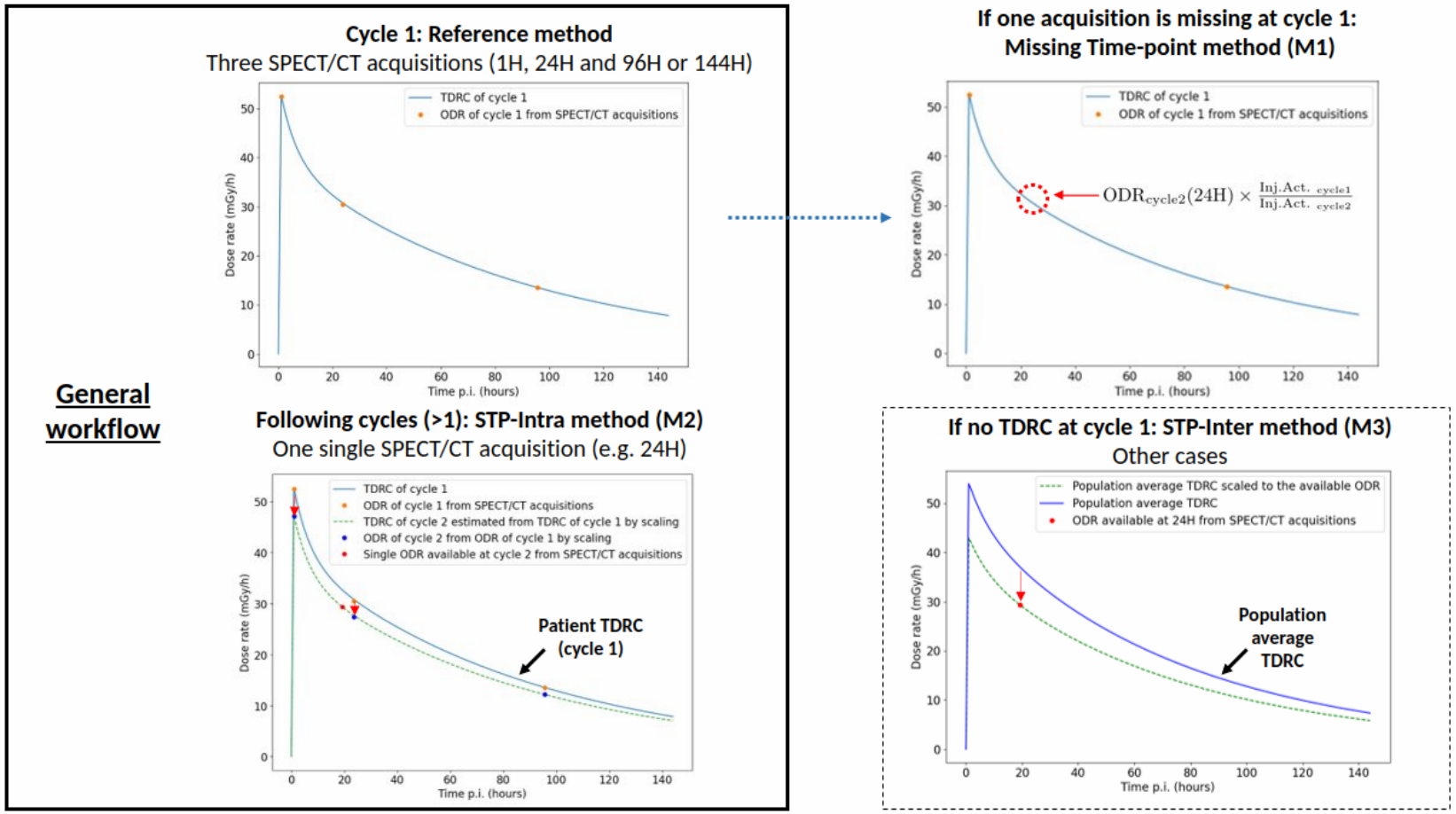

FIGURE 6.3 – Scheme of the proposed dosimetric workflow illustrated with the left kidney of patient 3 (cycles 1 and 2) of the patient cohort. When three SPECT/CT acquisitions are available at cycle 1, the TDRC was fitted with a tri-exponential function: it is the reference method (at the top left). If one acquisition was missing at cycle 1 but there was an acquisition at the same time-point for a following cycle, the missing ODR was approximated by the ODR of the first next cycle scaled according to injected activities: it is the Missing Time-Point method M1 (at the top right). TDRC of following cycles with one single acquisition were estimated by TDRC at cycle 1 scaled to the single available ODR (all points were scaled by the ratio between the ODR of the single time-point and the ODR computed at the same time on the TDRC): it is the STP-Intra method M2 (at the bottom left). In all other cases, TDRC were estimated by population averaged TDRC scaled by the lastest ODR available: it is the STP-Inter method M3 (at the bottom right).

Cette thèse est accessible à l'adresse : https://theses.insa-lyon.fr/publication/2023ISAL0068/these.pdf
© [L. Vergnaud], [2023], INSA Lyon, tous droits réservés

6.3 Results

6.3.1 Dosimetric results of the patient cohort

6.3.1.1 Deadtime

Dead time estimation Figure 6.4 shows the experimental results obtained when estimating the dead time using the decaying source method.

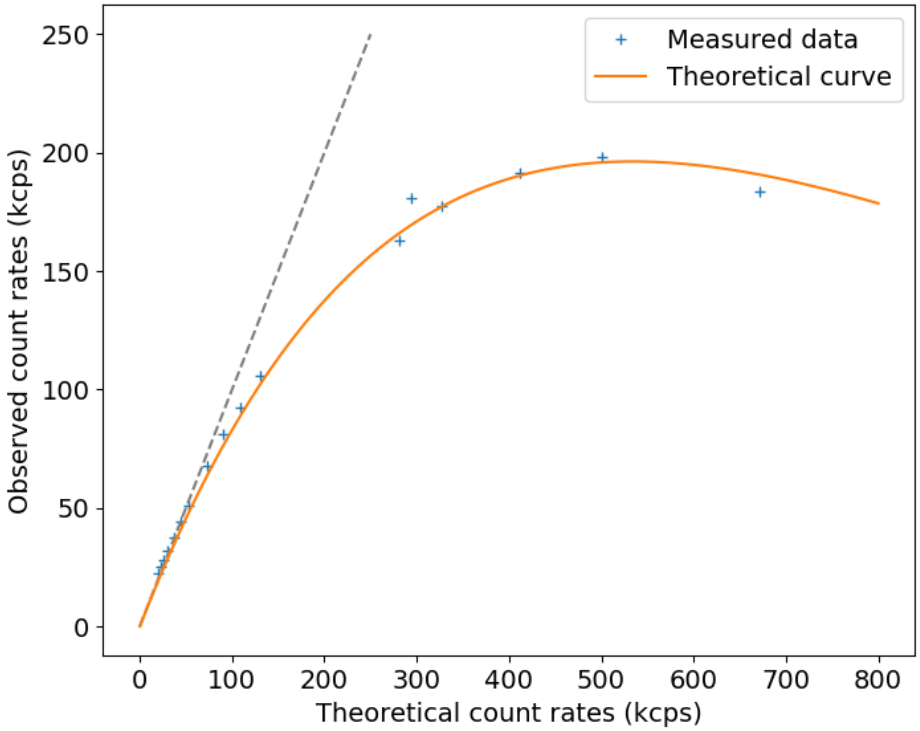

FIGURE 6.4 – Observed count rates for a 39.7 MBq source moved from 34 cm to 2.37 m according to theoretical count rates. The experimental data are shown as blue crosses and the theoretical model curve is shown in orange.

The dead time was 1.87µs for the GE Discovery NM CT 670 and a dead time correction was applied for the patient cohort.

Dosimetric impact of dead time For the *patient cohort*, for patients and cycles with three SPECT/CT acquisitions, we compared the absorbed doses for all VOI between reconstructions with and without dead time correction at the first acquisition.

The impact of dead time on the absorbed doses appears very limited whatever the volume of interest: less than 3% with a maximum of 6% for bone marrow.

6.3.1.2 Liver, kidneys and spleen

Absorbed doses estimated for all patients in the patient cohort for left and right kidneys, liver and spleen are given in the figure 6.6. When data were not available (missing acquisitions or cycles due to the COVID pandemic), absorbed doses were approximated by the mean of absorbed doses available multiplied by the number of cycle(s) missing (in white with dotted line). Note that the scale is not the same for each graph.

Cette thèse est accessible à l'adresse : https://theses.insa-lyon.fr/publication/2023ISAL0068/these.pdf
© [L. Vergnaud], [2023], INSA Lyon, tous droits réservés

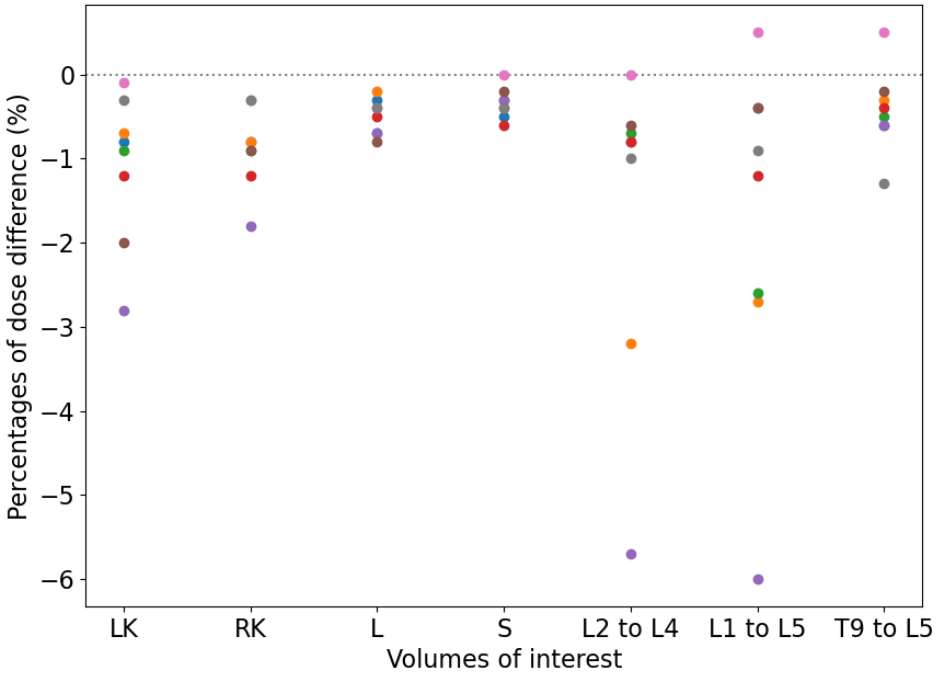

FIGURE 6.5 – Percentages of dose difference (%) estimated with or without dead time correction after the first injection for 8 cycles (one color for each) of 7 patients having three SPECT/CT acquisitions.

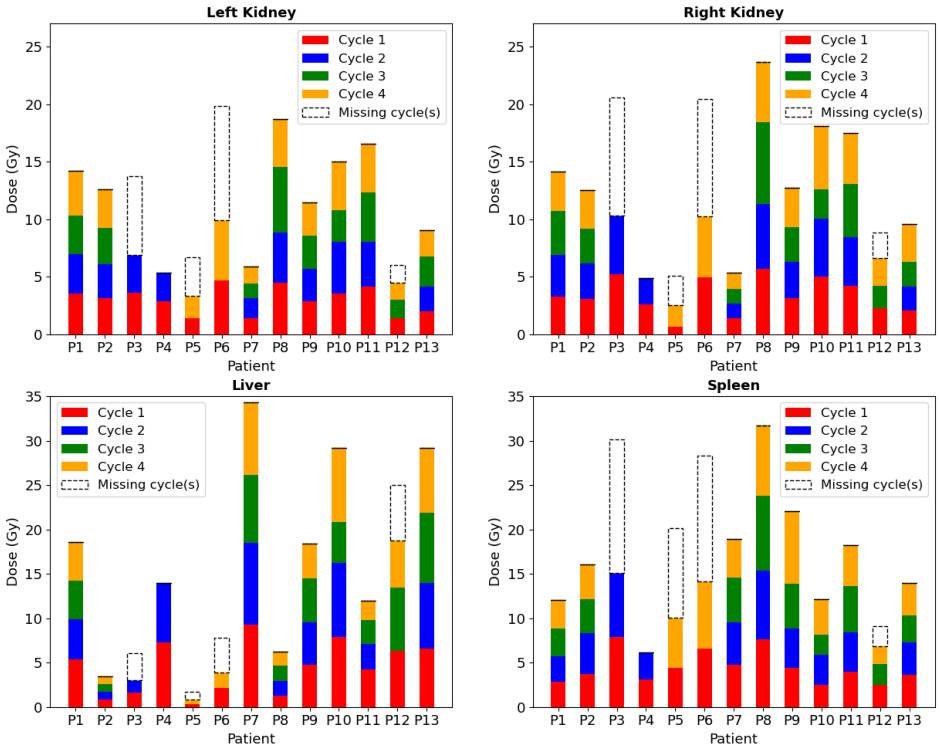

FIGURE 6.6 – Absorbed doses (Gy) for 13 patients of the patient cohort and for four volumes (Left Kidney, Right Kidney, Liver and Spleen) for all available cycles. For missing cycles, absorbed dose estimations are in white dotted line

Cette thèse est accessible à l'adresse : https://theses.insa-lyon.fr/publication/2023ISAL0068/these.pdf
© [L. Vergnaud], [2023], INSA Lyon, tous droits réservés

The *inter-patient* variability of cumulative absorbed doses were large for all organs ([Minimum (Gy), Median (Gy), Maximum (Gy)]: left kidney: [5.9 ; 13.2 ; 19.8], right kidney: [5.1 ; 13.4 ; 23.6], liver: [1.7 ; 18.4 ; 34.3] and spleen: [9.1 ; 18.6 ; 31.7]). Overall, the *intra-patient* variability of the absorbed dose for all cycles were low : the mean of variations coefficients of absorbed doses between cycles were: 10.4% for LK, 14.9% for RK, 15.5% for L and 11.5% for S.

Doses per injected activity [mGy/MBq] were averaged on all cycles for each patient and represented in figure 6.7 for the four organs. For bone marrow, doses per injected activity were given as mean $\pm$ std: 0.04 $\pm$ 0.02 mGy/MBq for L2 to L4, 0.04 $\pm$ 0.03 mGy/MBq for L1 to L5 and 0.04 $\pm$ 0.02 mGy/MBq for T9 to L5.

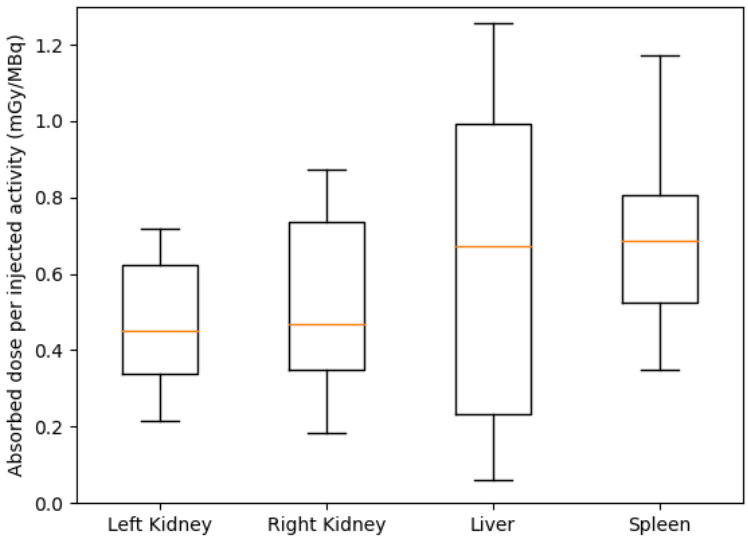

FIGURE 6.7 – Boxplots representing doses per injected activity (mGy/MBq) averaged on all cycles available for each patient of the patient cohort and each organ (Left Kidney, Right Kidney, Liver and Spleen)

Coefficients of variation (CV) of doses per injected activity between different cycles were computed for each organ and each patient of the patient cohort. For kidneys and spleen, CV were inferior to 16% in 85% of patients whereas for liver, L2 to L4, L1 to L5 and T9 to L5, this percentage decreased to 77%, 61%, 69% and 69% respectively.

Finally, figure 6.8 summarizes the workflow used for the patient cohort. The corresponding estimated errors of all cases are proposed below in the form [Minimum ; Median ; Maximum ; Mean].

Cette thèse est accessible à l'adresse : https://theses.insa-lyon.fr/publication/2023ISAL0068/these.pdf
© [L. Vergnaud], [2023], INSA Lyon, tous droits réservés

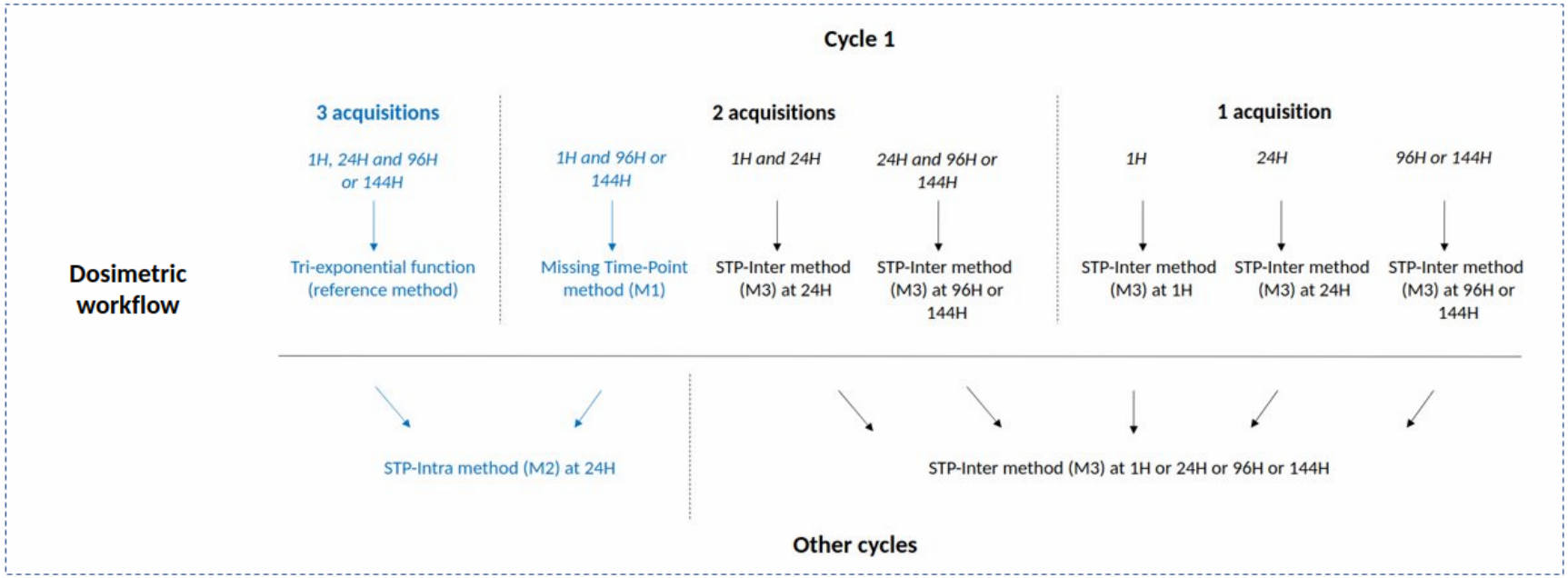

Errors associated with each alternative method

Errors associated with each alternative	Missing Time-Point at 24H (M1)	STP-Intra method at 24H (M2)	STP-Inter method at 1H (M3)	STP-Inter method at 24H (M3)	STP-Inter method at 96H or 144H (M3)
LK:	[-20.2 ; 0.6 ; 45.7 ; 2.0]	[-27.0 ; -3.7 ; 25.5 ; 0.7]	[-26.6 ; -3.6 ; 69.7 ; 4.5]	[-13.9 ; -0.6 ; 46.5 ; 1.3]	[-59.0 ; 7.7 ; 33.0 ; 5.3]
RK:	[-17.1 ; 0.5 ; 35.4 ; 1.5]	[-2.5 ; 13.6 ; 90.4 ; 19.4]	[-51.5 ; 3.5 ; 83.5 ; 7.7]	[-43.9 ; 5.6 ; 32.0 ; 2.0]	[-18.3 ; 0.4 ; 37.3 ; 1.5]
L:	[-17.2 ; 3.3 ; 26.3 ; 2.7]	[-44.8 ; 1.6 ; 30.2 ; 2.1]	[-40.1 ; 6.4 ; 98.9 ; 8.8]	[-20.0 ; 0.7 ; 98.5 ; 3.9]	[-99.1 ; 5.0 ; 49.8 ; 6.8]
S:	[-14.4 ; 0.9 ; 56.5 ; 9.0]	[-30.3 ; 1.9 ; 31.8 ; 4.9]	[-23.8 ; -1.8 ; 126.7 ; 9.0]	[-19.9 ; -1.2 ; 78.2 ; 3.2]	[-99.3 ; 3.4 ; 44.0 ; 6.0]
L2-L4:	[-12.4 ; 0.1 ; 8.9 ; 0.4]	[-19.1 ; 10.0 ; 37.6 ; 9.4]	[-29.7 ; 1.4 ; 106.4 ; 7.3]	[-55.0 ; -4.9 ; 27.3 ; -9.9]	[-6.9 ; 0.2 ; 9.7 ; 0.2]
L1-L5:	[-15.4 ; 0.0 ; 9.4 ; -0.1]	[-19.9 ; 18.6 ; 31.1 ; 9.3]	[-30.0 ; 3.9 ; 81.3 ; 4.3]	[-45.0 ; -4.6 ; 32.8 ; -7.5]	[-12.0 ; 0.0 ; 8.7 ; 0.1]
T9-L5:	[-7.3 ; 0.0 ; 7.6 ; 0.2]	[-27.0 ; 6.3 ; 28.2 ; 4.1]	[-18.6 ; -0.2 ; 68.0 ; 2.9]	[-51.1 ; -9.0 ; 36.0 ; -7.0]	[-9.1 ; 0.5 ; 8.1 ; 0.1]

FIGURE 6.8 – Scheme of the simplified dosimetric workflow used for the estimation of absorbed doses for the patient cohort to the left (LK) and right (RK) kidneys, liver (L), spleen (S) and the three surrogates of bone marrow (L2-L4, L1-L5 and T9-L5). The observed errors were computed on the patient and the validation cohorts and are provided as [minimum ; median ; maximum ; mean].

Cette thèse est accessible à l'adresse : https://theses.insa-lyon.fr/publication/2023ISAL0068/these.pdf
© [L. Vergnaud], [2023], INSA Lyon, tous droits réservés

6.3.1.3 Bone marrow

Absorbed doses estimated for bone marrow are shown in figure 6.9. For each patient, the three first bars represent the absorbed doses measured for each surrogate volume of bone marrow (L2 to L4, L1 to L5 and T9 to L5). The fourth bar depicts the doses absorbed by the humerus as a control. For patient 1, the L5 vertebrae was not visible on the CT image at 96H of cycle 1. The delineation of the humerus depends on the patients and the position of arm on the table and was not possible for few images: for patient 13 for example.

6.3.2 Comparison of M1, M2 and M3 methods vs reference method (patient and validation cohorts)

6.3.2.1 Variation coefficients of ODR

The variation coefficients of ODR give an indication of differences between ODR at the same time-point but different cycles scaled to injected activities. They were estimated from all patients' data of the two cohorts at 24H, with the validation cohort and patients 8, 9 and 10 at 1H/6H and with only the validation cohort at 7D. Medians of variations coefficients (%) of ODR were shown in table 6.3.

Organs	Median (1H/6H) [Min ; Max]	Median (24H) [Min ; Max]	Median (96H/7D) [Min ; Max]
LK	4.0% [0.2 ; 49.5]	8.2% [1.7 ; 46.8]	26.1% [1.0 ; 64.9]
RK	5.0% [1.1 ; 47.8]	8.0% [1.2 ; 68.5]	14.3% [0.5 ; 72.2]
L	15.6% [2.2 ; 45.7]	9.8% [1.4 ; 47.9]	19.5% [0.4 ; 139.9]
S	22.3% [8.4 ; 49.7]	12.1% [0.3 ; 58.6]	34.7% [16.4 ; 140.0]
L2-L4	9.5% [1.1 ; 35.7]	15.4% [2.8 ; 43.8]	6.2% [1.2 ; 43.0]
L1-L5	12.5% [0.7 ; 31.3]	14.9% [0.5 ; 36.0]	8.0% [0.5 ; 40.2]
T9-L5	9.4% [2.4 ; 33.5]	13.5% [2.8 ; 34.6]	4.4% [0.4 ; 15.6]

TABLE 6.3 – Medians of variations coefficients (%) of ODR obtained for each VOI and each time-point on all patients (patient and validation cohorts).

6.3.2.2 Impact of cross-dose

the patient 5 of the *patient cohort* had a large isolated lesion away from all other segmented VOIs. In Table 6.4, the doses to the OARs were estimated from SPECT with and without the activity present in the lesion. In addition, for each volume, the self-dose and cross-dose contributions were evaluated.

6.3.2.3 Data used to evaluate simplified methods M1, M2 and M3

To estimate the error associated with each method, only cycles with three SPECT/CT acquisitions were used for the M1 and M3 methods (data of the patients 1, 2, 3, 4, 6, 8 at cycle 1 and patient 10 at cycles 3 and 4 of the *patient cohort* and

Cette thèse est accessible à l'adresse : https://theses.insa-lyon.fr/publication/2023ISAL0068/these.pdf
© [L. Vergnaud], [2023], INSA Lyon, tous droits réservés

	With lesion	Without lesion	Self-dose contribution	Cross-dose contribution
LK	1390 mGy	1362 mGy	98%	2%
RK	663 mGy	330 mGy	50%	50%
L	288 mGy	152 mGy	53%	47%
S	4471 mGy	4283 mGy	96%	4%
L2 to L4	352 mGy	15 mGy	4%	96%
L1 to L5	361 mGy	18 mGy	5%	95%
T9 to L5	337 mGy	24 mGy	7%	93%

TABLE 6.4 – Doses estimated from SPECT with and without activity in the lesion of patient 5 of the *patient cohort*. Self-dose and cross-dose contributions were also calculated.

all patient's data of the *validation cohort*). For the M2 method, two cycles with three SPECT/CT acquisitions were required (data of the patient 10 of the *patient cohort* and all patient's data of the *validation cohort*).

6.3.2.4 Error associated with the Missing Time-Point (M1) at cycle 1

Figure 6.10 depicts percentages of dose difference (PDD) between absorbed doses estimated from the Missing Time-Point method (M1) and the reference method (tri-exponential fit) for each VOI and each time-point. Medians were inferior to 1.0%, 3.3% and 2.5% in absolute value when the replaced acquisition was at 1H/6H, at 24H and at 96H/7D whatever the VOI. Standard deviations were between 3.0% and 7.1% at 1H/6H, between 3.8% and 18.9% at 24H and between 5.7% and 31.8% at 96H/7D except for spleen (54.7%) because of the outliers of patient 6 of the validation cohort. Note that the scales are not the same between the figure 6.10 and the figures 6.11, 6.12 and 6.13.

6.3.2.5 Error associated with the STP-Intra method (M2)

Figure 6.11 depicts PDD between absorbed doses estimated from the STP-Intra method (M2) and the reference method for each VOI and each time-points. The lowest medians are obtained when the single time-point available is at 7 days: they were between -6.3% and 5.4% whereas they were between -16.3% and 12.7% and between -3.7% and 18.6% for time-points at 6H and 24H respectively for the validation cohort only. Medians of surrogates of bone marrow were inferior to 10.0% for L2 to L4, to 18.6% for L1 to L5 and 6.3% for T9 to L5 whatever the time-point. Standard deviations were between 10.4% and 41.9% at 1H/6H, between 17.3% and 32.3% at 24H and between 6.1% and 74.6% at 96H/7D for the validation cohort only. The variability of the PDD of surrogate volumes of bone marrow was almost the same as other VOI at 24H (mean $\pm$ std: 0.7 $\pm$ 17.3% for LK, 19.4 $\pm$ 32.3% for RK, 2.1 $\pm$ 25.2% for L, 4.9 $\pm$ 20.7% for S, 9.4 $\pm$ 23.6% for L2 to L4, 9.3 $\pm$ 21.1% for L1 to L5 and 4.1 $\pm$ 21.9% for T9 to L5).

Cette thèse est accessible à l'adresse : https://theses.insa-lyon.fr/publication/2023ISAL0068/these.pdf
© [L. Vergnaud], [2023], INSA Lyon, tous droits réservés

6.3.2.6 Error associated with the STP-Inter method (M3)

Figures 6.12 and 6.13 represent PDD between absorbed doses estimated with the STP-Inter method (M3) and the reference method using leave-one-out cross-validation, for the three time-points 1H/6H, 24H and last one (96H or 144H or 7D), and for all VOI (LK, RK, L and S in the figure 6.12 and L2-L4, L1-L5 and T9-L5 in the figure 6.13). Medians (standard deviation) were between -3.6% and 7.7% (14.9% and 21.6%) for LK, 0.4% and 5.6% (11.3% and 29.0%) for RK, 0.7% and 6.4% (25.9% and 33.0%) for L, -1.8% and 3.4% (20.9% and 36.9%) for S, -4.9% and 1.4% (4.2% and 27.4%) for L2 to L4, -4.6% and 3.9% (4.1% and 21.1%) for L1 to L5 and -9.0% and 0.5% (4.0% and 20%) for T9 to L5 regardless of the time. The variability seems to be lowest for surrogates of bone marrow for late time-points: for example, for L2 to L4, mean and standard deviation of PDD were equal to 1.4 $\pm$ 27.4% at 1H/6H, -4.9 $\pm$ 23.3% at 24H and 0.2 $\pm$ 4.2% at 96H/7D.

Cette thèse est accessible à l'adresse : https://theses.insa-lyon.fr/publication/2023ISAL0068/these.pdf
© [L. Vergnaud], [2023], INSA Lyon, tous droits réservés

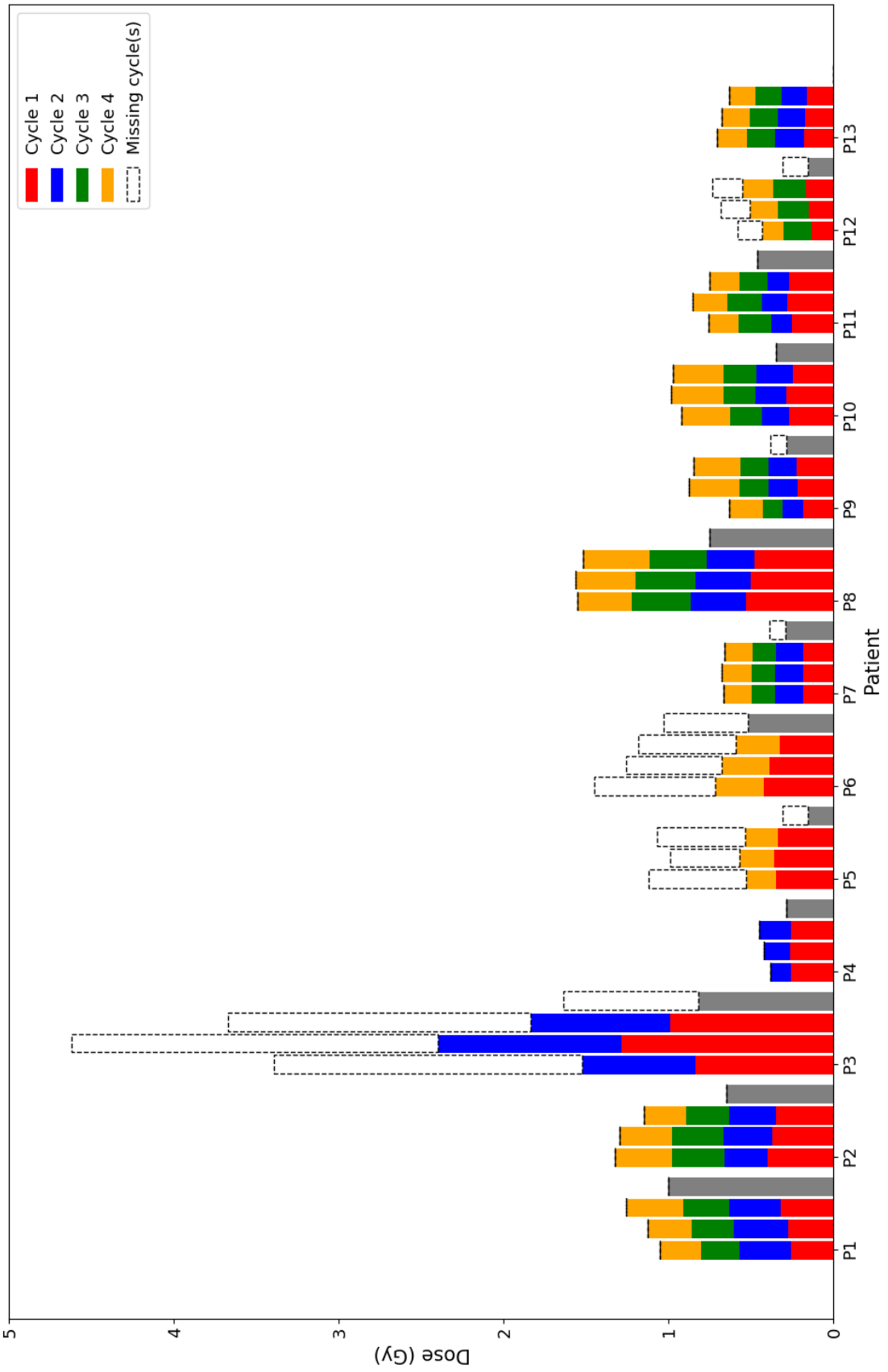

FIGURE 6.9 – Absorbed doses (Gy) estimated for 13 patients of the patient cohort, for three bone marrow VOI types (trabecular part of vertebrae from L2 to L4, from L1 to L5 and from T9 to L5) and, for humerus as a control. For patient 13, the arms are not in the field of view of any of the images.

Cette thèse est accessible à l'adresse : https://theses.insa-lyon.fr/publication/2023ISAL0068/these.pdf
© [L. Vergnaud], [2023], INSA Lyon, tous droits réservés

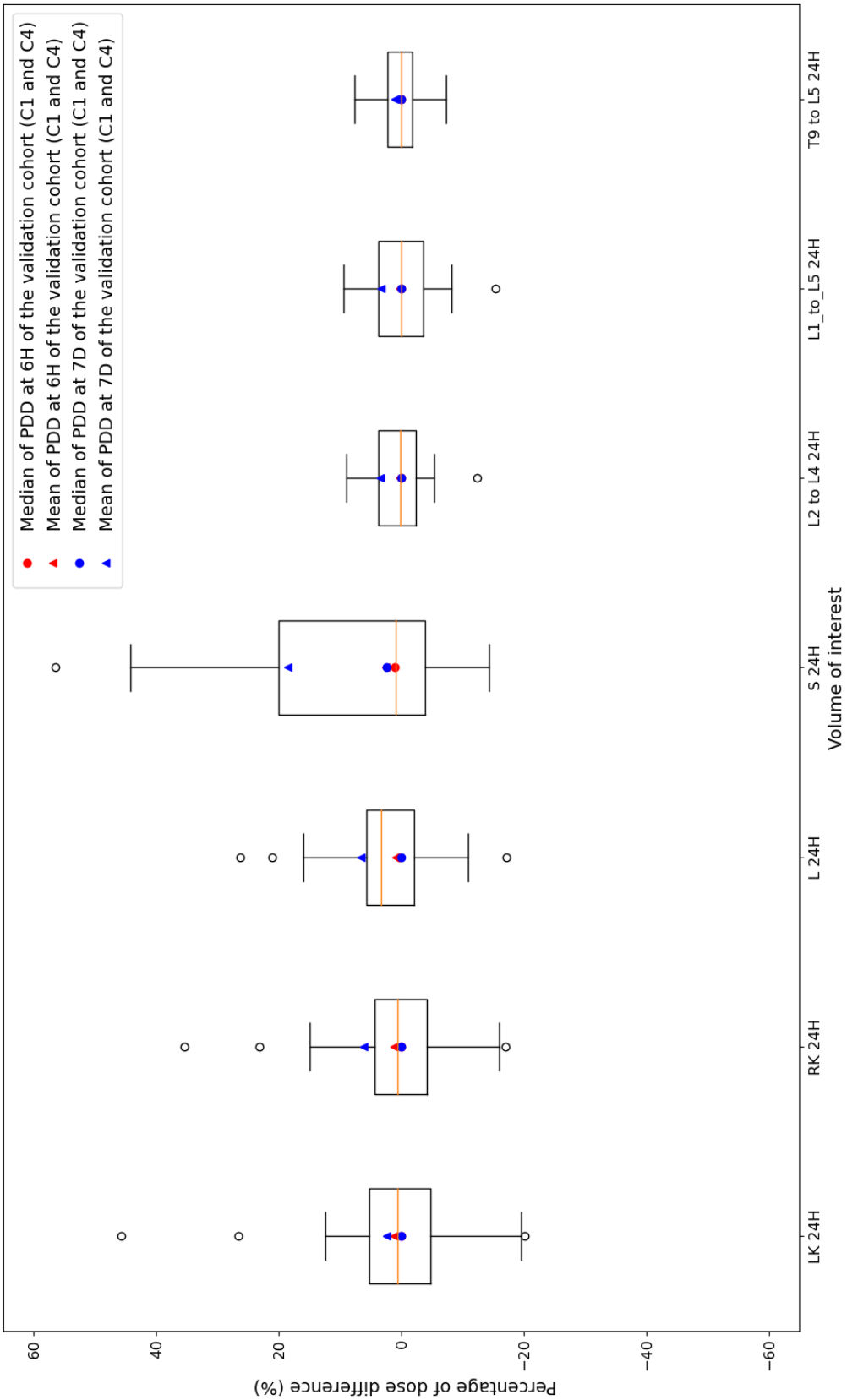

FIGURE 6.10 – Boxplots of percentages of dose difference (PDD) between absorbed doses estimated with the Missing Time-Point method (M1) at 24H and absorbed doses estimated with the reference method (tri-exponential function for fitting TDRC) for each VOI: LK, RK, L, S, L2 to L4, L1 to L5 and T9 to L5. Each boxplot includes PDD of the patient cohort at 24H (only cycles with three SPECT/CT acquisitions as shown in table 6.1) and PDD of the validation cohort at 24H of cycles 1 and 4. For the two other time-points (6H in red and 7D in blue), PDD are estimated from the validation cohort only (cycles 1 and 4) and the mean and the median are represented by triangles and circles respectively.

Cette thèse est accessible à l'adresse : https://theses.insa-lyon.fr/publication/2023ISAL0068/these.pdf
© [L. Vergnaud], [2023], INSA Lyon, tous droits réservés

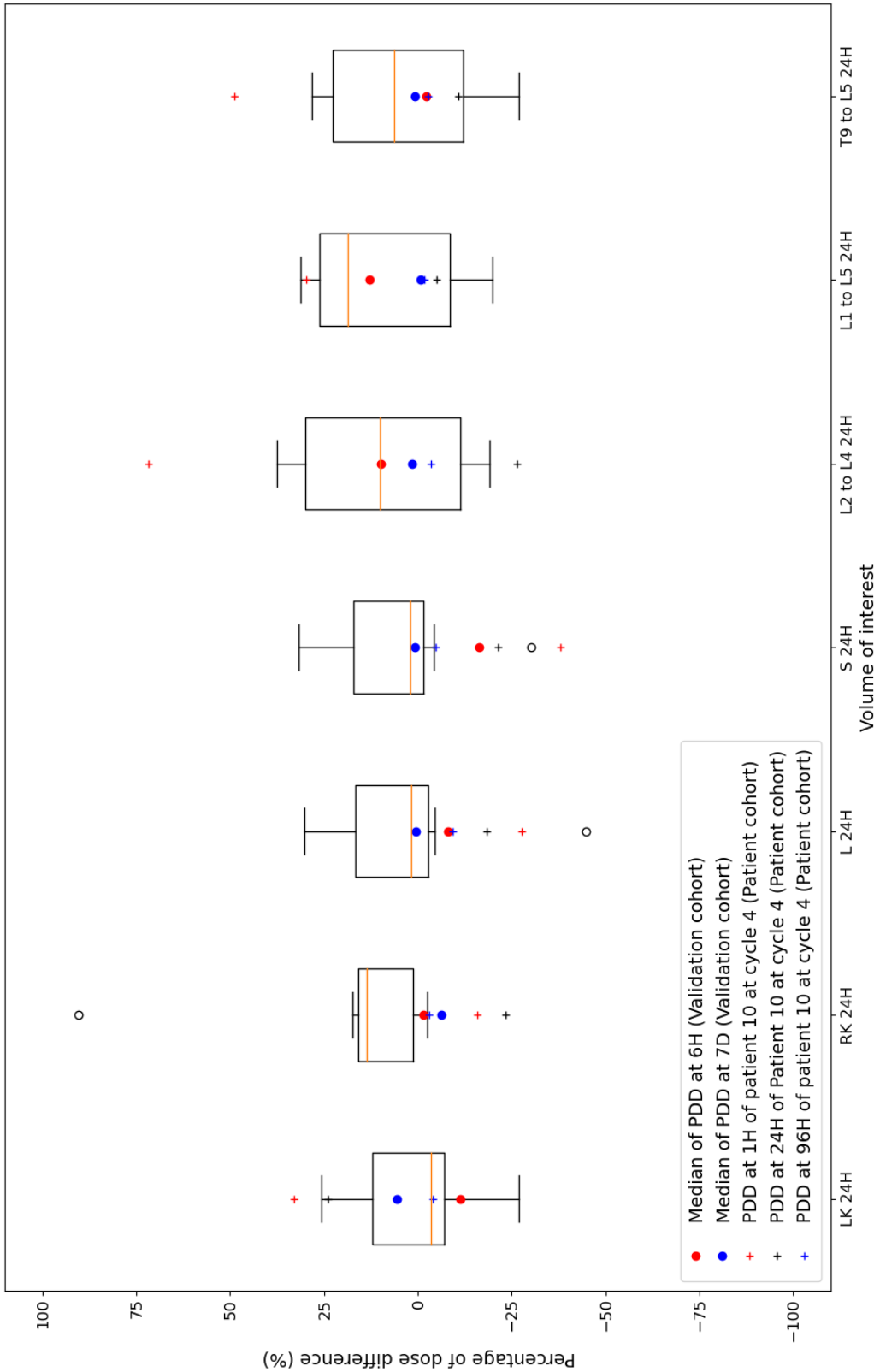

FIGURE 6.11 – Boxplots of percentages of dose difference (PDD) between absorbed doses estimated with the STP-Intra method (M2) at 24H and absorbed doses estimated with the reference method (tri-exponential function for fitting TDRC) for each VOI: LK, RK, L, S, L2 to L4, L1 to L5 and T9 to L5. Each boxplot includes PDD of the validation cohort at 24H of cycle 4 (TDRC of cycle 1 is used to estimate absorbed doses at cycle 4 from the acquisition at 24H). PDD are also calculated for the patient 10 of the patient cohort between cycles 3 and 4 (red, black and blue crosses for respectively 1H, 24H and 96H). For the two other time-points (6H in red and 7D in blue), PDD are estimated from the validation cohort only and medians of PDD are represented by circles.

Cette thèse est accessible à l'adresse : https://theses.insa-lyon.fr/publication/2023ISAL0068/these.pdf
© [L. Vergnaud], [2023], INSA Lyon, tous droits réservés

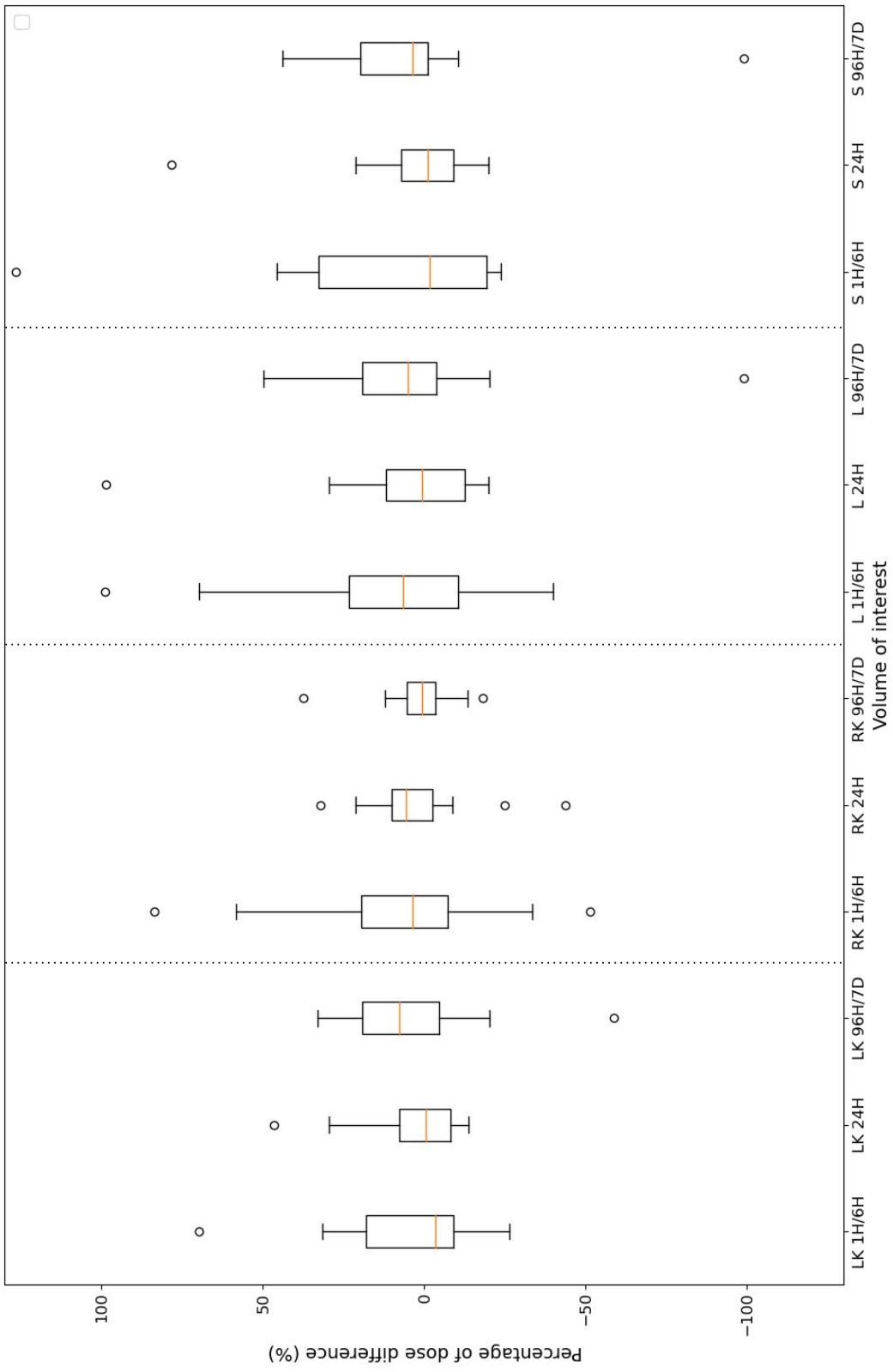

FIGURE 6.12 – Boxplots of the percentages of dose difference (PDD) between absorbed doses estimated with the STP-Inter method (M3) and with the reference method (tri-exponential function for fitting TDRC) for each time-point (1H/6H, 24H and 96H/7D) and for each VOI with a high uptake (LK in purple, RK in green, L in blue and S in red). Each boxplot includes PDD of the patient cohort at each time-point (only cycles with three SPECT/CT acquisitions as shown in table 6.1) and PDD of the validation cohort at each time-point of cycles 1 and 4.

Cette thèse est accessible à l'adresse : https://theses.insa-lyon.fr/publication/2023ISAL0068/these.pdf
© [L. Vergnaud], [2023], INSA Lyon, tous droits réservés

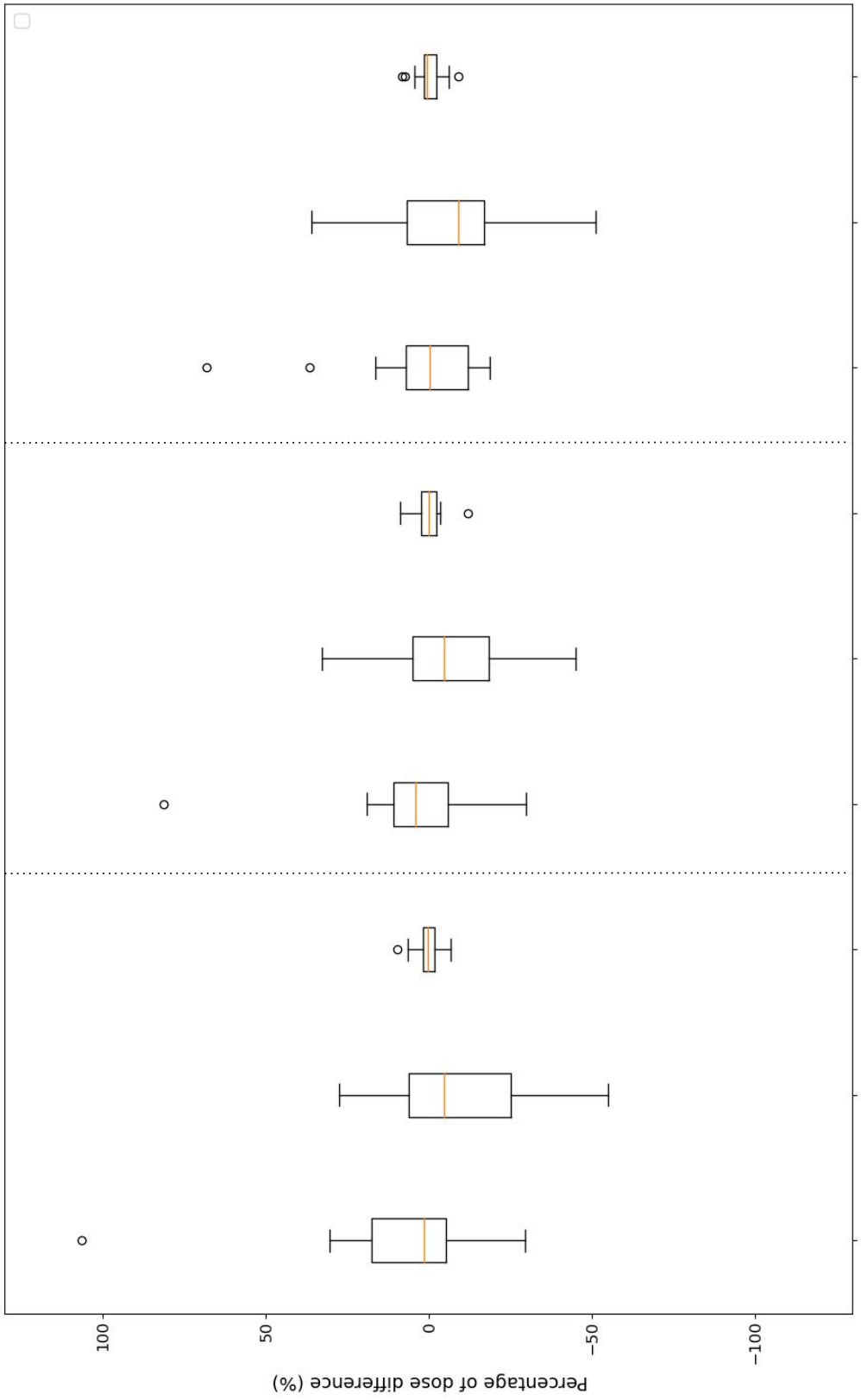

FIGURE 6.13 – Boxplots of the percentages of dose difference (PDD) between absorbed doses estimated with the STP-Inter method (M3) and with the reference method (tri-exponential function for fitting TDRC) for each time-point (1H/6H, 24H and 96H/7D) and for each surrogate of bone marrow (L2 to L4 in purple, L1 to L5 in green, T9 to L5 in blue). Each boxplot includes PDD of the patient cohort at each time-point (only cycles with three SPECT/CT acquisitions as shown in table 6.1) and PDD of the validation cohort at each time-point of cycles 1 and 4.

Cette thèse est accessible à l'adresse : https://theses.insa-lyon.fr/publication/2023ISAL0068/these.pdf
© [L. Vergnaud], [2023], INSA Lyon, tous droits réservés

6.4 Discussion

In this work, we proposed an image-based patient-specific dosimetric workflow adaptable to a limited number of SPECT time-points, e.g. three for the first cycle and a single one for the other cycles. It is based on tri-exponential fitting of Monte Carlo computed dose-rate images. It can be used in a clinical context and allows to perform dosimetry even if some acquisitions are missing.

Dosimetric workflow Several authors proposed methods to estimate absorbed doses from a low number of acquisitions (Willowson et al., 2018a; Madsen et al., 2019; Hänscheid et al., 2018; Zhao et al., 2019; Jackson et al., 2020a; Garske et al., 2012; Devasia et al., 2020) by using an approximation of time-integrated activity from mono-exponential model (Madsen et al., 2019; Hänscheid et al., 2018) or a bi-exponential model (Devasia et al., 2020) or by exploiting a priori information about pharmacokinetic properties (ex: pharmacokinetic parameters are homogeneous between patients). In this study, the tri-exponential model was chosen to take into account patients' physiology and seems to be better than the mono-exponential model (Guerriero et al., 2013). Delker et al. (Delker et al., 2015) proposed to not use early acquisitions in order to reduce the dose estimation error. In our case, the comparison of the estimated doses with a tri-exponential compared to mono-exponential function with acquisitions at 24H and 96H/144H shows that the dose difference is small ($< 3\%$) for kidney, liver and spleen but can be as high as 3000% if the ODR at 24H is less than or equal to the ODR at 96H/144H for bone marrow substitutes (low activity in these regions). An early acquisition is necessary to estimate the uptake phase which is very fast. During the 1H imaging session, the distribution in the patient may change rapidly compared to the acquisition time. However, the rotating acquisition of 15 min (one bed) tends to smooth out the activity and we did not observe large distribution changes between the first and the last projections of the sequence.

Moreover, dosimetry was performed with Monte Carlo simulations to take into account patients' images and cross-irradiation (Grimes and Celler, 2014; Finocchiaro et al., 2020). The cross-dose contribution is significant for bone marrow (Forrer et al., 2009a) and may be significant for kidneys if its self-absorbed dose is low or if the tumour burden is high (Sandström et al., 2018). It is the case of patient 5 presented in figure 6.14 who has a large isolated tumour that contributes more than 93% to the bone marrow dose, 2% and 50% to the left and right kidneys. The computational time was larger than analytical approaches (Local Deposition Method or DPK convolution), approximately 10 minutes of computation time on a conventional workstation for each acquisition. For low activity regions (such as vertebrae), 1 hour computation time (5×10^6 simulated primary decays on a single core) is necessary to reach less than 5% uncertainty in all VOI.

Dosimetry Inter-patient variability in the doses absorbed by each organ (figure 6.6) were high: coefficients of variations of cumulative absorbed doses were 38.4% for LK, 43.6% for RK, 70.9% for L and 38.3% for S (when patient 4 was excluded, two cycles only). This inter-patient variability can be partly explained by the proximity of lesions or organs with a high uptake (liver for the right kidney and spleen for the left kidney). For example, doses to the liver were 3.4 Gy for P2 and 34.3 Gy for P7 (all four cycles were taken into account) because the latter depicted intra-hepatic lesions. This variability illustrates the importance of performing personalized dosimetry to analyze treatment effects.

Cette thèse est accessible à l'adresse : https://theses.insa-lyon.fr/publication/2023ISAL0068/these.pdf
© [L. Vergnaud], [2023], INSA Lyon, tous droits réservés

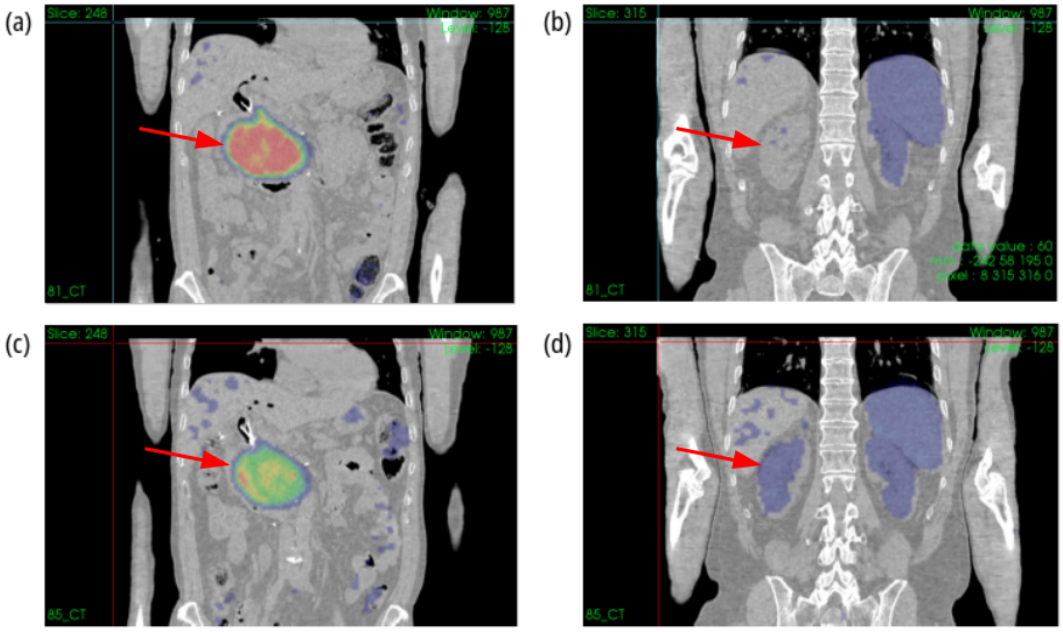

FIGURE 6.14 – SPECT images superimposed on CT scans for patient 5 of the patient cohort at cycles 1 (a and b) and 4 (c and d) showing the evolution of biodistribution of activity from one cycle to another at the lesion level (a and c) and at the right kidney level (b and d). The same color scale was used for all images.

The intra-patient inter-cycle variability is illustrated in figures 6.6 and 6.9. It was relatively low for organs with high uptake: coefficients of variation of doses per injected activity were inferior to 16% for 85% of patients for LK, RK and S and 77% of patients for L. However, this was not the case for bone marrow (61% for L2 to L4, 69% for L1 to L5 and for T9 to L5). Sundlöv et al., 2017 calculated biologically effective dose and also observed large inter-cycle variability in the kidneys for different patients. They supposed that these changes came from the blood pressure and degree of hydration (Sundlöv et al., 2017). In their study, medians of absorbed doses per activity injected were, for LK and RK, close to the ones found here (medians were 0.45 mGy/MBq and 0.47 mGy/MBq for LK and RK respectively). For patient 5, CV were higher for all VOI: between 17.6% and 68.5%. This variation is related to observed changes in the activity distribution between cycles 1 and 4: indeed, activity decreases in a large lesion and increases in the right kidney and the liver as shown in the figure 6.14.

For OAR, maximum tolerated dose (MTD) thresholds from EBRT have been considered: 23 Gy for kidneys and 2 Gy for bone marrow (Sandström et al., 2013). For kidneys, one patient (P8 with 19 Gy and 24 Gy for LK and RK respectively) exceeded the threshold if we consider missing cycles too, but no severe renal toxicity was observed. Sundlöv et al. (Sundlöv et al., 2017) chose different thresholds for patients with and without risk factors (27 Gy and 40 Gy, biologically effective dose) and they observed a moderate decline of renal function after treatment, some patients receiving up to 8 cycles of 7.4 GBq.

In order to estimate the absorbed doses by bone marrow, three VOI were delineated as surrogates instead of using blood samples or biopsy (Sgouros, 1993). The

Cette thèse est accessible à l'adresse : https://theses.insa-lyon.fr/publication/2023ISAL0068/these.pdf
© [L. Vergnaud], [2023], INSA Lyon, tous droits réservés

normality of the series of cumulative absorbed doses (only available cycles) was assessed with a Shapiro-Wilk test (p-value = 0.1038 for L2 to L4, p-value = 0.01875 for L1 to L5 and p-value = 0.07838 for T9 to L5). The difference observed between the series of accumulated absorbed doses of L2 to L4 and L1 to L5 was significant (Wilcoxon signed rank test: p-value = 0.02) which was not the case for the other comparisons (Wilcoxon signed rank test: p-value = 0.45 between L2 to L4 and T9 to L5 and p-value = 0.09 between L1 to L5 and T9 to L5). When comparing the three types of VOI, the cumulative absorbed doses were close (maximum difference: 0.2 Gy in absolute value) except for the patient 3 (maximum difference: 0.9 Gy in absolute value). In this study, patients did not have bone marrow lesions, but for patients who did, the dosimetry with BM substitutes would need to be changed. This is for example the case of patients treated with ^{177}Lu-PSMA. For patient 3, the absorbed doses have been evaluated over two cycles only and the 2 Gy limit was already almost reached. It is likely that the limit was reached with the two other cycles, but no significant toxicity was observed. In contrast, patient 10 shows grade 2 toxicity for platelets and for leukocytes and grade 3 toxicity for lymphocytes after cycle 2 while MTD was not reached which led to a halving of the injected activity.

Finally, doses in bone marrow surrogates were compared to the dose absorbed by the upper part of the humerus to assess that the dose estimates in the vertebrae were different than the activity in the blood. Cumulative absorbed doses (only cycles where humerus is visible) were significantly different for the three surrogates of bone marrow (Wilcoxon signed rank test: p-value = 0.0005 for L2 to L4, p-value = 0.0005 for L1 to L5 and p-value = 0.0005 for T9 to L5).

Evaluation of the uncertainties The proposed methods are based on tri-exponential fit and assumed that pharmacokinetics remains approximately the same from one cycle to another for the same patient. Calculations of variation coefficients were performed in the worst case (ODR of cycles 1 and 4 only for the validation cohort) and the medians of variation coefficients were limited at 15.4% at 24H (22.3% at 1H/6H and 34.7% at 96H/7D). The assumption seems to be globally verified, until there is no significant toxicity or a significant variation in the distribution of activity. For P5 of the patient cohort, the activity in the lesion decreased between cycles 1 and 4 in contrast to the activity in right kidney and liver: CV were respectively 68.5% and 47.9%. Overall, the impact on the percentage of dose difference (PDD) remains moderate: medians of PDD were inferior to 3.3% whatever the VOI and the time-point. As a conclusion, replacing the 24H dose-rate with the one of another cycle allowing tri-exponential fit seems a reasonable workaround. For cycles with one acquisition, two methods were proposed: STP-Intra (M2) method and STP-Inter method (M3). The lowest median errors were estimated when the acquisition takes place at 96H, 144H or 7D whatever the VOI with the STP-Intra method (M2). With the STP-Inter method (M3), it does not seem to be a preferred time-point unless one wishes to limit the error made in dose estimation at the bone marrow level in which case a late time-point should also be selected. This observation has also been made by other authors such as Rinscheid et al., 2020. However, delayed acquisitions (96H or 144H) may not always be possible, for example when patients live far from the hospital or due to logistical issues. For the STP-Intra method (M2) only, the errors made with 24H acquisition are smaller than those made at 1H for kidney, liver, spleen and bone marrow. The STP-Intra method (M2) was preferred to the STP-Inter method (M3) because if the patient's TDRC is not homogeneous with the TDRC of other patients then the error is likely to be large, as explained in Jackson et al., 2020a and Hänscheid and Lassmann, 2020. For example, for the P7 of the validation cohort, PDD

Cette thèse est accessible à l'adresse : https://theses.insa-lyon.fr/publication/2023ISAL0068/these.pdf
© [L. Vergnaud], [2023], INSA Lyon, tous droits réservés

of the liver for cycle 4 were equal to -9.8%, -1.0% and 1.1% for 6H, 24H and 7D with the STP-Intra method (M2) and -40.0%, -20.0% and 15.5% with the STP-Inter method (M3).

The proposed methods were evaluated for all VOI, including bone marrow, while other studies are mostly focused on kidneys only (Devasia et al., 2020; Madsen et al., 2019; Zhao et al., 2019; Willowson et al., 2018a) or does not include bone marrow (Jackson et al., 2020a; Garske et al., 2012; Hänscheid et al., 2018). For bone marrow, three surrogates VOI were assessed. The errors appear to be lower for T9 to L5 with the STP-Intra method (M2) whereas they are equivalent whatever the VOI with the STP-Inter method (M3). The variability of absorbed doses in bone marrow is higher with the STP-Intra method (M2) than with the STP-Inter method (M3) as illustrated in figures 6.11, 6.12 and 6.13. One hypothesis could be that this variability is linked to the volume delineation. Indeed, ODR corresponds to the mean of dose-rates in the VOI. If the delineation included voxels that are not actually in the volume and which have lower dose-rates than those in the VOI, the ODR will be impacted.

Limits and recommendations This workflow was assessed for twenty patients (thirteen in the patient cohort and seven in the validation cohort) treated with ^{177}Lu-DOTATATE. At cycle 1, TDRC were modeled with a tri-exponential function which was considered as reference. For other cycles, they were estimated from the TDRC of the first cycle by assuming a conservation of pharmacokinetics parameters. However, the preservation of the patient's physiology may not really be verified if an important toxicity occurs or if the distribution of activity in the patient changes significantly between cycles. It may therefore be interesting to add acquisitions in the event that toxicities occur. Errors committed with each method (Missing Time-Point M1, STP-Intra M2 and STP-Inter M3) depend on the chosen time-point: we recommend to select a late time-point in order to limit the error made in particular with the STP-Intra method (M2). However, in clinical practice, these time-points can be the most difficult to obtain because they require the patient to return to the hospital: that's why we continue to acquire a single SPECT/CT image at 24H despite the results. The STP-Inter method is an alternative method when the standard method (tri-exponential fitting or STP-Intra method M2) cannot be applied but it has two major disadvantages: it requires the TDRC of other patients to be available prior to dosimetry and errors committed are linked to the homogeneity of the patient and cohort TDRC. The STP-Intra method should be preferred as much as possible in order to limit the errors made.

6.5 Conclusion

This study proposes a patient-specific image-based dosimetric workflow applicable in clinic, based on adaptive tri-exponential fitting process of Monte Carlo computed dose-rate distributions at organ-level. It can be used for any VOI, including bone marrow, and have been applied to patients treated with ^{177}Lu-DOTATATE. The workflow adapts to a different number of SPECT/CT acquisitions per cycle in particular when acquisitions are missing, preserves the patient's physiology and automatically accounts for cross-irradiation caused by lesions of different shape, fixation and location. All methods are associated to an estimate of the error made.

Cette thèse est accessible à l'adresse : https://theses.insa-lyon.fr/publication/2023ISAL0068/these.pdf
© [L. Vergnaud], [2023], INSA Lyon, tous droits réservés

Chapter 7

Dosimetric impact of breathing movement

In this second chapter, we assessed the dosimetic impact of motion-compensated reconstruction in SIRT planning. This work was published in EJNMMI Physics in 2023 under the title "Dosimetric impact of 3D motion-compensated SPECT reconstruction for SIRT planning" (Vergnaud et al., 2023) and has been adapted in this chapter.

7.1 Previous published studies

Selective Internal Radiation Therapy (SIRT) is a local cancer treatment used for hepatocellular carcinoma (HCC) (Vilgrain et al., 2017), intrahepatic cholangiocarcinoma (ICC) and liver metastases (breast cancer (Barakat et al., 2022; Cheng et al., 2021), neuroendocrine tumours (King et al., 2008), uveal melanoma (Gonsalves et al., 2019), colorectal and pancreatic cancer (Helmberger et al., 2021)). It consists in injecting ^{90}Y-microspheres in the hepatic artery to deliver a high dose to the lesions. Before ^{90}Y delivering, a planning step is performed to plan the activity to be injected (Garin et al., 2021) and to evaluate potential risk of toxicities, such as radiation pneumonitis (Leung et al., 1995; Wright et al., 2012), following the recommendations provided in Levillain et al., 2021 and Salem et al., 2019. During this planning step, ^{99m}Tc macroaggregated albumin (MAA) is administered to the patient and the biodistribution, assumed to be the same as the microspheres (Knešaurek et al., 2018), is assessed from SPECT/CT images. However, these images are affected by several physical phenomena or limitations such as attenuation, scatter, resolution (Zeintl et al., 2010; Allred et al., 2018) and breathing movement that deteriorate the images. While the first three phenomena are routinely accounted for by reconstruction software, breathing motion is usually not corrected. Different methods have been proposed in the literature to retrieve and correct for breathing motion in SPECT images, e.g. using external breathing monitoring device (Beach et al., 2005), fluoroscopic images (Dietze et al., 2019; Dietze et al., 2021), or data-driven approaches (Sanders et al., 2016; Robert et al., 2021a). Motion correction was for example applied to myocardial perfusion (Kortelainen et al., 2019; Kovalski et al., 2007). However, to our knowledge, it is not used during SIRT although the liver movement due to breathing is well known (Brandner et al., 2006). Bastiaannet et al., 2017 and Lu et al., 2022 studied the dosimetric impact of breathing motion on numerical phantoms (physical phantoms in Santoro et al., 2022) and showed that it is the main undesirable effect for the quantification in radioembolisation. To our knowledge, this impact has only been evaluated by Santoro et al., 2022 on 12 SPECT patients images with a single

Cette thèse est accessible à l'adresse : https://theses.insa-lyon.fr/publication/2023ISAL0068/these.pdf
© [L. Vergnaud], [2023], INSA Lyon, tous droits réservés

liver lesion, which is not representative of all patients treated by SIRT. Such an evaluation was performed on post-treatment PET imaging (Osborne et al., 2018) and has shown dose differences in the lesions and in the liver (Ausland et al., 2018).

In this work, we assessed on real patient images the dosimetric impact of breathing movement during SIRT treatment planning thanks to an innovative data-driven motion-compensated method that does not require any additional material during SPECT acquisition. Absorbed dose comparisons were performed between 3D and 3D motion-compensated reconstructions (Robert et al., 2021a) for several regions of interest. Prescribed activities and lung shunt fractions computed with the two methods were also compared.

7.2 Material and methods

7.2.1 Patient

Data from 29 patients (14 women and 15 men) treated by radioembolisation between March 2019 and July 2021 were included. Eighteen patients from this cohort were also included in the study by Robert et al., 2021a. The patient numbers common to both studies have been bolded in Table 7.1. During treatment planning, patients received 243 ± 92 MBq of ^{99m}Tc − MAA and a total of 31 SPECT/CT were available (two patients received two treatment sessions). Ten patients were treated for hepatocellular carcinoma (HCC), three for cholangiocarcinoma, four for metastasis of colorectal cancer (mCRC), seven for metastasis of breast cancer and five for hepatic metastasis of other cancers. Resin spheres (Sirtex™) were administered to eleven patients and glass spheres (TheraSphere™) to 18 patients. No distinction was made between patients in this study. More details are available in the table 7.1. The patient data included in this study comply with current regulations for human protection and GDPR regulations (MR004).

Cette thèse est accessible à l'adresse : https://theses.insa-lyon.fr/publication/2023ISAL0068/these.pdf
© [L. Vergnaud], [2023], INSA Lyon, tous droits réservés

Patient number	Patient sex	Type of spheres	Strategy of treatment	SPECT number delineated	Number of lesion(s)	Volumes (mL)
1	M	Glass	HCC / Lobectomy	1	1	30.89
2	F	Glass	mCRC / Bilobar	2	NA	NA
3	F	Resin	HCC / Lobectomy	3	NA	NA
4	F	Glass	MBC / Lobectomy	4	NA	NA
5	F	Glass	mCRC / Lobectomy	5	NA	NA
6	F	Resin	mCRC / Lobectomy	6	NA	NA
7	M	Glass	HCC / Lobectomy	7	1	54.89
8	M	Glass	MBC / Lobectomy	8	NA	NA
9	F	Glass	MBC / Lobectomy	9	1	176
10	F	Glass	MBC / Lobectomy	10	5	35.54 / 7.004 / 11.56 / 6.331
11	F	Resin	MBC / Lobectomy	11	1	63.74
12	F	Resin	MBC / Lobectomy	12	NA	NA
13	M	Glass	HCC / Lobectomy	13	3	436.6 / 44.83 / 432.5 (nodules)
14	M	Glass	MLC / Lobectomy	14	NA	NA
15	M	Glass	ICC / Lobectomy	15	1	228.6
16	**M**	**Resin**	**HCC / Lobectomy**	16	1	278
				17	NA	NA
17	**M**	**Glass**	**ICC / Lobectomy**	18	1	223
				19	NA	NA
18	F	Resin	MLC / Lobectomy	20	1	3.444
19	M	Resin	HCC / Lobectomy	21	1	428.7
20	M	Resin	HCC / Lobectomy	22	2	105.2 / 23.35
21	M	Glass	HCC / Lobectomy	23	NA	NA
22	F	Glass	mCRC / Lobectomy	24	1	14.15
23	M	Glass	M / Lobectomy	25	1	1828
24	F	Resin	MBC / Lobectomy	26	1	213.9
25	M	Resin	HCC / Lobectomy	27	1	37.01
26	M	Glass	HCC / Lobectomy	28	2	12.99 / 225.8
27	F	Glass	MPC / Lobectomy	29	4	121.4 / 106.6 / 92.65 / 46.76
28	F	Resin	MNT / Lobectomy	30	1	106.1
29	M	Glass	ICC / Lobectomy	31	2	13.94 / 19.38

TABLE 7.1 – Characteristics (Sex, Type of sphere, Number of lesions, their volumes and strategy of treatment) of patients included in this study. MBC: Metastasis of Breast Cancer, MLC: Metastasis of Lung Cancer, M: Metastasis, MPC: Metastasis of Pancreatic Cancer, Metastatsis of Neuroendocrine tumours, HCC: hepatocellular carcinoma, mCRC: colorectal cancer metastases, ICC: intrahepatic cholangiocarcinoma

Cette thèse est accessible à l'adresse : https://theses.insa-lyon.fr/publication/2023ISAL0068/these.pdf
© [L. Vergnaud], [2023], INSA Lyon, tous droits réservés

7.2.2 Image acquisition

SPECT/CT images were acquired with a two heads GE Discovery NM CT 670, using LEHR (Low Energy High Resolution) collimator and 3/8" thick crystal. The acquisition consisted of 60 projections over 360°, each with 128 × 128 pixels, 4.418 mm isotropic spacing, 25 s duration for each projection, in step and shoot mode. Energy windows were centered on 140.5 keV ± 20% width for primary, and 120 keV ± 5% for scatter.

7.2.3 Reconstruction

Images were reconstructed with two methods: conventional ordered subset expectation maximization (OSEM), denoted 3D, and motion-compensated OSEM, denoted 3Dcomp (Robert et al., 2021a). In both cases, OSEM was performed with attenuation correction, dual energy window scatter correction and depth-dependent PSF correction (resolution recovery). The 3Dcomp method first consisted in extracting a breathing motion signal from the list mode data thanks to Laplacian Eigenmaps analysis. This signal was then split into 8 respiratory phases and the acquired projections were sorted according to the phase to which they belong. 2D affine registrations were performed between each phase and the phase selected for the reconstruction. Affine transformations were applied to the list mode data to correct the projections. The final 3D motion-compensated image was obtained by OSEM reconstruction from all motion-corrected list-mode data. 3Dcomp reconstruction can be performed on any respiratory phases. For attenuation correction, a single 3D CT acquisition was available and it was assumed that locally the CT was acquired during one of the phases of the respiratory movement. Reconstruction was hence performed on this corresponding phase, which has been visually determined from 4D SPECT gated reconstruction (Robert et al., 2021b) (except for the estimation of the breathing motion amplitude). Note that, as shown in Robert et al., 2021a, motion compensated reconstruction leads to better image quality than 4D gated reconstruction (Robert et al., 2021b) because it uses all list-mode data and does not increase noise compared to 3D. All reconstructions (3D and 3Dcomp) were performed with 15 subsets and 15 iterations per subsets. Images were reconstructed with 128^3 voxel grid, with spacing of 4.41806 mm. All reconstructions were performed with the RTK software (Rit et al., 2014). No spatial filters were applied in post-reconstruction.

7.2.4 Volumes of interest

In order to estimate the activity of ^{90}Y to be injected to the patient, it is necessary to estimate the average doses that will be absorbed by different VOIs. Indeed, international guidelines set tolerance limits for absorbed doses depending on the type of spheres used (glass or resin), the patient's pathology and the treatment strategy (Table 7.1) (Weber et al., 2022; Levillain et al., 2021). In this study, seven volumes of interest (VOI) were delineated for each patient. For liver, lungs and tumour(s), manual delineations were performed on CT scans. Note that in 50% of cases, the upper quarter of the lungs is not in the field of view (15/31). The healthy liver (HL) was obtained by removing the lesions from the whole liver. The perfused liver (PL) was estimated by intersecting the volume obtained by thresholding the SPECT image with 5% of the maximum number of liver counts with the CT volume of liver. The hepatic reserve (HR) corresponded to the liver minus the perfused volume and lesions. The healthy perfused liver (HPL) was the perfused liver minus lesions (Garin

Cette thèse est accessible à l'adresse : https://theses.insa-lyon.fr/publication/2023ISAL0068/these.pdf
© [L. Vergnaud], [2023], INSA Lyon, tous droits réservés

et al., 2020). When liver and lungs VOIs overlapped, voxels in common were assigned to the liver and removed from the lungs. If a patient has several distinct lesions, all are contoured.An example is given in Figure 7.1.

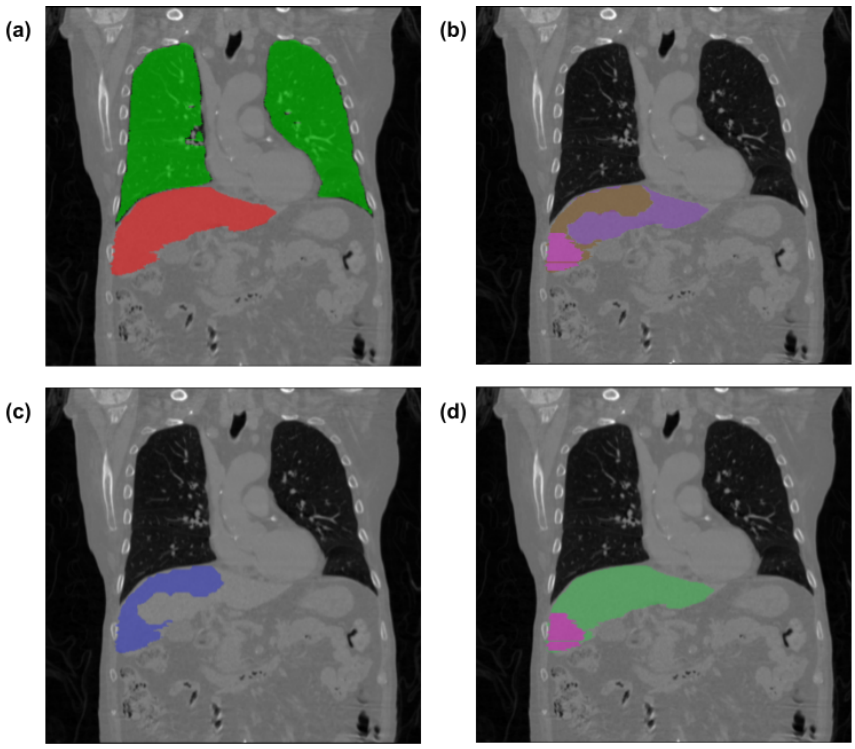

FIGURE 7.1 – Example of VOIs delineated for the patient 7. (a) liver (red) and lungs (green), (b) HPL (brown), HR (purple) and tumour (pink), (c) PLV (green) and (d) HL and tumour.

7.2.5 Breathing motion amplitude estimation

A local rigid (translation only) registration of the liver VOI was performed between inhale and exhale phases 3Dcomp reconstructions. Registrations were performed with Mutual Information as similarity measure and done with Elastix (Klein et al., 2010). The breathing motion amplitude was defined as the norm of the obtained 3D translation.

7.2.6 Dosimetric workflow

A dosimetry workflow based on Monte Carlo simulations was adapted from Vergnaud et al., 2022 to estimate the average absorbed doses for all VOI from 3D and 3Dcomp reconstructions. All steps are described in Figure 7.2. ^{99m}Tc SPECT images were normalized according to the injected activity by considering all detected counts in the liver and lungs VOIs. Monte Carlo simulations were performed via GATE (Sarrut et al., 2021) with 1 MBq of ^{90}Y during 1s, then scaled according to the activity really injected. CT images were resampled to the same voxel size as the SPECT in order to reduce the simulation time. For each SPECT, a 3D dose-rate map was obtained and the mean of dose-rates was computed for each VOI. The final absorbed dose per VOI was estimated by considering mono-exponential decay, with ^{90}Y half-life of 64h. Statistical uncertainties of the Monte Carlo simulations were

Cette thèse est accessible à l'adresse : https://theses.insa-lyon.fr/publication/2023ISAL0068/these.pdf
© [L. Vergnaud], [2023], INSA Lyon, tous droits réservés

lower than 1% in all ROIs, and computation times were around 10 min (Vergnaud et al., 2022).

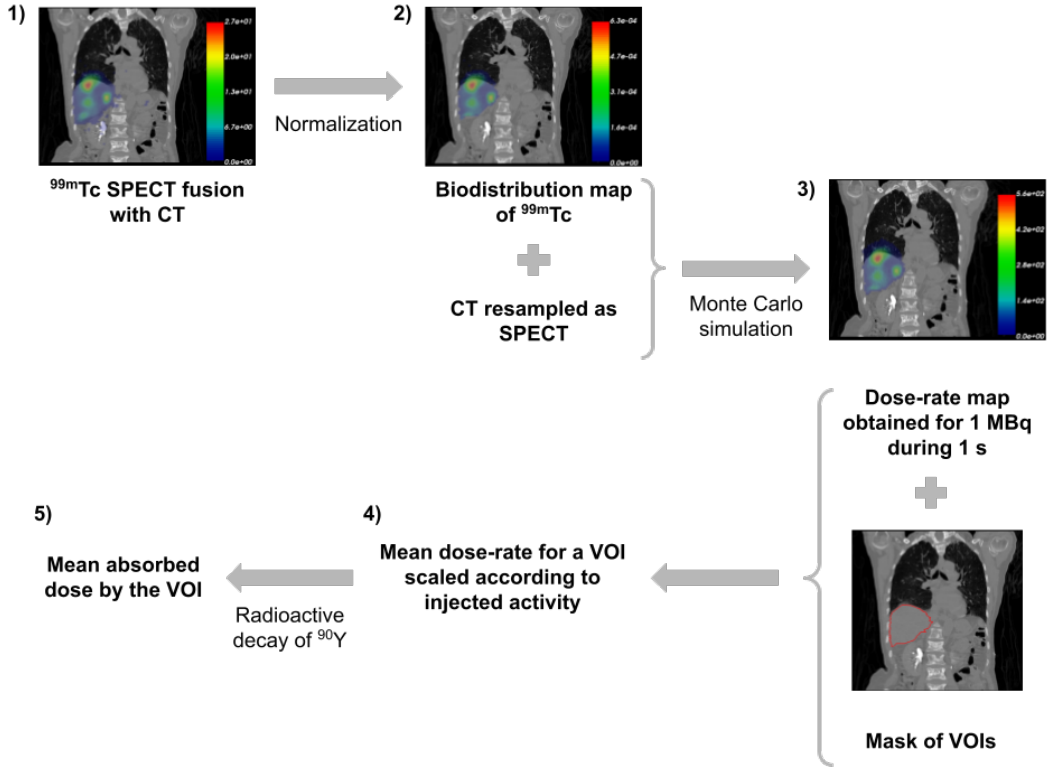

FIGURE 7.2 – Scheme of the dosimetric workflow used to estimated absorbed doses by the VOIs in radioembolisation.

7.2.7 Analysis

7.2.7.1 Percentages of dose difference (PDD)

To compare the estimated absorbed doses for each reconstruction, percentages of dose difference (PDD) were computed for each VOI as expressed in equation (7.1) with D_{3D} and D_{3Dcomp} the average absorbed doses estimated with the 3D and the 3D compensated reconstructions respectively.

$$PDD[\%] = \frac{(D_{3Dcomp}[\text{Gy}] - D_{3D}[\text{Gy}]) \times 100}{D_{3D}[\text{Gy}]} \tag{7.1}$$

Doses absorbed by the lungs were estimated by Monte Carlo simulations for each patient and lung shunt fractions (LSF) were calculated from equation 7.2 where C_{Lungs} is the number of reconstructed counts in the lungs and C_{Liver} is the number of reconstructed counts in the liver.

$$LSF(\%) = \frac{C_{Lungs}}{C_{Lungs} + C_{Liver}} \times 100 \tag{7.2}$$

Cette thèse est accessible à l'adresse : https://theses.insa-lyon.fr/publication/2023ISAL0068/these.pdf
© [L. Vergnaud], [2023], INSA Lyon, tous droits réservés

7.2.7.2 TN ratio

Tumour-to-normal ratios (TN ratio) were obtained from the equation (7.3) where C_T and C_{HL} are the number of counts detected in all tumours and healthy liver respectively. V_T and V_{HL} are volumes of all tumours and healthy liver, respectively. The densities of the tumours and the healthy liver are assumed to be the same, allowing us to use volumes instead of masses.

$$TN = \frac{C_T / V_T}{C_{HL} / V_{HL}} \tag{7.3}$$

7.2.7.3 Activity to be prescribed

The estimation of activity to be prescribed was based on absorbed doses calculated for each reconstruction considering the absorbed dose recommendations defined in the international guidelines according the type of sphere (Weber et al., 2022; Levillain et al., 2021). The percentage difference in activity (PDA) was computed for each patient between the 3D and 3Dcomp reconstructions as in equation (7.1) and was not affected by the choice of the value of prescribed dose.

7.2.7.4 Impact of overlapped contours

When contouring the liver and lung VOIs, some voxels may overlap. In order to verify the dosimetric impact of assigning voxels to one or the other of the two volumes, we estimated the difference in absorbed dose (DAD) between these two choices for the two available reconstructions using equation 7.4.

$$DAD(VOI) = DVLiver(VOI) - DVLungs(VOI) \tag{7.4}$$

Where $DVLiver(VOI)$ is the absorbed dose estimated for the VOI when the overlapping voxels are assigned to the liver and $DVLungs(VOI)$ when they are assigned to the lungs.

7.2.7.5 Statistical assessment

Normality tests of the distribution over all patients of absorbed dose and activity distributions were estimated for each reconstruction and assessed with a Shapiro-Wilk test before being compared either with a paired Wilcoxon's test or with a paired t-test (3D vs 3Dcomp). These tests were also applied to compare lung dose and TN ratios with two reconstructions.

7.2.7.6 Correlations

In order to predict for which patient this respiratory motion correction would be really relevant, Spearman's correlation test was applied between PDD of tumours and seven different parameters described next. The first parameter was the volume (1) of the tumour estimated from the CT. For the next two parameters, a distance map was calculated between the tumour and the borders of the liver. The minimum (2) and average (3) distance could be estimated. The other four parameters were: (4) the minimum distance between the top of the tumour and the liver in the craniocaudal (CC) direction (Santoro et al., 2022), (5) the amplitude of tumour movement in the CC direction, (6) the overall minimum distance between the center of mass

Cette thèse est accessible à l'adresse : https://theses.insa-lyon.fr/publication/2023ISAL0068/these.pdf
© [L. Vergnaud], [2023], INSA Lyon, tous droits réservés

of the tumour and the liver, and (7) this same distance but only in the CC direction. Correlations were also tested on these parameters divided by the volume as proposed in Kruis et al., 2013.

7.3 Results

The mean amplitude of the movement of the liver was 9.5 ± 2.7mm (range: 3.4-16.8mm) and that of the tumours was 10.9 ± 2.4mm (range: 5.6-17.1mm). If we consider only the amplitudes of liver movement associated with tumour contours, considering as many times the amplitude as there are lesions, the average amplitude of the liver was 10.8 ± 2.4mm. No statistical significant differences were observed between the amplitude of the liver and the amplitude of the tumours (two-sided paired t-test p-value = 0.474). Figure 7.3 illustrates, for one patient, the 3D and 3Dcomp reconstructed images with associated contours of the tumour, showing the impact of breathing motion.

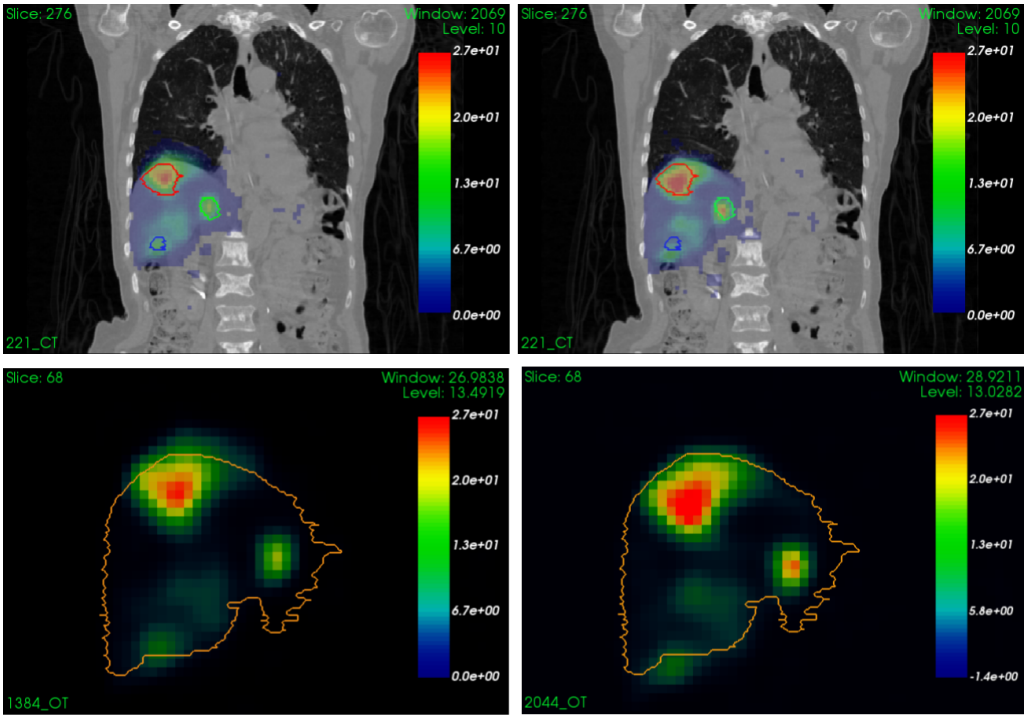

FIGURE 7.3 – 3D (left) and 3Dcomp (right) reconstructions overlapped on CT (top) and reconstructions alone. Red, green and blue contours correspond to lesion contours initially drawn on the CT image. Orange contour is the mask of the liver.

Figure 7.4 shows the percentages of dose difference between absorbed doses estimated from 3D and 3Dcomp reconstructions for each VOI (liver, lungs, tumour(s), PL, HR, HPL and HL). 3D and 3Dcomp absorbed dose series of lungs, PL, HR, HPL did not follow a normal distribution (Shapiro-Wilk's test, $p<0.05$), while liver, HL and tumours did (only the 3D absorbed dose serie). Statistically, the averages of the differences between series were not significantly different from zero (Wilcoxon's test $p>0.05$ for lungs, PL, HR, HPL and tumours; Student's test $p>0.05$ for liver and HL). Median, IQR, minimum and maximum values for PDD of lesions were -0.25%, [-3.3%,1.1%], -29.0% and 23.9%.

Cette thèse est accessible à l'adresse : https://theses.insa-lyon.fr/publication/2023ISAL0068/these.pdf
© [L. Vergnaud], [2023], INSA Lyon, tous droits réservés

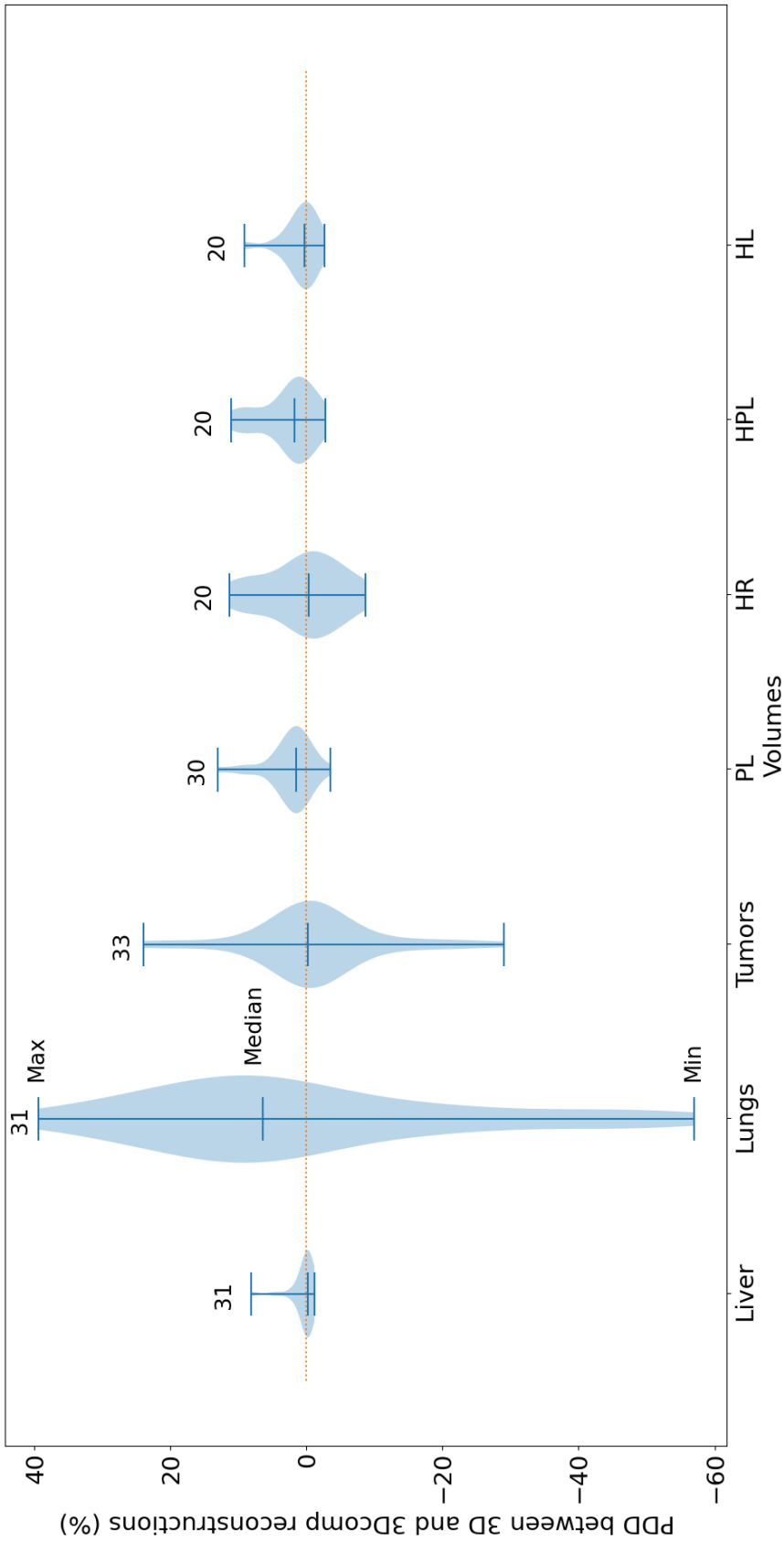

FIGURE 7.4 – Boxplots of percentages of dose difference (PDD) between 3D and 3Dcomp reconstructions for each VOI (Liver, Lungs, tumours, PL, HR, HL, HPL). The number of contours used is written above each boxplot.

Cette thèse est accessible à l'adresse : https://theses.insa-lyon.fr/publication/2023ISAL0068/these.pdf
© [L. Vergnaud], [2023], INSA Lyon, tous droits réservés

Figure 7.5, 7.8 and 7.9 show Bland-Altman plots between the 3D and 3Dcomp reconstructions of lung dose, LSF and TN ratio respectively. Bland-Altman plots for the absorbed doses to the left (Figure 7.6) and right (Figure 7.7) lungs are also available.

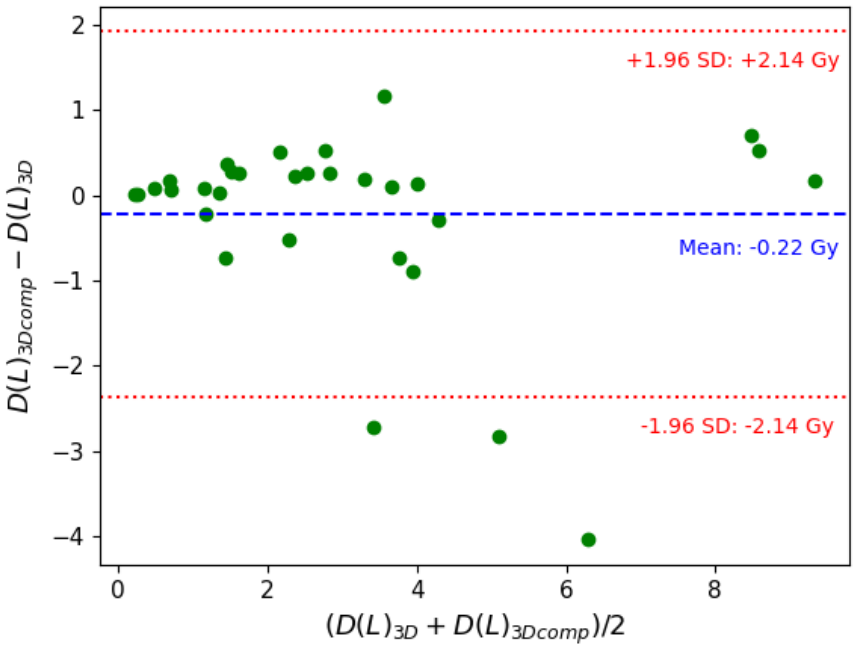

FIGURE 7.5 – Bland-Altman plot of the lung dose (Gy) between 3D and 3Dcomp reconstructions for each patient. $D(L)_{3D}$ and $D(L)_{3Dcomp}$ correspond to the lung dose estimated from the 3D and 3Dcomp reconstructions respectively.

None of the series of differences and means follow a normal distribution: the limits of agreement are therefore given for information only. For lungs and tumours, the limits of agreements in the Bland-Altman plots were 2 Gy and 38 Gy. The data is available in Table 7.2. The mean, minimum and maximum doses estimated from the 3D reconstruction were 1.2 Gy, 0.06 Gy and 5.8 Gy for the left lung and 4.7 Gy, 0.2 Gy and 14.3 Gy for the right lung. There was no statistically significant difference for each lung with and without correction for respiratory motion (Wilcoxon's test: p-value > 0.05). No statistically significant correlation was found between the left and right lungs.

Cette thèse est accessible à l'adresse : https://theses.insa-lyon.fr/publication/2023ISAL0068/these.pdf
© [L. Vergnaud], [2023], INSA Lyon, tous droits réservés

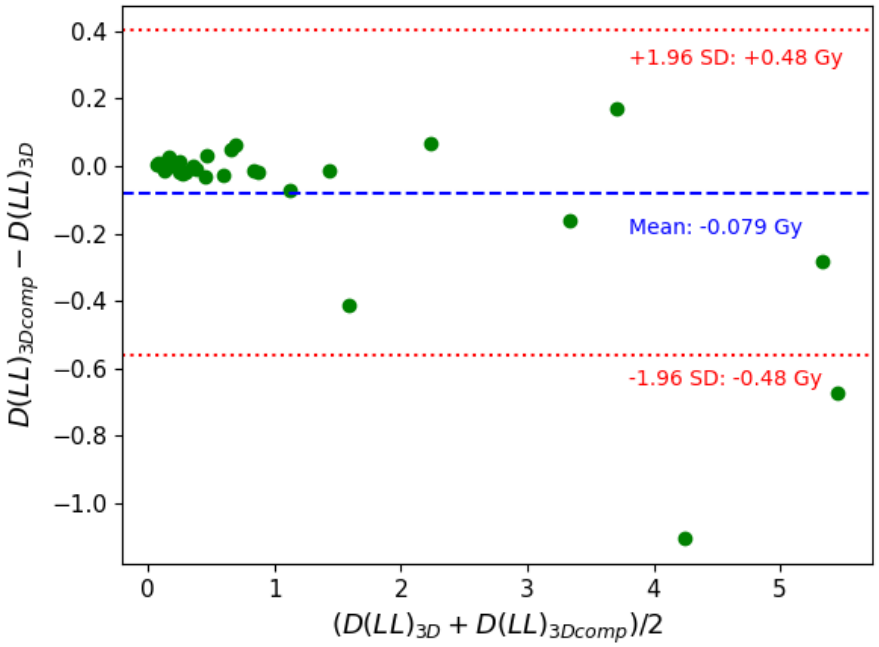

FIGURE 7.6 – Bland-Altman plot of the left lung dose (Gy) between 3D and 3Dcomp reconstructions for each patient. $D(LL)_{3D}$ and $D(LL)_{3Dcomp}$ correspond to the left lung dose estimated from the 3D and 3Dcomp reconstructions respectively.

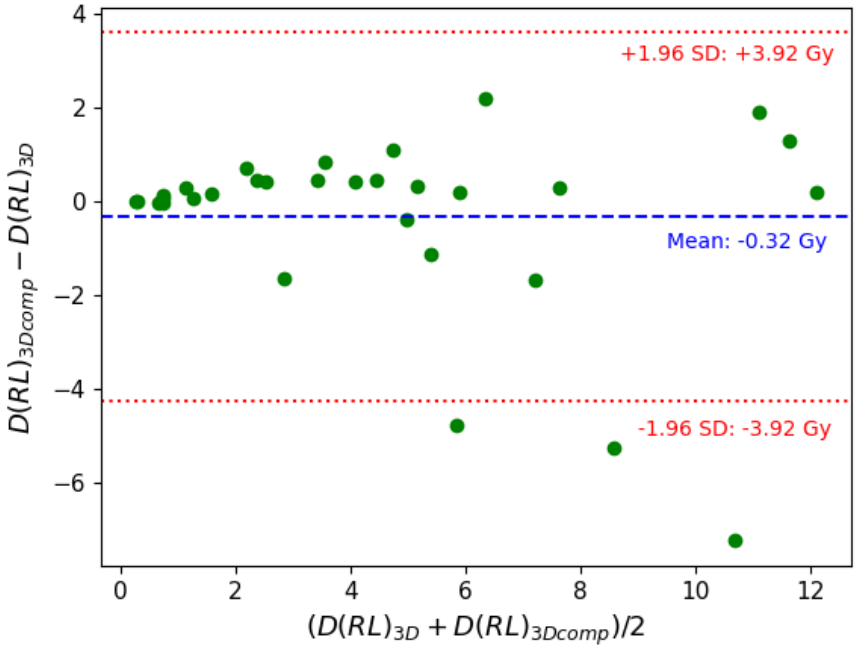

FIGURE 7.7 – Bland-Altman plot of the right lung dose (Gy) between 3D and 3Dcomp reconstructions for each patient. $D(RL)_{3D}$ and $D(RL)_{3Dcomp}$ correspond to the right lung dose estimated from the 3D and 3Dcomp reconstructions respectively.

Cette thèse est accessible à l'adresse : https://theses.insa-lyon.fr/publication/2023ISAL0068/these.pdf
© [L. Vergnaud], [2023], INSA Lyon, tous droits réservés

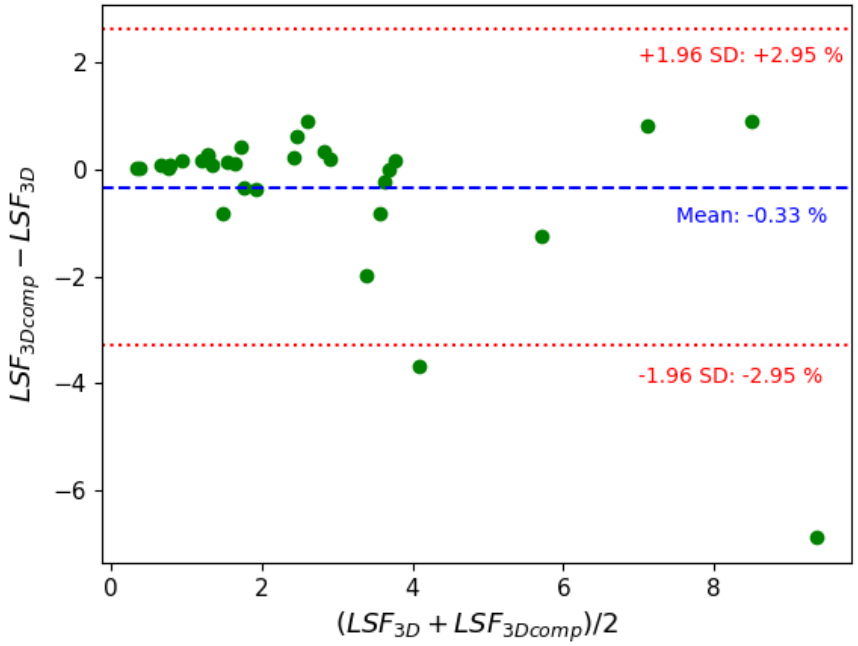

FIGURE 7.8 – Bland-Altman plot of the LSF (%) between 3D and 3Dcomp reconstructions for each patient. LSF_{3D} and LSF_{3Dcomp} correspond to the LSF estimated from the 3D and 3Dcomp reconstructions respectively.

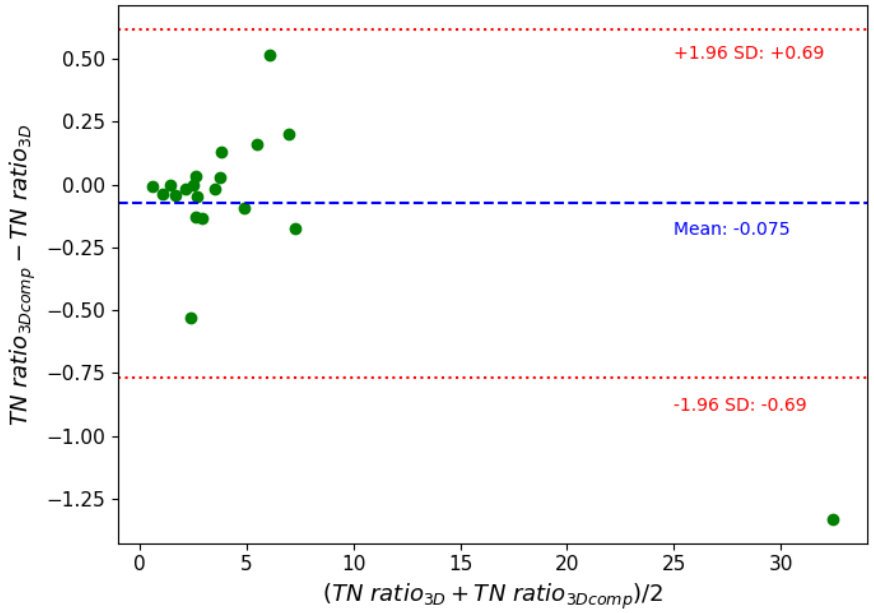

FIGURE 7.9 – Bland-Altman plot of the tumour-to-normal liver ratio between 3D and 3Dcomp reconstructions for patients for whom lesion contours are available. $TN\ ratio_{3D}$ and $TN\ ratio_{3Dcomp}$ correspond to the TN ratio estimated from the 3D and 3Dcomp reconstructions respectively.

Cette thèse est accessible à l'adresse : https://theses.insa-lyon.fr/publication/2023ISAL0068/these.pdf
© [L. Vergnaud], [2023], INSA Lyon, tous droits réservés

Number of Patients	Lungs Dose Gy (3D)	Lungs Dose Gy (3Dcomp)	PDD of lungs (%)	tumour Dose Gy (3D)	tumour Dose Gy (3Dcomp)	PDD of tumour (%)
1	9.2	9.4	1.9	179.3	180.4	0.6
				245.0	242.4	-1.1
2	4.4	4.1	-6.4	NA	NA	NA
3	1.3	1.1	-17.2	NA	NA	NA
4	1.3	1.4	2.6	NA	NA	NA
5	1.5	1.7	17.4	NA	NA	NA
6	1.1	1.2	8.4	NA	NA	NA
7	2.2	2.5	10.3	331.4	354.0	6.8
8	2.5	3.0	21.2	NA	NA	NA
9	0.3	0.3	4.0	186.2	184.4	-1.0
				229.3	284.1	23.9
				147.8	166.1	12.4
10	8.3	4.3	-48.6	91.5	71.5	-21.8
				175.6	155.0	-11.7
				118.7	84.2	-29.0
11	0.7	0.7	9.7	76.0	73.1	-3.7
12	4.8	2.1	-56.9	NA	NA	NA
				49.3	49.9	1.2
13	3.6	3.7	2.9	103.2	109.5	6.1
				105.1	104.8	-0.3
14	0.6	0.8	28.2	NA	NA	NA
15	3.0	4.2	39.4	170.6	164.5	-3.6
16	1.4	1.7	20.1	148.4	148.6	0.2
16	0.4	0.5	17.2	NA	NA	NA
17	4.1	3.4	-17.7	49.0	48.1	-1.9
17	3.2	3.4	6.0	NA	NA	NA
18	4.4	3.5	-20.3	88.4	72.0	-18.6
19	8.1	8.8	8.8	190.3	186.7	-1.8
20	1.3	1.6	29.8	73.2	69.4	-5.1
				116.1	116.1	-0.02
21	0.2	0.2	6.8	NA	NA	NA
22	2.4	2.7	11.0	182.0	183.2	0.7
23	8.3	8.9	6.4	41.3	40.8	-1.2
24	3.9	4.1	3.7	173.3	175.3	1.2
25	1.8	1.1	-41.1	157.4	158.9	0.9
26	6.5	3.7	-43.3	297.5	354.8	19.2
				258.6	258.4	-0.1
				12.5	11.1	-11.3
27	2.7	3.0	10.0	114.1	111.0	-2.7
				49.2	49.9	1.5
				166.1	164.1	-1.2
28	2.5	2.0	-20.4	76.4	73.9	-3.3
29	1.9	2.4	26.2	152.7	154.4	1.1
				116.4	116.4	-0.01

TABLE 7.2 – Table of estimated absorbed doses to lungs and tumours from 3D and 3Dcomp reconstructions. For each patient and volume, the PDDs were also calculated. NA: tumour contours are not available

Cette thèse est accessible à l'adresse : https://theses.insa-lyon.fr/publication/2023ISAL0068/these.pdf
© [L. Vergnaud], [2023], INSA Lyon, tous droits réservés

Figures 7.10 and 7.11 represent percentages of tumour dose difference between 3D and 3Dcomp with respect to the tumour volume and amplitude of the movement of the tumours. The estimation of tumour motion was only performed for 32/33 because one of them had a too small volume which did not allow the registration between the two reconstructions and therefore the calculation of the amplitude of motion. In Figure 7.10, one of the volumes was very large (1828 cm^3) compared to the others and made it difficult to read the figure: this point was therefore removed for better readability.

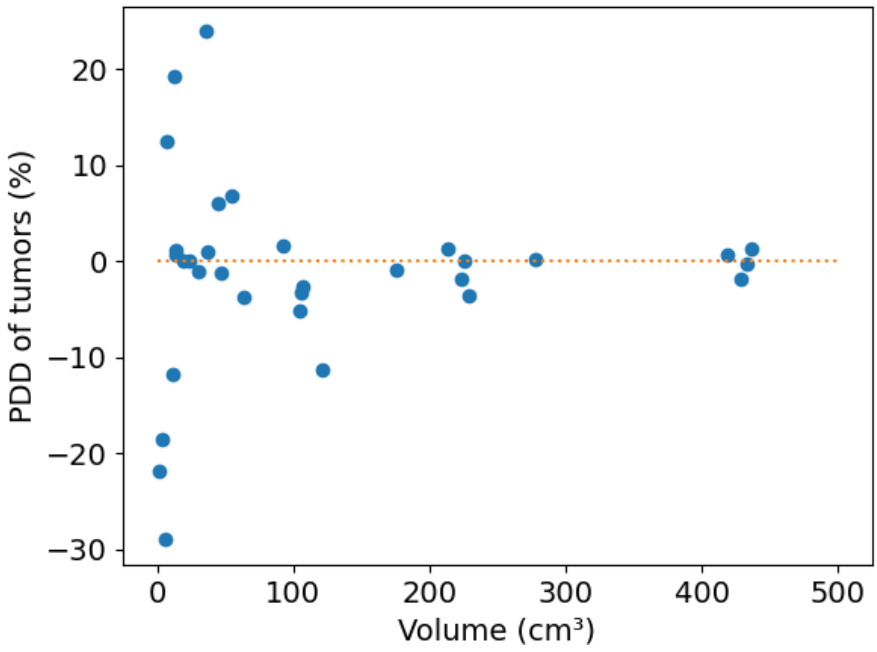

FIGURE 7.10 – Percentages of tumour dose difference between 3D and 3Dcomp reconstructions by tumour volume.

For lungs, DAD(Lungs) were superior to 1 Gy for only one patient for the two types of reconstruction. This discrepancy can be explained by the location of a lesion in the hepatic dome, at the border with the lungs, whose absorbed dose was estimated at 229 Gy.

For the liver, there was less than 5% of DAD(Liver) whatever the type of the reconstruction because the dose absorbed by the liver was much higher than that of the lungs (on average 3 Gy vs 46 Gy).

More details are provided in Table 7.3.

Finally, we compared the planned injected activities with both reconstructions (Table 7.4). The mean and standard deviation of the absolute value of PDA were 3.1 ± 5.1 % between prescribed activities obtained from 3D and 3Dcomp. The maximum absolute difference was 22.8 % (1.28 GBq for 3D reconstruction vs 1.57 GBq for 3Dcomp reconstruction) and was obtained for patient 20. Series of injected activities (3D and 3Dcomp) did not follow a normal distribution (Shapiro-Wilk's test, $p<0.05$). The average of the differences between prescribed activities was not significantly different from zero ($p>0.05$ with the Wilcoxon's test).

Only two moderate statistically significant correlations (figure 7.12) could be found between PDD of tumours and: 1. the minimum distance in CC direction between the upper part of the lesion and the hepatic dome (corr=-0.38;$p<0.05$) and

Cette thèse est accessible à l'adresse : https://theses.insa-lyon.fr/publication/2023ISAL0068/these.pdf
© [L. Vergnaud], [2023], INSA Lyon, tous droits réservés

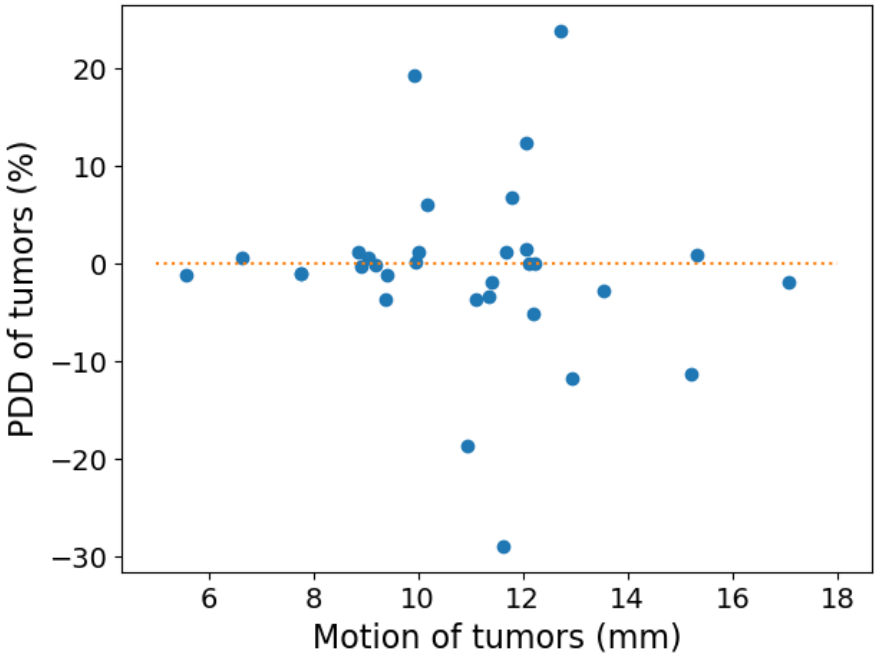

FIGURE 7.11 – Percentages of tumour dose difference between 3D and 3Dcomp reconstructions with respect to the amplitude of the movement.

		3D reconstruction	3Dcomp reconstruction
DAD(Lungs)	Minimum	-0.0032 Gy	-0.00019 Gy
	1^{st} quartile	5.4e^{-6} Gy	8.3e^{-6} Gy
	Median	0.0036 Gy	0.0024 Gy
	Mean	0.13 Gy	0.15 Gy
	3^{rd} quartile	0.11 Gy	0.15 Gy
	Maximum	1.2 Gy	1.1 Gy
DAD(Liver)	Minimum	-0.77 Gy	-2.9 Gy
	1^{st} quartile	-0.19 Gy	0 Gy
	Median	0.021 Gy	0.0032 Gy
	Mean	0.16 Gy	-0.034 Gy
	3^{rd} quartile	0.19	0.12 Gy
	Maximum	1.8 Gy	0.48 Gy

TABLE 7.3 – DAD calculated for the liver and the lungs for the two reconstructions (3D and 3Dcomp). For each, the minimum, 1^{st} quartile, median, mean, 3^{rd} quartile and maximum DAD are given.

2. the minimum distance of the centre of mass of the lesion in the CC direction and the hepatic dome (corr=-0.38;$p<0.05$).

Cette thèse est accessible à l'adresse : https://theses.insa-lyon.fr/publication/2023ISAL0068/these.pdf
© [L. Vergnaud], [2023], INSA Lyon, tous droits réservés

Number of patient	Activity in GBq (3D)	Activity in GBq (3Dcomp)	Recommended dose tolerance limit reached	Relative difference between 3D and 3Dcomp (%)
1	4.263	4.298	Normal liver dose	0.8
7	2.470	2.538	Normal liver dose	2.8
9	13.651	13.051	Normal liver dose	-4.4
10	1.632	1.496	Normal liver dose	-8.3
11	1.312	1.362	tumour dose	3.8
13	6.604	6.582	Normal liver dose	-0.3
15	3.525	3.553	Normal liver dose	0.8
16	2.907	2.907	Normal perfused liver dose	0
17	4.510	4.495	Normal liver dose	-0.3
18	1.280	1.572	tumour dose	22.8
19	2.514	2.530	Normal perfused liver dose	0.6
20	2.324	2.450	tumour dose	5.4
22	1.202	1.219	Normal liver dose	1.4
23	5.077	5.076	Normal liver dose	0.0
24	5.793	5.907	Normal liver dose	2.0
25	1.227	1.194	Normal perfused liver dose	-2.7
26	4.694	4.560	Normal liver dose	-2.9
27	4.251	4.262	Normal liver dose	0.3
28	3.459	3.419	Normal liver dose	-1.2
29	2.354	2.372	Normal liver dose	0.8

TABLE 7.4 – Activites to be prescribed for each patient and each reconstruction (3D and 3Dcomp) estimated from international recommendations (Weber et al., 2022; Levillain et al., 2021). The relative difference of dose was also computed. The criterion corresponded to the limit that led to the choice of this activity to prescribe.

Cette thèse est accessible à l'adresse : https://theses.insa-lyon.fr/publication/2023ISAL0068/these.pdf
© [L. Vergnaud], [2023], INSA Lyon, tous droits réservés

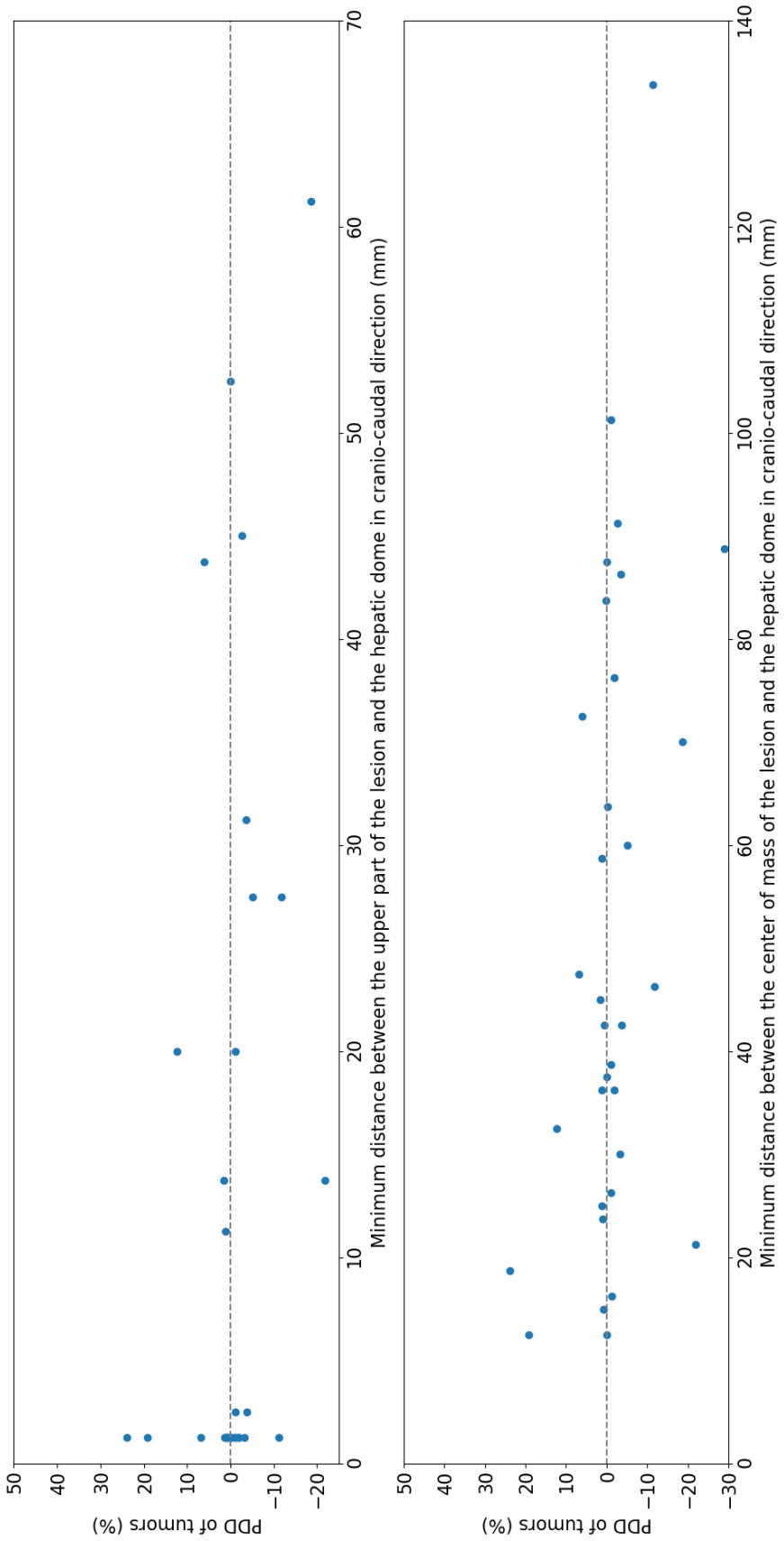

FIGURE 7.12 – Percentages of tumour dose difference according to the minimum distance between the upper part of the lesion and the hepatic dome in cranio-caudal direction (top) and the minimum distance between the center of mass of the lesion and the hepatic dome in carnio-caudal direction (bottom).

Cette thèse est accessible à l'adresse : https://theses.insa-lyon.fr/publication/2023ISAL0068/these.pdf
© [L. Vergnaud], [2023], INSA Lyon, tous droits réservés

7.4 Discussion

This paper presents the evaluation of the dosimetric impact of respiratory movement during SIRT planning. We worked on real patient data with different characteristics (number of tumours, volumes, localisations, pathologies, type of spheres) representative of the diversity of what is found in the clinic. For each, we compared the estimated doses from the 3D and 3Dcomp reconstructions as well as the TN ratio and the activity to be injected.

Few studies have been published on the subject. In Bastiaannet et al., 2017 and Lu et al., 2022, the authors evaluated dosimetric impacts of motion by performing simulations from digital XCAT phantoms with different sets of parameters (body type, Lung Shunt Fraction (LSF), tumour volume and localisation). Likewise, Santoro et al., 2022 tested a novel method to compensate for motion on a modified CIRS dynamic phantom, and applied it on the data of twelve selected patients (HCC, single lesion). However, the realism of simulations and phantoms is limited (perfect respiratory cycle and simplifications in the movement, characteristics of each patient, assumption of a perfectly compensated scatter (Lu et al., 2022)). In contrast to our method based on list mode data, Santoro et al., 2022 corrected for respiratory motion by realigning the barycentres of the lesions in the projections with each other before realigning them on the CT to improve attenuation correction and VOI definitions (Lu et al., 2021). The latter registration consisted to have the same distance between the hepatic dome defined on the CT and the top of the lesion on two imaging modalities (SPECT and CT). However, lesion contours were obtained by thresholding on projections, themselves impacted by the respiratory movement (15 s/projection vs 5 s for one respiratory cycle): they are dependent on the distribution of the detected counts and influence the registration with the CT. Here, a 4D gated reconstruction was performed to select the phase that most visually matches the CT to avoid the impact of the breathing movement. Then, a 3Dcomp reconstruction was performed to take into account all detected counts. We assumed that CT acquisition is fast enough (10-15 seconds in total) to correspond locally to a respiratory phase (in the region of the hepatic dome), considering that the residual motion during the CT acquisition is low. The exact impact of this assumption is currently unknown. 3Dcomp reconstruction using other breathing phases is feasible but they will be marred by errors because of a mismatched CT, as also observed in Lu et al., 2021. In both studies, VOI (liver, lungs and tumours) were delineated on CT to obtain anatomical contours independent of the distribution of the radiopharmaceutical. Although some of the patients included in the Robert et al., 2021a study are also included in this one, the results are not comparable. Firstly, the tumours are not segmented in the same way (CT vs. thresholding) and the compensation of the respiratory movement was only carried out on the end-expiratory phase in their study, unlike ours.

The median PDD was close to zero for all VOI considered except for the lungs (6.4%). The estimated absorbed doses to the lungs are overall higher with 3Dcomp reconstruction than with 3D reconstruction. Lu et al., 2021 proposed an explanation of over- and under-estimation: counts in the liver that border on the lungs can be reconstructed in the lungs and not in the liver. Similarly, counts in the lungs can be reconstructed outside the lungs. Some CT images can also have motion artifacts which can be taken into account when contouring the liver (segmented livers have a larger volume than real liver volumes): this could explain the low impact of motion

Cette thèse est accessible à l'adresse : https://theses.insa-lyon.fr/publication/2023ISAL0068/these.pdf
© [L. Vergnaud], [2023], INSA Lyon, tous droits réservés

on the lung doses despite the movement of the liver. This is equivalent to taking an extra margin around the liver (Allred et al., 2018; Kao et al., 2014) to account for respiratory motion. There was no statistically significant difference for lung doses between the two reconstructions (same for LSF) which is in agreement with the results of Bastiaannet et al., 2017 for the LSF. However, Lu et al., 2022 showed that the LSF was overestimated when the respiratory motion was not corrected. The lesions considered are only located in segments V, VI and VIII of the liver unlike ours and in particular at the level of the hepatic dome where larger dose differences are expected. Moreover, the ranges of motion used in the simulations are higher than those estimated for our patients: between 1 and 2 cm vs 0.9 cm in the cranio-caudal direction and between 0.6 and 1.2 cm vs 0.4 cm in the antero-posterior direction that could also explain differences in conclusions. There was no significant difference in the TN ratio between the two reconstructions in contrast to other authors who found an underestimation of the TN ratio in the absence of respiratory motion correction (Bastiaannet et al., 2017; Lu et al., 2022). In the article by Bastiaannet et al., 2017, the lesions have a volume of less than 35 mL, in contrast to those of our patients (between 1.7 mL and 1828 mL). The volume seems to have an impact on the error made in the absence of correction of the respiratory movement (figure 7.10): the smaller the volume, the greater the error (Lu et al., 2022; Ausland et al., 2018). For this type of system, the central spatial resolution without scatter for ^{99m}Tc at 10 cm with a LEHR collimator is 7.4 mm (Peters et al., 2019). This implies that the partial volume effect can be particularly impactful for volumes whose dimensions are less than 2.5 times the spatial resolution, i.e. 3.3 mL. The majority of the lesions studied have a larger volume: the partial volume effect alone does not explain the dose differences observed between 3D and 3Dcomp for small volumes. The tumours had very diverse characteristics among patients, for example in terms of volume and shape. These are likely explanations for the discrepancies observed for the TN ratio. Other studies, focused on the breathing motion impact in post-treatment (Ausland et al., 2018; Osborne et al., 2018) (mathematical models and patient data), also showed that the doses to the lesions were underestimated. On patient cohort, Santoro et al., 2022 compared mean absorbed doses of lungs and tumours and showed a variability of $\pm$ 4 Gy and $\pm$ 50 Gy respectively which is consistent with our results ($\pm$ 2 Gy and $\pm$ 38 Gy). The impact of respiratory movement on the activity to be prescribed does not appear to have been studied previously.

In this study, no significant average of differences was found between the estimated activities with each reconstruction ([min: -8.3% ; median: 0.4% ; max: 22.8%]). Only two significant moderate correlations ($p<0.05$) were found between the PDD of tumours and: (1) the minimum distance between the upper part of tumour and the liver in the CC direction and (2) the minimal distance between the centre of mass of the lesion and the liver in the CC direction. Globally, the means of the differences between 3D and 3Dcomp reconstructions for the absorbed doses and in particular the lungs, the TN ratios and the prescribed activities are not statistically significantly different from zero. However, for some patients, absolute lung dose differences between 1 Gy and 4 Gy (4/31) were observed, which could change the management of patients in cases where the lung dose is close to the recommended dose tolerance limit. In this study, all patients had a low pulmonary shunt (maximum 3D lung dose: 9.2 Gy) compared to the recommended limits, so that management was not impacted by the correction of respiratory motion. For example, for patient 10, there is a factor of two between the estimated lung doses between the 3D and 3Dcomp

Cette thèse est accessible à l'adresse : https://theses.insa-lyon.fr/publication/2023ISAL0068/these.pdf
© [L. Vergnaud], [2023], INSA Lyon, tous droits réservés

reconstructions (8 Gy vs 4 Gy). Note that in this study, when liver and lung voxels overlapped, they were assigned to the liver. We assessed the dose difference if voxels were assigned to the liver or lungs and observed small dose differences compared to the doses in the VOIs (maximum absolute value for liver: 2.9 Gy and 1.2 Gy for lungs) with the exception of one patient for lungs. We chose to assign the voxels to the liver in order to avoid overestimating the absorbed dose to the lungs in cases where tumours are located in the liver dome. In addition, Robert et al., 2021a showed that the recovery activity was better estimated with the 3Dcomp than with the 3D and 4D gated reconstructions. We still, therefore, consider relevant to apply a correction for respiratory movement in order to improve quantification.

The CT acquisition is a limitation of this work. Indeed, it has a preponderant role in the quantification because it influences the attenuation correction but also the accuracy of the VOI if the CT and the SPECT are not correctly aligned. Here, only a CT acquired in free breathing was available. We therefore assumed that locally (upper part of the liver), the CT was acquired in a single phase in order to perform a 3Dcomp reconstruction. The selection of the phase was done visually using the CT and there may be uncertainty even though double validation has been done. However, a quantitative approach such as choosing the phase with the highest number of counts in the segmented lung mask on CT may be very sensitive to the segmentation and low number of counts in this region. In this case, the choice of criterion needs to be robust. Ideally, a 4D CT should be acquired because, in some cases, respiratory motion can create artifacts in the 3D CT. If this acquisition is not possible, we recommend acquiring breath-hold CT in order to perform the 3Dcomp reconstruction at the same respiratory phase.

A second limitation was the limited number of patients included. Indeed, patients' data were heterogeneous (shape and volumes of tumours, pathologies, number of tumours) which makes it more difficult to establish with certainty the presence or absence of correlations. A larger scale study could answer this question by grouping patients according to their characteristics. Segmentations of tumours were not available for all patients therefore the number data available depends on VOI: only 20 treatments out of 31 were considered to compute PDD of tumours, HL, HPL and HR contrary to liver, lungs and PL where all treatments were taken into account. Finally, multiple injection sites were required to treat some patients: in this case, we performed the calculations assuming that they had received a single overall injection.

A third limitation of this study was the relationship between the biodistribution of ^{99m}Tc-MAA and ^{90}Y microspheres. Indeed, several authors reported a good correlation of doses to tumours in the case of HCC but have shown a weaker correlation in the case of metastatic disease (Jadoul et al., 2020; Garin et al., 2016). Similarly, the positioning of the catheter between the pre-treatment and treatment stages may influence the agreement of the predicted and measured doses (Thomas et al., 2020). The differences between 3D and 3Dcomp dosimetry were not compared to the dosimetric differences obtained between ^{99m}Tc and ^{90}Y as this was not the focus of this study but it is a point that would be of interest later.

Cette thèse est accessible à l'adresse : https://theses.insa-lyon.fr/publication/2023ISAL0068/these.pdf
© [L. Vergnaud], [2023], INSA Lyon, tous droits réservés

7.5 Conclusions and perspectives

In this study, we demonstrated the feasibility of correcting respiratory motion on real pre-treatment SPECT images for radioembolisation. The method does not need additional external devices or acquisition changes. We have shown that this correction impacts the absorbed dose to the lungs (the median percentage dose difference between 3Dcomp and 3D was 6.4% for lungs) which could impact the management of some patients in cases where the dose is close to the recommended dose tolerance limit. This correction also affects the tumour dose, where the largest dose differences were estimated for the smallest lesions.

Cette thèse est accessible à l'adresse : https://theses.insa-lyon.fr/publication/2023ISAL0068/these.pdf
© [L. Vergnaud], [2023], INSA Lyon, tous droits réservés

Cette thèse est accessible à l'adresse : https://theses.insa-lyon.fr/publication/2023ISAL0068/these.pdf
© [L. Vergnaud], [2023], INSA Lyon, tous droits réservés

Chapter 8

Feasability of ^{177}Lu quantification with a 360° CZT gamma camera

This chapter is an adaptation of the article "Performances study of a 360° CZT camera for monitoring ^{177}Lu treatments" currently submitted (summer 2023) in EJNMMI Physics.

8.1 Introduction

Radiopharmaceutical therapy (RPT) targeting the prostate-specific membrane antigen (PSMA) (Miyahira and Soule, 2022), labelled with lutetium-177 (^{177}Lu-PSMA) in patients with metastatic castration-resistant prostate cancer (mCRPC) has shown remarkable responses in several clinical studies (Ahmadzadehfar et al., 2016; Kratochwil et al., 2016b; Hofman et al., 2021; Rahbar et al., 2017; Sartor et al., 2021) and is now clinically proposed to eligible patients in an increasing number of nuclear medicine departments worldwide. However, the therapeutic window, i.e. the response to treatment without adverse effects, depends on several factors including patient-specific organ function, tracer pharmacokinetics and tumor uptake, implying the need for treatment monitoring. The European Association of Nuclear Medicine (EANM) has recently provided general guidelines to ensure good practice standards to follow for this treatment (Kratochwil et al., 2019). In particular, the implementation of individualised dosimetry according to the European Directive 2013/59/Euratom is mentioned. This stage involves calculating the absorbed dose in tumours and healthy organs for each treated patient.

SPECT imaging is currently the only source of information for estimating absorbed dose after a patient's therapeutic administration. Quantification can be performed with 2D planar scintigraphy (Paganelli et al., 2020; Zhang et al., 2019; Yadav et al., 2017) or from 3D reconstructed images (Violet et al., 2019; Vergnaud et al., 2022), the latter showing better accuracy (Rosar et al., 2021). More details about absorbed dose estimation from 3D SPECT images maybe found in Ljungberg et al., 2016 and Sjögreen Gleisner et al., 2022.

However, SPECT/CT acquisition is time consuming. With a conventional Anger gamma camera, a whole-body SPECT examination (about 5 $\times$ 40 cm bed positions (BP) for a patient measuring 170-180 cm) takes around 12 to 30 minutes per BP, therefore around 60 to 150 minutes overall, depending upon the acquisition parameters (Beauregard et al., 2011; Santoro et al., 2018; Sundlöv et al., 2018; Ilan et al., 2015). Such long acquisition times are problematic for patients in pain and have consequences on the availability of medical staff and camera scheduling. Thus scan acquisition time has been an impediment to routine clinical implementation of ^{177}Lu treatment monitoring.

Cette thèse est accessible à l'adresse : https://theses.insa-lyon.fr/publication/2023ISAL0068/these.pdf
© [L. Vergnaud], [2023], INSA Lyon, tous droits réservés

More recently, Cadmium-Zinc-Telluride (CZT) detector SPECT/CT cameras have been available. The advantages of direct digital conversion with CZT detectors compared to conventional Anger-based analog technology have been reported (Takahashi et al., 2013; Ito et al., 2021; Ritt, 2022; Vaz et al., 2020). Instead of converting incident gamma photons into visible light photons and then into electrical signals using photomultiplier tubes, CZT technology enables direct photon energy conversion, thus improving detection efficiency, energy resolution and spatial resolution, and therefore enabling reduced acquisition times. However, Ritt, 2022 recently reminded that these enhancements cannot be attributed to CZT detectors alone, but are also due to additional improvements, including adapted collimation and pixelated detectors.

Among the commercially available CZT-based SPECT and SPECT/CT systems (D-SPECT and Discovery NM 530c for myocardial applications; Discovery NM/CT 670 or 870 CZT and StarGuide (Song et al., 2023) for other applications), the VERITON-CT camera (Spectrum Dynamics Medical) is composed of twelve mobile CZT detector heads covering 360°. Detectors can be rotated and moved independently to be as close as possible to the patient's surface contour to increase the solid angle and thus improve photon collection efficiency, as described by Goshen et al., 2018. These features enable significant time reductions for whole-body SPECT image acquisition compared to conventional gamma-cameras. Consequently, it facilitates the opportunity for clinical implementation of ^{177}Lu treatment dosimetry. Recent studies evaluating VERITON performances have been conducted for various clinical procedures with ^{99m}Tc radionuclides. Indeed, Bordonne et al., 2020 compared ^{99m}Tc-HMPAO brain perfusion SPECT using this system and a conventional Anger camera (Symbia T2, Siemens Healthineers). They found two-fold higher sensitivity for the CZT camera and enhancement of grey/white matter contrast. Imbert et al., 2021b investigated ^{99m}Tc-Sestamibi myocardial perfusion in morbidly obese patients and concluded that it can replicate the characteristics of a dedicated cardiac CZT camera, thus enabling easier management of severely obese patients. Desmonts et al., 2020 evaluated the CZT camera performance by comparison with a conventional dual-head Anger camera (dual-head Symbia, Siemens Healthineers) for several radioelements (^{99m}Tc, ^{123}I, ^{201}Tl, ^{111}In). They found the CZT camera had an energy resolution, depending on radioisotope, ranging between 1.68 and 2.55 times higher than Anger camera. The sensitivity for a point source placed in air was between 1.6 and 8 times higher for the CZT camera compared with the Anger camera, depending on whether the focus mode was activated, which reduces the swipe motion of detectors to a user-defined region of interest.

The CZT detection system for the VERITON-CT 200 series camera used in this study has a SPECT energy range of 40-200 keV, therefore preventing the acquisition of the higher ^{177}Lu photopeak (208 keV, 10.4%), thus restricting acquisition to the lower photopeak (113 keV, 6.2%) and affected by additional scattered photons of higher energy. To our knowledge, only one case report has been published for this system in association with ^{177}Lu treatment of neuroendocrine tumors (Chevalier et al., 2020). Another study was conducted on the CZT StarGuide gamma camera to determine if it enables faster post-therapy whole-body SPECT/CT acquisitions (^{177}Lu-DOTATATE and ^{177}Lu-PSMA) compared to a conventional camera, while maintaining equal or higher detection rates. This study did not focus on the quantitative aspects of the acquired images (Song et al., 2023). Finally, Kennedy et al., 2020 have evaluated the accuracy of activity concentration measurements for ^{177}Lu therapy using the Discovery 670 CZT camera (conventional camera geometry). They computed

Cette thèse est accessible à l'adresse : https://theses.insa-lyon.fr/publication/2023ISAL0068/these.pdf
© [L. Vergnaud], [2023], INSA Lyon, tous droits réservés

recovery coefficients for a NEMA IEC phantom and compared the estimated activity concentration in the bladder (images) with the actual activity concentration in the urinary of patients undergoing ^{177}Lu-PSMA treatment.

In this work, we studied performance of the VERITON-CT camera for ^{177}Lu imaging with various phantoms and characterised the current absolute quantification capabilities of the system for monitoring and dosimetry of ^{177}Lu-PSMA treatments.

8.2 Material and Methods

8.2.1 SPECT imaging system

This study was performed with the VERITON-CT (Spectrum Dynamics, Caesarea, Israel) hybrid CZT-camera installed at the nuclear medicine department of the Léon Bérard Center (Lyon, France). The system is composed of twelve CZT detector columns regularly spaced around 360 degrees, that swivel to acquire data from the entire field of view of 32 cm in axial direction, as detailed in Desmonts et al., 2020. Each detector module consists of 128 x 16 pixel solid state detectors with non-removable tungsten parallel hole collimators. This system detects photons in the energy range 40-200 keV, which limits the use of certain isotopes and/or photopeaks (e.g. 208 keV peak of ^{177}Lu).

8.2.2 Phantom experiments

Quantification performances were investigated using three different phantoms: a uniform water cylinder (*Ph1*), a standard NEMA IEC Body phantom (*Ph2*) and a NEMA IEC Body phantom modified with two internal hot vials (*Ph3)* (Figure 8.1). Table 8.1 gives detailed information for these three phantoms. The phantoms were filled with different activity concentrations of ^{177}Lu as indicated in the Table 8.1 (activities shown are those at first time-point acquisition). Ph1 phantom was used for calibration, Ph2 was used for conventional analysis of different-sized spheres and Ph3 contained larger hot volumes, surrounded by water, simulating two "organs" (129 and 521 mL). Acquisitions were performed with a ratio of 7:1 for Ph2 like Santoro et al., 2018. Note that other ratios were also used from 2.7:1 to 13:1 (Delker et al., 2023; Peters et al., 2020; De Nijs et al., 2014; Staanum, 2023; Ryu et al., 2019).

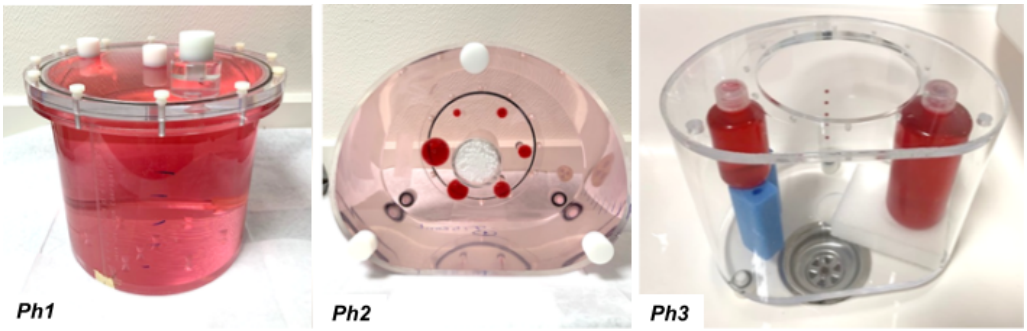

FIGURE 8.1 – Phantoms used for ^{177}Lu quantification performances evaluation. From left to right : uniform water cylinder (*Ph1*), NEMA IEC Body (*Ph2*) and NEMA IEC Body modified with two internal hot vials (*Ph3*). The red color indicates the ^{177}Lu radioactive volumes in each phantom.

Cette thèse est accessible à l'adresse : https://theses.insa-lyon.fr/publication/2023ISAL0068/these.pdf
© [L. Vergnaud], [2023], INSA Lyon, tous droits réservés

	Ph1	Ph2	Ph3
Phantom description	Uniform water cylinder	NEMA IEC Body	Modified NEMA IEC with hot vials
Usage	Calibration	ARC and CRC calculations	Large volumes testing
Radioactive background volume (mL)	6805	9658	NA
Inserts volume (mL)	None	100 (stock solution)	vial 1 = 130 vial 2 = 535
Activity in background (MBq)	814	783	None
Activity in inserts (MBq)(or in stock solution)	None	58	vial 1 = 129 vial 2 = 521

TABLE 8.1 – Description of the phantoms used for this study. The activity values are given at the first acquisition time of each phantom. (NA : Not Applicable)

8.2.3 Image acquisitions

All SPECT images were acquired with 4 angular acquisition steps (or orbits to cover the entire field of view) around the phantom, and one single bed position. During each orbit, the detector columns swept through 60 angular projections of 3.75 seconds each in step-and-shoot mode, giving a total data acquisition duration of 900 seconds. The energy windows used for photopeak and scatter are described in Table 8.2. Acquisitions were performed for all three phantoms, at 8 timepoints, from 4 to 339 hours after injection, as shown Table 8.3.

Low dose CT acquisitions were performed for attenuation correction. A voltage of 120 kVp and a current/time product of 17 mAs effective (mAs effective = mAs / pitch factor) were used to generate the X-ray beam. The CT images had slice thicknesses of 2.5 mm in the cranio-caudal direction and less than 1 mm in the other two directions.

8.2.4 Reconstruction parameters

Two reconstruction protocols were investigated, the first for quantification and dosimetry purposes, denoted RecQuant, and the second one for visualisation assessment, denoted RecVis.

The initial parameters used for RecQuant and RecVis are given in Table 8.2. In a whole-body acquisition, the final volumes were composed of around 700-800 slices. Attenuation correction was performed using the CT image. Scatter correction was based on the equation described in De Nijs et al., 2014 : C_{prim} =

Cette thèse est accessible à l'adresse : https://theses.insa-lyon.fr/publication/2023ISAL0068/these.pdf
© [L. Vergnaud], [2023], INSA Lyon, tous droits réservés

$C_{total} - (k_1 - k_2 \times k_3)C_{ds} - k_2 \times C_s$, where C_{prim}, C_{total}, C_{ds} and C_s are the absolute number for counts of unscattered, total, downscatter and scatter photons, respectively. Here, $k_1 = k_2 = 0.5$ and $k_3 = 0$. No scatter correction was used for RecVis as this is partially performed within the High Peak Correction (HPC) option, which is used to correct for high-energy photons passing through the collimator (parameter: 0.4 by default; parameter $\in$ [0;10[ ). Energy windows were the same for both protocols. *Point Spread Function Recovery display* (PSFRd) models the detector-collimator response and corrects for blurring effects (scatter); this was optimised for visualisation only. For RecVis, two additional filters were used: a convolution filter was applied during reconstruction and a median filter post-reconstruction.

	RecQuant	**RecVis**
Reconstruction algorithm	OSEM	OSEM
(Software)	Veriton 2.3.0.1234	Veriton 2.3.0.1234
Iterations	4	4
Subsets	8	8
Attenuation correction	CT-based	CT-based
Scatter correction	Yes	No
Main photopeak window (keV)	[101.6;124.2]	[101.6;124.2]
Peak scatter windows	[79;101.6]	[79;101.6]
at 113 keV	[124.2;146.8]	[124.2;146.8]
PSFR	No	PSFRd
HPC	No	Yes (HPC = 0.4)
Intra-filter	No	Convolution (pr: 0.125, freq: 2)
Post-filter	No	Median (p: 3)
In-plane size	256×256	256×256
Pixel size	2.46^2 mm^2	2.46^2 mm^2

TABLE 8.2 – Initial reconstruction parameters used for quantification and visualisation

8.2.5 Camera calibration

The calibration factor (CF) was used to convert the number of detected counts into activity concentration in Bq/mL. We followed the MIRD pamphlet n°26 (Ljungberg et al., 2016) and acquired a SPECT image of a large uniform hot water cylinder (*Ph1* phantom here), where the total injected activity was assumed to be entirely

Cette thèse est accessible à l'adresse : https://theses.insa-lyon.fr/publication/2023ISAL0068/these.pdf
© [L. Vergnaud], [2023], INSA Lyon, tous droits réservés

N° acquisition	**Ph1**	**Ph2**	**Ph3**
1	5.1h	4h	3.5h
2	27.6h	25.3h	18.5h
3	43.5h	42.3h	43.1h
4	72.4h	74.4h	NA
5	187.9h	186.5h	170.5h
6	194.5h	194.9h	NA
7	241.4h	241h	218.9h
8	338.6h	338.4h	NA

TABLE 8.3 – SPECT/CT image acquisitions performed for Ph1, Ph2 and Ph3 at different time-points after phantom injection of the first acquisition session. CT acquisitions with 17 mAs effective. (NA: Not acquired)

within the phantom. The CF could be computed using CF $= \frac{C_{est}[Bq/mL]}{C_{inj}[Bq/mL]}$ where C_{inj} is the actual injected activity concentration in the phantom and C_{est} is the estimated activity concentration inside the phantom. To do this, the activity concentrations of the voxels within the phantom are averaged and then multiplied by its volume. The CF is therefore dimensionless. The number of reconstructed counts taking into account the corrections is not accessible, which does not allow estimating the calibration factor in counts/s/MBq as usually done in the literature. More details are available in Figure 8.2.

Cette thèse est accessible à l'adresse : https://theses.insa-lyon.fr/publication/2023ISAL0068/these.pdf
© [L. Vergnaud], [2023], INSA Lyon, tous droits réservés

Procedure to calibrate the system and to estimate ARCs and CRCs.
Initially, SPECT reconstructions are expressed in Bq/mL and are not calibrated by default.

Step 1: Estimation of the calibration factor for each set of reconstruction parameters

- Anatomical contouring of the internal volume of the Ph1 phantom.

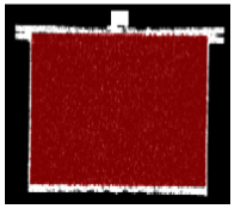

- Resampling of the SPECT image like CT to preserve anatomical contours.
- Averaging of the activity concentrations of the voxels included in the contour
  => uncalibrated average activity concentration (C_{est})
- **Calibration factor: CF = C_{est} / C_{inj}**

  where C_{inj} is the activity concentration injected

Step 2: Estimation of ARCs

- Anatomical contouring of the internal volume of each sphere of the Ph2 phantom

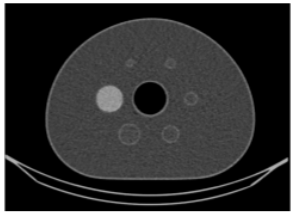

- Resampling of the SPECT like CT
- Averaging of the activity concentrations of the voxels included in each sphere contour
  => uncalibrated average activity concentration (C_{est})
- Divided C_{est} by the Calibration factor estimated during Step 1
  => Calibrated average activity concentration (C_S^*)
- For each sphere, **ARC = C_S^* / C_S** where C_S is the activity concentration in the sphere

Step 3: Estimation of CRCs

- Calculations of C_S^* were presented in Step 2
- For each sphere size, 48 spheres of the same dimension were drawn in the background (4 planes of 12 spheres).

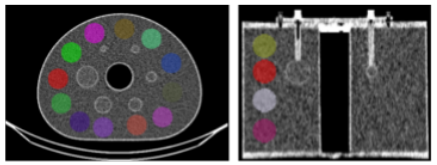

- For each sphere, the calibrated average activity concentration is estimated as in Step 2.
- For each set of 48 spheres of the same size, an average of the calibrated average activity concentrations is calculated.
  => Calibrated average activity concentration of the background (C_B^*)
- For each sphere, **CRC = ((C_S^* / C_B^*)-1)/((A_S / A_B)-1)** where A_S / A_B is the ratio of activities between the spheres and background

FIGURE 8.2 – Schematic diagram showing the steps involved in estimating the calibration factor, ARCs and, CRCs.

Cette thèse est accessible à l'adresse : https://theses.insa-lyon.fr/publication/2023ISAL0068/these.pdf
© [L. Vergnaud], [2023], INSA Lyon, tous droits réservés

Ph1 acquisition was repeated at different time points after injection corresponding to ^{177}Lu radioactive concentrations ranging from 122.1 ± 0.5 kBq/mL to 28.7 ± 0.2. All prepared activities of ^{177}Lu were measured using a Lemerpax scintiDOSE dose calibrator initially calibrated with a calibration vial of ^{177}Lu provided by Advanced Accelerator Applications (Saint Genis Pouilly, France). Quality control of the sensitivity was performed before each acquisition time using the dedicated ^{57}Co calibration source according to the manufacturer's recommendations. Note that CF depends on the reconstruction parameters and was computed for all different reconstructions, as described in the next section.

8.2.6 Evaluation criteria

To optimise the reconstruction parameters for quantification, the activity concentration recovery coefficients ARC (Dickson et al., 2022) (for quantification), the contrast recovery coefficients CRC (for visual detection), and the variability in spheres and background (noise estimation) were computed on the Ph2 phantom shown in Figure 8.1. The mean ARCs were computed with equation (8.1), given in the MIRD pamphlet n°23 (Dewaraja et al., 2012), with C_S^*, the estimated activity concentration in the ^{177}Lu sphere and C_S, the actual activity concentration in the sphere. Activity in the sphere was estimated by averaging activity concentrations in the sphere multiplied by the volume of the sphere. A CF estimated for each set of acquisition/reconstruction parameters was then applied. Spheres were delineated on the CT scan: therefore calculated volumes were close but not strictly equal to actual volumes, which explains why activities have been replaced by activity concentrations in equation (8.1). Differences between calculated and actual volumes were less than 9.5% (6.1 mL calculated vs 5.6 mL actual) except for the smallest sphere volume with a difference of 31% (0.36 mL calculated vs 0.52 mL actual).

$$ARC = \frac{C_S^*}{C_S} \tag{8.1}$$

The Contrast recovery coefficients (CRC) were computed as proposed in NEMA 2007. In equation (8.2), C_S^* was the estimated activity concentration in the ^{177}Lu sphere and C_B^* the estimated background activity concentration. $\frac{A_S}{A_B}$ was the ratio of activity between the spheres and background. To compute C_B^*, 48 spheres, with the same size as the ^{177}Lu sphere, were segmented into four sections of the phantom in the cranio-caudal direction (with 12 3D spheres per section) of the CT scan (see Figure 8.3). Activities were computed in all spheres, as was done for the ^{177}Lu sphere, and then averaged. Note that activity of the background was computed for all spheres of different sizes. The variability in spheres and background was computed with the RMS formula (Root Mean Square) as proposed by Ramonaheng et al., 2021 or found in NEMA 2007. For the background, the contours used were those of the 48 segmented spheres for each sphere volume. More details about ARCs and CRCs are available in Figure 8.2.

$$CRC = \frac{\frac{C_S^*}{C_B^*} - 1}{\frac{A_S}{A_B} - 1} \tag{8.2}$$

$$RMS(\%) = \frac{SD}{Mean} \times 100 \tag{8.3}$$

Cette thèse est accessible à l'adresse : https://theses.insa-lyon.fr/publication/2023ISAL0068/these.pdf
© [L. Vergnaud], [2023], INSA Lyon, tous droits réservés

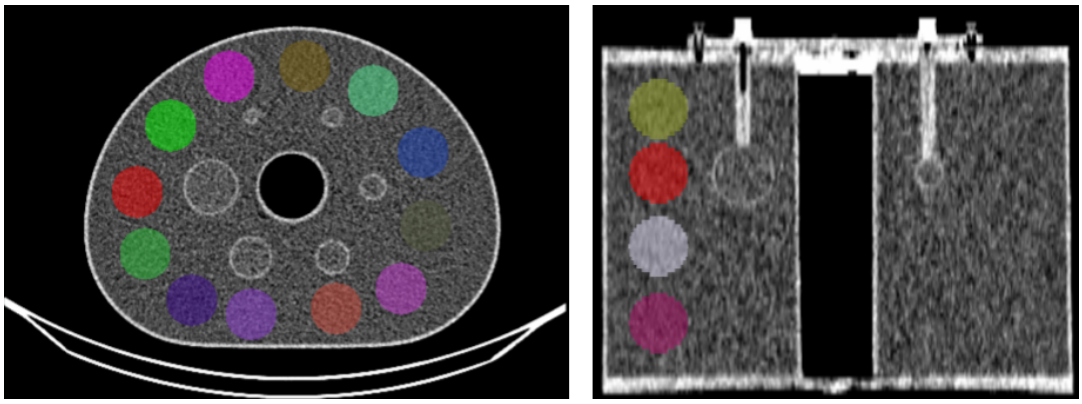

FIGURE 8.3 – Positioning the spheres to estimate the concentration of activity in the background. Twelve spheres were drawn (left) in each of the four planes (right).

8.2.7 Optimisation and evaluation of reconstruction parameters

All reconstructions were performed with OSEM, CT-based attenuation correction and geometry modelling. In addition, four sets of additional parameters were tested for various updates (iterations $\times$ subsets) as shown in Table 8.4. For set n°1, scatter correction was added. For set n°2, penalized likelihood (PL) regularisation was added in addition to scatter correction. The PL implementation of the manufacturer is inspired by Webster Stayman and Fessler, 2000 and De Pierro, 1995 and allows an increase in the number of iterations without much increase in noise. The penalty strength can be adjusted with two parameters: a regularisation parameter β that controls "the noise-resolution trade-off" and the frequency ($freq$). Default values are $\beta = 1$ and $freq = 2$. For sets n°3 and n°4, PSFRq (Point Spread Function Recovery optimised for quantification) option was used. PSFRq includes conventional, spatially invariant PSF together with blur corrections (scatter). Test n°3 was with and test n°4 was without additional scatter correction. No PL was applied for n°3 and n°4. Note that a specific calibration factor was computed for each set of reconstruction parameters. In addition, ARC was also estimated for the Ph3 phantom.

	Set n°1	**Set n°2**	**Set n°3**	**Set n°4**
Reconstruction algorithm	OSEM	OSEM	OSEM	OSEM
Regularisation	No	Yes (PL)	No	No
Attenuation correction	CT-based	CT-based	CT-based	CT-based
Scatter correction	Yes	Yes	Yes	No
PSFRq option	No	No	Yes	Yes

TABLE 8.4 – Reconstruction parameters associated with each set whose number of updates varies between 32 and 384.

Cette thèse est accessible à l'adresse : https://theses.insa-lyon.fr/publication/2023ISAL0068/these.pdf
© [L. Vergnaud], [2023], INSA Lyon, tous droits réservés

8.2.8 Impact of the segmentation

To our knowledge, there is no consensus in the literature on how to determine the ROI used to compute ARC and CRC. Some authors used contours from the CT image (M1) (Delker et al., 2016; Sanders et al., 2015), others reduced those contours to obtain smaller spheres inside the "physical" spheres (M2) (Sandström et al., 2010; Marin et al., 2018). Other authors used thresholding on the SPECT image (M3) (Peters et al., 2020) as in equation 8.4 where AC_{thresh}, $AC_{Max}(Sph)$ and $AC_{Mean}(bg)$ correspond to the threshold estimated for one sphere, the maximum activity concentration in the sphere and the mean activity concentration in the background. The ARCs were estimated from the mean and maximum activity concentration as proposed by Peters et al., 2019. We compared the different approaches.

$$AC_{thresh} = \frac{1}{2} \times (AC_{Max}(Sph) + AC_{Mean}(bg)) \tag{8.4}$$

8.2.9 Patient images

The estimated count rates in the phantoms (in particular Ph2) were compared to the estimated count rates from each BP (6 or 7 total) for three patients (administered activities: 6027 MBq, 6259 MBq and, 7309 MBq) at three different timepoints (5h-6.1h, 23.1h-25.7h and, 142.1h-144.1h) to evaluate whether count rates in the phantoms are representative of those in patients. The number of counts detected in the projections as well as the acquisition time for each BP, could be obtained using the Time Reduction application (TR) on the gamma camera workstation. For illustration purposes, ^{68}Ga-PSMA PET and ^{177}Lu-PSMA-1 SPECT images of a patient treated for metastatic castration-resistant prostate cancer are given. A SPECT image was acquired 24h after each therapeutic administration (5 injections in total). Images were reconstructed with RecVis and projected (MVP "multi-view planar" option) to obtain a planar image. For the first therapy, the 24h SPECT image was also reconstructed with RecQuant (12 iterations and 8 subsets). Acquisition duration was reported.

8.3 Results

8.3.1 Iterations and subsets

Figures 8.4, 8.5 and 8.6 show activity concentration recovery coefficients (ARC), contrast recovery coefficients (CRC) and percentages of root mean square (RMS) respectively for different numbers of updates and different reconstruction parameters. Background RMS percentages were also evaluated. The calculations were performed using the M1 segmentation method (CT-based contours) using the mean and not the maximum in order to be as close as possible to the patient dosimetry. With increased numbers of updates for OSEM reconstructions with scatter correction and without PSFRq option, the RMS percentage increased from 27%-30% for 32 updates to 91%-95% for 384 updates whatever the size of the sphere considered. Similarly, the ARC, CRC and RMS percentages increased with the number of updates. Based on these results, a set of optimal parameters was selected. We defined the best compromise by limiting the variability in homogeneous regions (spheres and background) below 50%, which corresponded to 96 updates (12 iterations and 8 subsets). For all subsequent experiments, each reconstruction was performed with OSEM, CT-based attenuation correction, scatter correction, 12 iterations, 8 subsets, no filters, no PSFRq and no regularisation.

Cette thèse est accessible à l'adresse : https://theses.insa-lyon.fr/publication/2023ISAL0068/these.pdf
© [L. Vergnaud], [2023], INSA Lyon, tous droits réservés

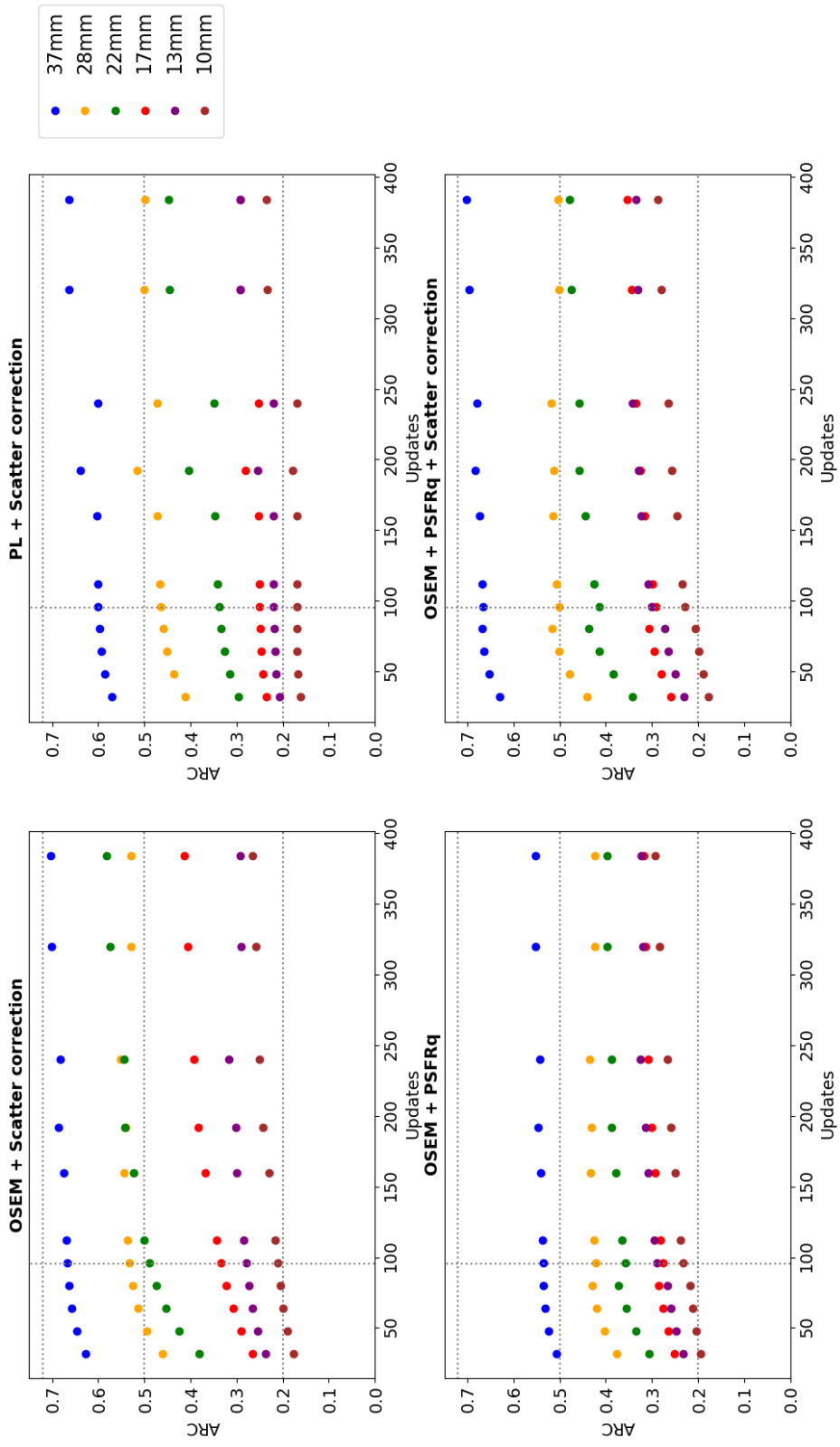

FIGURE 8.4 – Activity concentration recovery coefficients (ARC) for different volumes of spheres as a function of the number of updates. At the top left, a scatter correction is applied. Top right, a PL reconstruction is used as well as a scatter correction. Below, the PSFRq option is applied with (right) or without scatter correction (left).

Cette thèse est accessible à l'adresse : https://theses.insa-lyon.fr/publication/2023ISAL0068/these.pdf
© [L. Vergnaud], [2023], INSA Lyon, tous droits réservés

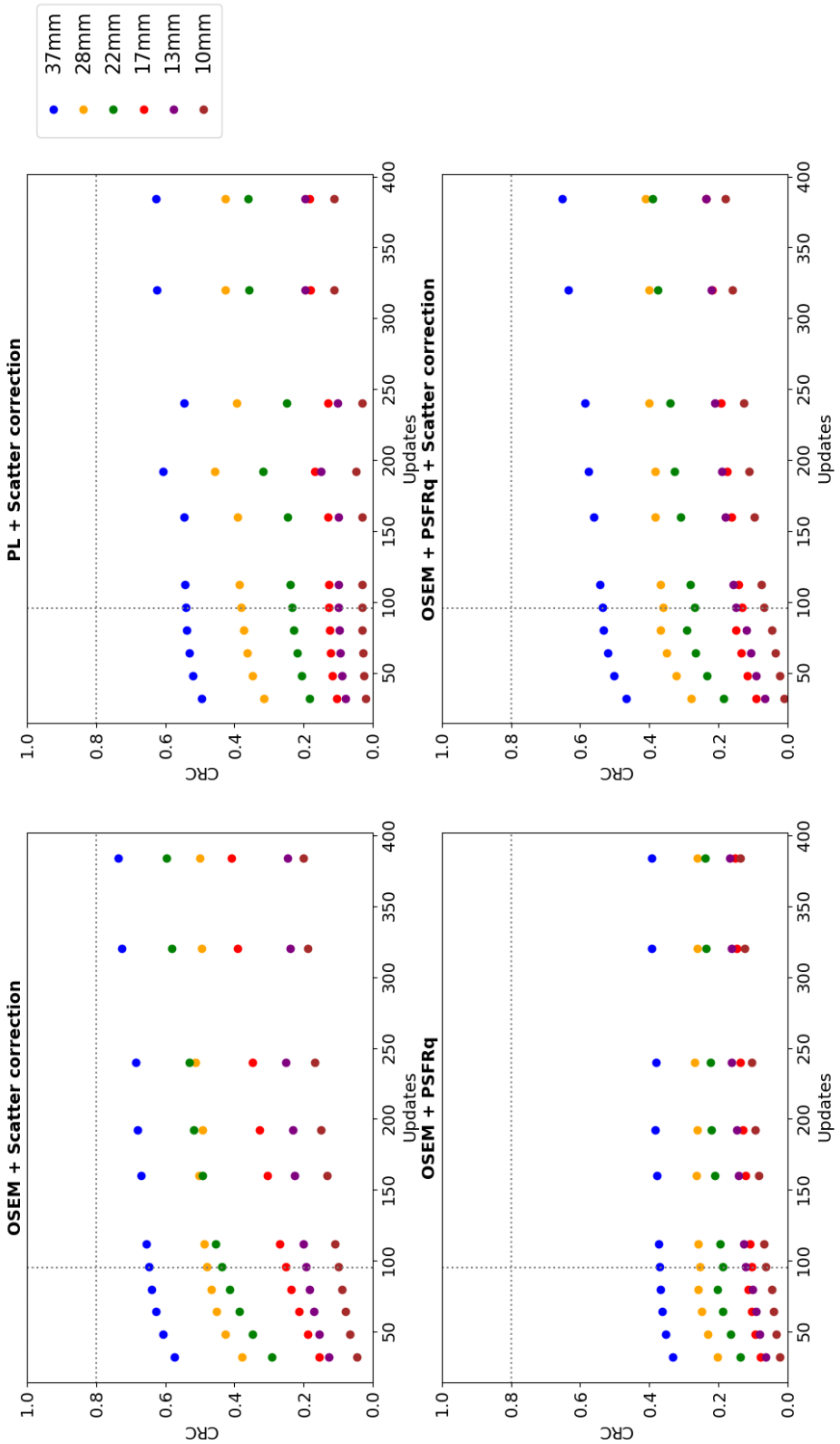

FIGURE 8.5 – Contrast recovery coefficients (CRC) for different volumes of spheres and vials as a function of the number of updates. At the top left, a scatter correction is applied. Top right, a PL reconstruction is used as well as a scatter correction. Below, the PSFRq option is applied with (right) or without scatter correction (left).

Cette thèse est accessible à l'adresse : https://theses.insa-lyon.fr/publication/2023ISAL0068/these.pdf
© [L. Vergnaud], [2023], INSA Lyon, tous droits réservés

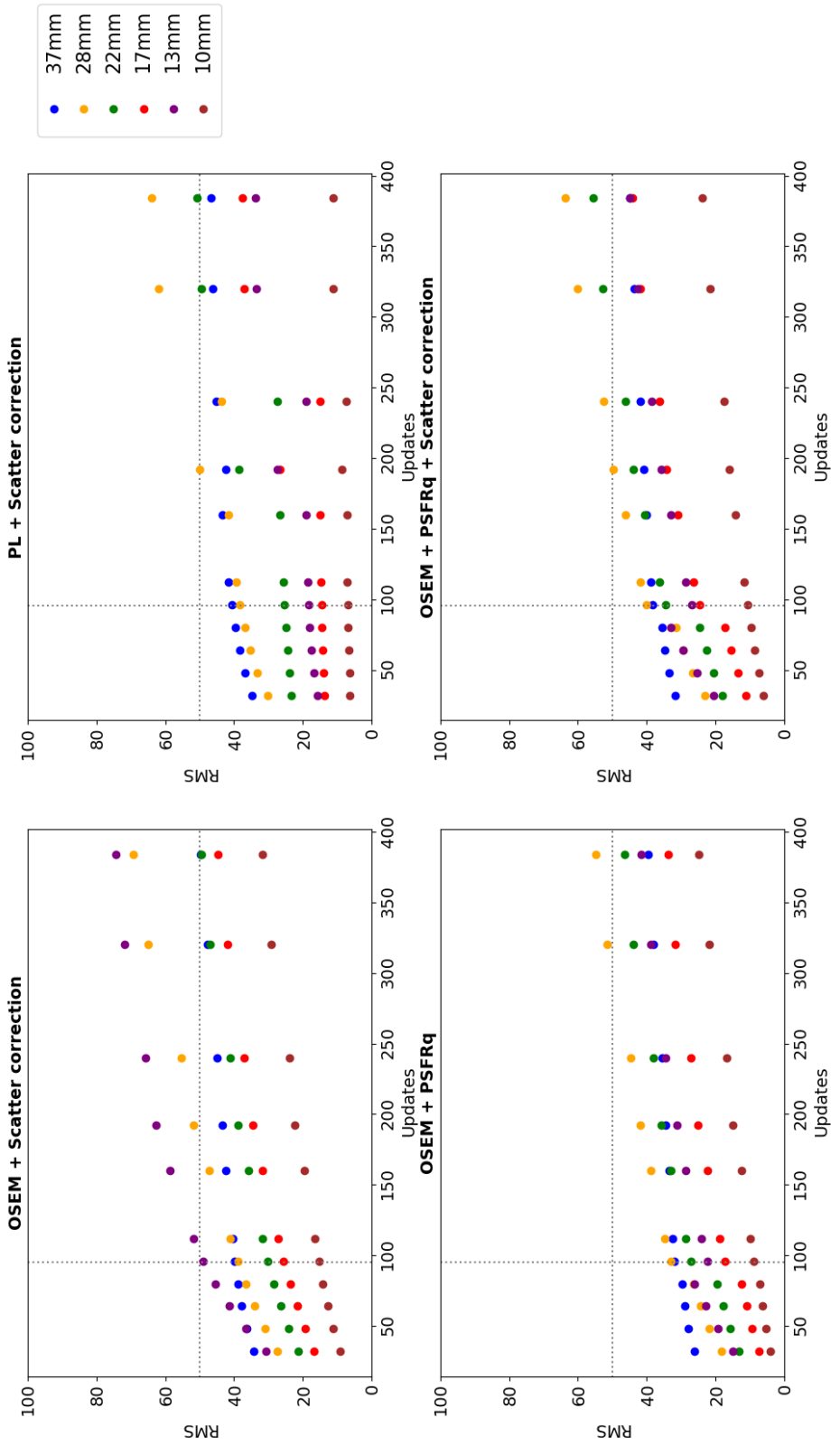

FIGURE 8.6 – Percentages of root mean square (%) for different volumes of spheres as a function of the number of updates. At the top left, a scatter correction is applied. Top right, a PL reconstruction is used as well as a scatter correction. Below, the PSFRq option is applied with (right) or without scatter correction (left).

Cette thèse est accessible à l'adresse : https://theses.insa-lyon.fr/publication/2023ISAL0068/these.pdf
© [L. Vergnaud], [2023], INSA Lyon, tous droits réservés

8.3.2 Calibration factors

The calibration factor was evaluated for eight different activity concentrations by using reconstruction parameters determined previously (12 iterations, 8 subsets). This factor was 0.176 $\pm$ 0.00444, i.e. a coefficient of variation (CoV) of 2.5% for Ph1.

8.3.3 Quantification on large volumes

RecQuant was used on phantom Ph3 with hot volumes larger than the spheres, for 5 different concentrations. ARCs were on average 0.91 $\pm$ 0.0117 (CoV = 1.3%) for the small "organ" and 0.91 $\pm$ 0.0082 (CoV = 0.9%) for the large "organ".

8.3.4 Influence of the ROI delineation

ARCs were estimated for the Ph2 phantom reconstructed with the selected parameters from different segmentation methods (M1, M2 and M3 described in section *Material and methods*) for average or maximum based figures of merit (Table 8.5). An example of each segmentation method is given in Figure 8.7 for the 37mm sphere.

	S1	**S2**	**S3**	**S4**	**S5**	**S6**
$M1_{Mean}$	0.67	0.53	0.49	0.33	0.28	0.21
$M1_{Max}$	1.37	1.15	0.82	0.49	0.56	0.28
$M2_{Mean}$	0.84	0.64	0.60	0.37	0.32	0.18
$M2_{Max}$	1.37	1.15	0.82	0.49	0.53	0.23
$M3_{Mean}$	0.97	0.81	0.59	0.36	0.39	0.25
$M3_{Max}$	1.37	1.15	0.82	0.49	0.56	0.46

TABLE 8.5 – Mean and maximum activity concentration recovery coefficients estimated for each delineation method (M1, M2 and M3). Spheres 1 to 6 have a respective diameter of S1 (37mm), S2 (28mm), S3 (22mm), S4 (17mm), S5 (13mm) and S6 (10mm).

8.3.5 Patient images

Count rates were estimated for all BP, from image acquisitions at three timepoints for three patients. The count rates ranged from 0.1 kcps to 35.3 kcps. Count rates were also evaluated for Ph2 phantom with eight different activity concentrations and ranged from 3.1 kcps to 13.0 kcps. Each BP covers 31.5 cm, with a scan duration of 5 minutes maximum, reducing to around 2 min/BP for regions without pathological uptake (e.g., legs). A whole-body acquisition (i.e., vertex to toes), requires 6 or 7 BPs depending on patient size. Hence, total SPECT acquisition duration was between 24 and 26 minutes overall, including time for detector movements. Typical CT acquisition time is around 1 minute. Figure 8.8 illustrates SPECT and corresponding ^{68}Ga-PSMA PET images for one patient. Five SPECT images were reconstructed using RecVis visualisation parameters and transformed into planar images. Figure 8.9 shows normalised SPECT images acquired 24H after patient treatment with ^{177}Lu-PSMA and reconstructed with RecVis and optimised RecQuant parameters respectively. For a patient for whom 6 BP have been acquired, the RecQuant

Cette thèse est accessible à l'adresse : https://theses.insa-lyon.fr/publication/2023ISAL0068/these.pdf
© [L. Vergnaud], [2023], INSA Lyon, tous droits réservés

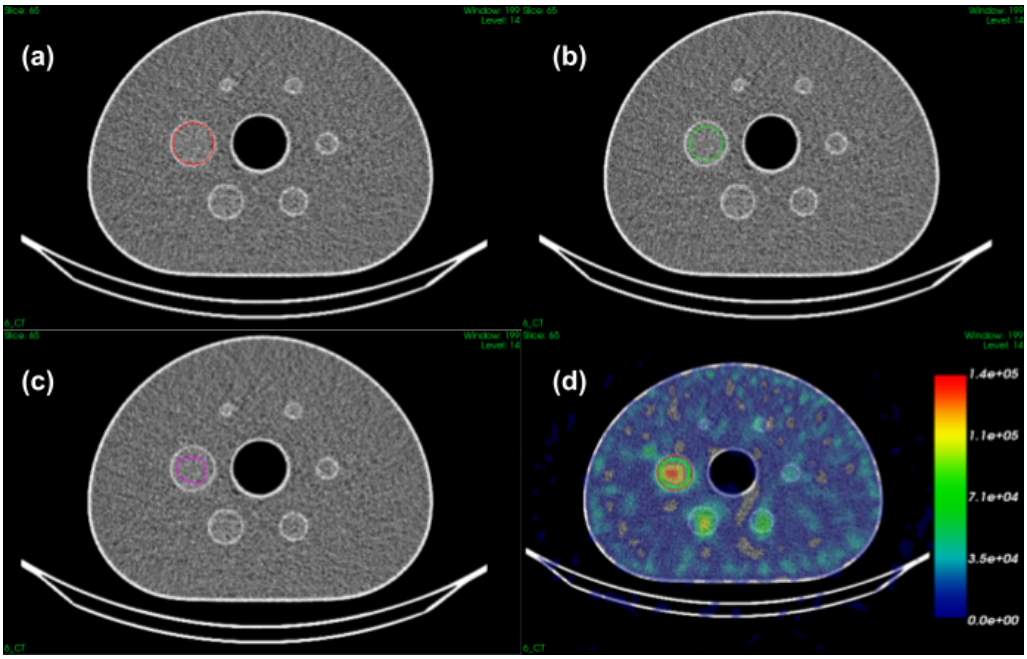

FIGURE 8.7 – Superposition of the CT and the contour of the 37 mm diameter sphere of the NEMA IEC phantom obtained by (a) anatomical segmentation of the CT (M1), (b) anatomical segmentation of the CT with a margin (M2) or (c) by thresholding the SPECT image (M3). Image (d) is the fusion of the CT and SPECT image and the superposition of the contours obtained with the three methods (M1, M2 and M3).

reconstruction takes 19 min before scatter correction and 27 min in total when scatter correction is applied.

8.4 Discussion

The objective of this study was to evaluate quantitative performance of the CZT VERITON 360° gamma camera (VERITON-CT 200 series, SW version 2.3.0.1234) and to optimize the reconstruction parameters in the follow-up of patients treated with ^{177}Lu-PSMA. Unlike conventional gamma cameras that use a recommended ^{177}Lu energy peak at 208 keV (more photons, less scatter) (D'Arienzo et al., 2016), the VERITON system evaluated in this study has a SPECT energy range of 40-200 keV, therefore is only able to recover the 113 keV photopeak (<200 keV). However, solid-state detectors have better (in the range of 2 to 5% (Ben Bouallègue et al., 2015)) energy resolution than Anger cameras because it only takes a few eV to create electron-hole pairs (Usman and Patil, 2018). Moreover, CZT has also demonstrated better sensitivity (Ben Bouallègue et al., 2015) (factor 5 to 10 for mycardial applications). The performance of CZT gamma cameras means that ^{177}Lu SPECT images could be improved both qualitatively and quantitatively.

8.4.1 Determination of optimal reconstruction parameters for quantification

The SPECT image reconstruction was based on iterative OSEM with CT-based attenuation correction (Dewaraja et al., 2012) and no inter- and/or post-filtering to

Cette thèse est accessible à l'adresse : https://theses.insa-lyon.fr/publication/2023ISAL0068/these.pdf
© [L. Vergnaud], [2023], INSA Lyon, tous droits réservés

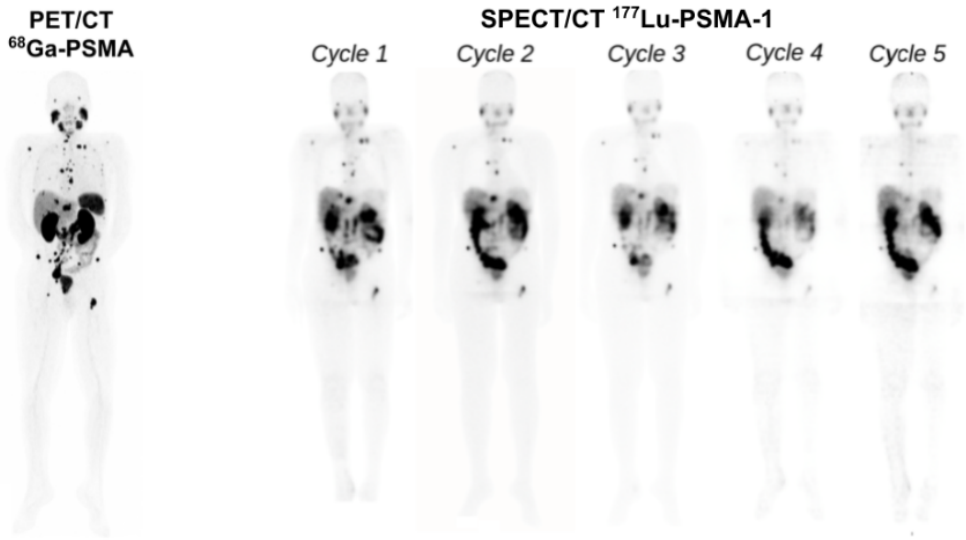

FIGURE 8.8 – On the left, ^{68}Ga-PSMA PET image for a patient with a metastatic castration-resistant prostate cancer. On the right, 5 planar images obtained from SPECT reconstructions (RecVis) after the first five injections of ^{177}Lu-PSMA-1. The PSA levels measured at each treatment are 28, 15.7, 5.74, 3.02 and 1.71 ng/mL respectively.

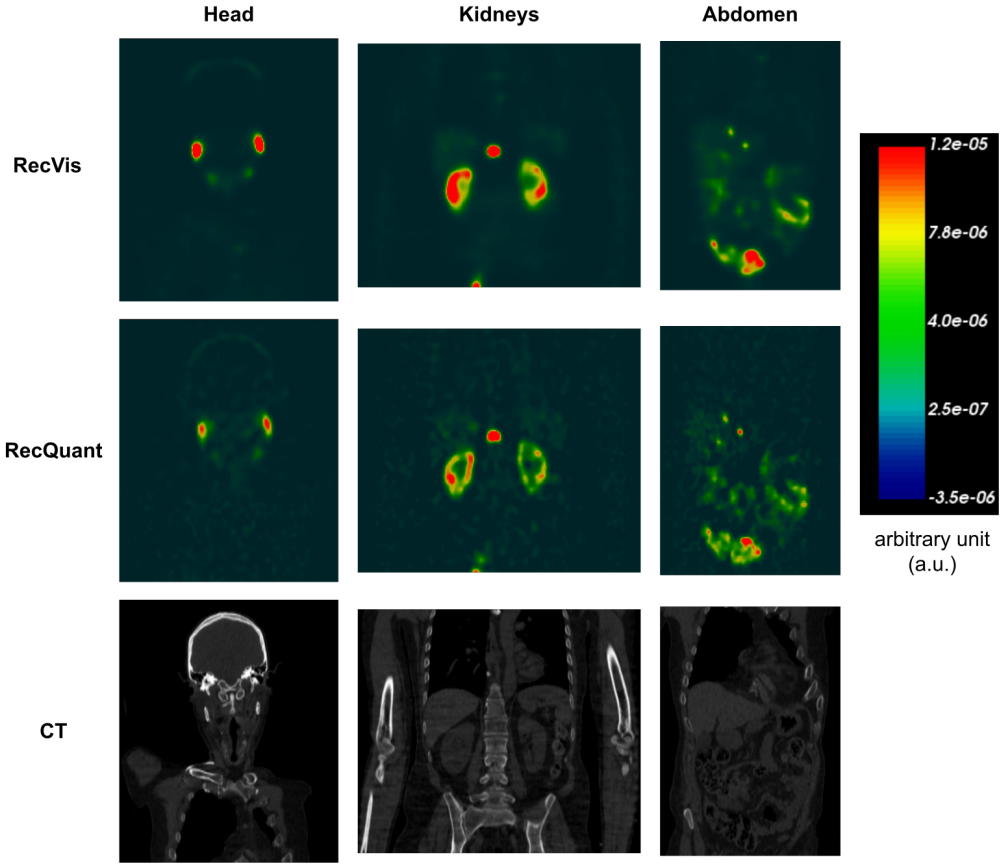

FIGURE 8.9 – Normalized SPECT reconstructions (RecVis and RecQuant) in arbitrary unit of a patient treated with ^{177}Lu-PSMA-1 24H after the first injection. The focus is on three regions: the head, the kidneys and the abdomen. Associated CT scans are also available.

Cette thèse est accessible à l'adresse : https://theses.insa-lyon.fr/publication/2023ISAL0068/these.pdf
© [L. Vergnaud], [2023], INSA Lyon, tous droits réservés

avoid impacting the quantification (Dickson et al., 2022). Scatter windows were 22.6 keV width, wide enough to limit noise when using TEW (Dewaraja et al., 2012). Reconstruction included a model of the system geometry whose uncertainties are partly corrected with the PSFRq option, which corresponds to a conventional spatially invariant PSF and a correction for blurring effects (e.g. scatter). There is a risk of scatter being corrected twice when the scatter correction is used simultaneously with PSFRq option. For this reason, sets n°1, n°3 and n°4 were tested. For each case, the number of updates was modified in order to determine the best compromise between quantification accuracy and noise. Finally, a fourth case was considered: scatter correction + PL regularisation (case n°2) which should allow an increase in the number of updates whilst controlling the noise. For all four sets of parameters, as the number of updates was increased, ARC, CRC and RMS also increased. The minimum number of updates considered corresponds to the default parameters.

These results are consistent with the literature since there is a convergence of ARC and CRC (Peters et al., 2020) and an increase in noise (Ramonaheng et al., 2021). In the following, all the intervals given are those of the 37 mm sphere, whatever the number of updates. Where this is not the case, an indication is given. The ARCs were highest for cases n°1 and n°4, i.e., with scatter correction, and without/with PSFRq (ARC $\in$ [0.63;0.70]). However, ARCs for the 28mm sphere were higher without PSFRq (ARC $\in$ [0.46;0.53] whatever the number of updates) than with (ARC $\in$ [0.44;0.50]) whereas the noise was lower with PSFRq option. Without scatter correction, ARCs were low ($\in$ [0.51; 0.55]) even with PSFRq. Scatter correction is thus essential and recommended for 113 keV, contaminated by downscatter from 208 keV. The use of PL regularization together with scatter correction led to lower ARCs ([0.57;0.66] with 0.66 for a number of updates superior to 300) compared to scatter correction alone. Similarly, the CRCs ($\in$ [0.50;0.63]) are lower with set n°2 than with set n°1 ($\in$ [0.57;0.74]). The noise remained low up to 160 updates which shows the benefit of the PL regularization. The PL regularization has not been studied in depth because it is still under development by the company Spectrum Dynamics. Set n°1 (scatter correction only) is thus recommended as it offers the best quantitative results. The recommended number of updates was 96 (12 iterations and 8 subsets) to keep noise below 50%.

In the literature, a few ARC and CRC values are available for CZT imaging systems using ^{177}Lu. For example, Kennedy et al., 2020 present ARC results for the Discovery 670 CZT for ^{177}Lu as a function of the energy peak and collimator chosen. For the 37mm sphere, for the 113 keV peak with a LE collimator and TEW scatter correction, they obtained an ARC close to 1.2, while for the 208 keV peak, the ARC was 0.6. For the same sphere, the ARC estimated with the set of optimized parameters is 0.7. This can be explained by the difference in geometry and collimator between systems. A second system designed by the Huh et al., 2023 team was evaluated by Monte Carlo simulation. They obtained CRCs of around 0.55 for the 37mm sphere compared with 0.65 with the optimized parameters of our system. If we compare these results with a conventional gamma camera, as presented in the study by Tran-Gia and Lassmann, 2019, the attenuation recovery coefficients (ARCs) for the 37 mm sphere are 0.8 vs. 0.7 with the VERITON camera. This difference can be attributed to the use of the 208 keV peak as well as the six times longer acquisition times for the Symbia Intevo Bold compared to the VERITON. In clinical practice, it is not always feasible to maintain long acquisition times.

Cette thèse est accessible à l'adresse : https://theses.insa-lyon.fr/publication/2023ISAL0068/these.pdf
© [L. Vergnaud], [2023], INSA Lyon, tous droits réservés

8.4.2 Influence of ROI definition

ARC and CRC depend on contours of the spheres. In the literature, several methodologies have been used (Delker et al., 2016; Sanders et al., 2015; Sandström et al., 2010; Marin et al., 2018; Peters et al., 2020) and, among them, three have been studied here (M1, M2 and M3 illustrated in Figure 8.7). Moreover, ARC and CRC can be computed with average or maximum concentration within the ROI. This has a major influence on the ARCs, e.g. for the largest sphere using the mean, ARCs were 0.67, 0.84 and 0.97 for M1, M2 and M3 respectively (Table 8.5). With the maximum, ARCs were identical for most spheres except the smallest ones. Using maximum is noise sensitive and only relies on a single voxel, whilst using average lowers the ARCs by integrating the heterogeneity of the concentrations within a volume but is less sensitive to noise. Segmentation based on the SPECT image (M3) is dependent on the reconstruction parameters unlike M1 and M2. Here, the mean-based M1 method was chosen because during patient dosimetry, the organs at risk are segmented anatomically on the CT (the only available information) and the mean absorbed dose is calculated within a ROI. In the case of lesions, anatomical contouring can be challenging, making the M1 method unusable. To our knowledge, accurate tumour segmentation is still an open question. In the MIRD n°23, ARCs superior to 0.9 are considered to be highly accurate reconstructions, however the methodology associated with these results was not described. In our study, the ARCs reached 0.9 with the M3 method but not with the M1 method.

8.4.3 Evaluation of the reconstruction parameters

Calibration factor Image acquisitions of the Ph1 calibration phantom were performed at different times in order to vary the activity concentration. The calibration factor was stable with CoV equal to 2.5%. Note that CT contours of the inner edges of the cylinder have been delineated on all images and may be an additional source of uncertainty.

Activity recovery in large hot volumes With volumes close to those of patient organs such as kidneys or spleen (129 and 521 mL), ARCs were greater than 0.9 and therefore suitable for dosimetry. For smaller volumes, additional Partial Volume Correction is advised.

8.4.4 Patient acquisitions

The RecVis reconstruction shown in Figure 8.8 was performed with the parameters recommended by the manufacturer. The HPC option takes account of high energy photons passing through the collimator, hence scatter correction is not applied. PSFR option was also applied and has been optimised for visualisation. The acquisition time of a whole-body SPECT scan was reduced by at least half when compared to that of a conventional gamma camera. This is important for patients in pain who may find it difficult to remain still for long periods and where multiple SPECT/CT acquisitions will be performed. In practice, it is also possible to perform more SPECT/CT acquisitions in one day. In our institution, more than 60 patients have already been imaged with this camera for monitoring their treatment. The latest version of VERITON (400 series) allows acquisitions of higher energy photons (up to 400 keV) and thus, the ability to use the peak at 208 keV of ^{177}Lu.

Cette thèse est accessible à l'adresse : https://theses.insa-lyon.fr/publication/2023ISAL0068/these.pdf
© [L. Vergnaud], [2023], INSA Lyon, tous droits réservés

8.5 Conclusion

We evaluated the quantitative performance of VERITON for ^{177}Lu treatments and proposed a set of recommended reconstruction parameters for quantification purposes called RecQuant. We advocate the use of two sets of reconstruction parameters: one for quantification and one for visualisation with the same acquisition parameters. For quantification, CT-based attenuation correction, scatter correction, 12 iterations, 8 subsets and no filter provided the best compromise between ARC and RMS values. For large volumes such as kidneys, ARCs were in the order of 0.91. In this work, the VERITON 200 series system with SW version 2.3.0.1234 was used. The reconstruction software is still evolving and additional improvements are expected in future versions. While the system is limited to 113 keV detection for ^{177}Lu, the ARC obtained with RecQuant demonstrates it can be used for ^{177}Lu dosimetry purpose. The acquisition time for a whole-body image of about 1.8 m length is around 25 minutes, which is about three times faster than with conventional dual-head cameras.

Cette thèse est accessible à l'adresse : https://theses.insa-lyon.fr/publication/2023ISAL0068/these.pdf
© [L. Vergnaud], [2023], INSA Lyon, tous droits réservés

Cette thèse est accessible à l'adresse : https://theses.insa-lyon.fr/publication/2023ISAL0068/these.pdf
© [L. Vergnaud], [2023], INSA Lyon, tous droits réservés

Chapter 9

Dosimetry for ^{177}Lu-PSMA patients based on 3D whole-body acquisitions

This chapter presents a preliminary dosimetric study conducted at the Léon Bérard Centre within the context of ^{177}Lu-PSMA therapy. It complies the initial findings obtained for kidneys, spleen and liver for a cohort of 13 patients. This work is still ongoing as patient data continues to be collected.

9.1 Introduction

^{177}Lu-PSMA radiopharmaceutical therapy is a novel treatment for patients diagnosed with metastatic castration-resistant prostate cancer, and its therapeutic efficacy has been confirmed through the phase III VISION study (refer to Chapter 2). Each patient receives between 4 and 6 injections of 7.4 GBq. However,similar to ^{177}Lu-DOTATATE therapy (refer to Chapter 6), large variations in absorbed doses have been observed (see Tables 5.4, 5.5, 5.6, 5.7 and 5.8). Additionally, the response to treatment varies among patients (Scarpa et al., 2017; Fendler et al., 2017; Zhang et al., 2019).

To estimate absorbed doses to both OARs and tumours, it is necessary to acquire images with a field of view that extends from the pelvis to the head. This encompasses infiltrating bone metastases, salivary glands, and lacrimal glands, which are considered OARs. While many studies employ planar images (organ and tumour superimposition) to reduce acquisition time, it is recommended to based dosimetry on 3D SPECT images obtained through multiple field of view acquisitions (Sjögreen Gleisner et al., 2022). The hybrid method, which involves multiple planar acquisitions and one SPECT acquisition, is commonly chosen as a suitable compromise between acquisition time and dosimetry accuracy. CZT gamma cameras offer a potential solution to this challenge by enabling shorter whole-body SPECT acquisition (Song et al., 2023, 2 to 3 times shorter). The performance of CZT cameras for dosimetry of ^{177}Lu therapies was evaluated on phantoms in Chapter 8. However, to our knowledge, the evaluation using patient images has not been conducted yet, except for two abstracts written by Imbert et al., 2020 and Imbert et al., 2021a, which were not peer-reviewed studies.

In this study, the dosimetry of kidneys, spleen, and liver was performed using whole-body SPECT images of patients treated with ^{177}Lu-PSMA.

Cette thèse est accessible à l'adresse : https://theses.insa-lyon.fr/publication/2023ISAL0068/these.pdf
© [L. Vergnaud], [2023], INSA Lyon, tous droits réservés

9.2 Material and methods

9.2.1 Patients

Thirteen patients diagnosed with metastatic castration-resistant prostate cancer underwent treatment with ^{177}Lu-PSMA-1, except for two patients (P11 and P12) who received ^{177}Lu-PSMA-617. This treatment was administered at the Léon Bérard Centre in Lyon, France, between June 2021 and May 2022. Each patient received between four and six injections of 6601 $\pm$ 437 MBq, with a six-week interval between each injection. In cases where there was no response after two treatment cycles, the treatment was discontinued due to disease progression).

9.2.2 3D whole-body SPECT/CT acquisition

Similar to ^{177}Lu-DOTATATE, three whole-body SPECT/CT acquisitions were acquired after the initial treatment cycle at 4h, 24h and either 96h or 144h. Subsequently, a single acquisition was performed at 24h after each subsequent treatment cycle. Whole-body SPECT/CT images (6-7 BP) were obtained using the VERITON 200 series (Spectrum Dynamics, Caesarea, Israel). The data available for dosimetry is given in Table 9.1.

		P1	**P2**	**P3**	**P4**	**P5**	**P6**	**P7**	**P8**	**P9**	**P10**	**P11**	**P12**	**P13**
Cycle 1	4H	X	X	X	X	X	X	X	X	X	X	X	X	X
	24H	X	X	X	X	X	X	X	X	X	X	X	X	X
	96H	X	X	X	X	X	X	X	X	X	X	X	X	X
Cycle 2	24H	X	X	X	X	X	X	X	X		X	X		
Cycle 3	24H		X		X	X	X		X		X			
Cycle 4	24H		X			X	X				X			
Cycle 5	24H		X			X			X					
Cycle 6	24H		X						X					

TABLE 9.1 – SPECT/CT acquisition time-points for all patients treated with ^{177}Lu-PSMA, all cycles. X: available.

9.2.3 Reconstruction parameters

The reconstruction parameters employed were determined in Chapter 8 and consisted of CT-based attenuation correction, scatter correction, 12 iterations, 8 subsets, and no filter.

9.2.4 Delineation of volumes of interest

Automatic anatomical segmentation of the patients' organs was performed using the *TotalSegmentator* extension of 3D slicer for all patients, cycles, and acquisitions. The contours of the kidneys, liver and spleen were extracted, and manual corrections were made as needed. The lacrimal and salivary glands are not automatically segmented by the algorithm, implying their exclusion from this preliminary dosimetry, even though they are within the FOV.

Cette thèse est accessible à l'adresse : https://theses.insa-lyon.fr/publication/2023ISAL0068/these.pdf
© [L. Vergnaud], [2023], INSA Lyon, tous droits réservés

9.2.5 Dosimetry method

Calibration factor The calibration factor was determining by using a uniform Jaszczak phantom, as described in Chapter 8 (Ph1). The internal contour of the phantom was outlined based on the CT image. The activity concentration was then evaluated and compared with the known activity concentration (refer to Section 8.2.5).

Kidneys, liver and spleen absorbed doses The dosimetric workflow employed in this study follows the same approach as proposed in Chapter 6. Specifically, three SPECT/CT acquisitions are consistently obtained after the initial cycle. This enables the reuse of pharmacokinetic parameters for subsequent cycles, previously referred to as the *STP-Intra method M2*).

9.3 Results

Calibration factor The calibration factor estimated for this particular set of parameters was 0.177.

Absorbed doses The absorbed doses for the kidneys (left and right), liver and spleen are provided in Figure 9.1. Across all patients and treatment cycles, the doses by injected activity to the left and right kidneys, liver, and spleen were 0.56 $\pm$ 0.19 Gy/GBq, 0.61 $\pm$ 0.18 Gy/GBq, 0.12 $\pm$ 0.10 Gy/GBq and 0.11 $\pm$ 0.07 Gy/GBq, respectively.

9.4 Discussion

In this preliminary study, we estimated the absorbed doses of kidneys, liver, and spleen in thirteen patients undergoing ^{177}Lu-PSMA.

Comparing our estimated absorbed doses with those reported in the literature, calculated from 3D SPECT images, we found similar in terms of magnitude. For the kidneys, the obtained doses were 0.56 Gy/GBq and 0.61 Gy/GBq, compared to 0.39 Gy/GBq (Violet et al., 2019), 0.49 Gy/GBq (Privé et al., 2021; Peters et al., 2022), 0.54 Gy/GBq (Rosar et al., 2021), and 0.67 Gy/GBq (Mix et al., 2022). similarly, for the liver, the doses were 0.12 Gy/GBq, whereas previous studies reported 0.09 Gy/GBq (Peters et al., 2022; Privé et al., 2021) and 0.10 Gy/GBq (Violet et al., 2019; Rosar et al., 2021). Regarding the spleen, the doses were 0.11 Gy/GBq compared to 0.08 Gy/GBq (Violet et al., 2019). Overall, the doses calculated using planar and hybrid methods were higher than those estimated using 3D SPECT images (refer to Chapter 5 for further details).

The STP-Intra method used for cycles 2 and above was evaluated in Chapter 6 for ^{177}Lu-DOTATATE therapy, but not specifically for ^{177}Lu-PSMA therapy. The simplified methods mainly relied on mono-exponential rather than tri-exponential fits, with the exception of the study by Jackson et al., 2020a. They estimated absorbed doses (^{177}Lu-PSMA) using average pharmacokinetics of a population by removing outliers, instead of relying on data from a previous cycle. While using pharmacokinetic parameters from a previous cycle might yield better results, further research is needed to validate this hypothesis. Unfortunately, our patient cohort does not allow us to conduct such analysis as it would require at least two cycles with three post-injection acquisitions.

Cette thèse est accessible à l'adresse : https://theses.insa-lyon.fr/publication/2023ISAL0068/these.pdf
© [L. Vergnaud], [2023], INSA Lyon, tous droits réservés

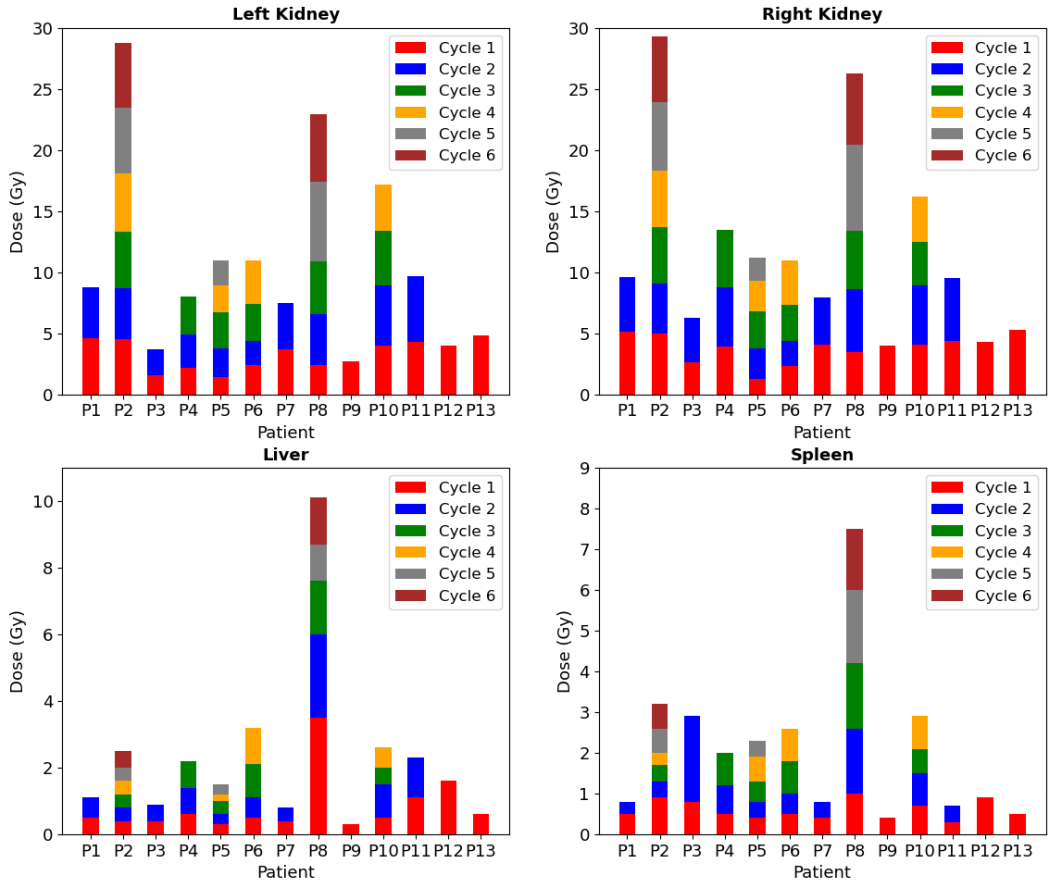

FIGURE 9.1 – Absorbed doses (Gy) for each treatment cycle of patients receiving ^{177}Lu-PSMA-1, excluding patients 14 and 15 who received ^{177}Lu-PSMA-617.

Currently, planar acquisitions are sometimes combined with a SPECT acquisition due to the potentially long acquisition times for SPECT images, which involve multiple FOVs. The use of CZT gamma cameras has facilitated faster acquisitions and more accurate dosimetry based on 3D SPECT images. Furthermore, a study by Komber et al., 2021 demonstrated that patient experience was not degraded when using this type of system compared to conventional gamma cameras.

9.5 Conclusions and perspectives

The dosimetric analysis of the kidneys, liver, and spleen in patients treated with ^{177}Lu-PSMA has shown results comparable to those available in the literature. However, it is important to note that this study represents a preliminary investigation that could be expanded through the inclusion of additional patients. Most studies referenced in Chapter 5 had a limited sample size, typically around 30 patients, with the exception of the study conducted by Schuchardt et al., 2022, which involved 138 patients. To provide a more comprehensive evaluation, it is necessary to incorporate the salivary and lacrimal glands into the dosimetry assessment. Developing a delineation methodology that considers the partial volume effect of these small structures would be crucial. Assessing uncertainties between treatment cycles could also be considered, comparing the three acquisitions in Cycle 1 with a single acquisition in subsequent cycles. Additionally, variations in pharmacokinetics between

Cette thèse est accessible à l'adresse : https://theses.insa-lyon.fr/publication/2023ISAL0068/these.pdf
© [L. Vergnaud], [2023], INSA Lyon, tous droits réservés

Cycle 1 and Cycle 4 are expected to be greater than those between Cycle 1 and Cycle 2. Thus, it is essential to conduct this evaluation between cycles. Lastly, in terms of lesion dosimetry, it would be valuable to define an overall tumour volume, as proposed by Violet et al., 2019. This would allow for the exploration of correlations between dosimetry and biological response.

Cette thèse est accessible à l'adresse : https://theses.insa-lyon.fr/publication/2023ISAL0068/these.pdf
© [L. Vergnaud], [2023], INSA Lyon, tous droits réservés

Cette thèse est accessible à l'adresse : https://theses.insa-lyon.fr/publication/2023ISAL0068/these.pdf
© [L. Vergnaud], [2023], INSA Lyon, tous droits réservés

Conclusions and perspectives

Summary of the work

This thesis focused on investigating the dosimetric and quantitative aspects of SIRT and ^{177}Lu TRT therapies. While the value of dosimetry in personalising and improving the effectiveness of SIRT therapies has been recognised, its systematic application in ^{177}Lu TRT therapies is not yet common practice.One of the challenges lies in establishing a clinical dosimetric workflow that can adapt to the specific constraints of each hospital. Additionally, in many countries, it is still not feasible to personalise treatment for individual patients. This formed the basis of the **first contribution** in this thesis. Considering the reduction in the number of post-injection acquisitions that is often envisaged, we proposed a dosimetric workflow that can adapt to the available number and timing of acquisitions. In France, where patients are typically not hospitalised for more than 24 hours post-injection, we performed a single acquisition shortly before the patient's departure. Simplified dosimetry methods were evaluated specifically for ^{177}Lu-DOTATATE therapy, with a focus on a time-point at 24h. In this study, the errors were estimated for extreme cases, as the STP-Intra method uses pharmacokinetic parameters from cycle 1 for cycle 4, which can span approximately 6 months. To summarise, this research has led to the development of an adaptive dosimetry protocol suitable for hospitals that cannot perform multiple acquisitions and have a limited time-point available, typically 24 hours.

In SIRT, the accuracy of predictive dosimetry, which is based on a ^{99m}Tc-MAA SPECT acquisition, relies on the corrections applied during the reconstruction, such as attenuation and scatter corrections. Interestingly, respiratory movement, despite its impacton the liver where the injected activity is concentrated, is typically disregarded during SPECT acquisitions that span several minutes. The **second contribution** of this thesis aimed to evaluate the dosimetric consequences of incorporating respiratory motion correction in a diverse cohort of patients (different pathologies, different number of tumours and location) undergoing SIRT. The objective was to determine if this correction could potentially alter patient management. Although this study did not reveal any statistically significant differences in terms of absorbed doses or required injected activities, some variations were observed in a small subset of patients. To validate or refute these findings, further investigations with more homogeneous patient cohorts should be conducted.

Lastly, SPECT acquisitions for patients undergoing ^{177}Lu-PSMA treatment pose challenges due to the larger field of view (FOV) required to encompass multiple OARs and diffuse metastase. As a results, multiple FOVs are necessary, leading to increased acquisition time. Adressing this issue, CZT gamma cameras offer a potential solution by enabling 3D whole-body SPECT imaging in a shorter time frame. However, the camera we used (VERITON) lacked the capability to acquire the recommended 208 keV energy peak. In our **third contribution**, we demonstrated the feasibility of ^{177}Lu dosimetry using this camera, utilising the 113 keV peak and providing a set of parameters for quantification. This study represents a milestone, with the potential for further parameter refinement as the system evolves. Finally, in our

Cette thèse est accessible à l'adresse : https://theses.insa-lyon.fr/publication/2023ISAL0068/these.pdf
© [L. Vergnaud], [2023], INSA Lyon, tous droits réservés

fourth contribution, we initiated a dosimetric study for patients undergoing ^{177}Lu-PSMA treatment, reconstructing images using the optimised parameters determined earlier. The preliminary dosimetric results are consistent with the existing literature on 3D dosimetry and appear to support the possibility of conducting dosimetry with CZT gamma cameras even in the absence of the 208 keV peak.

Building upon these findings, the subsequent sections will provide a detailed exploration the short-term, medium-term, and long-term perspectives stemming from this work and the literature.

Short-term perspectives

Dosimetry of salivary and lacrimal glands and tumour volume

Building upon the existing work, it would be beneficial to include the dosimetry of salivary and lacrimal glands as OARs. To achieved this, a specific segmentation methodology needs to be implemented, considering the partial volume effect and the challenges in contouring these structures on CT due to their dimensions. Additionally, individual lesion segmentation and estimation of tumour volume should be undertaken. It is important to note that the biological response of the patient to the treatment may not be solely attributed to a single lesion, but rather, the dose received by each lesion could provide valuable information in determining minimum absorbed dose thresholds for eliciting a response.

Increase in patient cohort size

One of the challenges we face is the limited amount of data, which hinders the establishment of statistically significant correlations. Moreover, standardised ^{177}Lu therapies result in minimal toxicities, making it crucial to establish correlations between absorbed doses and toxicities in order to personalise the injected activity for each patient. Increasing the number of patients included in each cohort would improve the statistical robustness of the studies. Furthermore, it would enable the creation of sub-cohorts to account for the individual specificities of each patient. For instance, in the case of ^{177}Lu-DOTATATE therapies, Minczeles et al., 2022 demonstrated a higher occurence of severe toxicities (platelets and hemoglobin) in women compared to men. These sub-cohorts could also enhance the accuracy of STP methods. By estimating average pharmacokinetic parameters for each sub-cohort, criteria could be established to assign new patients to the appropriate cohort. This approach would help mitigate significant uncertainties that may arise from outliers in overall pharmacokinetic parameters.

Validation of simplified methods

The simplified dosimetry methods studied in this thesis were evaluated for ^{177}Lu-DOTATATE. They should also be tested for ^{177}Lu-PSMA. Comparative studies of simplified dosimetry methods have been conducted using cohorts specific to each therapy. To comprehensively understand the uncertainties associated with all simplified dosimetry methods documented in the literature, a multicentre study could be conducted. Such a study would provide valuable insights and recommendations tailored to the constraints faced by each individual centre.

Cette thèse est accessible à l'adresse : https://theses.insa-lyon.fr/publication/2023ISAL0068/these.pdf
© [L. Vergnaud], [2023], INSA Lyon, tous droits réservés

Evaluation of inter-cycle errors with simplified methods

Throughout the course of treatment, the biodistribution of the radiopharmaceutical can undergo changes. When using the pharmacokinetic parameters from cycle 1 for subsequent cycles, it is important to consider that uncertainties may vary when analyzing cycle 2 or cycle 4. A comprehensive study should be conducted to assess the variations in uncertainties that can arise from using this type of method across different treatment cycles. This will provide valuable insights into the potential differences in accuracy and reliability associated with each cycle.

Automation of workflow using CE-marked dosimetry tools

Finally, in the short term, it could be relevant to adapt the dosimetric workflow developed in research for clinical use, using the available CE-marked dosimetric tools. The objective would be to initiate the inclusion of clinical dosimetry in all ^{177}Lu therapies, thereby identifying the practical challenges of implementation and adapting nuclear medicine departments.

Middle-term perspectives

Data collection

In the medium term, the establishment and provision of imaging database content (post-injection SPECT/CT acquisition of ^{177}Lu therapies) would enhance the validation and comparison of dosimetric methods. This data sharing would provide access to a wide range of different acquisition times and various types of images (planar and/or SPECT), allowing for the verification of the conditions of use for each method. Furthermore, hospitals facing limited camera availability could use multiple acquisitions of patients from other centres to derive average pharmacokinetic parameters for a given population. This approach would enable the direct application of simplified dosimetry methods. Finally, this pooling of data would facilitate the development of standards regarding the information required for dosimetry and the sharing of data.

Radiobiology

Radiobiology would enable the consideration of the biological effects associated with low dose rates of radiation and cellular repair (Pouget et al., 2021). Its incorporation could enhance the understanding of dose-response relationships and correlations between dose and toxicity.

Location of active bone marrow

While the occurrence of haematological toxicities in standardised ^{177}Lu therapies is generally low, accurately estimating the absorbed dose in the bone marrow is crucial for tailoring the administered activity. Increasing the activity could potentially raise absorbed doses, leading to elevate risks of toxicity. However, determining this estimate can be challenging due to the patient-specific variability in the location and volume of remaining bone marrow. In cases of metastatic prostate cancer, infiltrating bone metastases may have replaced active bone marrow, and the activity present in

Cette thèse est accessible à l'adresse : https://theses.insa-lyon.fr/publication/2023ISAL0068/these.pdf
© [L. Vergnaud], [2023], INSA Lyon, tous droits réservés

the bone lesions may have led to greater dose deposition in the bone marrow. Additionally, prior therapies may have caused damage to certain regions of the bone marrow. Conducting an assessment to identify the remaining bone marrow (Gosewisch et al., 2019) would offer a more precise evaluation of the absorbed dose within this organ.

Evaluating the impact of uncertainties on correlations

The number and duration of acquisitions can vary across different treatment cycles. Simplified methods like the M1, M2, and M3 methods presented in Chapter 6 can be employed. However, it's important to note that the uncertainties (Stabin, 2008) and doses differ between these methods. Therefore, it is crucial to assess these uncertainties to determine if they have any influence on potential correlations between doses and toxicities. The objective is to ascertain whether it is necessary to utilize a single dosimetric method for all cycles in order to establish correlations between dose and toxicity.

Enhancement of Patient Selection

Enhancing the criteria for patient inclusion can help avoid unnecessary treatments by utilizing PET imaging, which provides valuable information on the uptake of the radiopharmaceutical.

Long-term perspectives

Maximum Tolerated Dose

As shown in Chapter 1, the deposition of dose varies between EBRT and TRT. The maximum tolerated dose limits established for EBRT are not applicable to PRRT, as evidenced by Bergsma et al., 2016b and Bergsma et al., 2016a, in relation to haematological and renal toxicity, respectively. Therefore, it is necessary to define new maximum tolerated dose limits specifically tailored to TRT. This approach would enhance the customization of treatment, ensuring optimal patient care and safety.

Evaluation of new radioisotopes

TRT encompasses the utilisation of radioisotopes emitting various types of particles, including α and β^- particles. In both SIRT and TRT, β^- emitters are commonly employed, with an average path length of approximately 1-2 mm. However, there has been recent interest in α emitters such as ^{225}Ac, coupled with PSMA, which exhibit a mean path length in the range of tens of micrometers. Incorporating these α emitters could potentially mitigate toxicities by reducing cross-dose effects. For instance, in the case of active bone marrow, the cross-dose originating from bone lesions would be significantly diminished.

Enhancement of SPECT Image Quality

The restricted spatial resolution of gamma cameras represents a significant factor contributing to dosimetric uncertainties. This limitation leads to the partial volume effect, which results in signal blurring. Enhancements in the spatial resolution of gamma cameras would effectively diminish dosimetric uncertainties and enable more accurate dose calculations at the voxel level.

Cette thèse est accessible à l'adresse : https://theses.insa-lyon.fr/publication/2023ISAL0068/these.pdf
© [L. Vergnaud], [2023], INSA Lyon, tous droits réservés

Résumé étendu

Introduction

Le cancer est une maladie caractérisée par la multiplication incontrôlée de cellules anormales, qui échappent aux mécanismes de régulation (*Definition* 2023). En France, le nombre de nouveaux cas de cancer va continuer d'augmenter en raison du vieillissement de la population, des avancées dans les diagnostics et d'une augmentation des comportements à risque (*Cancer figures* 2023). Chaque patient bénéficie d'une prise en charge personnalisée afin de déterminer les meilleures options thérapeutiques parmi lesquelles on peut retrouver la radiothérapie interne sélective (RIS) ainsi que la radiothérapie interne vectorisée (RIV). Cette dernière est une thérapie standardisée qui tend à être personnalisée comme l'est la RIS pour améliorer la réponse au traitement (Garin et al., 2021).

En France, depuis 2018, le code de la santé publique (article R1333-62) stipule que l'exposition aux radiations des tissus doit être "évaluée et planifiée pour chaque individu". Cette exposition est mesurée en estimant l'énergie absorbée par unité de masse dans le tissue, i.e la *dose absorbée*. Elle dépend du radioisotope, de son activité, de sa proximité au tissu ainsi que de la durée d'exposition. Pour la dosimétrie, le suivi de la biodistribution du radioisotope au cours du temps est essentiel, en particulier, en RIV où le radiopharmaceutique (médicaments radioactif) va soit se fixer aux tumeurs ou aux organes à risque (OAR) soit être éliminé (urine).

Le ^{177}Lu est un radioisotope intéressant pour la RIV car il se désintègre en émettant des particules β^- qui servent à traiter les lésions et des photons gamma sortant du patient utilisés pour localiser le radiopharmaceutique. La détection est généralement réalisée à l'aide d'une gamma caméra de type Anger même si plus récemment, les caméras CZT se sont développées et ont montré une résolution en énergie et une efficacité de détection supérieures (Wernick and Aarsvold, 2004; Guérin et al., 2008). Cela leur permettraient de réduire les temps d'acquisition sans altérer la qualité d'image. A noter que le suivi de la biodistribution du radiopharmaceutique est l'une des difficultés majeures puisqu'il est conditonné par le nombre d'acquisitions (planaires et/ou TEMP) post-traitement réalisables : ce nombre étant lui-même limité par les contraintes cliniques. De plus, ces acquisitions sont impactées par des phénomènes physiques partiellement ou entièrement corrigés durant la reconstruction.

Dans cette thèse, nous nous sommes intéressés aux aspects dosimétriques et quantitatifs des thérapies RIS et RIV au ^{177}Lu. Une première partie est dédiée à l'état de l'art afin de présenter les thérapies par rayonnement et de mettre en lumière les challenges cliniques liés à la RIV. Elle inclut également une présentation de deux radiopharmaceutiques que sont le ^{177}Lu-DOTATATE et le ^{177}Lu-PSMA, des radioisotopes ^{99m}Tc et ^{177}Lu ainsi que des gamma caméras disponibles en clinique (Anger et CZT). Elle est suivi d'une description succincte des reconstructions tomographiques, des méthodes de correction des phénomènes physiques et des méthodes dosimétriques avant de se conclure par une revue de la littérature des workflows dosimétriques mis en place pour la dosimétrie des thérapies au ^{177}Lu. Un

Cette thèse est accessible à l'adresse : https://theses.insa-lyon.fr/publication/2023ISAL0068/these.pdf
© [L. Vergnaud], [2023], INSA Lyon, tous droits réservés

focus a été fait sur les méthodes n'utilisant que peu d'acquisitions post-traitement. La seconde partie est consacrée aux contributions réalisées au cours de cette thèse. Premièrement, un workflow dosimétrique s'adaptant au nombre d'acquisitions à disposition a été mis en place pour pouvoir estimer les doses absorbées par les OAR lors des thérapies au ^{177}Lu-DOTATATE. Une évaluation des méthodes simplifiées a également été fournie. Deuxièmement, l'impact de la correction du mouvement respiratoire lors de la plannification de la RIS a été évaluée ainsi que son influence sur la prise en charge des patients. Troisièmement, une étude a été menée quant à la faisabilité de la quantification au ^{177}Lu avec une gamma caméra CZT qui ne permet pas d'acquérir les photons de haute énergie. Elle a aussi permis de sélectionner des paramètres de reconstruction optimaux qui ont été appliqués lors d'une étude dosimétrique incluant des patients traités au ^{177}Lu-PSMA. Les résultats préliminaires ont été fournis dans une quatrième contribution.

Radiothérapies externe et interne

Cette section vise à présenter les différentes thérapies utilisant les rayonnements pour le traitement du cancer, afin de positionner la RIV parmi ces approches. Une description plus approfondie de la RIS et de la RIV est également fournie.

Radiothérapie externe (RE)

Principe La radiothérapie externe consiste à focaliser un faisceau ionisant sous différents angles sur une cible à traiter. La dose de rayonnement à délivrer est prescrite et un plan de traitement spécifique est mis en place (balistique du faisceau, nombre de séances et doses délivrées par séance) afin d'optimiser l'irradiation (destruction des tissus tumoraux et préservation des tissus sains) (*Radiothérapie externe* 2023).

Effets des rayonnements ionisants sur les cellules Les rayonnements ionisants endommagent et/ou fragmentent les brins d'ADN des cellules (cassures simple brin ou double brin) par une interaction directe ou indirecte suite à la création de radicaux libres (hydroxyle) lors de la radiolyse de l'eau (Kassis and Adelstein, 2005). La nature des dommages impacte le devenir des cellules (mort cellulaire, réparation fidèle ou non, mutation, anomalie, *Arbre des évolutions possibles de la cellule* 2023). Chaque tissu possède sa propre capacité de réparation qui peut être totale entre deux séances de radiothérapie (Dale and Carabe-Fernandez, 2005). De plus, des réponses biologiques (effets bystander) ainsi que l'implication du système immunitaire pourraient également être impliquées dans les dommages aux cellules tumorales (Pouget et al., 2022).

Dose absorbée L'exposition au rayonnement peut être caractérisée grâce à la **dose absorbée** en Gy. Elle correspond à l'énergie (E) fournie par les radiations et absorbée dans une masse de tissu, divisé par la masse (M) de ce tissu (Eq. 9.1).

$$D[Gy] = \frac{E[J]}{M[kg]} \tag{9.1}$$

Les doses sont importantes pour établir un plan de traitement pour traiter au mieux les lésions tout en limitant les doses absorbées par les OAR.

Cette thèse est accessible à l'adresse : https://theses.insa-lyon.fr/publication/2023ISAL0068/these.pdf
© [L. Vergnaud], [2023], INSA Lyon, tous droits réservés

Organes à risque Au cours du traitement, les tissus sains peuvent être traversés par le faisceau ionisant et être endommagés. Des seuils de tolérance de dose (Milano et al., 2007) ont été fixés afin de limiter les risques de toxicité et sont pris en compte au cours de la plannification.

Radiothérapie interne (RI)

Irathérapie L'irathérapie, également appelée thérapie à l'iode radioactif, est utilisée pour traiter l'hyperthyroïdie (Kaplan et al., 1998) et les cancers de la thyroïde (Sweeney and Johnston, 1995). Cette thérapie consiste à administrer de l'iode 131 radioactif au patient par voie orale ou par injection, car les cellules thyroïdiennes le captent naturellement, tout comme les cellules cancéreuses bien différenciées.

Traitement des métastases osseuses douloureuses La radiothérapie interne peut être utiliser pour traiter la douleur associée aux métastases osseuses du cancer de la prostate ou du sein, par exemple. En effet, certains radionucléides (89Sr, 223Ra, 32P) sont absorbés par les os en se comportant biologiquement comme le calcium. Liepe and Kotzerke, 2011 ont proposé une revue des radionucléides disponibles pour ce type de traitement.

Brachythérapie Elle consiste à positionner une source radioactive scellée à proximité ou à l'intérieur de la tumeur, de manière temporaire ou permanente. Cette technique permet d'irradier intensément la lésion tout en préservant les tissus sains environnants. Ses caractéristiques ont été décrites par Skowronek, 2017 et ses applications par Tanderup et al., 2017.

Radiothérapie interne sélective Cette thérapie est un traitement local pour les tumeurs hépatiques inopérables, indiqué et remboursé en France pour les carcinomes hépatocellulaires (CHC), les cholangiocarcinomes intra-hépatiques et les métastases de cancers colorectaux. D'autres applications sont disponibles dans la littérature (Barakat et al., 2022, King et al., 2008, Gonsalves et al., 2019, Helmberger et al., 2021). Ce traitement consiste à amener des microsphères de 90Y aussi près que possible de la lésion, via l'artère hépatique à l'aide d'un microcathéter, lors d'une procédure de radiologie interventionnelle. La désintégration des atomes de ^{90}Y générera des émissions β^- dont la distance moyenne et l'énergie sont de l'ordre de 3 mm et 0,93 MeV (Rathke et al., 2019) et qui endommageront les cellules tumorales. Deux types de microsphères à l'^{90}Y existent (résine, SIR-Sphère® ; verre, TheraSphere®). Leurs caractéristiques diffèrent (Labour, 2021) et influencent l'homogénéité de l'activité dans les tissus. Pour chaque patient, un choix est réalisé et un traitement personnalisé est proposé afin d'améliorer le taux de réponse comme démontré par Garin et al., 2021. Pour cela, une angiographie et une scintigraphie au ^{99m}Tc-MAA (macroaggrégats d'albumine) sont réalisées pour vérifier la sécurité du traitement pour le patient (critères d'inclusion) ainsi que pour personnaliser l'activité à injecter. En effet, l'angiographie permet de connaître la vascularisation du foie afin d'éviter les dérivations extra-hépatiques notamment pulmonaires (Kim et al., 2019) et gastro-intestinales qui pourraient survenir lors de l'injection des microsphères, de savoir où positionner le cathéter et le flux sanguin. Quant à l'acquisition TEMP/CT au ^{99m}Tc-MAA, elle permet de simuler la biodistribution des microsphères dans le foie et de réaliser une dosimétrie prédictive afin de personnaliser l'activité d'^{90}Y à injecter. A noter que le ^{99m}Tc-MAA est un substitut de l'^{90}Y et que de bonnes corrélations

Cette thèse est accessible à l'adresse : https://theses.insa-lyon.fr/publication/2023ISAL0068/these.pdf
© [L. Vergnaud], [2023], INSA Lyon, tous droits réservés

des doses entre les deux radioisotopes a été démontré pour les CHC mais pas pour les métastases hépatiques (Jadoul et al., 2020; Garin et al., 2016). Les microsphères à l'^{166}Ho sont utilisables pour la plannification et le traitement des patients et ont récemment été testées par (Stella et al., 2022). Une fois la biodistribution estimée, une dosimétrie prédictive est initiée en fonction de l'activité injectée afin de la moduler pour respecter les recommandations internationales pour les limites de tolérance. Après l'injection des microsphères d'^{90}Y, une vérification de leur biodistribution est réalisée à l'aide d'une acquisition PET/CT. Une dosimétrie post-traitement peut permettre de vérifier la thérapie par rapport à la prédiction. Une acquisition TEMP du rayonnement de freinage est également possible mais plus rare (Dewaraja et al., 2017; Siman et al., 2016). Certains aspects de cette thérapie sont à prendre avec précaution. Par exemple, l'utilisation du ^{99m}Tc-MAA comme substitut des microsphères d'^{90}Y est encore débattue, la position du cathéter peut influencer la biodistribution (Kim et al., 2019) et les contourages réalisés sur la TEMP/CT et recalés sur la PET/CT peuvent engendrer des différences de doses au niveau des tumeurs (Della Gala et al., 2022).

Radiothérapie interne vectorisée La RIV est une option de traitement pour les tumeurs inopérables et inaccessibles ainsi que les métastases surexprimant un certain type de récepteur. Pour chaque pathologie considérée, un radiopharmaceutique spécifique a été développé. Il se compose d'un radioisotope qui est la source de rayonnement pour le traitement, d'un vecteur moléculaire (ex : peptide, antigène, anticorps) qui permet l'internalisation du radioisotope (ex : ^{177}Lu, ^{90}Y, ^{225}Ac) dans la cellule tumorale, et d'un chélateur qui lie le radioisotope au vecteur, comme décrit dans la Figure 1.4. Il est injecté par intraveineuse, circule dans le flux sanguin et se fixe aux recepteurs tumoraux. Une fixation physiologique par certains organes du radiopharmaceutique peut être observé due à la présence de récepteurs cibles dans ces tissus (Demirci et al., 2016). Par la suite, nous nous interesserons aux radiopharmaceutiques ^{177}Lu-DOTATATE et ^{177}Lu-PSMA.

Comparaison de la RE et de la RIV

Bien que les principes radiobiologiques en jeu soient les mêmes, les réponses cellulaires diffèrent entre la RE et la RIV (Dale and Carabe-Fernandez, 2005). De fait, en RE, le faisceau est connu, focalisé sur une tumeur solide bien différentiée, avec un débit de dose élevé (1-2 Gy/min) et un temps d'irradiation court (environ 1 min). Une dosimétrie est ainsi réalisée pour personaliser le traitement pour chaque patient. A l'inverse, la RIV est indiquée pour les tumeurs inopérables ou inatteignables ou les métastases avec un débit de dose faible (<0.5 Gy/h), hétérogène (fixation aux recepteurs), variable et continu au cours du temps. Ce traitement est pour l'heure standardisé et requiert des mesures de radioprotection spécifiques une fois que le radiopharmaceutique a été injectée (Morris et al., 2021; Pouget et al., 2021; Dale and Carabe-Fernandez, 2005; Sadeghi et al., 2010; Kassis and Adelstein, 2005).

Challenges cliniques

La RIV a prouvé son intérêt thérapeutique au cours d'études de phase III. Cependant, certians patients inclus ne répondent pas au traitement : il conviendrait donc d'améliorer les critères de sélection afin d'éviter les traitements inutiles et les toxicités associées. De plus, les thérapies sont actuellement standardisées alors que

Cette thèse est accessible à l'adresse : https://theses.insa-lyon.fr/publication/2023ISAL0068/these.pdf
© [L. Vergnaud], [2023], INSA Lyon, tous droits réservés

l'ajustement de l'activité injectée pourrait augmenter les doses absorbées par les lésions (Del Prete et al., 2019) et potentiellement, leur efficacité. L'établissement de relations dose-effet et dose-toxicité restent des challenges pour la personnalisation des thérapies. La mise en place d'une dosimétrie clinique peut être compliqué due à l'augmentation de la thérapie en clinique ainsi que du temps d'occupation des caméras. Des workflows dosimétriques s'adaptant aux conditions cliniques doivent ainsi être proposés. Enfin, une sécurisation de l'approvisionnement de certains radiopharmaceutiques (Czernin and Calais, 2023) tel que le ^{177}Lu-PSMA devrait être mis en place pour éviter des pertes de chances pour le patient.

Radiothérapie interne vectorisée avec du ^{177}Lu

Cette section est une brève revue de la littérature des radiopharmaceutiques ^{177}Lu-DOTATATE et ^{177}Lu-PSMA utilisés en thérapie et vise à fournir les éléments cliniques nécessaires pour comprendre la thèse.

Essais cliniques de Phase III

Les études de Phase III NETTER-1 (Strosberg et al., 2017b; Strosberg et al., 2021) et VISION (Sartor et al., 2021) ont été menées afin de mettre en évidence l'intérêt thérapeutique du ^{177}Lu-DOTATATE et du ^{177}Lu-PSMA par rapport au traitement standard respectivement. Dans les deux cas, une augmentation de la survie sans progression et de la survie globale a été mise en évidence.

Imagerie pré-traitement

Acquisition TEP/CT au ^{68}Ga L'acquisition TEP/CT au ^{68}Ga est nécessaire pour sélectionner les patients qui pourront bénéficier de la RIV au ^{177}Lu. En effet, la captation du radiopharmaceutique par les lésions doit être supérieure à la captation du foie (Hope et al., 2020; Sartor et al., 2021). Pour chaque pathologie, plusieurs ligands sont disponibles : DOTATATE, DOTATOC et DOTANOC pour les tumeurs neuroendocrines et PSMA-11, PSMA-617 et PSMA-I&T pour les cancers de la prostate métastatiques résistants à la castration. Leurs taux de détection sont comparables (Hope et al., 2023,Berliner et al., 2017) bien que leurs biodistributions soient statistiquement significativement différentes (Gühne et al., 2022). Des corrélations significatives ont été observées entre la captation sur l'image pré-traitement et les doses absorbées (Stenvall et al., 2022; Violet et al., 2019; Wang et al., 2019).

Acquisition PET/CT au ^{18}F-FDG L'imagerie PET au ^{18}F-FDG est une imagerie complémentaire à l'imagerie au 68Ga (Seifert et al., 2023a) en fournissant une valeur pronostique (hétérogénéité tumorale, Hofman et al., 2015) et des informations sur l'agressivité de la lésion (Severi et al., 2013). En effet, elle permet de localiser les régions métaboliquement actives où le développement tumoral est susceptible d'être rapide. Cependant, cette acquisition n'est pas obligatoire, mais fortement recommandée. En général, ce sont les discordances potentielles avec la TEP au ^{68}Ga qui sont recherchées.

Plan de traitement

Standard Actuellement, en France, les plans de traitement pour les thérapies au ^{177}Lu sont standardisés. Chaque patient reçoit 4 injections de 7.4 GBq (TNE) et

Cette thèse est accessible à l'adresse : https://theses.insa-lyon.fr/publication/2023ISAL0068/these.pdf
© [L. Vergnaud], [2023], INSA Lyon, tous droits réservés

jusqu'à 6 injections pour les cancers de la prostate espacées de 8 ou 6 semaines respectivement. Toutefois, si le cancer continue de progresser malgré la thérapie, le traitement peut être interrompu après deux injections. En cas d'effets indésirables, l'activité injectée peut être réduite (Ladrière et al., 2023) ou le traitement peut être arrêté.

Personnalisé De nombreuses études ont montré des différences de doses absorbées entre les patients lorsque le traitement est standardisé (Sundlöv et al., 2017; Violet et al., 2019). Plusieurs auteurs ont mené des essais cliniques de phase II pour vérifier la faisabilité, la sécurité et l'efficacité d'un traitement personnalisé pour chaque patient. Pour personnaliser le traitement, l'activité injectée (P-PRRT, NCT02754297, Del Prete et al., 2019), le nombre de cycles (ILUMINET, NCT01456078, Sundlöv et al., 2022; Garske-Román et al., 2018) ou encore le temps entre deux cycles peuvent être modifiés (LUTHREE, NCT03454763). Lorsque l'activité ou le nombre de cycles est augmenté, la dose absorbée et/ou le taux de réponse est/sont augmenté(s) également.

Retraitement Quelques études se sont intéressées au retraitement des patients au ^{177}Lu-DOTATATE avec notamment une comparaison avec l'everolimus (NCT05773274, RETREAT), l'ajout de cycles additionnels au moins six mois après le traitement initial (NCT05816720) ou encore la comparaison entre l'ajout de deux ou de quatre cycles additionnels (NCT04954820, ReLUTH, Deshayes et al., 2022). Aucune étude ne semble être en cours pour la thérapie au ^{177}Lu-PSMA.

Effets indésirables

Pour ces thérapies, les effets indésirables restent limités, principalement de grades 1 et 2. Les toxicités de grade 3 ont affecté moins de 10% des patients inclus dans les essais NETTER-1 et VISION, à l'exception de l'anémie pour le ^{177}Lu-PSMA (12,9%). Une liste non exhaustive est donnée dans le Tableau 2.1. Certains organes présentent un risque plus élevé de développer des toxicités en raison de leur forte absorption du radiopharmaceutique. Pour la thérapie au ^{177}Lu-DOTATATE, les reins, le foie, la rate et la moelle osseuse sont considérés comme des OAR (Marin et al., 2018), même si seuls les reins et la moelle osseuse sont des organes limitants (LO) (Sandström et al., 2013). Pour la thérapie au ^{177}Lu-PSMA, les glandes lacrymales et salivaires doivent être ajoutées en tant que LO. Une forte absorption a également été observée dans le duodénum et l'iléon lors de la TEP au ^{68}Ga (Demirci et al., 2016). Pour protéger les reins, des acides aminés sont administrés au patient traité au ^{177}Lu-DOTATATE (Barone et al., 2004; Rolleman et al., 2003). Cependant, cela semble inefficace pour les thérapies au ^{177}Lu-PSMA (Yadav et al., 2017) : présence de récepteurs PSMA dans les tubules proximaux des reins (Baccala et al., 2007). L'infusion de mannitol n'a également pas prouvé son efficacité pour les reins (Sarnelli et al., 2019). L'utilisation d'un refroidissement externe n'a pas limité l'absorption dans les glandes salivaires (Yilmaz et al., 2019) contrairement aux comprimés de polyglutamate de folate ont entraîné une diminution significative de la dose moyenne absorbée par les glandes parotides (Sarnelli et al., 2019).

Imagerie post-traitement

Pendant le traitement, le patient est surveillé à l'aide d'analyses biologiques. Il est possible, mais pas nécessaire, d'ajouter des acquisitions post-traitement pour

Cette thèse est accessible à l'adresse : https://theses.insa-lyon.fr/publication/2023ISAL0068/these.pdf
© [L. Vergnaud], [2023], INSA Lyon, tous droits réservés

vérifier si les lésions identifiées sur la TEP au ^{68}Ga ont été traitées. Cependant, elles sont essentielles pour estimer les doses absorbées par les organes à risque et les lésions, et établir d'éventuelles corrélations avec les toxicités et l'efficacité (Cremonesi et al., 2018).

Evaluation de la réponse

L'évaluation de la réponse au traitement peut se faire à travers des données biologiques, l'imagerie, la qualité de vie et la douleur ressentie par le patient. Les marqueurs tumoraux comme le PSA pour le cancer de la prostate (Lilja et al., 2008) et la chromogranine A (Belli et al., 2009) pour les TNE permettent de suivre l'évolution de la maladie. Les critères de réponse métabolique (EORTC, PERCIST et RECIP 1.0) et anatomique (OMS et RECIST 1.1) basés sur l'imagerie TEP/CT sont également utilisés. Des questionnaires et des critères cliniques sont employés pour évaluer la qualité de vie (FACT-P Esper et al., 1997) et la douleur (BPI Stanhope, 2016). De nouveaux cadres ont été proposés pour améliorer l'organisation des données et définir des normes de reporting dans les études cliniques : PROMISE et PROMISEV2 (Seifert et al., 2023b; Eiber et al., 2018).

Predictive and prognostic factors

Dans le but d'améliorer la sélection des patients pour ces traitements, de nombreuses études se sont penchées sur la prédiction des réponses en utilisant l'imagerie pré-traitement et les analyses biologiques. Des biomarqueurs cliniques pertinents ont été identifiés, tels que l'âge, la présence de métastases viscérales ou hépatiques, l'invasion osseuse, la progression biochimique, et des critères d'imagerie tels que les résultats des images PET FDG et PSMA (Heidegger et al., 2022). Des évaluations des biomarqueurs sanguins ont également été effectuées. Des essais cliniques sont en cours pour évaluer si les informations issues de plusieurs modalités d'imagerie peuvent prédire la réponse tumorale individuelle ((NCT01842165, LUMEN ; NCT05513469, Radio-Marker ; NCT03667092 ; GENEBIOLuNET). De plus, des modèles prédictifs tels que des nomogrammes ont été développés pour prédire la survie globale, la survie sans progression du PSA et la diminution du PSA d'au moins 50% pour chaque patient traité au ^{177}Lu-PSMA (Gafita et al., 2021). Enfin, des études ont examiné la corrélation entre la fixation du radiopharmaceutique dans les volumes tumoraux et les doses absorbées estimées à partir des images TEMP, ainsi que l'utilisation de modèles d'apprentissage automatique et de régression pour la prédiction de la dose tumorale (Akhavanallaf et al., 2023) et la dosimétrie rénale (Peterson et al., 2023b).

Essais cliniques en cours

De nouvelles utilisations des radiopharmaceutiques sont en cours d'étude pour d'autres maladies et/ou différents stades de la maladie. Des essais cliniques sont en cours pour évaluer l'efficacité du ^{177}Lu-DOTATATE pour les TNE du grêle, les TNE pancréatiques, bronchiques, les paragangliomes, les phéochromocytomes, les méningiomes, les neuroblastomes, les glioblastomes, les carcinomes des cellules de Merkel, le cancer nasopharyngé métastatique et le cancer du sein de stade IV ou récurrent. Pour les métastases hépatiques des TNE, différentes modalités

Cette thèse est accessible à l'adresse : https://theses.insa-lyon.fr/publication/2023ISAL0068/these.pdf
© [L. Vergnaud], [2023], INSA Lyon, tous droits réservés

d'administration du ^{177}Lu-DOTATATE sont évaluées. Le ^{177}Lu-PSMA-617 est principalement utilisé pour les cancers de la prostate métastatiques résistants à la castration, et des essais sont en cours pour évaluer son efficacité en association avec d'autres traitements. D'autres applications, comme les cancers des glandes salivaires avancés et les gliomes récurrents de grade 3-4, sont également en phase d'essai. De plus, le ^{177}Lu-PSMA peut être combiné avec un autre ligand I&T dont l'intérêt thérapeutique est en cours d'évaluation dans une étude de phase III pour les cancers de la prostate métastatiques résistants à la castration.

Radioisotopes et systèmes d'imagerie

En médecine nucléaire, les produits radiopharmaceutiques sont administrés aux patients à des fins diagnostiques et/ou thérapeutiques. Un même radioisotope peut être utilisé pour différentes pathologies dès lors que le vecteur associé, s'il y en a un, soit adapté. Dans ce chapitre, nous nous concentrerons sur deux radioisotopes (^{99m}Tc et ^{177}Lu) dont la biodistribution peut être visualisée à l'aide d'une caméra-caméra à scintillation Anger NaI(Tl) ou à semi-conducteur par imagerie planaire et/ou TEMP. D'autres systèmes d'imagerie et radioisotopes existent mais ne seront pas décrits.

Description des radioisotopes

^{99m}Tc Le ^{99m}Tc provient de la désintégration du ^{99}Mo (émission β^-) et se désintégrera lui-même en ^{99}Tc en émettant des photons gamma dont l'énergie est d'environ 140 keV (87,8 %). Il a une demi-vie de 6,01 heures. En pratique, le ^{99m}Tc est largement utilisé en médecine nucléaire pour les scintigraphies car il émet des photons de faible énergie qui peuvent être détectés par une gamma-caméra. L'activité à injecter est donc limitée et permet de réduire l'irradiation du patient (beaucoup de photons, peu de dépôt d'énergie).

^{177}Lu Le ^{177}Lu est un radioisotope qui se désintègre en ^{177}Hf en émettant des particules β^- (Emean/EMax (%) : 47,66/177,0 keV (11,61) ; 78,61/248,6 keV (0,006) ; 111,69/385,3 keV (9,0) ; 149,35/498,3 keV (79,4)) et des photons gamma (112,95 keV (6,17%) et 208,37 keV (10,36 %)). Il a une demi-vie de 6,6463 jours. Le ^{177}Lu permet à la fois de traiter le patient grâce aux particules β^- avec un déplacement moyen de 0,67 mm dans les tissus mous (Dash et al., 2015) et de visualiser le traitement par des photons gamma recueillis à l'aide d'une gamma caméra.

Acquisitions avec une gamma caméra

Acquisition planaire L'acquisition planaire consiste en des acquisitions multiples par projection dans le plan du patient lorsque les détecteurs sont placés de part et d'autre du patient (antérieur et postérieur). Ce type d'acquisition est rapide et permet d'acquérir un large champ de vue. Cependant, les images obtenues correspondent à des projections antéro-postérieures de la biodistribution de l'activité chez le patient avec un chevauchement des organes et des lésions sur les images. Cela peut être particulièrement gênant pour l'étude d'une région spécifique.

Acquisition TEMP (Tomographie par émission monophotonique Lors des acquisitions TEMP, les têtes de détection tournent autour du patient et acquièrent des projections de la biodistribution du radiopharmaceutique dans le champ de vue sous

Cette thèse est accessible à l'adresse : https://theses.insa-lyon.fr/publication/2023ISAL0068/these.pdf
© [L. Vergnaud], [2023], INSA Lyon, tous droits réservés

différents angles. À la fin, une image 3D de la biodistribution peut être reconstruite à partir des projections. Contrairement aux images planaires, il est possible de corriger des phénomènes physiques tels que l'atténuation, la diffusion par exemple qui peuvent être incluses dans la reconstruction. Cependant, elle a un champ de vue limité. Par conséquent, pour réaliser une acquisition TEMP 3D du corps entier, plusieurs acquisitions TEMP sont nécessaires ce qui augmente les temps d'acquisition.

Gamma camera

Gamma caméra à scintillation Anger NaI(Tl) Les gamma-caméras de type Anger sont composées de deux ou trois têtes de détection constituée d'un collimateur pour sélectionner les photons arrivant perpendiculairement au détecteur, d'un cristal scintillateur pour transformer les photons gamma en photons lumineux, d'un guide de lumière pour amener les photons lumineux à l'entrée des photomultiplicateurs et de photomultiplicateurs pour transformer les photons de lumière en un signal électrique. La conversion des photons en un signal électrique est une conversion dite indirecte (passage des photons gamma en photons lumineux puis en signal électrique). Cette conversion peut entraîner une perte de signal et ajouter du bruit.

Gamma caméra à semi-conducteurs CZT Les gamma caméras à semi-conducteurs ont une meilleure sensibilité que les caméras de type Anger, ce qui a permis de réduire les temps d'acquisition et/ou l'activité injectée pour des performances diagnostiques comparables (Esteves et al., 2009; Duvall et al., 2011).

Les semi-conducteurs sont des matériaux avec des propriétés intermédiaires entre les conducteurs et les isolants. Contrairement aux conducteurs, ils ont une bande interdite qui limite le passage des électrons. Cependant, cette bande interdite est plus petite que celle des isolants, ce qui permet aux électrons de passer lorsqu'ils reçoivent de l'énergie. En pratique, chaque pixel des détecteurs fonctionne comme une jonction PN : d'un côté, le semi-conducteur est dopé N (excès d'électrons) et de l'autre côté, il est dopé P (déficit d'électrons). À la jonction, les trous et les électrons se recombinent pour créer des paires : cette région est appelée zone de déplétion. Cette région est polarisée en inverse à l'aide d'un générateur de tension pour minimiser le courant qui la traverse. Ainsi, lorsque les photons gamma créent des paires électron-trou dans la zone de déplétion, le courant mesuré est proportionnel à l'énergie du photon qui interagit. Initialement, les principaux semi-conducteurs utilisés dans les détecteurs étaient le silicium et le germanium car ils offrent une bonne résolution en termes d'énergie (Darambara and Todd-Pokropek, 2002). Cependant, dans les conditions d'utilisation clinique de la médecine nucléaire (température ambiante), ils ne fonctionnent pas correctement. En effet, la bande interdite de ces matériaux est petite (1,12 eV pour le silicium et 0,68 eV pour le germanium, Collings, 1980), de sorte que en l'absence de photons, les électrons de la bande de valence peuvent passer dans la bande de conduction grâce à l'énergie thermique. Le CZT a une bonne résolution en énergie. Il peut être utilisé à température ambiante grâce à sa largeur de bande (1,57 eV). De plus, son numéro atomique élevé lui permet d'avoir une meilleure puissance d'arrêt (Cherry et al., 2012) et donc une meilleure efficacité de détection que les caméras gamma de type Anger. Sa densité élevée favorise l'interaction photoélectrique. Enfin, l'épaisseur du semi-conducteur a un impact sur l'efficacité de l'absorption des rayonnements gamma, qui dépend également de l'énergie des photons.

Cette thèse est accessible à l'adresse : https://theses.insa-lyon.fr/publication/2023ISAL0068/these.pdf
© [L. Vergnaud], [2023], INSA Lyon, tous droits réservés

VERITON Le système VERITON utilise des détecteurs à semi-conducteurs solides et a une géométrie spécifique (douze têtes de détecteur indépendantes attachées à un anneau). Le but de cette conception est d'optimiser la collecte de photons en rapprochant les détecteurs du patient et en utilisant toute la surface du détecteur pour améliorer l'image TEMP.

Applications cliniques Plusieurs études ont testé les performances du système VERITON pour différentes procédures cliniques à partir d'images de fantômes et/ou de patients : perfusion cérébrale Bordonne et al., 2020; Cassol et al., 2019, scintigraphie osseuse Bahloul et al., 2021 et scintigraphie myocardique Imbert et al., 2021b. Ces études ont montré une sensibilité et un contraste améliorés par rapport aux caméras de type Anger, ce qui a permis d'améliorer la qualité des images.

Comparaison des gamma caméras

Les gamma caméras CZT offrent une meilleure résolution en énergie, une meilleure résolution spatiale intrinsèque et permet une conversion directe des photons en signal électrique.

Quantification TEMP et dosimétrie

Reconstruction TEMP

Une fois que l'acquisition TEMP a été réalisée, une reconstruction est nécessaire pour obtenir une représentation tridimensionnelle de la biodistribution du radiopharmaceutique dans le patient à un moment spécifique.

Transformée de Radon L'ensemble de projections bidimensionnelles prises à différents angles ϑ correspond au modèle mathématique connu sous le nom de transformée de Radon de la fonction de densité tridimensionnelle (Groch and Erwin, 2000). L'inverser permet d'obtenir la fonction de densité. Cependant, en raison du nombre fini de projections disponibles et de la présence de bruit dans les projections, il n'y a pas d'unicité dans la recherche d'une solution. Le problème inverse est mal posé, et deux types principaux de méthodes sont utilisés pour le résoudre : les méthodes analytiques et les méthodes itératives.

Rétroprojection filtrée La méthode de rétroprojection filtrée est une méthode analytique qui implique de filtrer les projections à l'aide d'un filtre en rampe pour améliorer la qualité de la reconstruction 3D obtenue par rétroprojection. Cette méthode est simple et rapide, mais elle ne prend pas facilement en compte les phénomènes physiques (par exemple, l'atténuation, la diffusion) et peut être perturbée par le bruit.

Reconstruction itérative Cette méthode vise à reconstruire une distribution d'activité à partir de projections mesurées. À cet effet, une estimation initiale de la distribution d'activité est définie (ex : image uniforme). Cette distribution est ensuite projetée pour obtenir des projections estimées, qui sont comparées aux projections mesurées afin de déterminer une matrice de correction qui est ensuite appliquée à la distribution estimée, la mettant à jour pour la prochaine itération. Il existe deux

Cette thèse est accessible à l'adresse : https://theses.insa-lyon.fr/publication/2023ISAL0068/these.pdf
© [L. Vergnaud], [2023], INSA Lyon, tous droits réservés

types de méthodes itératives : les méthodes algébriques et les méthodes statistiques. Une revue exhaustive de la littérature a été fournie par Hutton et al., 2006.

ML-EM L'algorithme ML-EM (Maximum Likelihood Expectation Maximization) est une méthode itérative statistique basée sur le modèle de vraisemblance avec une statistique de Poisson, qui représente la probabilité d'obtenir la distribution d'activité mesurée à partir de la distribution d'activité estimée. L'objectif est de maximiser la vraisemblance, et donc la probabilité que les projections mesurées et estimées soient identiques. Cette maximisation est réalisée à l'aide d'un algorithme d'espérance-maximisation qui met à jour la distribution d'activité estimée à chaque itération.

OSEM L'algorithme OSEM (Ordered Subset Expectation Maximization) est un algorithme qui réduit le temps de calcul par rapport aux algorithmes MLEM. En effet, la mise à jour des projections ne se fait plus sur l'ensemble des projections, mais sur un sous-ensemble de projections. De nos jours en clinique, la plupart des méthodes de reconstruction disponibles dans l'industrie sont basées sur OSEM.

Contrôle du bruit augmentation du bruit qui peut être contrôlée en utilisant un filtre de post-reconstruction ou des méthodes de régularisation telles que la méthode de vraisemblance pénalisée (**Depierro1995**; Webster Stayman and Fessler, 2000) directement intégrée dans la reconstruction.

Deep learning Une revue de la littérature de l'utilisation du deep learning en reconstruction tomographique a été proposée par Wang et al., 2020, tandis que Visvikis et al., 2022 ont mis en évidence les applications de l'intelligence artificielle dans les domaines de la médecine nucléaire et de l'imagerie moléculaire.

Correction des phénomènes physiques

Atténuation L'atténuation des photons gamma primaires se produit lorsqu'ils interagissent avec le tissu qu'ils traversent. Cela peut entraîner leur absorption totale par l'effet photoélectrique, ou une absorption partielle et une diffusion par diffusion Compton, ou uniquement une diffusion par diffusion cohérente.

Le coefficient d'atténuation linéaire, noté μ et exprimé en cm^{-1}, est utilisé pour caractériser la probabilité d'interaction entre les photons et le tissu traversé par unité de longueur. Ce coefficient est couramment utilisé pour décrire l'atténuation des photons gamma primaires en imagerie médicale et en radiothérapie. Les informations relatives à l'atténuation et au coefficient d'atténuation linéaire proviennent des travaux de Zaidi and Hasegawa, 2003.

En 1978, Chang, 1978 a proposé l'utilisation d'un seul coefficient d'atténuation linéaire pour l'ensemble du patient bien que le champ de vue comprenne des régions hétérogènes. Un nombre croissant de gamma caméras sont désormais équipées d'un scanner pour estimer des cartes d'atténuation pouvant être utilisées pour la correction (Fleming, 1989). Pour cela, les unités de Hounsfield sont associées à des coefficients d'atténuation linéaires par le biais de courbes de conversion déterminées pour chaque système et pour différentes énergies. Cette méthode peut être impactée par des incertitudes liées au recalage entre les images CT et TEMP et aux mouvements du patient. De plus, toutes les caméras ne sont pas associées à un scanner : c'est pourquoi, certains auteurs ont utilisé l'intelligence artificielle pour corriger l'atténuation Shi et al., 2020; Mostafapour et al., 2021.

Pour les thérapies au ^{177}Lu, la dose absorbée due aux rayonnements X est très faible par rapport aux doses délivrées aux organes et aux lésions (de l'ordre de Gy).

Cette thèse est accessible à l'adresse : https://theses.insa-lyon.fr/publication/2023ISAL0068/these.pdf
© [L. Vergnaud], [2023], INSA Lyon, tous droits réservés

Diffusion La diffusion correspond à la modification de la direction d'un photon par interaction avec la matière. L'effet principal est l'effet Compton (*Compton effect* 2023) qui se produit lorsque le photon interagit avec une couche d'électrons libres ou de valence. Une partie de l'énergie du photon est transférée à l'électron et la direction du photon est modifiée. Le deuxième effet, moins courant et se produisant avec des photons de plus faible énergie (<100 keV), est la diffusion cohérente (*Coherent scattering* 2023). Cette fois-ci, le photon conserve son énergie qui est trop faible pour libérer un électron et ne change que de direction. La diffusion a un impact à la fois sur la qualité de l'image TEMP et sur la quantification (Jaszczak et al., 1984). Elle se produit dans le patient, dans le collimateur et dans le cristal (De Nijs et al., 2014). Une revue de la littérature détaillée a été proposée par Hutton et al., 2011. Les deux principales méthodes utilisées en cliniques sont la méthode de la double fenêtre en énergie et la méthode de la triple fenêtre en énergie. Elles consistent à acquérir la fenêtre du primaire ainsi qu'une ou deux fenêtre(s) adjacente(s) afin d'estimer le diffusé et de le corriger.

D'autres méthodes basées sur la distribution d'énergie ont été présentées et comparées dans l'article de De Nijs et al., 2014. L'estimation précise de la diffusion obtenue par simulation de Monte Carlo reste la méthode de référence (Dewaraja et al., 2017, mais elle n'est généralement pas utilisée à cause des temps de calcul. Par conséquent, Xiang et al., 2020, ont comparé les reconstructions réalisées avec des estimations obtenues par apprentissage profond et celles obtenues par simulation de Monte Carlo et ont montré des résultats similaires, notamment en termes de récupération du contraste.

La méthode de correction de la triple fenêtre en énergie est recommandée pour la quantification du ^{177}Lu pour les deux pics de photons (Ljungberg and Sjögreen Gleisner, 2016), même si elle entraîne des inexactitudes significatives dans la quantification lorsque l'activité est faible et/ou en présence de bruit de fond.

Effet de volume partiel (EVP) Les gamma-caméras sont connues pour avoir une faible résolution spatiale (à 10 cm pour le ^{177}Lu, entre 18 et 22 mm Full Width at Half Maximum (FWHM) avec une reconstruction FBP Ryu et al., 2019), ce qui entraîne une sous-estimation de la concentration d'activité lorsque les volumes d'intérêt sont inférieurs à 2/3 de la FWHM (Marquis et al., 2023). Cela est connu sous le nom d'effet de volume partiel.

La contamination croisée est l'une des principales causes de l'effet de volume partiel en raison de la fonction d'étalement ponctuel du système (PSF), même si l'effet de fraction tissulaire qui est lié à l'échantillonnage de l'image a également un impact. L'EVP peut être impacté par les caractéristiques du système (résolution spatiale et échantillonnage de l'image), de l'objet (taille, forme, tissus environnants) et de la méthode de mesure. La non correction de l'EVP conduit à une sous-estimation significative des doses absorbées dans les lésions (Marquis et al., 2023). En pratique clinique, deux méthodes sont principalement utilisées : les coefficients de recouvrement et l'inclusion de la fonction d'étalement ponctuel (FEP) dans la reconstruction. Pour les autres méthodes, elles sont détaillées dans la revue proposée par Erlandsson et al., 2012.

Méthode n°1 : Elle consiste à estimer la FEP en utilisant une source ponctuelle dans l'air acquise à différentes distances du détecteur. Pour chaque acquisition, la largeur à mi-hauteur (FWHM) peut être estimée avant que la FEP soit modélisée par une gaussienne. La déconvolution de la FEP lors de la reconstruction réduirait l'effet de volume partiel, mais augmenterait le bruit et pourrait créer des artefacts de Gibbs.

Cette thèse est accessible à l'adresse : https://theses.insa-lyon.fr/publication/2023ISAL0068/these.pdf
© [L. Vergnaud], [2023], INSA Lyon, tous droits réservés

Méthode n°2 : Elle consiste en une correction post-reconstruction des volumes d'intérêt en utilisant des facteurs de correction estimés expérimentalement à partir d'un fantôme NEMA IEC sphères appelés Coefficients de Recouvrement (RC). Les facteurs de corrections dépendent du volume de la région considérée.

Temps mort Il correspond au temps minimum nécessaire entre deux photons successifs pour qu'ils soient tous les deux détectés par le système. Si le taux de comptage est trop élevé, le système ne pourra pas détecter tous les événements, ce qui entraînera une perte de photons détectés. Le taux de comptage estimé sera inférieur au taux de comptage réel. Les détecteurs peuvent suivre deux modèles idéaux de comportement en temps mort : le modèle paralysable et le modèle non paralysable. En général, la réponse du détecteur combine les deux (Yousaf et al., 2015; Lee and Gardner, 2000; Patil and Usman, 2009), mais parfois l'un est supposé prédominant sur l'autre, et un modèle idéal est considéré.

Modèle paralysable Lorsqu'un deuxième photon arrive pendant le temps mort créé par le premier, ce deuxième photon n'est pas détecté et le temps mort nécessaire pour détecter un nouvel événement recommence à zéro.

Modèle non paralysable Avec ce deuxième modèle, le deuxième photon incident n'est également pas détecté, mais contrairement au modèle bloqué, le temps mort ne recommence pas à partir du deuxième événement, mais seulement à partir du premier.

Deux méthodes permettent généralement de remonter jusqu'au temps mort : la méthode des deux sources et la méthode de la source en décroissance. La première consiste à réaliser trois acquisitions successives avec une première source (1), puis à ajouter la deuxième (1+2) et à retirer la première (2). Leurs taux de comptage réels sont notés R1, R12 et R2, respectivement. R_BG représente le taux de comptage de l'arrière-plan (Gardner and Liu, 1997). Le temps mort est estimé grâce à l'équation 4.2.4.3. La seconde consiste à positionner une source d'activité connue au plus près du détecteur et de réaliser des acquisitions régulière dans le temps avant d'ajuster un modèle de comportement pour en extraire le temps mort. Une variante de cette méthode consiste à éloigner progressivement la source du détecteur afin de faire varier le taux de comptage. Une fois que le temps mort a été évalué, sa correction peut être appliquée soit aux projections, soit à la reconstruction. Si le temps mort est important et/ou s'il y a des asymétries dans l'image, la précision de la quantification sera meilleur avec une correction directe du temps mort dans les projections (Cohalan et al., 2020).

Desy et al., 2020 recommandent de corriger le temps mort pour améliorer la quantification, en particulier si la PRRT est personnalisée. Les caméras à semi-conducteurs ne sont pas sujettes à une perte d'événements détectés car le temps de collecte de charge est très court. Cependant, lorsque deux événements se produisent successivement, une seule impulsion combinée est créée au lieu de deux : c'est ce qu'on appelle l'effet de superposition (pile-up) (Usman and Patil, 2018).

Filtres Des filtres intra- et/ou post-reconstruction peuvent être proposés pour réduire le bruit dans les reconstructions. Cependant, l'application de filtres modifiera la quantification dans les images : c'est pourquoi les filtres ne sont pas recommandés pour les reconstructions qui seront utilisées pour la dosimétrie (Dickson et al., 2022).

Cette thèse est accessible à l'adresse : https://theses.insa-lyon.fr/publication/2023ISAL0068/these.pdf
© [L. Vergnaud], [2023], INSA Lyon, tous droits réservés

Facteur de calibration

La calibration permet de convertir les images TEMP, exprimées en coups par mL, en activité (Bq). Cette conversion peut être réalisée soit avec un facteur de calibration (FC) , soit avec un facteur de sensibilité FS (équations 4.13 et 4.14 respectivement). Dans les deux cas, ces derniers doivent être déterminés pour chaque système d'imagerie, chaque radionucléide et chaque ensemble de paramètres d'acquisition et de reconstruction. Deux principales méthodes existent dans la littérature pour estimer le FC (Ljungberg and Sjögreen Gleisner, 2016; Dewaraja et al., 2012) : 1. Acquisition TEMP d'un grand fantôme uniforme d'activité connue avec les mêmes paramètres d'acquisition et de reconstruction que pour les patients (D'Arienzo et al., 2016). 2. Acquisition planaire d'une source ponctuelle dans l'air.

Méthodes dosimétriques

Une fois les images TEMP reconstruites et calibrées, la biodistribution de l'activité dans le patient pour chaque temps d'acquisition est connue. Les volumes d'intérêt (organes à risque et/ou tumeurs) sont alors segmentés soit sur l'image CT, soit sur l'image TEMP, soit sur les deux pour chaque acquisition. ou les deux pour chaque acquisition. Les activités dans les volumes sont estimées pour chaque temps, puis la courbe d'activité temporelle (Time Activity Curve, TAC) est calculée. Elle est ajustée à l'aide d'un modèle (trapézoïdal, mono exponentiel, bi exponentiel). L'intégrale de cette courbe correspond à l'activité cumulée du volume. Enfin, les méthodes dosimétriques permettent d'estimer les doses absorbées.

1. La méthode de dépôt local suppose que toute l'énergie des désintégrations d'un voxel source est déposée dans le même voxel correspondant au voxel cible.

2. Le formalisme du MIRD (Furhang et al., 1997) s'appuie sur des S-valeurs précalculées à partir de fantômes numériques pour les organes à risque (Chauvin et al., 2020) et les lésions (Olguin et al., 2020) qui permettent de remonter à la dose absorbée. L'équation correspondante est 4.15. Les S-valeurs dépendent du radionucléide, des caractéristiques du modèle (âge, sexe, masse, taille) et du tissu d'intérêt (Bardiès and Gear, 2021).

3. La méthode du noyau de dose ponctuelle consiste à convoluer un noyau de points de dose, généralement estimé par simulation de Monte Carlo, avec une carte de distribution d'activité (Furhang et al., 1996) pour obtenir une carte de dose absorbée. Les noyaux de points de dose représentent l'énergie déposée par une source ponctuelle à différentes distances dans un milieu uniforme.

4. La méthode des S-valeurs à l'échelle du voxel Les S-valeurs sont précalculées (Xin et al., 2023) et dépendent du radionucléide, de la taille du voxel et de l'activité cumulée. radionucléide, de la taille et de la géométrie des voxels.

5. La simulation Monte Carlo est utilisée pour simuler le transport de particules (par exemple, électrons, photons) à travers les différents tissus et pour estimer les dépôts d'énergie dans l'espace en fonction des interactions entre le rayonnement et la matière. Chaque tissu est caractérisé par un numéro atomique et une densité obtenus à partir du scanner, tandis que la distribution de l'activité du radionucléide est extraite des images TEMP ou TEP. Une carte du débit de dose au niveau du voxel est ainsi estimée. C'est la méthode gold standard.

Dosimétrie SIRT

La méthode de calcul de l'activité ^{90}Y à injecter dépend du type de sphères choisi : mono-compartimentale (sphères de verre) ou compartimentale (sphères de résine

Cette thèse est accessible à l'adresse : https://theses.insa-lyon.fr/publication/2023ISAL0068/these.pdf
© [L. Vergnaud], [2023], INSA Lyon, tous droits réservés

ou de verre), également appelé " partition model " (Levillain et al., 2021; Weber et al., 2022). Ces méthodes sont basées sur le formalisme MIRD. Le shunt pulmonaire est également évalué à l'aide de la fraction de shunt pulmonaire (LSF décrite dans Bastiaannet et al., 2018) dont la valeur ne doit pas être trop élevée afin d'éviter les pneumopathies d'irradiation. Des recommandations internationales (Weber et al., 2022; Levillain et al., 2021) ont été élaborées pour établir des limites de dose maximale tolérée en fonction du type de traitement et de la méthode de calcul utilisée. La correction des mouvements respiratoires en TEMP n'est pas nécessairement appliquée, bien que cela impacte l'estimation du volume moyen du dôme hépatique dans les poumons (Levillain et al., 2021). Kyme and Fulton, 2021 ont réalisé une revue de la littérature de toutes les méthodes de correction du mouvement dans le cas des acquisitions TEMP mais aussi PET et CT. Dans le cas de la radioembolisation, le mouvement respiratoire peut influencer la distribution estimée de l'activité (contribution à l'effet de volume partiel, Soret et al., 2007) présente presque entièrement dans le foie et pourrait avoir un impact sur la dosimétrie pré-traitement. Quelques études ont étudié l'impact de la correction des mouvements respiratoires sur les images TEMP Ausland et al., 2018; Bastiaannet et al., 2017; Santoro et al., 2022 et PET.

Revue des études dosimétrique des thérapies au ^{177}Lu

De nombreux workflows dosimétriques ont été mis en œuvre pour évaluer les doses absorbées chez les patients, en considérant les OAR et/ou les lésions, tout en tenant compte des contraintes cliniques et des données disponibles (par exemple, imagerie, biologie) propres à chaque hôpital. Dans une étude réalisée par Eberlein et al., 2017, la nécessité d'une dosimétrie individuelle pour les traitements théranostiques, tels que la thérapie à l'iode radioactif, la PRRT avec ^{177}Lu ou ^{90}Y, a été questionnée. L'étude a conclu que la dosimétrie est essentielle pour l'optimisation du traitement et la prédiction des réponses au traitement.

Contraintes cliniques

Les contraintes cliniques peuvent impacter la mise en place de la dosimétrie (état de santé du patient, nombre croissant de patients entraînant un temps d'occupation plus long de la caméra, et nécessité d'acquisitions multiples après chaque injection. Des lignes directrices de l'EANM (Gear et al., 2023) ont été fournies pour permettre la mise en œuvre de la dosimétrie tout en tenant compte des ressources disponibles (rôles des différents acteurs, partage des ressources et des exemples de protocoles de dosimétrie pour diverses thérapies).Les temps associés au workflow dosimétrique sont également à prendre en compte c'est pourquoi Dewaraja et al., 2022 ont proposé un workflow presque entièrement automatisé avec un temps de calcul total de 25 minutes.

Méthode de dosimétrie

Les workflows dosimétriques et/ou les doses absorbées ont été régroupés dans plusieurs revues de la littérature (Jackson et al., 2022; Alsadi et al., 2022; Sjögreen Gleisner et al., 2022; Huizing et al., 2018; Nautiyal et al., 2022 principalement pour le ^{177}Lu-PSMA. L'objectif de cette section est de fournir une description détaillée des flux de travail dosimétriques et des doses absorbées pour les thérapies au ^{177}Lu, sur la base des analyses documentaires existantes. En outre, les doses absorbées pour des volumes précédemment non pris en compte ont été incluses, ainsi que les études

Cette thèse est accessible à l'adresse : https://theses.insa-lyon.fr/publication/2023ISAL0068/these.pdf
© [L. Vergnaud], [2023], INSA Lyon, tous droits réservés

dosimétriques les plus récentes (tableaux 5.2 et 5.3 pour ^{177}Lu-SSRT et 5.4, 5.5, 5.6, 5.7 et 5.8 pour ^{177}Lu-PSMA).

Acquisition TEMP ou planaire ou les deux

L'estimation des doses absorbées dépend du type d'acquisitions utilisées. Willowson et al., 2018b ont montré les doses des reins obtenues à partir d'images planaires étaient trois fois plus élevées que celles obtenus avec des images TEMP (^{177}Lu-DOTATATE). De même que, Rosar et al., 2021 ont démontré qu'une acquisition TEMP associée à plusieurs acquisitions planaires (dosimétrie hybride) permettait d'obtenir une dosimétrie plus précise (référence : dosimétrie à partir des images TEMP) que seulement des acquisitions planaires. Les images planaires permettent d'obtenir une image corps entier du patient rapidement mais ce ne sont que des projections. Les acquisitions TEMP sont plus longues mais offrent une biodistribution 3D précise. Pour réduire ces temps d'acquisition tout en maintenant la précision, plusieurs alternatives ont été proposées : 1. Utilisation de la dosimétrie hybride 2. Utilisation de caméras gamma CZT (réduction du temps d'acquisition des TEMP) 3. Réduction du nombre de points temporels pour les acquisitions TEMP.

Dans le cas des thérapies au ^{177}Lu-PSMA, les patients présentent des métastases osseuses réparties dans tout le corps. Une acquisition corps entier devient nécessaire, mais difficile avec une gamma caméra conventionnelle. Par conséquent, la dosimétrie hybride est couramment utilisée. Dans les tableaux consacrés aux workflows dosimétriques pour les thérapies au ^{177}Lu-PSMA, seules 6 des 27 études utilisent plusieurs acquisitions TEMP.

Type de gamma caméra pour la dosimétrie

Les gamma caméras CZT permettent de réaliser des acquisitions TEMP corps entier plus rapide (2 à 3 fois plus vite Desmonts et al., 2020) sans déterioré les taux de détection par rapport à une gamma caméra de type Anger (Song et al., 2023). Un essai clinique (NCT04467567, EVADOVE177Lu) est actuellement en cours pour comparer les dosimétries obtenues avec les deux types de caméra.

Une ou plusieurs acquisitions post-thérapie

La multiplication du nombre de time-points étant difficile, plusieurs études se sont concentrées sur la réduction du nombre d'acquisitions en sélectionnant soigneusement les points temporels les plus pertinents.

Réduction et sélection des time-points Le passage de trois à deux time-points a été étudié par Chicheportiche et al., 2020 et ont comparé les d'activité cumulatée qui se sont montrées être les plus faible pour les time-points à 24h et à 168h. Le choix du modèle d'ajustement (mono- ou bi-exponentiel) et la réduction du nombre de points temporels pour les thérapies au ^{177}Lu-PSMA-I&T ont été spécifiquement discutés par Resch et al., 2023.

Méthodes à un seul time-point Lorsque l'objectif est de minimiser les acquisitions à une seule acquisition, des informations préalables (telles que des paramètres pharmacocinétiques du patient ou de la population) ou des simplifications deviennent nécessaires. Les différentes méthodologies et modèles pour le ^{177}Lu décrites dans la littérature sont répertoriés dans le tableau 5.1.

Comparaison de workflows dosimétriques simplifiés Plusieurs études ont comparé les workflows dosimétriques simplifiés (Hou et al., 2021; Zhao et al., 2019;

Cette thèse est accessible à l'adresse : https://theses.insa-lyon.fr/publication/2023ISAL0068/these.pdf
© [L. Vergnaud], [2023], INSA Lyon, tous droits réservés

Sundlöv et al., 2018; Brosch-Lenz et al., 2023. Diverses fonctions mathématiques simples, telles que les fonctions trapézoïdales, linéaires, mono-exponentielles, bi-exponentielles ou tri-exponentielles, sont couramment utilisées pour ajuster les courbes d'activité temporelle (TAC). certains effets sont communs à tous les patients (connus sous le nom d'effets fixes), tandis que d'autres sont propres à chaque individu (connus sous le nom d'effets aléatoires). Ces effets peuvent être efficacement décrits à l'aide de modèles mixtes non linéaires (NLMM) (Devasia et al., 2020). L'approche NLMM a présenté un biais plus faible et moins de valeurs aberrantes par rapport aux modèles mathématiques. De plus, il est intéressant de prendre en compte l'inclusion d'un modèle pharmacocinétique basé sur la physiologie (PBPK) pour incorporer les facteurs physiologiques du patient dans l'analyse (Hardiansyah et al., 2022). Pour réduire le nombre de time-points, d'autres approches ont vu le jour. Mix et al., 2022 ont introduit une méthode pour estimer la dose cumulative dans les reins uniquement sur la base de la dose estimée lors du premier cycle de traitement et des cycles 1 et 4 pour Pirozzi Palmese et al., 2023.

Time-points Le nombre limité de points temporels disponibles nécessite une sélection minutieuse. Plusieurs auteurs ont réalisé des comparaisons pour déterminer les time-points les plus importants (Sandström et al., 2020; Peterson et al., 2023b. Un time-point tardif semble nécessaire pour minimiser les erreurs d'estimation de dose, notamment pour les reins dans le cas du ^{177}Lu-DOTATATE (Larsson et al., 2012) et du ^{177}Lu-PSMA-I&T (Rinscheid et al., 2020), ou pour les glandes lacrymales dans le cas du ^{177}Lu-DKFZ-PSMA-617 (Hohberg et al., 2016).

Limitations Premièrement, un grand nombre d'études se concentrent uniquement sur l'évaluation et/ou la comparaison des doses aux reins uniquement. Deuxièmement, toutes les études ne suivent pas les mêmes protocoles de référence. Cela signifie que le time-point optimal estimé peut être optimal uniquement par rapport aux time-points disponibles. De plus, les méthodologies n'ont pas été évaluée pour tous les radiopharmaceutiques. Troisièmement, lors de l'estimation de la dosimétrie, les temps de demi-vie effective sont souvent approximés théoriquement, supposés être invariants pendant les cycles de traitement pour le même patient ou pris en moyenne à partir d'une population de patients. Cependant, il existe une variabilité inter-patients, en particulier dans la cinétique des lésions, ce qui peut influencer les résultats. Quatrièmement, bien qu'il soit souvent recommandé de réaliser une mesure tardive pour minimiser les erreurs, cela peut ne pas toujours être pratique en milieu clinique, notamment lorsque les patients sont renvoyés de l'hôpital dans les 24 heures. Enfin, chaque hôpital établit ses propres lignes directrices quant au nombre d'acquisitions post-traitement, ce qui peut ne pas toujours être réalisable en raison de la santé du patient, des limitations techniques ou de raisons logistiques.

Dosimétrie à l'échelle du voxel ou de l'organe Les évaluations de la dosimétrie des thérapies au ^{177}Lu présentées dans les tableaux précédemment cités ont principalement été réalisées au niveau de l'organe plutôt qu'au niveau du voxel, bien que cette dernière approche commence à émerger (Dewaraja et al., 2022; Violet et al., 2019; Akhavanallaf et al., 2021; Jackson et al., 2013 ; Sarrut et al., 2017b). La dosimétrie au niveau du voxel tient de l'hétérogénéité de l'absorption, alors qu'elles sont moyennées au niveau de l'organe. Enfin, la relation entre les doses absorbées et les réponses au traitement a été démontrée à la fois à l'échelle du voxel (Violet et al., 2019) et à l'échelle de l'organe (Alipour et al., 2023).

Cette thèse est accessible à l'adresse : https://theses.insa-lyon.fr/publication/2023ISAL0068/these.pdf
© [L. Vergnaud], [2023], INSA Lyon, tous droits réservés

Segmentation des régions d'intérêt Généralement, les images CT sont utilisées pour segmenter les OARs car elles fournissent des informations anatomiques. Pour simplifier le processus de contourage, l'extension de segmentation automatique d'organes basée sur l'apprentissage profond ("TotalSegmentator") du logiciel 3D Slicer ou d'autres approches d'apprentissage profond, comme celles utilisées par Dewaraja et al., 2022 peuvent être utilisées. Avec cette méthode, l'EVP n'est pas prise en compte c'est pourquoi certains auteurs tels que Gustafsson et al., 2017 ont utilisé les images TEMP pour le contourage des lésions.

Modélisation de la courbe d'activité temporelle La biocinétique des radiopharmaceutiques au ^{177}Lu comprend une phase de liaison suivie d'une phase d'élimination, divisée en élimination biologique (urine) et élimination radioactive (Jackson et al., 2013). Le choix de la modélisation dépend du nombre de points temporels disponibles et des contraintes cliniques. Généralement, des modèles mathématiques simples tels que des modèles trapézoïdaux, linéaires, mono-exponentiels, bi-exponentiels ou tri-exponentiels (Jackson et al., 2020a) sont utilisés, en particulier lorsque le nombre de points temporels est limité et dépendent du tissu. L'étude de Sarrut et al., 2017b a utilisé le critère d'Akaike pour déterminer le meilleur modèle ajusté.

Incertitudes À chaque étape du workflow dosimétrique, des incertitudes sont introduites. Des recommandations pratiques de l'EANM (Gear et al., 2018) offrent un cadre pour évaluer l'incertitude globale des flux de travail dosimétriques, elle est rarement rapportée dans la littérature bien qu'importante pour la comparaison des méthodologies

Organes à risque

Reins Ces organes filtrent le sang contenant les radiopharmaceutiques administrés et sont considérés comme des OARs dans les thérapies au ^{177}Lu. Après l'injection, la distribution du radiopharmaceutique dans les reins est hétérogène, comme le démontre Konijnenberg et al., 2007. La dose absorbée est généralement évaluée et comparée à la dose maximale tolérée en RE, qui est de 23 Gy afin de minimiser le risque de toxicité rénale. La dosimétrie rénale est essentielle car les reins sont souvent les organes limitant la dose (197 patients sur 200) selon Sandström et al., 2010 et sont couramment utilisés pour personnaliser les activités injectées. La toxicité rénale reste globalement très faible. Plusieurs études ont étudié les corrélations entre la dose et la toxicité rénale, comme le décrit Cremonesi et al., 2018.

Moelle osseuse La moelle osseuse, située à l'intérieur des os, est un organe composé de deux types principaux : la moelle rouge et la moelle jaune. La moelle rouge, également appelée moelle osseuse active (MOA), est responsable de la production de cellules sanguines. En revanche, la moelle jaune génère les tissus conjonctifs du corps. La distribution et la proportion de chaque type de moelle osseuse varient en fonction de l'âge et du sexe du patient (Dooms et al., 1985).

La MOA reçoit une dose absorbée à partir de l'activité présente dans la MOA elle-même (auto-dose), ainsi que dans le sang et le reste du corps (dose croisée). Plusieurs méthodes d'estimation de la dose à la MOA sont disponibles : 1. la biopsie pour déterminer l'activité présente dans la MOA (auto-dose) (Sgouros, 1993). 2. la concentration d'activité dans le sang est considérée comme étant la même que dans

Cette thèse est accessible à l'adresse : https://theses.insa-lyon.fr/publication/2023ISAL0068/these.pdf
© [L. Vergnaud], [2023], INSA Lyon, tous droits réservés

la MOA 3.l'imagerie. Une région spécifique de la MOA est sélectionnée comme substitut de l'ensemble de la MOA (vertèbres, Hagmarker et al., 2019).

De manière similaire aux reins, l'objectif de la dosimétrie de la MOA est de la comparer à la toxicité hématologique. Cependant, la présence de métastases osseuses peut compromettre l'utilisation de la dosimétrie basée sur l'imagerie. En effet, les métastases peuvent remplacer la MOA dans les vertèbres d'intérêt, les rendant inadaptées en tant que substituts. De plus, si les métastases sont proches de la MOA et présentent une forte captation, elles peuvent provoquer une irradiation significative de la MOA (Kind et al., 2022). De plus, les traitements précédents avant la thérapie au ^{177}Lu peuvent déjà avoir endommagé une partie de la MOA du patient. Il est donc crucial d'estimer la localisation restante de la MOA du patient pour évaluer avec précision la dose reçue par cet organe.

Glandes salivaires Les glandes salivaires sont des OAR lors des thérapies au ^{177}Lu-PSMA en raison de la présence de récepteurs PSMA auxquels le radiopharmaceutique se lie. Diverses stratégies ont été étudiées pour réduire la dose absorbée dans ces glandes : comprimés de polyglutamate (Paganelli et al., 2020) ou le refroidissement externe (Junqueira et al., 2021) ont été testés.

Glandes lacrymales Les glandes lacrymales sont des organes relativement petits qui sont considérés comme limitant la dose (Hohberg et al., 2016), ce qui peut poser des défis pour leur segmentation.

Tumeurs

Dosimétrie La dosimétrie des tumeurs est réalisée pour établir une relation entre la dose absorbée et la réponse de la tumeur (Alipour et al., 2023). L'hétérogénéité des récepteurs à la surface des cellules tumorales peut influencer la relation entre la dose absorbée et le nombre de cassures double brin par cellule (réponse) (Tamborino et al., 2022). Une revue des facteurs techniques et biologiques affectant la relation dose-réponse en RPT, ainsi que des questions non résolues, a été fournie par Sgouros et al., 2021. Dans la littérature, deux stratégies sont couramment utilisées : la dosimétrie des lésions individuelles (Delker et al., 2016; Okamoto et al., 2017; Feuerecker et al., 2022) ou la dosimétrie du volume tumoral total (Violet et al., 2019).

Tumour sink effect Le "tumour sink effect" fait référence à une augmentation de la captation du radiopharmaceutique par les tumeurs, accompagnée d'une diminution correspondante de la captation dans les tissus sains. Comprendre cet effet est essentiel pour personnaliser les traitements, notamment dans les cas de maladie étendue (Jackson et al., 2022), car cela permettrait de préserver les tissus sains tout en augmentant les doses administrées aux tumeurs.

Dose maximale tolérée

En général, les seuils de dose maximale tolérée utilisés en radiothérapie externe (Milano et al., 2007) sont généralement appliqués à la thérapie ciblée par radionucléides. Cependant, le type d'irradiation diffère entre les deux thérapies. Par exemple, en radiothérapie externe, la limite de dose pour le rein est fixée à 23 Gy, et pour la moelle osseuse, elle est de 2 Gy. La validité de ces seuils a été remise en question par Bergsma et al., 2016b et Bergsma et al., 2016a dans le contexte de la PRRT avec le

Cette thèse est accessible à l'adresse : https://theses.insa-lyon.fr/publication/2023ISAL0068/these.pdf
© [L. Vergnaud], [2023], INSA Lyon, tous droits réservés

^{177}Lu-DOTATATE. De plus, la fractionnement du traitement pourrait permettre de dépasser ces seuils (Eberlein et al., 2017) en augmentant la dose de 23 Gy à 35 Gy pour 4 cycles.

Contribution n°1 : Workflow dosimétrique adaptatif pour les traitements au ^{177}Lu-DOTATATE

Introduction

La PRRT (Peptide Receptor Radionuclide Therapy) est une option de traitement contre le cancer (Strosberg et al., 2017b) pour les patients atteints de tumeurs neuroendocrines inopérables qui expriment des récepteurs de la somatostatine (Mansi et al., 2020). Le traitement consiste à injecter par voie intraveineuse un analogue de la somatostatine radiomarqué avec le ^{177}Lu (^{177}Lu-DOTATATE). Bien que le traitement soit standardisé, il a été démontré que la distribution de la dose absorbée varie d'un patient à l'autre (Sandström et al., 2013) et la biodistribution du radiopharmaceutique évolue au fil du temps. C'est pourquoi aujourd'hui, la mise en œuvre d'une dosimétrie spécifique à chaque patient basée sur l'imagerie est un défi. La précision des estimations dosimétriques dépend du nombre d'acquisitions TEMP/CT disponibles après chaque injection. Idéalement, plusieurs points temporels seraient nécessaires pour construire une courbe d'activité temporelle dans les organes d'intérêt (Hänscheid and Lassmann, 2020; Bardiès and Buvat, 2011). Cependant, les acquisitions post-traitement ne sont pas obligatoires et leur nombre et leur fréquence dépendent de l'institution (contraintes cliniques). L'un des problèmes actuels est de mettre en place des workflows ne nécessitant qu'un faible nombre d'acquisitions TEMP/CT afin de faciliter la mise en œuvre de la dosimétrie en pratique clinique.

Dans ce travail, nous proposons un flux de workflow dosimétrique spécifique au patient basé sur l'imagerie avec un nombre réduit d'acquisitions pour la thérapie au ^{177}Lu-DOTATATE des tumeurs neuroendocrines, applicable en clinique. Des méthodes alternatives ont été mises en œuvre et évaluées afin d'utiliser le flux de travail même si certaines acquisitions manquent. De plus, plusieurs méthodes d'évaluation de la dose dans la moelle osseuse sont proposées et comparées.

Matériel et méthode

Patients Dans cette étude, deux cohortes de patients ont été incluses. La première cohorte (cohorte de patients, 13 patients) a été utilisée pour effectuer les calculs dosimétriques et valider les méthodes alternatives nécessitant peu d'acquisitions TEMP/CT. La deuxième cohorte a été utilisée uniquement pour la validation (cohorte de validation, 7 patients).

Images acquises Pour la cohorte de patients, trois acquisitions TEMP/CT étaient prévues à 1H, 24H et 96H ou 144H après la première injection. Pour les autres cycles, une seule acquisition à 24H était prévue. Cependant, certaines acquisitions ne peuvent pas être réalisées pour des raisons cliniques ou techniques, ou en raison de la pandémie de COVID. Pour la cohorte de validation, trois acquisitions TEMP/CT ont été réalisées et sont disponibles à 6H, à 24H et à 7 jours après les cycles 1 et 4.

Cette thèse est accessible à l'adresse : https://theses.insa-lyon.fr/publication/2023ISAL0068/these.pdf
© [L. Vergnaud], [2023], INSA Lyon, tous droits réservés

Acquisition TEMP/CT quantitative **Paramètres d'acquisitions** Les acquisitions d'images ont été réalisées avec un GE Discovery NM CT 670 pour la cohorte de patients et avec un GE Discovery NM CT 870 DR pour la cohorte de validation. Les systèmes d'imagerie sont composés de deux détecteurs à 180° équipés de collimateurs MEGP (Medium Energy General Purpose). Les paramètres d'acquisition pour chaque système sont indiqués dans le Tableau 6.2.

Paramètres de reconstruction Pour les deux cohortes, les images ont été reconstruites avec le logiciel Xeleris 3.0 à l'aide de l'algorithme OSEM 3D (8 itérations et 8 sous-ensembles) avec correction de la PSF (reconstruction de la résolution). L'atténuation a été corrigée à l'aide des images CT. La correction de la dispersion a été réalisée avec la méthode de la fenêtre à double énergie (la méthode TEW n'étant pas disponible dans le logiciel).

Calibration Un fantôme Jaszczak a été rempli avec une activité connue de 177 Lu avant d'être acquis avec le même protocole que pour les patients (Dewaraja et al., 2012; Ljungberg and Sjögreen Gleisner, 2016). Les facteurs de sensibilité en mode tomographique (c'est-à-dire en tenant compte des deux têtes de détecteur) étaient de 7,6 cps/MBq et 18 cps/MBq pour les caméras Discovery NM CT 670 et 870DR respectivement.

Temps mort Pour l'acquisition précoce, les images de la cohorte de patients ont été corrigées pour le temps mort selon une variation de la méthode de la source en décroissance. Pour les acquisitions ultérieures, le temps mort a été considéré comme négligeable (Desy et al., 2020) et n'a pas été pris en compte.

Workflow dosimétrique adaptatif **Volumes d'intérêt (VOI)** Les reins gauche et droit, le foie incluant les tumeurs et la rate (RG, RD, F, R), ont été segmentés manuellement sur la première image CT acquise. Les contours 3D obtenus ont ensuite été propagés à toutes les autres images CT grâce à des champs vectoriels déformables obtenus à partir de l'enregistrement d'images déformables (Delmon et al., 2013) avant d'être corrigés manuellement si besoin.

Approche générale Des simulations Monte Carlo avec GATE (Sarrut et al., 2014) ont été utilisées pour estimer les distributions des débits de dose. Les voxels sont considérés comme une source isotrope de décroissance du 177 Lu avec une activité proportionnelle à la valeur de comptage dans le voxel. En pratique, cela signifie que 1×10^6 (1 MBq) particules primaires (ions en décroissance) ont été simulées. La distribution finale du débit de dose a ensuite été mise à l'échelle en fonction de l'activité totale estimée à partir des images TEMP. Cette approche nous permet de prendre en compte à la fois l'auto-dose et la contre-dose dans la terminologie MIRD (Dewaraja et al., 2012). Pour tous les VOI et tous les time-points, le débit de dose absorbée (ODR, pour Organ Dose Rate) a été calculé en faisant la moyenne des valeurs des débits de dose de tous les voxels appartenant au VOI. Cette étape conduit à une courbe de débits de dose temporel (TDRC, pour Time Dose-Rate Curve) pour toutes les injections. Afin de calculer la dose absorbée totale correspondant à l'intégrale temporelle de ces courbes, la méthode analytique proposée par Jackson et al., 2020b basée sur une fonction tri-exponentielle a été utilisée en remplaçant l'activité par le débit de dose (6.1). À la fin, l'intégration temporelle de TDRC correspond à la dose absorbée par l'organe (6.2).

Cas particulier : l'acquisition à 24 heures était manquante lors du premier cycle Dans ce cas, l'ODR manquant a été substitué par l'ODR d'un autre cycle à 24 heures pour le même patient (le plus proche dans le temps) et sa durée exacte a été utilisée pour l'ajustement du TDRC. Étant donné que les activités injectées varient d'un cycle à l'autre, l'ODR substitué a été ajusté à l'activité du cycle. Cette méthode est appelée

Cette thèse est accessible à l'adresse : https://theses.insa-lyon.fr/publication/2023ISAL0068/these.pdf
© [L. Vergnaud], [2023], INSA Lyon, tous droits réservés

méthode du point temporel manquant (M1) et est illustrée dans la figure 6.3. La variabilité de l'ODR a été évaluée pour chaque patient et chaque VOI à 24 heures (par exemple, ODR du rein gauche à 24 heures des cycles 1, 2, 3 et 4). Pour estimer l'erreur associée, nous avons calculé les doses absorbées par les organes avec deux méthodes pour les patients qui avaient trois ODR : 1) à partir des trois ODR initiaux (méthode de référence) et 2) à partir de deux ODR initiaux et d'un ODR substitué à 24 heures (méthode du point temporel manquant M1). Le pourcentage de différence de dose entre les deux méthodes a été calculé pour les cohortes de patients et de validation.

Estimation de la dose absorbée pour les cycles avec une seule acquisition Lorsque les paramètres pharmacocinétiques ont pu être évalués au cours du cycle 1, ils sont réutilisés pour les cycles suivants. Cette méthode est appelée méthode STP-Intra (M2). Dans le cas inverse, les paramètres pharmacocinétiques d'une population ont été utilisés en supposant être homogènes avec ceux du patient. Cette méthode alternative est appelée méthode STP-Inter (M3). Les erreurs associées à cette approche ont été estimées pour le cycle 1 dans la cohorte de patients et pour les cycles 1 et 4 dans la cohorte de validation en utilisant la méthode leave-one-out, en comparant l'estimation de la dose tri-exponentielle à l'estimation de la dose STP-Inter et en calculant le pourcentage de différence de dose. La méthode leave-one-out a été appliquée indépendamment à chaque cohorte.

Workflow dosimétrique pour la moelle osseuse Le workflow était similaire, à l'exception de la délimitation de trois types de VOI différents pour estimer les doses absorbées, selon diverses propositions de la littérature : 1) la partie trabéculaire des vertèbres entre L2 et L4, 2) entre L1 et L5 et 3) entre T9 et L5. Notez que les patients des deux cohortes n'avaient pas de lésions dans les vertèbres. La dosimétrie de toutes les VOI a été comparée. De plus, la partie visible de l'humérus (partie supérieure) a également été délimitée afin d'avoir une référence pour le bruit de fond car c'est la seule région où il n'y a pas de tumeur ou d'organe présentant une forte captation mais qui contient de la moelle osseuse (2,3% Hindorf et al., 2010).

Résultats

Résultats dosimétriques de la cohorte de patients Le temps mort était de 1,87 µs pour le GE Discovery NM CT 670 et une correction du temps mort a été appliquée pour la cohorte de patients. Les doses absorbées estimées pour tous les patients de la cohorte de patients pour RG, RD, F et R sont présentées dans la figure 6.6. Lorsque les données n'étaient pas disponibles, les doses absorbées ont été approximées par la moyenne des doses absorbées disponibles multipliée par le nombre de cycle(s) manquant(s) (en blanc avec une ligne en pointillés). Notez que l'échelle n'est pas la même pour chaque graphique.

Liver, kidneys and spleen La variabilité inter-patients des doses absorbées cumulatives était élevée pour tous les organes tandis que la variabilité intra-patient des doses absorbées pour tous les cycles était faible. La moyenne des coefficients de variation des doses absorbées entre les cycles était de 10,4% pour le RG, 14,9% pour le RD, 15,5% pour le F et 11,5% pour la R. Les doses par activité injectée [mGy/MBq] ont été moyennées sur tous les cycles pour chaque patient et sont représentées dans la figure 6.7 pour les quatre organes. Pour la moelle osseuse, les doses par activité injectée ont été données sous la forme de moyenne ± écart-type : 0,04 ± 0,02 mGy/MBq pour L2 à L4, 0,04 ± 0,03 mGy/MBq pour L1 à L5 et 0,04 ± 0,02 mGy/MBq pour T9 à L5. Enfin, la figure 6.8 résume le flux de travail utilisé pour la cohorte de patients.

Cette thèse est accessible à l'adresse : https://theses.insa-lyon.fr/publication/2023ISAL0068/these.pdf
© [L. Vergnaud], [2023], INSA Lyon, tous droits réservés

Les erreurs estimées correspondantes de tous les cas sont proposées ci-dessous sous la forme [Minimum ; Médiane ; Maximum ; Moyenne].

Moelle osseuse Les doses absorbées estimées pour la moelle osseuse sont présentées dans la figure 6.9. Pour chaque patient, les trois premières barres représentent les doses absorbées mesurées pour chaque volume substitut de moelle osseuse (L2 à L4, L1 à L5 et T9 à L5). La quatrième barre représente les doses absorbées par l'humérus en tant que contrôle.

Comparaison des méthodes M1, M2 et M3 vs la méthode de référence **Coefficients de variation des ODR** Les coefficients de variation des ODR donnent une indication des différences entre les ODR au même instant mais pour des cycles différents, ajustés aux activités injectées. Les médianes des coefficients de variation (%) des ODR sont présentées dans le tableau 6.3.

Les erreurs associées aux méthodes M1, M2 et M3 sont données dans les figures 6.10, 6.11, 6.12 et 6.13.

Discussion

Dans cette étude, nous avons proposé un workflow dosimétrique adaptée aux patients basée sur l'imagerie, qui peut être utilisée même avec un nombre limité de points temporels TEMP. Cette méthode repose sur l'ajustement tri-exponentiel de débits de dose calculés par simulation Monte Carlo. Elle peut être utilisée dans un contexte clinique et permet d'effectuer la dosimétrie même en cas d'acquisitions manquantes.

Workflow dosimétrique Dans cette étude, le modèle tri-exponentiel a été choisi pour prendre en compte la physiologie des patients et semble être meilleur que le modèle mono-exponentiel (Guerriero et al., 2013). Une acquisition précoce est nécessaire pour estimer la phase d'absorption, qui est très rapide. Au cours de l'acquisition d'environ une heure, la distribution dans le patient peut changer. Cependant, l'acquisition rotative de 15 minutes (un lit) tend à lisser l'activité et nous n'avons pas observé de grands changements de distribution entre les premières et les dernières projections de la séquence. De plus, la dosimétrie a été réalisée avec des simulations Monte Carlo pour prendre en compte les images des patients et l'irradiation croisée (Grimes and Celler, 2014; Finocchiaro et al., 2020). La contribution de l'irradiation croisée est significative pour la moelle osseuse (Forrer et al., 2009a) et peut être importante pour les reins si sa dose auto-absorbée est faible ou si la charge tumorale est élevée (Sandström et al., 2018). Le temps de calcul était plus long que les approches analytiques (méthode de dépôt local ou convolution DPK), environ 10 minutes de calcul sur une station de travail classique pour chaque acquisition.

Dosimétrie La variabilité inter-patients des doses absorbées par chaque organe (figure 6.6) était élevée : les coefficients de variation des doses absorbées cumulatives étaient de 38,4 % pour RG, 43,6 % pour RD, 70,9 % pour F et 38,3 % pour R. Cette variabilité inter-patients peut être en partie expliquée par la proximité des lésions ou des organes avec une forte captation (le foie pour le rein droit et la rate pour le rein gauche). Cette variabilité illustre l'importance de réaliser une dosimétrie personnalisée pour analyser les effets du traitement.

Cette thèse est accessible à l'adresse : https://theses.insa-lyon.fr/publication/2023ISAL0068/these.pdf
© [L. Vergnaud], [2023], INSA Lyon, tous droits réservés

La variabilité intra-patiente entre les cycles était relativement faible pour les organes avec une forte captation. Cependant, ce n'était pas le cas pour la moelle osseuse (61 % pour L2 à L4, 69 % pour L1 à L5 et T9 à L5). Sundlöv et al., 2017 ont supposé que ces changements intra-patients étaient liés à la pression artérielle et au degré d'hydratation. Dans leur étude, les médianes des doses absorbées par unité d'activité injectée pour RG et RD étaient proches de celles trouvées ici (0,45 mGy/MBq et 0,47 mGy/MBq pour RG et RD respectivement). Pour les organes à risque, des seuils de dose maximale tolérée issus de la radiothérapie externe ont été pris en compte : 23 Gy pour les reins et 2 Gy pour la moelle osseuse. Pour les reins, un patient (P8 avec 19 Gy et 24 Gy pour RG et RD respectivement) dépassait le seuil si l'on tient compte des cycles manquants également, mais aucune toxicité rénale sévère n'a été observée. Pour estimer les doses absorbées par la moelle osseuse, trois VOI de substitution ont été délimitées. La normalité des séries de doses absorbées cumulatives (uniquement les cycles disponibles) a été évaluée avec un test de Shapiro-Wilk (p-value = 0,1038 pour L2 à L4, p-value = 0,01875 pour L1 à L5 et p-value = 0,07838 pour T9 à L5). La différence observée entre les séries de doses absorbées cumulatives de L2 à L4 et de L1 à L5 était significative (test de rang signé de Wilcoxon : p-value = 0,02), ce qui n'était pas le cas pour les autres comparaisons (test de rang signé de Wilcoxon : p-value = 0,45 entre L2 à L4 et T9 à L5 et p-value = 0,09 entre L1 à L5 et T9 à L5). Pour le patient 3, les doses absorbées ont été évaluées sur deux cycles seulement et la limite de 2 Gy était déjà presque atteinte. Il est probable que la limite ait été dépassée avec les deux autres cycles, mais aucune toxicité significative n'a été observée. En revanche, le patient 10 présente une toxicité de grade 2 pour les plaquettes, les leucocytes et de grade 3 pour les lymphocytes après le deuxième cycle, alors que la MTD n'a pas été atteinte, ce qui a conduit à une réduction de moitié de l'activité injectée.

Enfin, les doses dans les substituts de moelle osseuse ont été comparées à la dose absorbée par la partie supérieure de l'humérus pour évaluer si les estimations de dose dans les vertèbres étaient différentes de l'activité dans le sang. Les doses absorbées cumulatives (uniquement les cycles où l'humérus est visible) étaient significativement différentes pour les trois substituts de moelle osseuse (test de rang signé de Wilcoxon : p-value = 0,0005 pour L2 à L4, p-value = 0,0005 pour L1 à L5 et p-value = 0,0005 pour T9 à L5).

Evaluation des incertitudes Les calculs des coefficients de variation ont été effectués dans le pire des cas (ODR des cycles 1 et 4 seulement pour la cohorte de validation) et les médianes des coefficients de variation étaient limitées à 15,4 % à 24H (22,3 % à 1H/6H et 34,7 % à 96H/7D). L'hypothèse d'une pharmacocinétique reste approximativement la même d'un cycle à l'autre pour le même patient semble être globalement vérifiée, tant qu'il n'y a pas de toxicité significative ou de variation significative dans la distribution de l'activité. Le remplacement du débit de dose à 24H par celui d'un autre cycle permettant un ajustement tri-exponentiel semble une solution raisonnable. Pour les cycles avec une seule acquisition, deux méthodes ont été proposées : la méthode STP-Intra (M2) et la méthode STP-Inter (M3). Les erreurs médianes les plus faibles ont été estimées lorsque l'acquisition a lieu à 96H, 144H ou 7D, quelle que soit la VOI, avec la méthode STP-Intra (M2). Avec la méthode STP-Inter (M3), il ne semble pas y avoir de moment privilégié. Cette observation a également été faite par d'autres auteurs tels que Rinscheid et al., 2020. La méthode STP-Intra (M2) a été préférée à la méthode STP-Inter (M3) car si la TDRC du patient n'est pas homogène avec celle des autres patients, l'erreur est susceptible d'être importante, comme l'expliquent Jackson et al., 2020a; Hänscheid and Lassmann, 2020.

Cette thèse est accessible à l'adresse : https://theses.insa-lyon.fr/publication/2023ISAL0068/these.pdf
© [L. Vergnaud], [2023], INSA Lyon, tous droits réservés

Pour la moelle osseuse, trois VOI de substitution ont été évaluées. Les erreurs semblent être plus faibles pour T9 à L5 avec la méthode STP-Intra (M2), tandis qu'elles sont équivalentes quelle que soit la VOI avec la méthode STP-Inter (M3). Une hypothèse pourrait être que cette variabilité est liée à la délimitation du volume. En effet, l'ODR correspond à la moyenne des débits de dose dans la VOI. Si la délimitation inclut des voxels qui ne sont pas réellement dans le volume et qui ont des taux de dose inférieurs à ceux de la VOI, l'ODR sera affecté.

Limitations et recommandations Une première limitation est l'hypothèse faite dans les méthodes utilisées qui considère que la physiologie du patient est préservée au cours des cycles alors qu'elle peut ne pas être réellement vérifiée en cas de toxicité importante ou si la distribution de l'activité dans le patient change de manière significative entre les cycles. Il peut donc être intéressant d'ajouter des acquisitions en cas de toxicité. Nous recommandons de sélectionner un moment tardif afin de limiter l'erreur commise, en particulier avec la méthode STP-Intra (M2). Cependant, dans la pratique clinique, ces time-points peuvent être les plus difficiles à obtenir car ils nécessitent que le patient retourne à l'hôpital : c'est pourquoi nous continuons à acquérir une seule image TEMP/CT à 24H malgré les résultats. La méthode STP-Inter est une méthode alternative qui présente deux inconvénients majeurs : elle nécessite que les TDRC d'autres patients soient disponibles avant la dosimétrie et les erreurs commises sont liées à l'homogénéité des TDRC du patient et de la cohorte. La méthode STP-Intra devrait être privilégiée autant que possible afin de limiter les erreurs commises.

Conclusion

Cette étude propose une méthodologie dosimétrique spécifique au patient, basée sur un processus adaptatif d'ajustement tri-exponentiel des distributions de dose par simulation Monte Carlo au niveau des organes. Elle peut être utilisée pour n'importe quelle région d'intérêt, y compris la moelle osseuse, et a été appliquée à des patients traités avec du ^{177}Lu-DOTATATE. La méthodologie s'adapte à différents nombres d'acquisitions TEMP/CT par cycle, notamment en cas d'acquisitions manquantes, préserve la physiologie du patient et tient automatiquement compte de la dose croisée causée par des lésions de formes, de fixations et d'emplacements différents. Toutes les méthodes sont associées à une estimation de l'erreur commise.

Contribution n°2 :Impact dosimétrique du mouvement respiratoire

Introduction

L'impact dosimétrique du mouvement respiratoire lors de la thérapie de radioembolisation sélective (SIRT) est évalué dans cette étude. La SIRT est un traitement local du cancer utilisé pour le carcinome hépatocellulaire (HCC) (Vilgrain et al., 2017), le cholangiocarcinome intra-hépatique (ICC) et les métastases hépatiques (Helmberger et al., 2021). Ce traitement consiste à injecter des microsphères de ^{90}Y dans l'artère hépatique pour délivrer une dose élevée aux lésions. Une étape de planification est réalisée pour déterminer l'activité à injecter et évaluer les risques potentiels de toxicités (Garin et al., 2021). Pour cela, des macroaggrégats d'albumine

Cette thèse est accessible à l'adresse : https://theses.insa-lyon.fr/publication/2023ISAL0068/these.pdf
© [L. Vergnaud], [2023], INSA Lyon, tous droits réservés

(MAA) radiomarquée au ^{99m}Tc sont administrés au patient et sa biodistribution, supposée être similaire à celle des microsphères (Knešaurek et al., 2018), est évaluée à partir d'images SPECT/CT. Cependant, le mouvement respiratoire peut détériorer la qualité des images. A noter qu'il n'est généralement pas corrigé. Différentes méthodes ont été proposées dans la littérature pour récupérer et corriger le mouvement respiratoire dans les images SPECT, par exemple en utilisant des dispositifs de surveillance respiratoire externe (Beach et al., 2005), des images fluoroscopiques (Dietze et al., 2019) ou des approches basées sur les données (Robert et al., 2021a). Bien que le mouvement respiratoire du foie soit bien connu, il n'est pas corrigé lors de la SIRT. Cette étude évalue l'impact dosimétrique du mouvement respiratoire lors de la planification du traitement SIRT grâce à une méthode innovante de compensation du mouvement basée sur les données. Des comparaisons des doses absorbées ont été réalisées entre les reconstructions 3D classiques et les reconstructions 3D compensées du mouvement pour plusieurs régions d'intérêt. Les activités prescrites et les fractions de dérivation pulmonaire calculées avec les deux méthodes ont également été comparées.

Matériel et méthode

Patients Vingt-neuf patients ont été traités par radioembolisation et inclus dan cette étude. Les détails sont donnés dans le tableau 7.1.

Acquisition des images Les images SPECT/CT ont été acquises à l'aide d'une caméra GE Discovery NM CT 670 à deux têtes, en utilisant un collimateur LEHR (Low Energy High Resolution) et des cristaux d'une épaisseur de 3/8". L'acquisition était composée de 60 projections sur 360°, chacune avec une résolution de 128 × 128 pixels, un espacement isotrope de 4,418 mm, une durée de 25 s pour chaque projection, en mode pas à pas. Les fenêtres d'énergie étaient centrées sur 140,5 keV ± 20% de largeur pour les photons primaires et sur 120 keV ± 5

Reconstruction Les images ont été reconstruites à l'aide de deux méthodes : l'algorithme OSEM, noté 3D, et l'algorithme OSEM avec compensation du mouvement, noté 3Dcomp (Robert et al., 2021a). Des corrections d'atténuation, de diffusion (DEW) et une correction de la résolution dépendant de la profondeur (récupération de la résolution). La méthode 3Dcomp consistait tout d'abord à extraire un signal de mouvement respiratoire à partir des données brutes. Ce signal était ensuite divisé en 8 phases respiratoires et les projections acquises étaient triées selon la phase à laquelle elles appartenaient. Des recalages affines 2D ont été réalisés entre chaque phase et la phase sélectionnée pour la reconstruction. Les transformations affines ont été appliquées aux données brutes pour corriger les projections. L'image finale en 3D avec compensation du mouvement a été obtenue par une reconstruction OSEM à partir de toutes les données brutes corrigées du mouvement. Pour la correction d'atténuation, une seule phase était disponible et il a été supposé que localement le CT a été réalisée pendant l'une des phases du mouvement respiratoire. La reconstruction a donc été réalisée sur cette phase correspondante sélectionnée visuellement à partir de la reconstruction 4D SPECT (Robert et al., 2021b). Toutes les reconstructions (3D et 3Dcomp) ont été réalisées avec 15 sous-ensembles et 15 itérations par sous-ensemble. Toutes les reconstructions ont été réalisées avec le logiciel RTK (Rit et al., 2014). Aucun filtre spatial n'a été appliqué en post-reconstruction.

Volumes d'intérêt Les directives internationales établissent des limites de tolérance pour les doses absorbées en fonction du type de sphères utilisées (verre ou résine), de la pathologie du patient et de la stratégie de traitement (Tableau 7.1) (Weber et al., 2022; Levillain et al., 2021). Dans cette étude, sept VOI ont été délimités

Cette thèse est accessible à l'adresse : https://theses.insa-lyon.fr/publication/2023ISAL0068/these.pdf
© [L. Vergnaud], [2023], INSA Lyon, tous droits réservés

pour chaque patient. Pour le foie, les poumons et la ou les tumeur(s), des délimitations manuelles ont été réalisées sur les scanners CT. Le foie sain (HL) a été obtenu en retirant les lésions du foie entier. Le foie perfusé (PL) a été estimé en intersectant le volume obtenu en seuillant l'image SPECT avec 5% du nombre maximum de comptages hépatiques avec le volume CT du foie. La réserve hépatique (HR) correspondait au foie moins le volume perfusé et les lésions. Le foie sain perfusé (HPL) était le foie perfusé moins les lésions (Garin et al., 2020). Un exemple est donné dans la Figure 7.1.

Workflow dosimétrique Un workflow dosimétriquee basé sur des simulations Monte Carlo a été adapté à partir de Vergnaud et al., 2022 pour estimer les doses moyennes absorbées pour tous les VOI à partir des reconstructions 3D et 3Dcomp. Des simulations Monte Carlo ont été réalisées via GATE (Sarrut et al., 2021) avec 1 MBq d'^{90}Y pendant 1 seconde, puis mises à l'échelle en fonction de l'activité réellement injectée.La dose absorbée finale par VOI a été estimée en tenant compte de la décroissance mono-exponentielle, avec une demi-vie de 64 heures pour l'^{90}Y.

Analyses Pour chaque dose absorbée calculée, un calcul de pourcentage de différence de dose a été réalisé pour chaque volume d'intérêt en prenant comme référence la reconstruction 3D. Trois autres valeurs ont également été comparées : le shunt pulmonaire (LSF), le ratio dose à la tumeur sur dose au foie sain (TN) et l'activité d'^{90}Y à prescrire.

Evaluation statistique Des tests de normalité de la distribution de la dose absorbée et de l'activité sur l'ensemble des patients ont été estimés pour chaque reconstruction et évalués avec un test de Shapiro-Wilk avant d'être comparés soit avec un test de Wilcoxon apparié, soit avec un test t apparié (3D vs 3Dcomp). Ces tests ont également été appliqués pour comparer la dose pulmonaire et les rapports TN entre les deux reconstructions.

Corrélations Afin de prédire pour quel patient cette correction du mouvement respiratoire serait réellement pertinente, un test de corrélation de Spearman a été appliqué entre le PDD des tumeurs et sept paramètres différents décrits ci-dessous. Le premier paramètre était le volume (1) de la tumeur estimé à partir de la tomodensitométrie. Pour les deux paramètres suivants, une carte de distance a été calculée entre la tumeur et les bords du foie. La distance minimale (2) et la distance moyenne (3) ont pu être estimées. Les quatre autres paramètres étaient : (4) la distance minimale entre le sommet de la tumeur et le foie dans la direction crânio-caudale (CC) (Santoro et al., 2022), (5) l'amplitude du mouvement de la tumeur dans la direction CC, (6) la distance minimale globale entre le centre de masse de la tumeur et le foie, et (7) cette même distance mais seulement dans la direction CC. Des corrélations ont également été testées sur ces paramètres divisés par le volume, comme proposé dans Kruis et al., 2013.

Résultats

La Figure 7.4 montre les pourcentages de différence de dose entre les doses absorbées estimées à partir des reconstructions en 3D et 3Dcomp pour chaque VOI (foie, poumons, tumeur(s), PL, HR, HPL et HL). Sur le plan statistique, les moyennes des différences entre les séries n'étaient pas significativement différentes de zéro (test de Wilcoxon, p> 0,05 pour les poumons, PL, HR, HPL et les tumeurs ; test de Student, p> 0,05 pour le foie et HL).

La Figure 7.5, 7.8 et 7.9 montrent les graphiques de Bland-Altman entre les reconstructions en 3D et 3Dcomp pour respectivement la dose pulmonaire, le LSF et le

Cette thèse est accessible à l'adresse : https://theses.insa-lyon.fr/publication/2023ISAL0068/these.pdf
© [L. Vergnaud], [2023], INSA Lyon, tous droits réservés

ratio TN. Des graphiques de Bland-Altman pour les doses absorbées des poumons gauche (Figure 7.6) et droit (Figure 7.7) sont également disponibles.

Les figures 7.10 et 7.11 représentent les pourcentages de différence de dose dans les tumeurs entre les reconstructions 3D et 3Dcomp en fonction du volume de la tumeur et de l'amplitude du mouvement des tumeurs.

Enfin, nous avons comparé les activités injectées planifiées avec les deux reconstructions (Tableau 7.4). La moyenne et l'écart-type de la valeur absolue de la différence de dose étaient de 3,1 ± 5,1 % entre les activités prescrites obtenues à partir des reconstructions 3D et 3Dcomp. La différence absolue maximale était de 22,8 % (1,28 GBq pour la reconstruction 3D contre 1,57 GBq pour la reconstruction 3Dcomp) et a été obtenue pour le patient 20. Les séries d'activités injectées (3D et 3Dcomp) ne suivaient pas une distribution normale (test de Shapiro-Wilk, $p<0,05$). La moyenne des différences entre les activités prescrites n'était pas significativement différente de zéro ($p>0,05$ avec le test de Wilcoxon).

Seules deux corrélations statistiquement significatives modérées (figure 7.12) ont pu être trouvées entre la différence de dose dans les tumeurs et : 1. la distance minimale dans la direction CC entre la partie supérieure de la lésion et le dôme hépatique (corr=-0,38 ; $p<0,05$) et 2. la distance minimale entre le centre de masse de la lésion dans la direction CC et le dôme hépatique (corr=-0,38 ; $p<0,05$).

Discussion

Cette étude présente l'évaluation de l'impact dosimétrique du mouvement respiratoire lors de la planification de la SIRT. Nous avons travaillé sur des données de patients réels avec différentes caractéristiques (nombre de tumeurs, volumes, localisations, pathologies, type de sphères) représentatives de la diversité de ce que l'on trouve en clinique. Pour chaque cas, nous avons comparé les doses estimées à partir des reconstructions 3D et 3Dcomp, ainsi que le rapport TN et l'activité à injecter.

Peu d'études ont été publiées sur le sujet. Dans les travaux de Bastiaannet et al., 2017; Lu et al., 2022, les auteurs ont évalué l'impact dosimétrique du mouvement en effectuant des simulations à partir de fantômes numériques XCAT avec différents ensembles de paramètres (type de corps, fraction de shunt pulmonaire, volume et localisation de la tumeur). De même, Santoro et al., 2022 ont testé une nouvelle méthode de compensation du mouvement sur un fantôme dynamique CIRS modifié et l'ont appliquée aux données de douze patients sélectionnés (HCC, lésion unique). Cependant, le réalisme des simulations et des fantômes est limité (cycle respiratoire parfait et simplifications du mouvement, caractéristiques de chaque patient, hypothèse d'une dispersion parfaitement compensée (Lu et al., 2022)). Contrairement à notre méthode basée sur des données en mode liste, Santoro et al., 2022 ont corrigé le mouvement respiratoire en réalignant les barycentres des lésions dans les projections entre eux avant de les réaligner sur le CT pour améliorer la correction de l'atténuation et les définitions des VOI (Lu et al., 2021). Cette dernière étape consistait à avoir la même distance entre le dôme hépatique défini sur le CT et le sommet de la lésion sur deux modalités d'imagerie (SPECT et CT). Cependant, les contours des lésions ont été obtenus par seuillage sur les projections, elles-mêmes impactées par le mouvement respiratoire (15 s/projection vs 5 s pour un cycle respiratoire) : ils dépendent de la distribution des comptages détectés et influencent l'enregistrement avec le CT. Ici, une reconstruction 4D a été effectuée pour sélectionner la phase qui correspond le mieux visuellement au CT afin de corriger l'impact du mouvement respiratoire. Ensuite, une reconstruction 3Dcomp a été réalisée pour prendre en compte tous les comptages détectés.

Cette thèse est accessible à l'adresse : https://theses.insa-lyon.fr/publication/2023ISAL0068/these.pdf
© [L. Vergnaud], [2023], INSA Lyon, tous droits réservés

Le PDD médian était proche de zéro pour tous les VOI considérés, à l'exception des poumons (6,4 %). Les doses absorbées estimées pour les poumons sont globalement plus élevées avec la reconstruction 3Dcomp qu'avec la reconstruction 3D. Les comptages dans le foie proches des poumons peuvent être reconstruits dans les poumons et non dans le foie. De même, les comptages dans les poumons peuvent être reconstruits à l'extérieur des poumons. Une marge supplémentaire autour du foie peut être prise (Allred et al., 2018; Kao et al., 2014) pour tenir compte du mouvement respiratoire. Il n'y avait aucune différence statistiquement significative pour les doses pulmonaires entre les deux reconstructions (de même pour le LSF), ce qui est en accord avec les résultats de Bastiaannet et al., 2017 pour le LSF. Cependant, Lu et al., 2022 ont montré que le LSF était surestimé en l'absence de correction du mouvement respiratoire. Cela pourrait s'expliquer par le fait que la localisation des lésions considérées ainsi que les amplitudes de mouvements respiratoires diffèrent des nôtres. Il n'y avait pas de différence significative dans le ratio TN entre les deux reconstructions, contrairement à d'autres auteurs qui ont constaté une sous-estimation du ratio TN en l'absence de correction du mouvement respiratoire (Bastiaannet et al., 2017; Lu et al., 2022). Le volume semble avoir un impact sur l'erreur commise en l'absence de correction du mouvement respiratoire (figure 7.10) : plus le volume est petit, plus l'erreur est grande (Lu et al., 2022; Ausland et al., 2018). La majorité des lésions étudiées avaient un volume plus important donc l'effet de volume partiel seul n'explique pas les différences de dose observées entre les reconstructions 3D et 3Dcomp pour les petits volumes. Les tumeurs présentaient des caractéristiques très diverses d'un patient à l'autre, par exemple en termes de volume et de forme. Ce sont probablement des explications des divergences observées pour le ratio TN. D'autres études, axées sur l'impact du mouvement respiratoire en post-traitement (Ausland et al., 2018; Osborne et al., 2018 (modèles mathématiques et données de patients), ont également montré que les doses aux lésions étaient sous-estimées. L'impact du mouvement respiratoire sur l'activité à prescrire n'a semble-t-il pas été étudié auparavant.

Dans cette étude, aucune différence moyenne significative n'a été observée entre les activités estimées avec chaque reconstruction ([min : -8,3% ; médiane : 0,4% ; max : 22,8%]). Seules deux corrélations modérées significatives ($p < 0,05$) ont été trouvées entre le PDD des tumeurs et : (1) la distance minimale entre la partie supérieure de la tumeur et le foie dans la direction CC et (2) la distance minimale entre le centre de masse de la lésion et le foie dans la direction CC. Globalement, les moyennes des différences entre les reconstructions 3D et 3Dcomp pour les doses absorbées et en particulier pour les poumons, les ratios TN et les activités prescrites ne sont pas statistiquement significativement différentes de zéro. Dans cette étude, tous les patients présentaient un faible shunt pulmonaire (dose pulmonaire 3D maximale : 9,2 Gy) par rapport aux limites recommandées, de sorte que la prise en charge n'a pas été impactée par la correction du mouvement respiratoire. De plus, Robert et al., 2021a ont montré que l'activité de récupération était mieux estimée avec la reconstruction 3Dcomp qu'avec les reconstructions 3D et 4D. Nous considérons donc toujours pertinent d'appliquer une correction du mouvement respiratoire afin d'améliorer la quantification.

L'acquisition du CT est une limitation de cette étude. En effet, le CT a été acquis en respiration libre. Il ne correspond onc pas à une phase précise ce qui engendre des incertitudes auxquelles s'ajoutent celles du recalage avec la SPECT. Idéalement, un CT 4D devrait être acquis car, dans certains cas, le mouvement respiratoire peut créer des artefacts dans le CT 3D. Si cette acquisition n'est pas possible, nous recommandons d'acquérir un CT en apnée respiratoire afin de réaliser la reconstruction

Cette thèse est accessible à l'adresse : https://theses.insa-lyon.fr/publication/2023ISAL0068/these.pdf
© [L. Vergnaud], [2023], INSA Lyon, tous droits réservés

3Dcomp à la même phase respiratoire.

Une deuxième limitation était le nombre limité de patients inclus dont les caractéristiques étaient hétérogènes. La présence de corrélations pourrait être mieux évaluer sur des cohortes plus grandes et plus homogènes.

Une troisième limitation de cette étude concerne la corrélation entre la biodistribution de ^{99m}Tc-MAA et les microsphères de ^{90}Y. Plusieurs auteurs ont rapporté une bonne corrélation des doses aux tumeurs dans le cas du HCC, mais ont montré une corrélation plus faible dans le cas de la maladie métastatique (Jadoul et al., 2020; Garin et al., 2016). De même, le positionnement du cathéter entre les étapes de prétraitement et de traitement peut influencer l'accord entre les doses prédites et mesurées (Thomas et al., 2020).

Conclusion

Dans cette étude, nous avons démontré la faisabilité de corriger le mouvement respiratoire sur de véritables images SPECT pré-traitement pour la radioembolisation. La méthode ne nécessite pas de dispositifs externes supplémentaires ni de modifications d'acquisition. Nous avons montré que cette correction a un impact sur la dose absorbée par les poumons ce qui pourrait avoir des conséquences sur la prise en charge de certains patients dans les cas où la dose se rapproche de la limite de tolérance recommandée. Cette correction affecte également la dose délivrée aux tumeurs, les plus grandes différences de dose étant estimées pour les plus petites lésions.

Contribution n°3 : Faisabilité de la quantification du ^{177}Lu avec une caméra gamma CZT

Introduction

La thérapie par radiopharmaceutique au ^{177}Lu-PSMA permet de traiter les patients atteints de cancer de la prostate métastatique résistant à la castration (mCRPC). Cependant, la réponse au traitement sans effets indésirables, dépend du fonctionnement des organes, la pharmacocinétique du traceur et la captation tumorale, ce qui implique la nécessité d'une surveillance du traitement. L'Association européenne de médecine nucléaire (EANM) a récemment publié des lignes directrices générales pour garantir les bonnes pratiques à suivre pour ce traitement (Kratochwil et al., 2016b). En particulier, la mise en œuvre d'une dosimétrie individualisée conformément à la directive européenne 2013/59/Euratom est mentionnée. Cette étape consiste à calculer la dose absorbée dans les tumeurs et les organes sains pour chaque patient traité.

L'imagerie TEMP est actuellement la seule source d'information permettant d'estimer la dose absorbée après l'injection d'une dose thérapeutique chez un patient. La quantification peut être réalisée avec une scintigraphie planaire 2D (Paganelli et al., 2020) ou à partir d'images reconstruites en 3D (Violet et al., 2019), cette dernière montrant une meilleure précision (Rosar et al., 2021).

Cependant, l'acquisition TEMP/CT peut être longue avec une gamma caméra conventionnelle. Cela pose problème pour les patients souffrant de douleur et ont des conséquences sur la disponibilité du personnel médical et la planification des caméras. Ainsi, le temps d'acquisition des scintigraphies constitue un obstacle à la mise en œuvre clinique routinière du suivi du traitement par ^{177}Lu.

Cette thèse est accessible à l'adresse : https://theses.insa-lyon.fr/publication/2023ISAL0068/these.pdf
© [L. Vergnaud], [2023], INSA Lyon, tous droits réservés

Plus récemment, les caméras TEMP/CT équipées de détecteurs à base de tellurure de cadmium-zinc (CZT) sont devenue disponibles. Elles ont de meilleures efficacité de détection, résolution en énergie et résolution spatiale ce qui permet donc de réduire les temps d'acquisition.

Le système de détection CZT pour la caméra VERITON-CT de la série 200 utilisé dans cette étude a une plage d'énergie de 40 à 200 keV, empêchant ainsi l'acquisition du photopic supérieur du ^{177}Lu (208 keV, 10,4%), restreignant donc l'acquisition au photopic inférieur (113 keV, 6,2%) et affecté par des photons diffusés supplémentaires d'énergie plus élevée. À notre connaissance, un seul cas clinique a été publié pour ce système en association avec le traitement du 177Lu des tumeurs neuroendocrines (Chevalier et al., 2020).

Dans ce travail, nous avons étudié les performances de la caméra VERITON-CT pour l'imagerie du ^{177}Lu avec différents fantômes et caractérisé les capacités actuelles de quantification absolue du système pour le suivi et la dosimétrie des traitements par ^{177}Lu-PSMA.

Matériel et méthode

Système d'imagerie Cette étude a été réalisée avec la caméra CZT hybride VERITON-CT (Spectrum Dynamics, Caesarea, Israël). Elle possède douze têtes incluant chacune un module de détection lui-même composé de 128 x 16 détecteurs à semi-conducteurs avec des collimateurs parallèles en tungstène non amovibles.

Fantômes Trois fantômes ont été préparés : un cylindre d'eau uniforme pour la calibration (Ph1), un fantôme NEMA IEC pour estimer les coefficients de recouvrement (Ph2) et un fantôme NEMA IEC modifié avec deux bouteilles afin de simuler deux "organes" (Ph3) (Figure 8.1). Le Tableau 8.1 donne des informations détaillées sur ces trois fantômes. Les acquisitions ont été réalisées avec un rapport de 7:1 pour Ph2.

Acquisition TEMP/CT . Chaque acquisition a duré 900 secondes.Elles ont été répétées pour les trois fantômes, pour 8 time-points compris entre 4 et 339 heures après l'injection, comme indiqué dans le Tableau 8.3. Des acquisitions CT à faible dose ont été réalisées pour la correction de l'atténuation. Une tension de 120 kVp et un produit courant/temps de 17 mAs ont été utilisés pour générer le faisceau de rayons X.

Paramètres de reconstruction Deux protocoles de reconstruction ont été étudiés, le premier à des fins de quantification et de dosimétrie, appelé RecQuant, et le deuxième à des fins d'évaluation de visualisation, appelé RecVis (Tableau 8.2. Le modèle Point Spread Function Recovery display (PSFRd) modélise la réponse détecteur-collimateur et corrige les effets de flou (diffusion) ; cela a été optimisé uniquement pour la visualisation. Pour RecVis, deux filtres supplémentaires ont été utilisés : un filtre de convolution a été appliqué pendant la reconstruction et un filtre médian après la reconstruction.

Calibration Le facteur de calibration a été estimé en suivant les recommandations du MIRD n°23 (Dewaraja et al., 2012. Un grand cylindre d'activité connue (Ph1 ici) a été acquis. La mesure a été répétée pour différentes concentrations en activité.

Cette thèse est accessible à l'adresse : https://theses.insa-lyon.fr/publication/2023ISAL0068/these.pdf
© [L. Vergnaud], [2023], INSA Lyon, tous droits réservés

Critères d'évaluation Pour optimiser les paramètres de reconstruction pour la quantification, les coefficients de récupération de la concentration d'activité (ARC) (Dickson et al., 2022) (pour la quantification), les coefficients de récupération de contraste (CRC) (pour la détection visuelle) et la variabilité de concentration en activité des sphères et de l'arrière-plan (estimation du bruit) ont été calculés sur le fantôme Ph2 (Ramonaheng et al., 2021). Les contours des sphères ont tous été réalisés à partir de l'image TEMP.

Optimisation et évaluation des paramètres de reconstruction Quatre ensembles de paramètres ont été testés avec différentes mises à jour (itérations × sous-ensembles). Pour l'ensemble n°1, une correction de diffusion a été ajoutée. Pour l'ensemble n°2, une régularisation par maximum de vraisemblance (PL) a été ajoutée en plus de la correction de diffusion (**Depierro1995**; Webster Stayman and Fessler, 2000). Pour les ensembles n°3 et n°4, l'option PSFRq (Récupération de la Fonction de Point de l'étalement de la réponse) a été utilisée. PSFRq comprend une PSF conventionnelle, spatialement invariante, ainsi que des corrections de flou (diffusion). L'ensemble n°3 était avec une correction de diffusion supplémentaire, tandis que le test n°4 était sans correction de diffusion supplémentaire. Aucune régularisation PL n'a été appliquée pour les ensembles n°3 et n°4.

Impact de la segmentation Trois méthodes de segmentation ont été utilisées pour les mêmes calculs d'ARC afin d'évaluer leur impact. La première méthode consistait à utiliser le contour anatomique, la seconde à réduire le contour anatomique de quelques millimètres et la troisième, d'utiliser un seuillage sur la TEMP.

Images patient Les taux de comptage estimés dans les fantômes (en particulier le fantôme Ph2) ont été comparés aux débits de comptage estimés pour chaque BP (6 ou 7 au total) pour trois patients à trois moments différents afin d'évaluer si les taux de comptage dans les fantômes sont représentatifs de ceux des patients.

Résultats

Itérations et subsets Les calculs ont été effectués à l'aide de la méthode de segmentation M1 en utilisant la moyenne et non le maximum afin d'être aussi proche que possible de la dosimétrie du patient. Nous avons défini le meilleur compromis en limitant la variabilité dans les régions homogènes (sphères et arrière-plan) à moins de 50 %, ce qui correspond à 96 mises à jour (12 itérations et 8 sous-ensembles).

Le facteur de calibration associé à ces paramètres a été estimé à 0,176 ± 0,00444. Les ARC des grands volumes (fantôme Ph3) ont des ARC de l'ordre 0.91. Enfin, le choix de la méthode de contourage influence directement les ARCs.

Images patient Les taux de comptage des fantômes sont représentatifs des taux de comptage que l'on retrouve chez les patients. Les durées totales d'acquisition TEMP étaient comprises entre 24 et 26 minutes au total en tenant compte du temps de déplacement des détecteurs.

Discussion

L'objectif de cette étude était d'évaluer les performances de la caméra gamma CZT VERITON 360° (série VERITON-CT 200, version logicielle 2.3.0.1234) dans le suivi des patients traités avec du ^{177}Lu-PSMA.

Cette thèse est accessible à l'adresse : https://theses.insa-lyon.fr/publication/2023ISAL0068/these.pdf
© [L. Vergnaud], [2023], INSA Lyon, tous droits réservés

Optimisation des paramètres de reconstruction Les paramètres de reconstruction finaux incluaientune correction d'atténuation basée sur les données CT (Dewaraja et al., 2012) et sans filtrage intermédiaire ou postérieur afin de ne pas impacter la quantification (Dickson et al., 2022). Les fenêtres de diffusion étaient de 22,6 keV de largeur, suffisamment larges pour limiter le bruit lors de l'utilisation de l'EWTE (Dewaraja et al., 2012). La reconstruction incluait un modèle de la géométrie du système dont les incertitudes sont en partie corrigées avec l'option PSFRq, qui correspond à une PSF (fonction de propagation du point source) conventionnelle spatialement invariante et à une correction des effets de flou (par exemple, la diffusion). Il y a un risque de correction double de la diffusion lorsque la correction de diffusion est utilisée simultanément avec l'option PSFRq. Le nombre recommandé de mises à jour était de 96 (12 itérations et 8 sous-ensembles) pour maintenir le bruit en dessous de 50%.

Influence de la méthode de segmentation ARC et CRC dépendent des contours des sphères et peuvent être calculés avec la concentration moyenne ou maximale à l'intérieur de la VOI. Avec la valeur maximale, les ARCs étaient identiques pour la plupart des sphères sauf les plus petites. L'utilisation de la valeur maximale est sensible au bruit et repose uniquement sur un voxel unique, tandis que l'utilisation de la moyenne diminue les ARCs en intégrant l'hétérogénéité des concentrations dans un volume mais est moins sensible au bruit. La segmentation basée sur l'image SPECT (M3) dépend des paramètres de reconstruction contrairement à M1 et M2. Ici, la méthode M1 basée sur la moyenne a été choisie car lors de la dosimétrie du patient, les organes à risque sont segmentés anatomiquement sur le CT (la seule information disponible) et la dose moyenne est calculée dans une ROI.

Reconstruction des images patient Le temps d'acquisition d'une acquisition TEMP corps entier a été réduit d'au moins la moitié par rapport à celui d'une caméra gamma conventionnelle. Cela est important pour les patients souffrant de douleurs qui peuvent avoir du mal à rester immobiles pendant de longues périodes et où plusieurs acquisitions TEMP/CT seront réalisées. En pratique, il est également possible de réaliser plus d'acquisitions TEMP/CT en une journée.

Conclusion

Nous avons évalué les performances quantitatives de VERITON pour les traitements au ^{177}Lu et proposé un ensemble de paramètres de reconstruction à des fins de quantification, appelé RecQuant. Nous préconisons l'utilisation de deux ensembles de paramètres de reconstruction : un pour la quantification et un pour la visualisation, avec les mêmes paramètres d'acquisition. Bien que le système soit limité à la détection de 113 keV pour le ^{177}Lu, l'ARC obtenu avec RecQuant démontre qu'il peut être utilisé à des fins de dosimétrie du ^{177}Lu. Le temps d'acquisition pour une image du corps entier d'environ 1,8 m de longueur est d'environ 25 minutes, ce qui est environ trois fois plus rapide qu'avec les caméras double tête conventionnelles.

Cette thèse est accessible à l'adresse : https://theses.insa-lyon.fr/publication/2023ISAL0068/these.pdf
© [L. Vergnaud], [2023], INSA Lyon, tous droits réservés

Contribution n°4 : Dosimétrie pour les thérapies au ^{177}Lu-PSMA

Introduction

La thérapie au ^{177}Lu-PSMA est une thérapie standardisée dont la réponse au traitement varie d'un patient à un autre (Scarpa et al., 2017; Fendler et al., 2017; Zhang et al., 2019. Il convient donc d'estimer les doses absorbées par les patients afin de pouvoir à terme personnaliser leur thérapie. Pour cela, il est nécessaire d'acquérir des images couvrant la zone allant du pelvis à la tête (métastases osseuses infiltrantes, glandes salivaires). Bien que de nombreuses études utilisent des images planaires (superposition des organes et des tumeurs) pour réduire le temps d'acquisition, il est recommandé de baser la dosimétrie sur des images 3D TEMP obtenues par des acquisitions de champ de vue multiples (Sjögreen Gleisner et al., 2022). La méthode hybride, est couramment choisie comme un compromis approprié entre le temps d'acquisition et la précision de la dosimétrie. Les caméras gamma CZT offrent une solution potentielle à ce défi en permettant des acquisitions TEMP corps entier plus courtes (Song et al., 2023, 2 à 3 fois plus courtes). Les performances des caméras CZT pour la dosimétrie des thérapies au 177Lu ont été évaluées sur des fantômes. Cependant, à notre connaissance, l'évaluation à partir d'images de patients n'a pas encore été réalisée, à l'exception de deux résumés rédigés par Imbert et al., 2020 et Imbert et al., 2021a qui n'étaient pas des études évaluées par des pairs.

Dans cette étude, la dosimétrie des reins, de la rate et du foie a été réalisée à partir d'images TEMP du corps entier de patients traités par ^{177}Lu-PSMA.

Matériel et Méthode

Patients Treize patients ont été traités avec du ^{177}Lu-PSMA dont onze avec du PSMA-1 et 2 avec du PSMA-617.

Acquisition TEMP/CT corps entier Trois acquisitions ont été réalisées après la première injection (4h, 24h et 96h ou 144h) puis une unique à 24h après chaque autre cycle.

Paramètres de reconstruction Ce sont ceux déterminés dans la contribution n°3 de même que le facteur de calibration.

Segmentation Des contours anatomiques des organes ont été réalisés sur le CT.

Dosimétrie Le workfflow dosimétrique utilisé est le même que celui présenté dans la contribution n°1.

Résultats

Sur l'ensemble des patients et des cycles de traitement, les doses par activité injectée pour les reins gauche et droit, le foie et la rate étaient respectivement de 0,56 ± 0,19 Gy/GBq, 0,61 ± 0,18 Gy/GBq, 0,12 ± 0,10 Gy/GBq et 0,11 ± 0,07 Gy/GBq.

Cette thèse est accessible à l'adresse : https://theses.insa-lyon.fr/publication/2023ISAL0068/these.pdf
© [L. Vergnaud], [2023], INSA Lyon, tous droits réservés

Discussion

Dans cette étude préliminaire, nous avons estimé les doses absorbées par les reins, le foie et la rate chez treize patients traités par ^{177}Lu-PSMA. En comparant nos doses absorbées estimées avec celles rapportées dans la littérature, calculées à partir d'images TEMP 3D, nous avons constaté des résultats similaires, du même ordre de grandeur. Actuellement, les acquisitions planaires sont parfois combinées à une acquisition TEMP en raison des temps d'acquisition potentiellement longs pour les images TEMP, qui impliquent plusieurs FOV. L'utilisation des caméras gamma CZT a permis des acquisitions plus rapides et une dosimétrie plus précise basée sur des images TEMP 3D. De plus, une étude de Komber et al., 2021 a démontré que l'expérience des patients n'était pas dégradée lors de l'utilisation de ce type de système par rapport aux caméras gamma conventionnelles.

Conclusion

L'analyse dosimétrique des reins, du foie et de la rate à partir d'acquisition TEMP corps entier chez les patients traités par ^{177}Lu-PSMA a montré des résultats comparables à ceux disponibles dans la littérature. Cependant, il est important de noter que cette étude représente une investigation préliminaire qui pourrait être étendue en incluant des patients ainsi que des VOI supplémentaires. Le développement d'une méthodologie de segmentation qui tient compte de l'effet de volume partiel de ces petites structures serait crucial. Enfin, en ce qui concerne la dosimétrie des lésions, il serait utile de définir un volume tumoral global, comme le propose Violet et al., 2019. Cela permettrait d'explorer les corrélations entre la dosimétrie et la réponse biologique.

Conclusions et perspectives

Résumé des contributions

Ce travail de thèse a été découpé en quatre contributions portant sur la quantification et la dosimétrie en TEMP/CT. La première contribution a eu pour objectif de fournir un workflow dosimétrique s'adaptant aux nombres d'acquisitions TEMP/CT disponibles étant donné les diverses contraintes cliniques. Cette étude a été menée pour des patients traités au ^{177}Lu-DOTATATE. La seconde contribution a permis d'évaluer l'impact clinique de la correction du mouvement respiratoire et de voir si elle influençait ou non la prise en charge du patient. La troisième contribution a eu pour but d'évaluer les performances quantitatives d'une gamma caméra CZT pour les ^{177}Lu avant de réaliser la dosimétrie des patients traités au ^{177}Lu-PSMA dans une quatrième contribution.

Perspectives A court terme, il serait pertinent d'inclure dans la dosimétrie les organes à risque telles les glandes salivaires et lacrymales ainsi que les tumeurs. Les cohortes de patients devraient être agrandies pour pouvoir établir s'il y en a des relations dose-effet et dose toxicité. Cela permettrait également de regrouper les patients en cohorte homogène et d'améliorer la méthode M3 utilisant les paramètres pharmacocinétiques d'une population. Les méthodes simplifiées devraient être validées pour les différents radiopharmaceutiques. Une étude multicentrique permettrait de donner des incertitudes précises et notamment, les incertitudes inter-cycles. Enfin,

Cette thèse est accessible à l'adresse : https://theses.insa-lyon.fr/publication/2023ISAL0068/these.pdf
© [L. Vergnaud], [2023], INSA Lyon, tous droits réservés

une automatisation du workflow dosimétrique permettrait de rendre plus accessible la dosimétrie au sein des hôpitaux.

A moyen terme, la mise en place d'une base de données partagées offrirait la possibilité à chaque hôpital de tester son workflow dosimétrique et d'avoir accès à un très grand nombre de données notamment lorsque les paramètres pharmacocinétiques moyens d'une population sont nécessaires. L'inclusion de la radiobiologie dans les calculs de doses pourrait permettre d'améliorer les corrélations dose-effet et dose-toxicité. Ces corrélations pourraient être influencées par les incertitudes liées aux calculs de dose : il faut donc évaluer le rôle que jouent les incertitudes. De plus, la localisation de la moelle osseuse active semble indispensable pour pouvoir estimer sa dose absorbée dans le cas des thérapies au ^{177}Lu-PSMA. Enfin, une amélioration de la sélection des patients permettrait de réduire les traitements inutiles.

A long terme, les limites de dose maximale tolérée pour les thérapies par radiopharmaceutiques devraient être établies étant donné que celles de la radiothérapie externe ne semblent valides. De plus, de nouveaux radioisotopes devraient être testés notamment les émetteurs α afin de réduire les toxicités. Enfin, une amélioration de la résolution spatiale des gamma caméras améliorerait la qualité d'image et permettrait de faire de la dosimétrie à l'échelle du voxel plus précise.

Cette thèse est accessible à l'adresse : https://theses.insa-lyon.fr/publication/2023ISAL0068/these.pdf
© [L. Vergnaud], [2023], INSA Lyon, tous droits réservés

Bibliography

Ahmadzadehfar, Hojjat et al. (2016). "Therapeutic response and side effects of repeated radioligand therapy with 177Lu-PSMA-DKFZ-617 of castrate-resistant metastatic prostate cancer". en. In: *Oncotarget* 7.11, pp. 12477–12488.

Akhavanallaf, Azadeh, Iscaac Shiri, Hossein Arabi, and Habib Zaidi (2021). "Whole-body voxel-based internal dosimetry using deep learning". In: *European Journal of Nuclear Medicine and Molecular Imaging* 48.3, pp. 670–682.

Akhavanallaf, Azadeh et al. (2023). "The predictive value of pretherapy [68 Ga] Ga - DOTA - TATE PET and biomarkers in [177 Lu] Lu - PRRT tumor dosimetry". In: *European Journal of Nuclear Medicine and Molecular Imaging*.

Akyurek, T. (2021). "A new dead-time determination method for gamma-ray detectors using attenuation law". In: *Nuclear Engineering and Technology* 53.12, pp. 4093–4097.

Alipour, R. et al. (2023). "The relationship between tumour dosimetry, response, and overall survival in patients with unresectable Neuroendocrine Neoplasms (NEN) treated with 177Lu DOTATATE (LuTate)". In: *European Journal of Nuclear Medicine and Molecular Imaging*.

Allred, J D et al. (2018). "The value of 99mTc-MAA SPECT/CT for lung shunt estimation in 90Y radioembolization: a phantom and patient study". In: *EJNMMI Research* 8.50.

Alsadi, Rahaf, Mehdi Djekidel, Othmane Bouhali, and Jim O Doherty (2022). "Towards Routine Clinical Use of Dosimetry in [177Lu]Lu-PSMA Prostate Cancer Radionuclide Therapy: Current Efforts and Future Perspectives". In: *Frontiers in Physics* 10.July, pp. 1–13.

Arbre des évolutions possibles de la cellule (2023). https://www.cea.fr/comprendre/PublishingImages/Pages/sante-sciences-du-vivant/essentiel-sur-effets-des-rayonnements-ionisants-sur-vivant/EffetsRI_ArbreDesEvolutionsPossiblesDeLaCellule.jpg.

Ausland, L, M E Revheim, A Skretting, and C Stokke (2018). "Respiratory motion during 90Yttrium PET contributes to underestimation of tumor dose and overestimation of normal liver tissue dose". In: *Acta Radiologica* 59.2, pp. 132–139.

Avanzo, Michele et al. (2021). "Artificial intelligence and the medical physicist: Welcome to the machine". In: *Applied Sciences* 11.4, pp. 1–17.

Baccala, Angelo, Linda Sercia, Jianbo Li, Warren Heston, and Ming Zhou (2007). "Expression of Prostate-Specific Membrane Antigen in Tumor-Associated Neovasculature of Renal Neoplasms". In: *Urology* 70.2, pp. 385–390.

Bahloul, Achraf et al. (2021). "Quantification of Bone Scintigraphy for the Longitudinal Monitoring of Vertebral Fractures With a High-speed Whole-body CZT-SPECT/CT System". In: *Research square*.

Barakat, Elie et al. (2022). "Transarterial Yttrium-90 Glass Microsphere Radioembolization of Chemotherapy-Refractory Breast Cancer Liver Metastases: Results of a Single Institution Retrospective Study". In: *Advances in Radiation Oncology* 7.1.

Cette thèse est accessible à l'adresse : https://theses.insa-lyon.fr/publication/2023ISAL0068/these.pdf
© [L. Vergnaud], [2023], INSA Lyon, tous droits réservés

Bardiès, M and I Buvat (2011). "Dosimetry in nuclear medicine therapy: what are the specifics in image quantification for dosimetry?" In: *The Quarterly Journal of Nuclear Medicine and Molecular imaging* 55.1, pp. 5–20.

Bardiès, M. and J. I. Gear (2021). "Scientific Developments in Imaging and Dosimetry for Molecular Radiotherapy". In: *Clinical Oncology* 33.2, pp. 117–124.

Barna, Sandra et al. (2020). "Dose Calculations and Dose-Effect Relationships in 177Lu-PSMA I&T Radionuclide Therapy for Metastatic Castration-Resistant Prostate Cancer". In: *Clinical nuclear medicine* 45.9, pp. 661–667.

Barone, Raffaella et al. (2004). "Metabolic effects of amino acid solutions infused for renal protection during therapy with radiolabelled somatostatin analogues". In: *Nephrology Dialysis Transplantation* 19.9, pp. 2275–2281.

Bastiaannet, R, M A Viergever, and H W.A.M. De Jong (2017). "Impact of respiratory motion and acquisition settings on SPECT liver dosimetry for radioembolization". In: *Medical Physics* 44.10, pp. 5270–5279.

Bastiaannet, Remco et al. (2018). "The physics of radioembolization". In: *EJNMMI Physics* 5.1.

Baum, Richard P. et al. (2016). "177Lu-labeled prostate-specific membrane antigen radioligand therapy of metastatic castration-resistant prostate cancer: Safety and efficacy". In: *Journal of Nuclear Medicine* 57.7, pp. 1006–1013.

Beach, Richard D. et al. (2005). "Stereo-infrared tracking to monitor and characterize rigid-body motion and respiration during cardiac SPECT imaging: Progress towards robust clinical utilization". In: *IEEE Nuclear Science Symposium Conference Record* 3, pp. 1731–1735.

Beauregard, Jean Mathieu, Michael S. Hofman, Jucilene M. Pereira, Peter Eu, and Rodney J. Hicks (2011). "Quantitative 177Lu SPECT (QSPECT) imaging using a commercially available SPECT/CT system". In: *Cancer Imaging* 11.1, pp. 56–66.

Becx, Morticia N. et al. (2022). "A Clinical Guide to Peptide Receptor Radionuclide Therapy with 177Lu-DOTATATE in Neuroendocrine Tumor Patients". In: *Cancers* 14.23.

Belli, Susana Haydée et al. (2009). "Chromogranin A as a biochemical marker for the management of neuroendocrine tumors: A multicenter study developed in Argentina". In: *Acta Gastroenterologica Latinoamericana* 39.3, pp. 184–189.

Ben Bouallègue, F., E. D'estanque, and D. Mariano-Goulart (2015). "Highlights in nuclear cardiology: Applications of new CZT cameras". In: *Medecine Nucleaire* 39.5, pp. 435–443.

Bergsma, Hendrik et al. (2016a). "Nephrotoxicity after PRRT with 177Lu-DOTA-octreotate". In: *European Journal of Nuclear Medicine and Molecular Imaging* 43.10, pp. 1802–1811.

Bergsma, Hendrik et al. (2016b). "Subacute haematotoxicity after PRRT with 177Lu-DOTA-octreotate: prognostic factors, incidence and course". In: *European Journal of Nuclear Medicine and Molecular Imaging* 43.3, pp. 453–463.

Berliner, Christoph et al. (2017). "Detection rate of PET/CT in patients with biochemical relapse of prostate cancer using [68Ga]PSMA I&T and comparison with published data of [68Ga]PSMA HBED-CC". In: *European Journal of Nuclear Medicine and Molecular Imaging* 44.4, pp. 670–677.

Bhardwaj, R, H T Wolterbeek, A G Denkova, and P Serra-Crespo (2019). "Radionuclide generator-based production of therapeutic 177Lu from its long-lived isomer 177mLu". In: *EJNMMI Radiopharmacy and Chemistry* 4.1.

Blanc, P., E. Cassol, E. Ouhayoun, and P. Payoux (2021). "CZT 360° VERITON-CT Gamma camera: The experience of Toulouse". In: *Medecine Nucleaire* 45.4, pp. 240–244.

Cette thèse est accessible à l'adresse : https://theses.insa-lyon.fr/publication/2023ISAL0068/these.pdf
© [L. Vergnaud], [2023], INSA Lyon, tous droits réservés

Bodei, Lisa et al. (2015). "Long-term tolerability of PRRT in 807 patients with neuroendocrine tumours: the value and limitations of clinical factors". In: *European Journal of Nuclear Medicine and Molecular Imaging* 42.1, pp. 5–19.

Bolch, Wesley E. et al. (1999). "MIRD pamphlet no. 17: The dosimetry of nonuniform activity distributions - Radionuclide S values at the voxel level". In: *Journal of Nuclear Medicine* 40.1.

Bordonne, Manon et al. (2020). "High-quality brain perfusion SPECT images may be achieved with a high-speed recording using 360° CZT camera". In: *EJNMMI Physics* 7.65.

Bournaud, C et al. (2019). "La radiothérapie interne vectorisée par les analogues de la somatostatine, en pratique, en 2019". In: *Medecine Nucleaire* 43.3, pp. 251–266.

Brandner, Edward D. et al. (2006). "Abdominal organ motion measured using 4D CT". In: *International Journal of Radiation Oncology Biology Physics* 65.2, pp. 554–560.

Brosch-Lenz, Julia et al. (2021). "Influence of dosimetry method on bone lesion absorbed dose estimates in PSMA therapy: application to mCRPC patients receiving Lu-177-PSMA-I&T". In: *EJNMMI Physics* 8.1.

Brosch-Lenz, Julia et al. (2023). "Toward Single-Time-Point Image-Based Dosimetry of 177Lu-PSMA-617 Therapy". In: *Journal of Nuclear Medicine* 64.5, pp. 767–774.

Bruvoll, Ragnar, Johan Blakkisrud, Lars Tore Mikalsen, James Connelly, and Caroline Stokke (2023). "Correlations between [68Ga]Ga-DOTA-TOC Uptake and Absorbed Dose from [177Lu]Lu-DOTA-TATE". In: *Cancers* 15.4, pp. 1–13.

Burgard, Caroline et al. (2023). "Tumor Sink Effect with Prostate-Specific Membrane Antigen-Targeted Theranostics in Patients with Metastatic Castration-Resistant Prostate Cancer: Intra-Individual Evaluations". In: *Cancers* 15.9.

Cancer figures (2023). https://www.fondation-arc.org/cancer/le-cancer-en-chiffres-france-et-monde.

Cancer treatments (2023). https://www.fondation-arc.org/cancer/cancer-les-traitements-et-les-soins-de-support.

Capala, Jacek et al. (2021). "Dosimetry for Radiopharmaceutical Therapy: Current Practices and Commercial Resources". In: *Journal of nuclear medicine : official publication, Society of Nuclear Medicine* 62.12, 3S–11S.

Carter, L. M., J. C. Ocampo Ramos, and A. L. Kesner (2021). "Personalized dosimetry of 177Lu-DOTATATE: A comparison of organ- And voxel-level approaches using open-access images". In: *Biomedical Physics and Engineering Express* 7.5, pp. 1–17.

Cassol, E., P. Gantet, and P. Payoux (2019). "Veriton system: Quantitative evaluation based on Jaszczak and striatal phantom". In: *Medecine Nucleaire* 43.2, pp. 237–240.

Chang, Lee Tzuu (1978). "A method for attenuation correction in radionuclide computed tomography". In: *IEEE Transactions on Nuclear Science* 25.1, pp. 638–643.

Chatachot, Kotchakorn, Shuichi Shiratori, Tawatchai Chaiwatanarat, and Kitiwat Khamwan (2021). "Patient dosimetry of 177Lu-PSMA I&T in metastatic prostate cancer treatment: the experience in Thailand". In: *Annals of Nuclear Medicine* 35.11, pp. 1193–1202.

Chauvin, M et al. (2020). "OpenDose: Open-Access Resource for Nuclear Medicine Dosimetry". In: *Journal of nuclear medicine : official publication, Society of Nuclear Medicine* 61.10, pp. 1514–1519.

Cheng, Bernard et al. (2021). "Yttrium-90 dosimetry and implications on tumour response and survival after radioembolisation of chemo-refractory hepatic metastases from breast cancer". In: *Nuclear Medicine Communications* 42.4, pp. 402–409.

Cherry, Simon, James Sorenson, and Michael Phelps (2012). *Physics in Nuclear Medicine*. Philadelphia: ELSEVIER SAUNDERS.

Cette thèse est accessible à l'adresse : https://theses.insa-lyon.fr/publication/2023ISAL0068/these.pdf
© [L. Vergnaud], [2023], INSA Lyon, tous droits réservés

Chevalier, Elodie, Caroline Boursier, Marine Claudin, Pierre-Yves Marie, and Laetitia Imbert (Nov. 2020). "Feasibility of 177Lu Therapy Monitoring Using Fast Whole-Body SPECT Recordings Provided by a High-Speed 360° CZT Camera". en. In: *Clin Nucl Med* 45.11, e493–e494. ISSN: 1536-0229, 0363-9762.

Chicheportiche, A et al. (2020). "Dosimetry after peptide receptor radionuclide therapy: impact of reduced number of post-treatment studies on absorbed dose calculation and on patient management". In: *EJNMMI Physics* 7.1, pp. 1–15.

Chicheportiche, Alexandre et al. (2021). "Simple model for estimation of absorbed dose by organs and tumors after PRRT from a single SPECT/CT study". In: *EJNMMI Research* 8.1.

Chiesa, Carlo, Manuel Bardiès, and Habib Zaidi (2019). "Voxel-based dosimetry is superior to mean absorbed dose approach for establishing dose-effect relationship in targeted radionuclide therapy". In: *Medical Physics* 46.12, pp. 5403–5406.

Choi, Hyeonjun, Ji yong Shin, Jaeho Jang, and Gyuseong Cho (2023). "A modified decaying source method for dead time measurement with non-negligible background counts". In: *Nuclear Instruments and Methods in Physics Research, Section A: Accelerators, Spectrometers, Detectors and Associated Equipment* 1048.

Cohalan, Claire, Marc André Morin, and Antoine Leblond (2020). "Practical considerations for establishing dead-time corrections in quantitative SPECT imaging". In: *Biomedical Physics and Engineering Express* 7.2.

Coherent scattering (2023). https://radiopaedia.org/articles/coherent-scattering.

Collings, Peter J. (1980). "Simple measurement of the band gap in silicon and germanium". In: *American Journal of Physics* 48.3, pp. 197–199.

Compton effect (2023). https://radiopaedia.org/articles/compton-effect?lang=us.

Cremonesi, Marta et al. (2018). "Correlation of dose with toxicity and tumour response to 90Y- and 177Lu-PRRT provides the basis for optimization through individualized treatment planning". In: *European Journal of Nuclear Medicine and Molecular Imaging* 45.13, pp. 2426–2441.

Czernin, Johannes and Jeremie Calais (2023). "The 177Lu-PSMA-617 (Pluvicto) Supply Problem Will Be Solved by Competition". In: *Journal of nuclear medicine : official publication, Society of Nuclear Medicine* 64.3, p. 343.

d'Aillon, Eric Gros (2005). "Etude des performances spectrometriques des detecteurs gamma CdTe CdZnTe monolithiques". PhD thesis. Service des Technologies de détection LETI CEA Recherche Technologique.

Dale, Roger and Alejandro Carabe-Fernandez (2005). "The radiobiology of conventional radiotherapy and its application to radionuclide therapy". In: *Cancer Biotherapy and Radiopharmaceuticals* 20.1, pp. 47–51.

Darambara, D.G. and A. Todd-Pokropek (2002). "Solid state detectors in nuclear medicine". In: *The quarterly journal of nuclear medicine* 46, pp. 3–7.

D'Arienzo, M. et al. (2016). "Gamma camera calibration and validation for quantitative SPECT imaging with 177Lu". In: *Applied Radiation and Isotopes* 112, pp. 156–164.

Dash, Ashutosh, F. F. Knapp, and M. R.A. Pillai (2013). "99Mo/99mTc separation: An assessment of technology options". In: *Nuclear Medicine and Biology* 40.2, pp. 167–176.

Dash, Ashutosh, Maroor Raghavan Ambikalmajan Pillai, and Furn F. Knapp (2015). "Production of 177Lu for Targeted Radionuclide Therapy: Available Options". In: *Nuclear Medicine and Molecular Imaging* 49.2, pp. 85–107.

Cette thèse est accessible à l'adresse : https://theses.insa-lyon.fr/publication/2023ISAL0068/these.pdf
© [L. Vergnaud], [2023], INSA Lyon, tous droits réservés

De Nijs, Robin, Vera Lagerburg, Thomas L. Klausen, and Søren Holm (2014). "Improving quantitative dosimetry in 177Lu-DOTATATE SPECT by energy window-based scatter corrections". In: *Nuclear Medicine Communications* 35.5, pp. 522–533.

De Pierro, Alvaro R. (1995). "A Modified Expectation Maximization Algorithm for Penalized Likelihood Estimation in Emission Tomography". In: *IEEE Transactions on Medical Imaging* 14.1, pp. 132–137.

Definition (2023). https://www.ligue-cancer.net/article/26088_quest-ce-que-le-cancer.

Del Prete, M, F A Buteau, and J M Beauregard (2017). "Personalized 177Lu-octreotate peptide receptor radionuclide therapy of neuroendocrine tumours: a simulation study". In: *European Journal of Nuclear Medicine and Molecular Imaging* 44.9, pp. 1490–1500.

Del Prete, Michela et al. (2019). "Personalized 177 Lu-octreotate peptide receptor radionuclide therapy of neuroendocrine tumours: initial results from the P-PRRT trial". In: *European Journal of Nuclear Medicine and Molecular Imaging* 46.3, pp. 728–742.

Del Sordo, Stefano et al. (2009). "Progress in the development of CdTe and CdZnTe semiconductor radiation detectors for astrophysical and medical applications". In: *Sensors* 9.5, pp. 3491–3526.

Delker, Andreas et al. (2015). "The Influence of Early Measurements Onto the Estimated Kidney Dose in [177Lu][DOTA0,Tyr3]Octreotate Peptide Receptor Radiotherapy of Neuroendocrine Tumors". In: *Molecular Imaging and Biology* 17.5, pp. 726–734.

Delker, Andreas et al. (2016). "Dosimetry for 177Lu-DKFZ-PSMA-617: a new radiopharmaceutical for the treatment of metastatic prostate cancer". In: *European Journal of Nuclear Medicine and Molecular Imaging* 43.1, pp. 42–51.

Delker, Astrid et al. (2023). "Biodistribution and dosimetry for combined [177Lu]Lu-PSMA-IT/[225Ac]Ac-PSMA-IT therapy using multi-isotope quantitative SPECT imaging". In: *European Journal of Nuclear Medicine and Molecular Imaging* 50.5, pp. 1280–1290.

Della Gala, Giuseppe et al. (2022). "How the Rigid and Deformable Image Registration Approaches Affect the Absorbed Dose Estimation Using Images Collected before and after Transarterial Radioembolization with 90Y Resin Microspheres in a Clinical Setting". In: *Applied Sciences* 12.24.

Delmon, V, S Rit, R Pinho, and D Sarrut (2013). "Registration of sliding objects using direction dependent B-splines decomposition". In: *Physics in medicine and biology* 58.5, pp. 1303–1314.

Demirci, Emre et al. (2016). "Normal distribution pattern and physiological variants of 68Ga-PSMA-11 PET/CT imaging". In: *Nuclear Medicine Communications* 37.11, pp. 1169–1179.

Deshayes, Emmanuel et al. (2022). "A prospective, randomized, phase II study to assess the schemas of retreatment with Lutathera® in patients with new progression of an intestinal, well-differentiated neuroendocrine tumor (ReLUTH)". In: *BMC Cancer* 22.1, pp. 1–6.

Desmonts, Cédric et al. (Dec. 2020). "Evaluation of a new multipurpose whole-body CzT-based camera: comparison with a dual-head Anger camera and first clinical images". en. In: *EJNMMI Phys* 7.1, p. 18. ISSN: 2197-7364.

Desy, A, G F Bouvet, A Frezza, P Després, and J M Beauregard (2020). "Impact of dead time on quantitative 177Lu-SPECT (QSPECT) and kidney dosimetry during PRRT". In: *EJNMMI Physics* 7.1, pp. 1–8.

Cette thèse est accessible à l'adresse : https://theses.insa-lyon.fr/publication/2023ISAL0068/these.pdf
© [L. Vergnaud], [2023], INSA Lyon, tous droits réservés

Desy, Alessandro et al. (2022). "Impact of the dead-time correction method on quantitative 177Lu-SPECT (QSPECT) and dosimetry during radiopharmaceutical therapy". In: *EJNMMI Physics* 9.1.

Devasia, T, Y K Dewaraja, K A Frey, K K Wong, and M J Schipper (2020). "A novel time-activity information sharing approach using nonlinear mixed models for patient-specific dosimetry with reduced imaging time points: application in SPECT/CT imaging post-177Lu-DOTATATE". In: *Journal of Nuclear Medicine* 62.6.

Dewaraja, Y K et al. (2012). "MIRD pamphlet no. 23: Quantitative SPECT for patient-specific 3-dimensional dosimetry in internal radionuclide therapy". In: *Journal of Nuclear Medicine* 53.8, pp. 1310–1325.

Dewaraja, Yuni K. et al. (2017). "Improved quantitative 90Y bremsstrahlung SPECT/CT reconstruction with Monte Carlo scatter modeling". In: *Medical Physics* 44.12, pp. 6364–6376.

Dewaraja, Yuni K. et al. (2022). "A Pipeline for Automated Voxel Dosimetry: Application in Patients with Multi-SPECT/CT Imaging After 177Lu-Peptide Receptor Radionuclide Therapy". In: *Journal of nuclear medicine : official publication, Society of Nuclear Medicine* 63.11, pp. 1665–1672.

Dickson, John C. et al. (2010). "The impact of reconstruction method on the quantification of DaTSCAN images". In: *European Journal of Nuclear Medicine and Molecular Imaging* 37.1, pp. 23–35.

Dickson, John C. et al. (2022). "EANM practice guideline for quantitative SPECT-CT". In: *European Journal of Nuclear Medicine and Molecular Imaging*.

Dietze, M M.A., B Kunnen, M G.E.H. Lam, and H W.A.M. De Jong (2021). "Interventional respiratory motion compensation by simultaneous fluoroscopic and nuclear imaging: A phantom study". In: *Physics in Medicine and Biology* 66.6.

Dietze, Martijn M.A. et al. (2019). "Respiratory motion compensation in interventional liver SPECT using simultaneous fluoroscopic and nuclear imaging". In: *Medical Physics* 46.8, pp. 3496–3507.

Dieudonné, Arnaud et al. (2013). "Study of the impact of tissue density heterogeneities on 3-dimensional abdominal dosimetry: Comparison between dose kernel convolution and direct monte carlo methods". In: *Journal of Nuclear Medicine* 54.2, pp. 236–243.

Dooms, G C et al. (1985). "Bone marrow imaging: magnetic resonance studies related to age and sex." In: *Radiology* 155.2, pp. 429–432.

Duvall, W. Lane et al. (2011). "Reduced isotope dose and imaging time with a high-efficiency CZT SPECT camera". In: *Journal of Nuclear Cardiology* 18.5, pp. 847–857.

Eberlein, Uta, Marta Cremonesi, and Michael Lassmann (2017). "Individualized dosimetry for theranostics: Necessary, nice to have, or counterproductive?" In: *Journal of Nuclear Medicine* 58.9, 97S–103S.

Eiber, Matthias et al. (2018). "Prostate cancer molecular imaging standardized evaluation (PROMISE): Proposed miTNM classification for the interpretation of PSMA-ligand PET/CT". In: *Journal of Nuclear Medicine* 59.3, pp. 469–478.

Elajami, Mohamad K., Lorena P. Burton, Hisham F. Bahmad, Gerard Chaaya, and Michael Schwartz (2022). "Repurposed Effect of 177Lu-DOTATATE in the Treatment of Mantle Cell Lymphoma". In: *Current Oncology* 29.10, pp. 7552–7557.

Elschot, Mattijs et al. (2014). "99mTc-MAA overestimates the absorbed dose to the lungs in radioembolization: a quantitative evaluation in patients treated with 166Ho-microspheres". In: *European Journal of Nuclear Medicine and Molecular Imaging* 41.10, pp. 1965–1975.

Cette thèse est accessible à l'adresse : https://theses.insa-lyon.fr/publication/2023ISAL0068/these.pdf
© [L. Vergnaud], [2023], INSA Lyon, tous droits réservés

Erlandsson, Kjell, Irène Buvat, P. Hendrik Pretorius, Benjamin A. Thomas, and Brian F. Hutton (2012). "A review of partial volume correction techniques for emission tomography and their applications in neurology, cardiology and oncology". In: *Physics in Medicine and Biology* 57.21, pp. 119–159.

Esper, Peg et al. (1997). "Measuring quality of life in men with prostate cancer using the functional assessment of cancer therapy-prostate instrument". In: *Urology* 50.6, pp. 920–928.

Esteves, Fabio P. et al. (2009). "Novel solid-state-detector dedicated cardiac camera for fast myocardial perfusion imaging: Multicenter comparison with standard dual detector cameras". In: *Journal of Nuclear Cardiology* 16.6, pp. 927–934.

External Beam Radiation Therapy for Cancer (2023). https://www.cancer.gov/about-cancer/treatment/types/radiation-therapy/external-beam.

Ezziddin, Samer et al. (2012). "Does the Pretherapeutic Tumor SUV in 68Ga DOTA-TOC PET Predict the Absorbed Dose of 177Lu Octreotate?" In: *Clinical Nuclear Medicine* 37.6, pp. 141–147.

Fanti, Stefano et al. (2021). "Consensus statements on PSMA PET/CT response assessment criteria in prostate cancer". In: *European Journal of Nuclear Medicine and Molecular Imaging* 48.2, pp. 469–476.

Fendler, Wolfgang P. et al. (2017). "Preliminary experience with dosimetry, response and patient reported outcome after 177Lu-PSMA-617 therapy for metastatic castration-resistant prostate cancer". In: *Oncotarget* 8.2, pp. 3581–3590.

Fendler, Wolfgang P et al. (2023). "PSMA PET/CT: joint EANM procedure guideline/SNMMI procedure standard for prostate cancer imaging 2.0". In: *European journal of nuclear medicine and molecular imaging* 50.5, pp. 1466–1486.

Ferrer, L et al. (2010). "Three methods assessing red marrow dosimetry in lymphoma patients treated with radioimmunotherapy". In: *Cancer* 15.116(SUPPL. 4), pp. 1093–1100.

Feuerecker, Benedikt et al. (2022). "Pre-therapeutic comparative dosimetry of 177Lu-rhPSMA-7.3 and 177Lu-PSMA-I&T in patients with metastatic castration resistant prostate cancer (mCRPC)". In: *Journal of Nuclear Medicine* 63.6, pp. 833–839.

Filss, Christian et al. (2018). "Relevant tumor sink effect in prostate cancer patients receiving 177Lu-PSMA-617 radioligand therapy". In: *NuklearMedizin* 57.1, pp. 19–25.

Finocchiaro, D et al. (2020). "Comparison of different calculation techniques for absorbed dose assessment in patient specific peptide receptor radionuclide therapy". In: *PLoS ONE* 15.8.

Finocchiaro, Domenico et al. (2019). "Partial volume effect of SPECT images in PRRT with 177Lu labelled somatostatin analogues: A practical solution". In: *Physica Medica* 57, pp. 153–159.

Fleming, J S (1989). "A technique for using CT images in attenuation correction and quantification in SPECT". In: *Nuclear medicine communications* 10.2, pp. 83–97.

Forrer, Flavio et al. (2009a). "Bone marrow dosimetry in peptide receptor radionuclide therapy with [177Lu-DOTA0,Tyr3]octreotate". In: *European Journal of Nuclear Medicine and Molecular Imaging* 36.7, pp. 1138–1146.

Forrer, Flavio et al. (2009b). "In vitro characterization of 177Lu-radiolabelled chimeric anti-CD20 monoclonal antibody and a preliminary dosimetry study". In: *European Journal of Nuclear Medicine and Molecular Imaging* 36.9, pp. 1443–1452.

Freedman, Nanette et al. (2020). "Personalized radiation dosimetry for PRRT—how many scans are really required?" In: *EJNMMI Physics* 7.1.

Cette thèse est accessible à l'adresse : https://theses.insa-lyon.fr/publication/2023ISAL0068/these.pdf
© [L. Vergnaud], [2023], INSA Lyon, tous droits réservés

Frey, E. C. and B. M.W. Tsui (1996). "New method for modeling the spatially-variant, object-dependent scatter response function in SPECT". In: *IEEE Nuclear Science Symposium & Medical Imaging Conference* 2, pp. 1082–1086.

Frey, Eric C., John L. Humm, and Michael Ljungberg (2012). "Accuracy and precision of radioactivity quantification in nuclear medicine images". In: *Seminars in Nuclear Medicine* 42.3, pp. 208–218.

Furhang, E. E., C. S. Chui, K. S. Kolbert, S. M. Larson, and G. Sgouros (1997). "Implementation of a Monte Carlo dosimetry method for patient-specific internal emitter therapy". In: *Medical Physics* 24.9, pp. 1163–1172.

Furhang, Eli E., Chen Shou Chui, and George Sgouros (1996). "A Monte Carlo approach to patient-specific dosimetry". In: *Medical Physics* 23.9, pp. 1523–1529.

Gafita, Andrei et al. (2021). "Nomograms to predict outcomes after 177Lu-PSMA therapy in men with metastatic castration-resistant prostate cancer: an international, multicentre, retrospective study". In: *The Lancet Oncology* 22.8, pp. 1115–1125.

Gafita, Andrei et al. (2022). "Novel Framework for Treatment Response Evaluation Using PSMA PET/CT in Patients with Metastatic Castration-Resistant Prostate Cancer (RECIP 1.0): An International Multicenter Study". In: *Journal of nuclear medicine : official publication, Society of Nuclear Medicine* 63.11, pp. 1651–1658.

Gardner, R P and L Liu (1997). "On extending the accurate and useful counting rate range of GM counter detector systems". In: *Applied Radiation and Isotopes* 48.10-12, pp. 1605–1615.

Garin, E et al. (2021). "Personalised versus standard dosimetry approach of selective internal radiation therapy in patients with locally advanced". In: *The Lancet Gastroenterology and Hepatology* 6.1, pp. 17–29.

Garin, Etienne, Xavier Palard, and Yan Rolland (2020). "Personalised dosimetry in radioembolisation for HCC: Impact on clinical outcome and on trial design". In: *Cancers* 12.6, pp. 1–17.

Garin, Etienne, Yan Rolland, and Julien Edeline (2019). "90Y-Loaded Microsphere SIRT of HCC Patients With Portal Vein Thrombosis: High Clinical Impact of 99mTc-MAA SPECT/CT-Based Dosimetry". In: *Seminars in Nuclear Medicine* 49.3, pp. 218–226.

Garin, Etienne, Yan Rolland, Sophie Laffont, and Julien Edeline (2016). "Clinical impact of 99mTc-MAA SPECT/CT-based dosimetry in the radioembolization of liver malignancies with 90Y-loaded microspheres". In: *European Journal of Nuclear Medicine and Molecular Imaging* 43.3, pp. 559–575.

Garkavij, Michael et al. (2010). "177Lu-[DOTA0,Tyr3] octreotate therapy in patients with disseminated neuroendocrine tumors: Analysis of dosimetry with impact on future therapeutic strategy". In: *Cancer* 116.SUPPL.4, pp. 1084–1092.

Garske, U et al. (2012). "Minor changes in effective half-life during fractionated 177Lu-Octreotate therapy". In: *Acta Oncologica* 51.1, pp. 86–96.

Garske-Román, Ulrike et al. (2018). "Prospective observational study of 177Lu-DOTA-octreotate therapy in 200 patients with advanced metastasized neuroendocrine tumours (NETs): feasibility and impact of a dosimetry-guided study protocol on outcome and toxicity". In: *European Journal of Nuclear Medicine and Molecular Imaging* 45.6, pp. 970–988.

Gear, Jonathan et al. (2023). "EANM enabling guide: how to improve the accessibility of clinical dosimetry". In: *European Journal of Nuclear Medicine and Molecular Imaging* 50.7, pp. 1861–1868.

Cette thèse est accessible à l'adresse : https://theses.insa-lyon.fr/publication/2023ISAL0068/these.pdf
© [L. Vergnaud], [2023], INSA Lyon, tous droits réservés

Gear, Jonathan I. et al. (2018). "EANM practical guidance on uncertainty analysis for molecular radiotherapy absorbed dose calculations". In: *European Journal of Nuclear Medicine and Molecular Imaging* 45.13, pp. 2456–2474.

Giammarile, Francesco et al. (2011). "EANM procedure guideline for the treatment of liver cancer and liver metastases with intra-arterial radioactive compounds". In: *European Journal of Nuclear Medicine and Molecular Imaging* 38.7, pp. 1393–1406.

Gianfaldoni, Serena et al. (2017). "An overview on radiotherapy: From its history to its current applications in dermatology". In: *Journal of Medical Sciences* 5.4, pp. 521–525.

Giap, H. B., D. J. Macey, J. E. Bayouth, and A. L. Boyer (1995). "Validation of a dose-point kernel convolution technique for internal dosimetry". In: *Physics in Medicine and Biology* 40.3, pp. 365–381.

Gonsalves, Carin F. et al. (2019). "A prospective Phase II trial of radioembolization for treatment of uveal melanoma hepatic metastasis". In: *Radiology* 293.1, pp. 223–231.

Gosewisch, Astrid et al. (2019). "3D Monte Carlo bone marrow dosimetry for Lu-177-PSMA therapy with guidance of non-invasive 3D localization of active bone marrow via Tc-99m-anti-granulocyte antibody SPECT/CT". In: *EJNMMI Research* 9.1.

Goshen, Elinor et al. (Dec. 2018). "Feasibility study of a novel general purpose CZT-based digital SPECT camera: initial clinical results". en. In: *EJNMMI Phys* 5.1, p. 6. ISSN: 2197-7364.

Graves, Stephen A., Ryan T. Flynn, and Daniel E. Hyer (2019). "Dose point kernels for 2,174 radionuclides". In: *Medical Physics* 46.11, pp. 5284–5293.

Grimes, J and A Celler (2014). "Comparison of internal dose estimates obtained using organ-level, voxel S-value, and Monte Carlo techniques". In: *Medical Physics* 41.9.

Grimes, Joshua, Anna Celler, Sergey Shcherbinin, Hanna Piwowarska-Bilska, and Bozena Birkenfeld (2012). "The accuracy and reproducibility of SPECT target volumes and activities estimated using an iterative adaptive thresholding technique." In: *Nuclear medicine communications* 33.12, pp. 1254–1266.

Groch, M. W. and W. D. Erwin (2000). "SPECT in the year 2000: Basic principles". In: *Journal of Nuclear Medicine Technology* 28.4, pp. 233–244.

Guerriero, F et al. (2013). "Kidney dosimetry in 177 Lu and 90 Y peptide receptor radionuclide therapy: influence of image timing, time-activity integration method, and risk factors". In: *BioMed research international*, pp. 1–12.

Gupta, Sandeep Kumar et al. (2017). "Radionuclide bone scan SPECT-CT: lowering the dose of CT significantly reduces radiation dose without impacting CT image quality". In: *American journal of nuclear medicine and molecular imaging* 7.2, pp. 63–73.

Gustafsson, Johan, Anna Sundlöv, and Katarina Sjögreen Gleisner (2017). "SPECT image segmentation for estimation of tumour volume and activity concentration in 177Lu-DOTATATE radionuclide therapy". In: *EJNMMI Research* 7.1.

Gustafsson, Johan and Jan Taprogge (2022). "Theoretical aspects on the use of single-time-point dosimetry for radionuclide therapy". In: *Physics in Medicine and Biology* 67.2.

Gustafsson, Johan et al. (2023). "Averaging of absorbed doses: How matter matters." In: *Medical Physics*.

Guérin, Lucie, Loïck Verger, Véronique Rebuffel, and Olivier Monnet (2008). "A new architecture for pixellated solid state gamma camera used in nuclear medicine". In: *IEEE Transactions on Nuclear Science* 55.3, pp. 1573–1580.

Cette thèse est accessible à l'adresse : https://theses.insa-lyon.fr/publication/2023ISAL0068/these.pdf
© [L. Vergnaud], [2023], INSA Lyon, tous droits réservés

Gühne, Falk et al. (2022). "Differences in distribution and detection rate of the [68Ga]Ga-PSMA ligands PSMA-617,-I&T and-11—inter-individual comparison in patients with biochemical relapse of prostate cancer". In: *Pharmaceuticals* 15.1.

Hagmarker, L, J Svensson, T Rydén, M Van Essen, and A Sundlöv (2019). "Bone marrow absorbed doses and correlations with hematologic response during 177Lu-DOTATATE treatments are influenced by image-based dosimetry method and presence of skeletal metastases". In: *Journal of Nuclear Medicine* 60.10, pp. 1406–1413.

Halty, Adrien, Jean Noël Badel, Olga Kochebina, and David Sarrut (2018). "Image-based SPECT calibration based on the evaluation of the Fraction of Activity in the Field of View". In: *EJNMMI Physics* 5.1.

Hardiansyah, D, P Kletting, N J Begum, M Eiber, and A J Beer (2020). "Important pharmacokinetic parameters for individualization of 177Lu-PSMA therapy: A global sensitivity analysis for a physiologically-based". In: *Medical Physics*.

Hardiansyah, Deni, Ade Riana, Ambros J. Beer, and Gerhard Glatting (2022). "Single-time-point estimation of absorbed doses in PRRT using a non-linear mixed-effects model". In: *Zeitschrift fur Medizinische Physik* 33.1, pp. 70–81.

Heidegger, Isabel et al. (2022). "Biomarkers to personalize treatment with 177Lu-PSMA-617 in men with metastatic castration-resistant prostate cancer - a state of the art review". In: *Therapeutic Advances in Medical Oncology* 14, pp. 1–10.

Heikkonen, Jorma, Hanna Mäenpää, Eero Hippeläinen, Vappu Reijonen, and Mikko Tenhunen (2016). "Effect of calculation method on kidney dosimetry in 177Lu-octreotate treatment". In: *Acta Oncologica* 55.9-10, pp. 1069–1076.

Helmberger, Thomas et al. (2021). "Clinical Application of Trans-Arterial Radioembolization in Hepatic Malignancies in Europe: First Results from the Prospective Multicentre Observational Study CIRSE Registry for SIR-Spheres Therapy (CIRT)". In: *CardioVascular and Interventional Radiology* 44.1, pp. 21–35.

Hemmingsson, Jens et al. (2023). "Specific Uptake in the Bone Marrow Causes High Absorbed Red Marrow Doses During [177Lu]Lu-DOTATATE Treatment". In: *Journal of Nuclear Medicine*.

Heynickx, Nathalie, Koen Herrmann Ken aand Vermeulen, Sarah Baatout, and An Aerts (2021). "The salivary glands as a dose limiting organ of PSMA- targeted radionuclide therapy: A review of the lessons learnt so far". In: *Nuclear Medicine and Biology* 98-99, pp. 30–39.

Hindorf, C, G Glatting, C Chiesa, O Lindén, and G Flux (2010). "EANM dosimetry committee guidelines for bone marrow and whole-body dosimetry". In: *European Journal of Nuclear Medicine and Molecular Imaging* 37.6, pp. 1238–1250.

Hofman, Michael S, W F Eddie Lau, and Rodney J Hicks (2015). "Somatostatin receptor imaging with 68Ga DOTATATE PET/CT: clinical utility, normal patterns, pearls, and pitfalls in interpretation." In: *Radiographics : a review publication of the Radiological Society of North America, Inc* 35.2, pp. 500–516.

Hofman, Michael S et al. (Feb. 2021). "[177Lu]Lu-PSMA-617 versus cabazitaxel in patients with metastatic castration-resistant prostate cancer (TheraP): a randomised, open-label, phase 2 trial". en. In: *The Lancet* 397.10276, pp. 797–804. ISSN: 01406736.

Hohberg, Melanie et al. (2016). "Lacrimal Glands May Represent Organs at Risk for Radionuclide Therapy of Prostate Cancer with [177Lu]DKFZ-PSMA-617". In: *Molecular Imaging and Biology* 18.3, pp. 437–445.

Hope, Thomas A. et al. (2020). "NANETS/SNMMI consensus statement on patient selection and appropriate use of 177Lu-DOTATATE peptide receptor radionuclide therapy". In: *Journal of Nuclear Medicine* 61.2, pp. 222–227.

Cette thèse est accessible à l'adresse : https://theses.insa-lyon.fr/publication/2023ISAL0068/these.pdf
© [L. Vergnaud], [2023], INSA Lyon, tous droits réservés

Hope, Thomas A. et al. (2023). "SNMMI Procedure Standard/EANM Practice Guideline for SSTR PET: Imaging Neuroendocrine Tumors". In: *Journal of nuclear medicine : official publication, Society of Nuclear Medicine* 64.2, pp. 204–210.

Hou, Xinchi et al. (2021). "Feasibility of Single-Time-Point Dosimetry for Radiopharmaceutical Therapies". In: *Journal of Nuclear Medicine* 62.7, pp. 1006–1011.

Howell, R W et al. (1999). "The MIRD perspective 1999. Medical Internal Radiation Dose Committee." In: *Journal of nuclear medicine : official publication, Society of Nuclear Medicine* 40.1, pp. 38–108.

Huh, Yoonsuk et al. (2023). "Simulation studies of a full-ring, CZT SPECT system for whole-body imaging of 99mTc and 177Lu". In: *Medical Physics* 50.6, pp. 3726–3737.

Huizing, Daphne Merel Valerie, Berlinda Jantina de Wit-van der Veen, Marcel Verheij, and Marcellus Petrus Maria Stokkel (2018). "Dosimetry methods and clinical applications in peptide receptor radionuclide therapy for neuroendocrine tumours: a literature review". In: *EJNMMI Research* 8.89.

Huizing, Daphne M.V. et al. (2020). "A head-to-head comparison between two commercial software packages for hybrid dosimetry after peptide receptor radionuclide therapy". In: *EJNMMI Physics* 7.1.

Hutton, B F, J Nuyts, and H Zaidi (2006). "FIterative Reconstruction Methods". In: *Quantitative Analysis in Nuclear Medicine Imaging*. Ed. by H. Zaidi. Boston, MA: Nuclear Medicine Imaging. Springer, pp. 107–140.

Hutton, Brian F., Irène Buvat, and Freek J. Beekman (2011). "Review and current status of SPECT scatter correction". In: *Physics in Medicine and Biology* 56.14, pp. 85–112.

Hänscheid, H, C Lapa, A K Buck, M Lassmann, and R A Werner (2017). "Absorbed dose estimates from a single measurement one to three days after the administration of 177Lu-DOTATATE/-TOC". In: *NuklearMedizin* 56.6, pp. 219–224.

— (2018). "Dose mapping after endoradiotherapy with 177 Lu-DOTATATE/DOTATOC by a single measurement after 4 days". In: *Journal of Nuclear Medicine* 59.1, pp. 75–81.

Hänscheid, H and M Lassmann (2020). "Will SPECT/CT Cameras Soon Be Able to Display Absorbed Doses? Dosimetry from Single-Activity-Concentration Measurements". In: *Journal of nuclear medicine : official publication, Society of Nuclear Medicine* 61.7, pp. 1028–1029.

Ilan, E et al. (2015). "Dose response of pancreatic neuroendocrine tumors treated with peptide receptor radionuclide therapy using 177Lu-DOTATATE". In: *Journal of Nuclear Medicine* 56.2, pp. 177–182.

Imbert, Laetitia, Elodie Chevalier, Marine Claudin, Gilles Karcher, and Pierre-Yves Marie (2020). "Absolute quantification provided by 177Lu SPECT images recorded by a high-speed 360° whole-body CZT camera: a feasibility study on phantom and patient". In: *Journal of Nuclear Medicine* 61.SUPPL.1, p. 1304.

— (2021a). "Feasibility of total body dosimetry of Lu-177 SPECT-CT images recorded by a CZT camera". In: *Journal of Nuclear Medicine* 62.SUPPL.1, p. 1509.

Imbert, Laetitia, Mathieu Perrin, Marine Claudin, Caroline Boursier, and Pierre-Yves Marie (2021b). "High quality attenuation-corrected myocardial perfusion images may be achieved in patients with morbid obesity using a whole-body CZT camera and a low-dose injection protocol." In: *Journal of nuclear cardiology : official publication of the American Society of Nuclear Cardiology* 28.4, pp. 1791–1792.

Imbert, Laetitia et al. (2012). "Compared performance of high-sensitivity cameras dedicated to myocardial perfusion SPECT: A comprehensive analysis of phantom and human images". In: *Journal of Nuclear Medicine* 53.12, pp. 1897–1903.

Cette thèse est accessible à l'adresse : https://theses.insa-lyon.fr/publication/2023ISAL0068/these.pdf
© [L. Vergnaud], [2023], INSA Lyon, tous droits réservés

Ishii, Kazunari et al. (2012). "Impact of CT attenuation correction by SPECT/CT in brain perfusion images". In: *Annals of Nuclear Medicine* 26.3, pp. 241–247.

Ito, Toshimune et al. (Feb. 2021). "Experimental evaluation of the GE NM/CT 870 CZT clinical SPECT system equipped with WEHR and MEHRS collimator". en. In: *J Appl Clin Med Phys* 22.2, pp. 165–177. ISSN: 1526-9914, 1526-9914.

Jackson, P A, M S Hofman, R J Hicks, M Scalzo, and J Violet (2020a). "Radiation Dosimetry in 177Lu-PSMA-617 Therapy Using a Single Posttreatment SPECT/CT Scan: A Novel Methodology to Generate Time- and Tissue-Specific Dose". In: *Journal of nuclear medicine : official publication, Society of Nuclear Medicine* 61.7, pp. 1030–1036.

Jackson, Price, Michael Hofman, Lachlan McIntosh, James Patrick Buteau, and Aravind Ravi Kumar (2022). "Radiation Dosimetry in 177Lu-PSMA-617 Therapy". In: *Seminars in Nuclear Medicine* 52.2, pp. 243–254.

Jackson, Price, Lachlan McIntosh, Michael S. Hofman, Grace Kong, and Rodney J. Hicks (2020b). "Technical Note: Rapid multiexponential curve fitting algorithm for voxel-based targeted radionuclide dosimetry". In: *Medical Physics* 47.9, pp. 1–8.

Jackson, Price et al. (2018). "Deep learning renal segmentation for fully automated radiation dose estimation in unsealed source therapy". In: *Frontiers in Oncology* 8.JUN, pp. 1–7.

Jackson, Price A. et al. (2013). "An automated voxelized dosimetry tool for radionuclide therapy based on serial quantitative SPECT/CT imaging". In: *Medical Physics* 40.11, pp. 1–8.

Jadoul, Alexandre et al. (2020). "Comparative dosimetry between 99m Tc-MAA SPECT / CT and 90 Y PET / CT in primary and metastatic liver tumors". In: *European Journal of Nuclear Medicine and Molecular Imaging* 47.4, pp. 828–837.

Jahn, Ulrika et al. (2020). "177 Lu-DOTATATE Peptide Receptor Radionuclide Therapy: Dose Response in Small Intestinal Neuroendocrine Tumors". In: *Neuroendocrinology* 110.7-8, pp. 662–670.

Jahn, Ulrika et al. (2021). "Peptide Receptor Radionuclide Therapy (PRRT) with 177Lu-DOTATATE; Differences in Tumor Dosimetry, Vascularity and Lesion Metrics in Pancreatic and Small Intestinal Neuroendocrine Neoplasms". In: *Cancers* 13.5.

Jaszczak, R. J., K. L. Greer, C. E. Floyd, C. C. Harris, and R. E. Coleman (1984). "Improved SPECT quantification using compensation for scattered photons". In: *Journal of Nuclear Medicine* 25.8, pp. 893–900.

Junqueira, Matheus Zanelatto, Nelisa Helena Rocha, and Marcelo Tatit Sapienza (2021). "68ga-psma pet/ct: Effect of external cooling on salivary gland uptake". In: *Radiologia Brasileira* 54.3, pp. 171–176.

Kabasakal, Levent et al. (2015). "Pre-therapeutic dosimetry of normal organs and tissues of 177Lu-PSMA-617 prostate-specific membrane antigen (PSMA) inhibitor in patients with castration-resistant prostate cancer". In: *European Journal of Nuclear Medicine and Molecular Imaging* 42.13, pp. 1976–1983.

Kabasakal, Levent et al. (2017). "Lu-177-PSMA-617 Prostate-Specific Membrane Antigen Inhibitor Therapy in Patients with Castration-Resistant Prostate Cancer: Stability, Bio-distribution and Dosimetry". In: *Molecular Imaging and Radionuclide Therapy* 26.2, pp. 62–68.

Kalogianni, Eleni, Glenn D. Flux, and Alessandra Malaroda (2007). "The use of BED and EUD concepts in heterogeneous radioactivity distributions on a multicellular scale for targeted radionuclide therapy". In: *Cancer Biotherapy and Radiopharmaceuticals* 22.1, pp. 143–150.

Cette thèse est accessible à l'adresse : https://theses.insa-lyon.fr/publication/2023ISAL0068/these.pdf
© [L. Vergnaud], [2023], INSA Lyon, tous droits réservés

Kamaldeep et al. (2021). "Examining Absorbed Doses of Indigenously Developed (177)Lu-PSMA-617 in Metastatic Castration-Resistant Prostate Cancer Patients at Baseline and During Course of Peptide Receptor Radioligand Therapy." In: *Cancer biotherapy & radiopharmaceuticals* 36.3, pp. 292–304.

Kao, Yung Hsiang et al. (2014). "Personalized predictive lung dosimetry by technetium-99m macroaggregated albumin SPECT/CT for yttrium-90 radioembolization". In: *EJNMMI Research* 4.1, pp. 1–12.

Kaplan, Michael M, Donald A Meier, and Howard J Dworkin (1998). "Treatment of hyperthyroidism with radioactive iodine". In: *Endocrinology and Metabolism Clinics of North America* 27.1, pp. 205–223.

Karimi Ghodoosi, Elham et al. (2018). "The effect of attenuation map, scatter energy window width, and volume of interest on the calibration factor calculation in quantitative 177Lu SPECT imaging: Simulation and phantom study". In: *Physica Medica* 56, pp. 74–80.

Kassis, Amin I. and S. James Adelstein (2005). "Radiobiologic principles in radionuclide therapy". In: *Journal of Nuclear Medicine* 46.1, pp. 4–12.

Kennedy, John A., Rachel Lugassi, Ronit Gill, and Zohar Keidar (2020). "Digital solid-state spect/ct quantitation of absolute 177lu radiotracer concentration: In vivo and in vitro validation". In: *Journal of Nuclear Medicine* 61.9, pp. 1381–1387.

Kim, Keon Min et al. (2022). "Comparison of voxel S-value methods for personalized voxel-based dosimetry of 177Lu-DOTATATE". In: *Medical Physics* 49.3, pp. 1888–1901.

Kim, S. Peter, Claire Cohalan, Neil Kopek, and Shirin A. Enger (2019). "A guide to 90Y radioembolization and its dosimetry". In: *Physica Medica* 68.February, pp. 132–145.

Kind, Felix et al. (2022). "Bone marrow impairment during early [177Lu]PSMA-617 radioligand therapy: Haematotoxicity or tumour progression?" In: *EJNMMI Research* 12.1, pp. 1–8.

King, Julie et al. (2008). "Radioembolization with selective internal radiation microspheres for neuroendocrine liver metastases". In: *Cancer* 113.5, pp. 921–929.

Klein, Stefan, Marius Staring, Keelin Murphy, Max A. Viergever, and Josien P.W. Pluim (2010). "Elastix: A toolbox for intensity-based medical image registration". In: *IEEE Transactions on Medical Imaging* 29.1, pp. 196–205.

Knešaurek, Karin, Abbas Tuli, Sara D. Pasik, Sherif Heiba, and Lale Kostakoglu (2018). "Quantitative comparison of pre-therapy 99mTc-macroaggregated albumin SPECT/CT and post-therapy PET/MR studies of patients who have received intra-arterial radioembolization therapy with 90Y microspheres". In: *European Journal of Radiology* 109, pp. 57–61.

Komber, Hend, David Little, Sarah Cade, Richard Graham, and Stewart Redman (2021). "Comparing the patient experience between a novel 360° gamma camera (VERITON-CT) and a conventional dual head gamma camera." In: *Journal of nuclear medicine technology* 50.2, pp. 132–136.

Konijnenberg, Mark, Marleen Melis, Roelf Valkema, Eric Krenning, and Marion De Jong (2007). "Radiation dose distribution in human kidneys by octreotides in peptide receptor radionuclide therapy". In: *Journal of Nuclear Medicine* 48.1, pp. 134–142.

Koral, K. F. et al. (1990). "SPECT dual-energy-window Compton correction: Scatter multiplier required for quantification". In: *Journal of Nuclear Medicine* 31.1, pp. 90–98.

Kortelainen, Matti J., Tuomas M. Koivumäki, Marko J. Vauhkonen, and Mikko A. Hakulinen (2019). "Effect of respiratory motion on cardiac defect contrast in

Cette thèse est accessible à l'adresse : https://theses.insa-lyon.fr/publication/2023ISAL0068/these.pdf
© [L. Vergnaud], [2023], INSA Lyon, tous droits réservés

myocardial perfusion SPECT: a physical phantom study". In: *Annals of Nuclear Medicine* 33.5, pp. 305–316.

Kovalski, Gil et al. (2007). "Correction of heart motion due to respiration in clinical myocardial perfusion SPECT scans using respiratory gating". In: *Journal of Nuclear Medicine* 48.4, pp. 630–636.

Kratochwil, Clemens et al. (2016a). "225Ac-PSMA-617 for PSMA-targeted a-radiation therapy of metastatic castration-resistant prostate cancer". In: *Journal of Nuclear Medicine* 57.12, pp. 1941–1944.

Kratochwil, Clemens et al. (2016b). "PSMA-targeted radionuclide therapy of metastatic castration-resistant prostate cancer with 177Lu-Labeled PSMA-617". In: *Journal of Nuclear Medicine* 57.8, pp. 1170–1176.

Kratochwil, Clemens et al. (2019). "EANM procedure guidelines for radionuclide therapy with 177Lu-labelled PSMA-ligands (177Lu-PSMA-RLT)". en. In: *European Journal of Nuclear Medicine and Molecular Imaging* 46.12, pp. 2536–2544.

Kruis, Matthijs F. et al. (2013). "PET motion compensation for radiation therapy using a CT-based mid-position motion model: Methodology and clinical evaluation". In: *International Journal of Radiation Oncology Biology Physics* 87.2, pp. 394–400.

Kyme, Andre Z. and Roger R. Fulton (2021). "Motion estimation and correction in SPECT, PET and CT". In: *Physics in Medicine and Biology* 66.18.

La Brachythérapie ou Curithérapie (2023). https://www.arcagy.org/infocancer/traitement-du-cancer/traitements-locoregionaux/radiotherapie/la-brachytherapie-ou-curietherapie.html.

Labour, Joey (2021). "Yttrium-90 quantification using SiPM PET and Monte Carlo simulations for radioembolisation monitoring". PhD thesis. University of Lyon.

Lacrimal glands (2023). https://www.cancerresearchuk.org/about-cancer/eye-cancer/stages-types/types/lacrimal-gland-cancer.

Ladrière, Typhanie et al. (2023). "Safety and Therapeutic Optimization of Lutetium-177 Based Radiopharmaceuticals". In: *Pharmaceutics* 15.4.

Larsson, Maria et al. (2012). "Estimation of absorbed dose to the kidneys in patients after treatment with 177Lu-octreotate: Comparison between methods based on planar scintigraphy". In: *EJNMMI Research* 2.1, pp. 1–13.

Lee, Min Sun, Donghwi Hwang, Joong Hyun Kim, and Jae Sung Lee (2019). "Deepdose: a voxel dose estimation method using deep convolutional neural network for personalized internal dosimetry". In: *Scientific Reports* 9.1, pp. 1–9.

Lee, Sang Hoon and Robin P. Gardner (2000). "A new G-M counter dead time model". In: *Applied Radiation and Isotopes* 53.4-5, pp. 731–737.

LET (2023). https://radiologykey.com/linear-energy-transfer-and-relative-biologic-effectiveness/.

Leung, Thomas W.T. et al. (1995). "Radiation pneumonitis after selective internal radiation treatment with intraarterial 90Yttrium-microspheres for inoperable hepatic tumors". In: *International Journal of Radiation Oncology, Biology, Physics* 33.4, pp. 919–924.

Levillain, H et al. (2021). "International recommendations for personalised selective internal radiation therapy of primary and metastatic liver diseases with yttrium-90 resin microspheres". In: *European Journal of Nuclear Medicine and Molecular Imaging* 48.5, pp. 1570–1584.

Li, Zongyu, Jeffrey A. Fessler, Justin K. Mikell, Scott J. Wilderman, and Yuni K. Dewaraja (2022). "DblurDoseNet: A deep residual learning network for voxel radionuclide dosimetry compensating for single-photon emission computerized tomography imaging resolution". In: *Medical Physics* 49.2, pp. 1216–1230.

Cette thèse est accessible à l'adresse : https://theses.insa-lyon.fr/publication/2023ISAL0068/these.pdf
© [L. Vergnaud], [2023], INSA Lyon, tous droits réservés

Liepe, K. and J. Kotzerke (2011). "Internal radiotherapy of painful bone metastases". In: *Methods* 55.3, pp. 258–270.

Lilja, Hans, David Ulmert, and Andrew J. Vickers (2008). "Prostate-specific antigen and prostate cancer: Prediction, detection and monitoring". In: *Nature Reviews Cancer* 8.4, pp. 268–278.

Ljungberg, M and K Sjogreen Gleisner (2018). "3-D Image-Based Dosimetry in Radionuclide Therapy". In: *IEEE Transactions on Radiation and Plasma Medical Sciences* 2.6, pp. 527–540.

Ljungberg, M and K Sjögreen Gleisner (2016). "Personalized dosimetry for radionuclide therapy using molecular imaging tools". In: *Biomedicines* 4.4, pp. 1–21.

Ljungberg, M et al. (2016). "MIRD pamphlet no. 26: Joint EANM/MIRD guidelines for quantitative 177Lu SPECT applied for dosimetry of radiopharmaceutical therapy". In: *Journal of Nuclear Medicine* 57.1, pp. 151–162.

Lu, Zhonglin, Gefei Chen, Kuan Heng Lin, Tung Hsin Wu, and Greta S.P. Mok (2021). "Evaluation of different CT maps for attenuation correction and segmentation in static 99mTc-MAA SPECT/CT for 90Y radioembolization treatment planning: A simulation study". In: *Medical Physics* 48.7, pp. 3842–3851.

Lu, Zhonglin, Gefei Chen, Yingqing Lyu, Yue Chen, and Greta S. P. Mok (2022). "Technical Note: Respiratory impacts on static and respiratory gated 99m Tc-MAA SPECT/CT for liver radioembolization- A simulation study". In: *Medical Physics*.

Madsen, M T, Y Menda, T M O'Dorisio, and M S O'Dorisio (2019). "Technical Note: Single time point dose estimate for exponential clearance". In: *Medical Physics* 45.5, pp. 2318–2324.

Maffey-Steffan, Johanna et al. (2020). "The 68Ga/177Lu-theragnostic concept in PSMA-targeting of metastatic castration-resistant prostate cancer: impact of post-therapeutic whole-body scintigraphy in the follow-up". In: *European Journal of Nuclear Medicine and Molecular Imaging* 47.3, pp. 695–712.

Mahajan, Sonia, Ravinder K. Grewal, Kent P. Friedman, Heiko Schöder, and Neeta Pandit-Taskar (2022). "Assessment of salivary gland function after 177Lu-PSMA radioligand therapy: Current concepts in imaging and management". In: *Translational Oncology* 21.

Mansi, R, G P Nicolas, L D Pozzo, K A Abid, and E Grouzmann (2020). "Evaluation of a new 177Lu-labeled somatostatin analog for the treatment of tumors expressing somatostatin receptor subtypes 2 and 5". In: *Molecules* 25.18.

Marin, Gwennaëlle et al. (2017). "Accuracy and precision assessment for activity quantification in individualized dosimetry of 177Lu-DOTATATE therapy". In: *EJNMMI Physics* 4.1.

Marin, Gwennaëlle et al. (2018). "A dosimetry procedure for organs-at-risk in 177Lu peptide receptor radionuclide therapy of patients with neuroendocrine tumours". In: *Physica Medica* 56, pp. 41–49.

Marquis, Harry, Kathy P. Willowson, and Dale L. Bailey (2023). "Partial volume effect in SPECT & PET imaging and impact on radionuclide dosimetry estimates". In: *Asia Oceania Journal of Nuclear Medicine and Biology* 11.1, pp. 44–54.

Matteucci, Federica et al. (2017). "Reduction of 68Ga-PSMA renal uptake with mannitol infusion: Preliminary results". In: *European Journal of Nuclear Medicine and Molecular Imaging* 44.13, pp. 2189–2194.

McCarthy, Michael, Tiffany Langton, Divesh Kumar, and Andrew Campbell (2017). "Comparison of PSMA-HBED and PSMA-I&T as diagnostic agents in prostate carcinoma". In: *European Journal of Nuclear Medicine and Molecular Imaging* 44.9, pp. 1455–1462.

Cette thèse est accessible à l'adresse : https://theses.insa-lyon.fr/publication/2023ISAL0068/these.pdf
© [L. Vergnaud], [2023], INSA Lyon, tous droits réservés

McGuire, Sarah M. et al. (2011). "[18F]FLT PET Quantification of Bone Marrow Response to Radiation Dose". In: *International Journal of Radiation Oncology Biology Physics* 81.3, pp. 888–893.

Mezzenga, Emilio et al. (2017). "Quantitative accuracy of 177Lu SPECT imaging for molecular radiotherapy". In: *PLoS ONE* 12.8, pp. 1–18.

Milano, Michael T, Louis S Constine, and Paul Okunieff (2007). "Normal tissue tolerance dose metrics for radiation therapy of major organs." In: *Seminars in radiation oncology* 17.2, pp. 131–140.

Minczeles, Noémie S. et al. (2022). "Dose-Limiting Bone Marrow Toxicities After Peptide Receptor Radionuclide Therapy Are More Prevalent in Women Than in Men". In: *Clinical Nuclear Medicine* 47.7, pp. 599–605.

Mix, Michael et al. (2022). "Kidney Doses in 177Lu-Based Radioligand Therapy in Prostate Cancer: Is Dose Estimation Based on Reduced Dosimetry Measurements Feasible?" In: *Journal of Nuclear Medicine* 63.2, pp. 253–258.

Miyahira, Andrea K. and Howard R. Soule (Mar. 2022). "The History of Prostate-Specific Membrane Antigen as a Theranostic Target in Prostate Cancer: The Cornerstone Role of the Prostate Cancer Foundation". en. In: *J Nucl Med* 63.3, pp. 331–338. ISSN: 0161-5505, 2159-662X.

Mora-Ramirez, Erick et al. (2020). "Comparison of commercial dosimetric software platforms in patients treated with 177Lu-DOTATATE for peptide receptor radionuclide therapy". In: *Medical Physics* 47.9, pp. 4602–4615.

Morris, Zachary S., Andrew Z. Wang, and Susan J. Knox (2021). "The Radiobiology of Radiopharmaceuticals". In: *Seminars in Radiation Oncology* 31.1, pp. 20–27.

Mostafapour, Samaneh et al. (2021). "Attenuation Correction for Myocardial Perfusion SPECT Imaging in the Image Domain". In: *2021 IEEE Nuclear Science Symposium and Medical Imaging Conference Record, NSS/MIC 2021 and 28th International Symposium on Room-Temperature Semiconductor Detectors, RTSD 2022* 9, pp. 434–447.

Nautiyal, Amit, Ashish K Jha, Sneha Mithun, and Venkatesh Rangarajan (2022). "Dosimetry in Lu-177-PSMA-617 prostate-specific membrane antigen targeted radioligand therapy: a systematic review". In: *Nuclear Medicine Communications* 43.4, pp. 369–377.

Nichols, Kenneth J., Andrew Tosh, and Christopher J. Palestro (2009). "Prospects for advancing nuclear cardiology by means of new detector designs". In: *Journal of Nuclear Cardiology* 16.5, pp. 691–696.

Odei, Bismarck C.L., Dustin Boothe, Shane Lloyd, and David K. Gaffney (2016). "A comprehensive analysis of brachytherapy clinical trials over the past 15 years". In: *Brachytherapy* 15.6, pp. 679–686.

Ogawa, Koichi, Yasuo Harata, Takashi Ichihara, Atsushi Kubo, and Shozo Hashimoto (1991). "A Practical Method for Position-Dependent Compton-Scatter Correction in Single Photon Emission CT". In: *IEEE Transactions on Medical Imaging* 10.3, pp. 408–412.

Okamoto, Shozo et al. (2017). "Radiation dosimetry for 177Lu-PSMA I&T in metastatic castration-resistant prostate cancer: Absorbed dose in normal organs and tumor lesions". In: *Journal of Nuclear Medicine* 58.3, pp. 445–450.

Olguin, E, B President, M Ghaly, E Frey, and G Sgouros (2020). "Specific absorbed fractions and radionuclide S-values for tumors of varying size and composition". In: *Physics in Medicine and Biology* 65.23.

Osborne, Dustin R. et al. (2018). "Feasibility assessment of yttrium-90 liver radioembolization imaging using amplitude-based gated PET/CT". In: *Nuclear Medicine Communications* 39.3, pp. 222–227.

Cette thèse est accessible à l'adresse : https://theses.insa-lyon.fr/publication/2023ISAL0068/these.pdf
© [L. Vergnaud], [2023], INSA Lyon, tous droits réservés

Paganelli, Giovanni et al. (2020). "Dosimetry and safety of 177Lu PSMA-617 along with polyglutamate parotid gland protector: preliminary results in metastatic castration-resistant prostate cancer patients". In: *European Journal of Nuclear Medicine and Molecular Imaging* 47.13, pp. 3008–3017.

Patil, Amol and Shoaib Usman (2009). "Measurement and application of paralysis factor for improved detector dead-time characterization". In: *Nuclear Technology* 165.2, pp. 249–256.

Peters, Steffie M B (2022). "[68 Ga]Ga-PSMA-11 PET imaging as a predictor for absorbed doses in organs at risk and small lesions in [177Lu]Lu-PSMA-617 treatment". en. In: *European Journal of Nuclear Medicine and Molecular Imaging*.

Peters, Steffie M.B. et al. (2019). "Towards standardization of absolute SPECT/ CT quantification: a multi-center and multi- vendor phantom study". In: *EJNMMI Physics* 6.1.

Peters, Steffie M.B. et al. (2020). "Variability in lutetium-177 SPECT quantification between different state-of-the-art SPECT/CT systems". In: *EJNMMI Physics* 7.1.

Peters, Steffie M.B. et al. (2022). "Intra-therapeutic dosimetry of [177Lu]Lu-PSMA-617 in low-volume hormone-sensitive metastatic prostate cancer patients and correlation with treatment outcome". In: *European Journal of Nuclear Medicine and Molecular Imaging* 49.2, pp. 460–469.

Peterson, Avery B, David M Mirando, and Yuni K Dewaraja (2023a). "Accuracy and uncertainty analysis of reduced time point imaging effect on time-integrated activity for 177Lu-DOTATATE PRRT in clinical patients and realistic simulations." In: *Research square*.

Peterson, Avery B. et al. (2023b). "177 Lu-DOTATATE Theranostics: Predicting Renal Dosimetry From Pretherapy 68 Ga-DOTATATE PET and Clinical Biomarkers". In: *Clinical Nuclear Medicine* 48.5, pp. 393–399.

Pillai, Maroor Raghavan Ambikalmajan, Ashutosh Dash, and F. F. Knapp (2013). "Sustained availability of 99mTc: Possible paths forward". In: *Journal of Nuclear Medicine* 54.2, pp. 313–323.

Pirozzi Palmese, Valentina et al. (2023). "A comparison of simplified protocols of personalized dosimetry in NEN patients treated by radioligand therapy (RLT) with [177Lu]Lu-DOTATATE to favor its use in clinical practice". In: *European Journal of Nuclear Medicine and Molecular Imaging* 50.6, pp. 1753–1764.

Plachouris, Dimitris et al. (2023). "A radiomic- and dosiomic-based machine learning regression model for pretreatment planning in 177Lu-DOTATATE therapy". In: *Medical Physics* 50, pp. 7222–7235.

Pouget, Jean Pierre, Catherine Lozza, Emmanuel Deshayes, Vincent Boudousq, and Isabelle Navarro-Teulon (2021). "Introduction to radiobiology of targeted radionuclide therapy". In: *Frontiers in Medicine* 2.12, pp. 1–11.

Pouget, Jean Pierre et al. (2022). "From the target cell theory to a more integrated view of radiobiology in Targeted radionuclide therapy: The Montpellier group's experience". In: *Nuclear Medicine and Biology* 104-105, pp. 53–64.

Privé, Bastiaan M. et al. (2021). "Lutetium-177-PSMA-617 in low-volume hormone-sensitive metastatic prostate cancer: A prospective pilot study". In: *Clinical Cancer Research* 27.13, pp. 3595–3601.

Radiothérapie externe (2023). https://www.e-cancer.fr/Patients-et-proches/Les-cancers/Cancer-du-sein/Radiotherapie/Radiotherapie-externe.

Rahbar, Kambiz et al. (2017). "German Multicenter Study Investigating 177Lu-PSMA-617 Radioligand Therapy in Advanced Prostate Cancer Patients". en. In: *Journal of Nuclear Medicine* 58.1, pp. 85–90.

Cette thèse est accessible à l'adresse : https://theses.insa-lyon.fr/publication/2023ISAL0068/these.pdf
© [L. Vergnaud], [2023], INSA Lyon, tous droits réservés

Ramnaraign, Brian and Oliver Sartor (2023). "PSMA-Targeted Radiopharmaceuticals in Prostate Cancer: Current Data and New Trials". In: *The Oncologist* 28.5, pp. 392–401.

Ramonaheng, Keamogetswe, Johannes A. van Staden, and Hanlie du Raan (2021). "The effect of calibration factors and recovery coefficients on 177Lu SPECT activity quantification accuracy: a Monte Carlo study". In: *EJNMMI Physics* 8.1.

— (2022). "Accuracy of two dosimetry software programs for 177Lu radiopharmaceutical therapy using voxel-based patient-specific phantoms". In: *Heliyon* 8.7, e09830.

Rathke, Hendrik et al. (2019). "Dosimetry estimate and initial clinical experience with 90Y-PSMA-617". In: *Journal of Nuclear Medicine* 60.6, pp. 806–811.

Resch, Sandra et al. (2023). "Investigation of image-based lesion and kidney dosimetry protocols for 177Lu-PSMA-I&T therapy with and without a late SPECT/CT acquisition". In: *EJNMMI Physics* 10.1.

Richetta, Elisa et al. (2019). "Physica Medica PET-CT post therapy dosimetry in radioembolization with resin 90 Y microspheres : Comparison with pre-treatment SPECT-CT 99m Tc-MAA results". In: *Physica Medica* 64, pp. 16–23.

Rinscheid, A, P Kletting, M Eiber, A J Beer, and G Glatting (2020). "Influence of sampling schedules on [177Lu]Lu-PSMA dosimetry". In: *EJNMMI Physics* 7.1.

Rit, S. et al. (2014). "The Reconstruction Toolkit (RTK), an open-source cone-beam CT reconstruction toolkit based on the Insight Toolkit (ITK)". In: *Journal of Physics: Conference Series* 489.1.

Ritt, P., J. Sanders, and T. Kuwert (2014). "SPECT/CT technology". In: *Clinical and Translational Imaging* 2.6, pp. 445–457.

Ritt, Philipp (May 2022). "Recent Developments in SPECT/CT". en. In: *Seminars in Nuclear Medicine* 52.3, pp. 276–285. ISSN: 00012998.

Robert, Antoine, Simon Rit, Thomas Baudier, Julien Jomier, and David Sarrut (2021a). "Data-driven motion compensated SPECT reconstruction for liver radioembolization". In: *Proceedings of the 16th International Meeting on Fully 3D Image Reconstruction in Radiology and Nuclear Medicine*.

— (2021b). "Data-Driven Respiration-Gated SPECT for Liver Radioembolization". In: *IEEE Transactions on Radiation and Plasma Medical Sciences*.

Robinson, Andrew P. et al. (2016). "Organ-specific spect activity calibration using 3d printed phantoms for molecular radiotherapy dosimetry". In: *EJNMMI Physics* 3.1, pp. 1–11.

Robinson, Andrew P et al. (2023). "Development of a validation imaging dataset for Molecular Radiotherapy dosimetry multicenter intercomparison exercises based on anthropomorphic phantoms". In: *Physica Medica* 109.

Rolleman, Edgar J., Roelf Valkema, Marion De Jong, Peter P.M. Kooij, and Eric P. Krenning (2003). "Safe and effective inhibition of renal uptake of radiolabelled octreotide by a combination of lysine and arginine". In: *European Journal of Nuclear Medicine and Molecular Imaging* 30.1, pp. 9–15.

Rong, Xing et al. (2012). "Development and evaluation of an improved quantitative 90Y bremsstrahlung SPECT method". In: *Medical Physics* 39.5, pp. 2346–2358.

Rosar, Florian et al. (2021). "Comparison of different methods for post-therapeutic dosimetry in [177Lu]Lu-PSMA-617 radioligand therapy". In: *EJNMMI Physics* 8.1, pp. 1–15.

Roth, Daniel et al. (2022). "Dosimetric Quantities in Neuroendocrine Tumors over Treatment Cycles with 177Lu-DOTATATE". In: *Journal of Nuclear Medicine* 63.3, pp. 399–405.

Cette thèse est accessible à l'adresse : https://theses.insa-lyon.fr/publication/2023ISAL0068/these.pdf
© [L. Vergnaud], [2023], INSA Lyon, tous droits réservés

Ryu, Hyunju, Steven R. Meikle, Kathy P. Willowson, Enid M. Eslick, and Dale L. Bailey (2019). "Performance evaluation of quantitative SPECT/CT using NEMA NU 2 PET methodology". In: *Physics in Medicine and Biology* 64.14.

Sadeghi, Mahdi, Milad Enferadi, and Alireza Shirazi (2010). "External and internal radiation therapy: Past and future directions". In: *Journal of Cancer Research and Therapeutics* 6.3, pp. 239–248.

Saffre, Dimitri (2011). "Radiolyse de l'eau dans des conditions extrêmes de température et de TEL. Capture de HO• par les ions Br-." PhD thesis. UNIVERSITE PARIS-SUD CENTRE SCIENTIFIQUE D'ORSAY.

Sakaguchi, Kenta, Hayato Kaida, Shuhei Yoshida, and Kazunari Ishii (2021). "Attenuation correction using deep learning for brain perfusion SPECT images". In: *Annals of Nuclear Medicine* 35.5, pp. 589–599.

Salem, Riad et al. (2019). "Clinical and dosimetric considerations for Y90: recommendations from an international multidisciplinary working group". In: *European Journal of Nuclear Medicine and Molecular Imaging* 46.8, pp. 1695–1704.

Salivary glands (2023). https://www.cancerresearchuk.org/about-cancer/salivary-gland-cancer/types.

Sanders, J. C., T. Kuwert, J. Hornegger, and P. Ritt (2015). "Quantitative SPECT/CT Imaging of 177Lu with In Vivo Validation in Patients Undergoing Peptide Receptor Radionuclide Therapy". In: *Molecular Imaging and Biology* 17.4, pp. 585–593.

Sanders, James C., Philipp Ritt, Torsten Kuwert, A. Hans Vija, and Andreas K. Maier (2016). "Fully Automated Data-Driven Respiratory Signal Extraction from SPECT Images Using Laplacian Eigenmaps". In: *IEEE Transactions on Medical Imaging* 35.11, pp. 2425–2435.

Sandström, M, N Freedman, K Fröss-Baron, T Kahn, and A Sundin (2020). "Kidney dosimetry in 777 patients during 177Lu-DOTATATE therapy: aspects on extrapolations and measurement time points". In: *EJNMMI Physics* 7.1.

Sandström, M, U Garske, D Granberg, A Sundin, and H Lundqvist (2010). "Individualized dosimetry in patients undergoing therapy with 177Lu-DOTA-D-Phe1-Tyr3-octreotate". In: *European Journal of Nuclear Medicine and Molecular Imaging* 37.2, pp. 212–225.

Sandström, M et al. (2013). "Individualized dosimetry of kidney and bone marrow in patients undergoing 177Lu-DOTA-octreotate treatment". In: *Journal of Nuclear Medicine* 54.1, pp. 33–41.

Sandström, Mattias et al. (2018). "Kidney dosimetry during 177Lu-DOTATATE therapy in patients with neuroendocrine tumors: aspects on calculation and tolerance". In: *Acta Oncologica* 57.4, pp. 516–521.

Santoro, L et al. (2018). "Implementation of patient dosimetry in the clinical practice after targeted radiotherapy using [177Lu-[DOTA0, Tyr3]-octreotate". In: *EJNMMI Research* 8.103, pp. 1–13.

Santoro, Lore et al. (2021). "Clinical implementation of PLANET® Dose for dosimetric assessment after [177Lu]Lu-DOTA-TATE: comparison with Dosimetry Toolkit® and OLINDA/EXM® V1.0". In: *EJNMMI Research* 11.1, pp. 1–17.

Santoro, Miriam et al. (2022). "A novel tool for motion-related dose inaccuracies reduction in 99mTc-MAA SPECT/CT images for SIRT planning". In: *Physica Medica* 98, pp. 98–112.

Sarnelli, Anna et al. (2019). "Dosimetry of 177Lu-PSMA-617 after mannitol infusion and glutamate tablet administration: Preliminary results of EUDRACT/RSO 2016-002732-32 IRST protocol". In: *Molecules* 24.3.

Cette thèse est accessible à l'adresse : https://theses.insa-lyon.fr/publication/2023ISAL0068/these.pdf
© [L. Vergnaud], [2023], INSA Lyon, tous droits réservés

Sarrut, D et al. (2014). "A review of the use and potential of the GATE Monte Carlo simulation code for radiation therapy and dosimetry applications". In: *Medical Physics* 41.6Part1.

Sarrut, D et al. (2017a). "3D absorbed dose distribution estimated by Monte Carlo simulation in radionuclide therapy with a monoclonal antibody targeting synovial sarcoma". In: *EJNMMI Physics* 4.1, pp. 1–16.

Sarrut, David, Adrien Halty, Jean Noel Badel, Ludovic Ferrer, and Manuel Bardiès (2017b). "Voxel-based multimodel fitting method for modeling time activity curves in SPECT images". In: *Medical Physics* 44.12, pp. 6280–6288.

Sarrut, David et al. (May 2021). "Advanced Monte Carlo Simulations of Emission Tomography Imaging Systems with GATE". In: *Physics in Medicine and Biology* 66.10, 10TR03. ISSN: 0031-9155.

Sartor, O et al. (2021). "Lutetium-177-PSMA-617 for Metastatic Castration-Resistant Prostate Cancer". In: *New England Journal of Medicine* 385.12, pp. 1091–1103.

Scarpa, Lorenza et al. (2017). "The 68Ga/177Lu theragnostic concept in PSMA targeting of castration-resistant prostate cancer: correlation of SUVmax values and absorbed dose estimates". In: *European Journal of Nuclear Medicine and Molecular Imaging* 44.5, pp. 788–800.

Schuchardt, Christiane et al. (2022). "Prostate-Specific Membrane Antigen Radioligand Therapy Using 177Lu-PSMA I&T and 177Lu-PSMA-617 in Patients with Metastatic Castration-Resistant Prostate Cancer: Comparison of Safety, Biodistribution, and Dosimetry". In: *Journal of Nuclear Medicine* 63.8, pp. 1199–1207.

Seifert, Robert et al. (2023a). "Is 18F-FDG PET Needed to Assess 177Lu-PSMA Therapy Eligibility? A VISION-like, Single-Center Analysis". In: *Journal of Nuclear Medicine* 64.5, pp. 731–737.

Seifert, Robert et al. (2023b). "Second Version of the Prostate Cancer Molecular Imaging Standardized Evaluation Framework Including Response Evaluation for Clinical Trials (PROMISE V2)". In: *European Urology* 83.5, pp. 405–412.

Serre, D. et al. (2021). "Contribution of 2D and 3D whole-body CZT cameras in the evolution of clinical practice". In: *Medecine Nucleaire* 45.4, pp. 234–239.

Severi, Stefano et al. (2013). "Role of 18FDG PET/CT in patients treated with 177Lu-DOTATATE for advanced differentiated neuroendocrine tumours". In: *European Journal of Nuclear Medicine and Molecular Imaging* 40.6, pp. 881–888.

Sgouros, G (1993). "Bone marrow dosimetry for radioimmunotherapy: Theoretical considerations". In: *Journal of Nuclear Medicine* 34.4, pp. 689–694.

Sgouros, George et al. (2021). "Tumor Response to Radiopharmaceutical Therapies: The Knowns and the Unknowns". In: *Journal of nuclear medicine : official publication, Society of Nuclear Medicine* 62.12, 12S–22S.

Shao, Wenyi, Martin G Pomper, and Yong Du (2021). "A Learned Reconstruction Network for SPECT Imaging". In: *IEEE transactions on radiation and plasma medical sciences* 5.1, pp. 26–34.

Shepp, L. A. and Y. Vardi (1982). "Maximum Likelihood Reconstruction for Emission Tomography". In: *IEEE Transactions on Medical Imaging* 1.2, pp. 113–122.

Shi, Luyao, John A. Onofrey, Hui Liu, Yi Hwa Liu, and Chi Liu (2020). "Deep learning-based attenuation map generation for myocardial perfusion SPECT". In: *European Journal of Nuclear Medicine and Molecular Imaging* 47.10, pp. 2383–2395.

Siebinga, Hinke et al. (2023). "Population pharmacokinetic dosimetry model using imaging data to assess variability in pharmacokinetics of 177Lu-PSMA-617 in prostate cancer patients". In: *CPT: Pharmacometrics and Systems Pharmacology*, pp. 1–12.

Cette thèse est accessible à l'adresse : https://theses.insa-lyon.fr/publication/2023ISAL0068/these.pdf
© [L. Vergnaud], [2023], INSA Lyon, tous droits réservés

Siman, W., J. K. Mikell, and S. C. Kappadath (2016). "Practical reconstruction protocol for quantitative 90Y bremsstrahlung SPECT/CT". In: *Medical Physics* 43.9, pp. 5093–5103.

Sjögreen Gleisner, Katarina et al. (2017). "Variations in the practice of molecular radiotherapy and implementation of dosimetry: results from a European survey". In: *EJNMMI Physics* 4.1, pp. 1–20.

Sjögreen Gleisner, Katarina et al. (2022). "EANM dosimetry committee recommendations for dosimetry of 177Lu-labelled somatostatin-receptor- and PSMA-targeting ligands". In: *European Journal of Nuclear Medicine and Molecular Imaging* 49.6, pp. 1778–1809.

Skowronek, Janusz (2017). "Current status of brachytherapy in cancer treatment - short overview". In: *Journal of Contemporary Brachytherapy* 9.6, pp. 581–589.

Smit Duijzentkunst, Daan A., Dik J Kwekkeboom, and Lisa Bodei (2017). "Somatostatin receptor 2-targeting compounds". In: *Journal of Nuclear Medicine* 58.9, 54S–60S.

Song, Hong et al. (2023). "SPECT at the speed of PET: a feasibility study of CZT-based whole-body SPECT/CT in the post 177Lu-DOTATATE and 177Lu-PSMA617 setting". In: *European Journal of Nuclear Medicine and Molecular Imaging*.

Soret, Marine, Stephen L. Bacharach, and Irène Buvat (2007). "Partial-volume effect in PET tumor imaging". In: *Journal of Nuclear Medicine* 48.6, pp. 932–945.

Srinivas, Shyam M. et al. (2009). "A recovery coefficient method for partial volume correction of PET images". In: *Annals of Nuclear Medicine* 23.4, pp. 341–348.

Staanum, Peter Frøhlich (2023). "Tumor dosimetry using 177Lu: influence of background activity, measurement method and reconstruction algorithm". In: *EJNMMI Physics* 10.1.

Stabin, Michael G. (2008). "Uncertainties in internal dose calculations for radiopharmaceuticals". In: *Journal of Nuclear Medicine* 49.5, pp. 853–860.

Stanhope, Jessica (2016). "Brief Pain Inventory review". In: *Occupational Medicine* 66.6, pp. 496–497.

Stella, Martina, Arthur J.A.T. Braat, Rob van Rooij, Hugo W.A.M. de Jong, and Marnix G.E.H. Lam (2022). "Holmium-166 Radioembolization: Current Status and Future Prospective". In: *CardioVascular and Interventional Radiology* 45.11, pp. 1634–1645.

Stenvall, Anna et al. (2022). "Relationships between uptake of [68Ga]Ga-DOTATATE and absorbed dose in [177Lu]Lu-DOTA-TATE therapy". In: *EJNMMI Research* 12.1.

Strigari, L et al. (2014). "The evidence base for the use of internal dosimetry in the clinical practice of molecular radiotherapy". In: *European Journal of Nuclear Medicine and Molecular Imaging* 41.10, pp. 1976–1988.

Strosberg, J, G El-Haddad, E Wolin, A Hendifar, and J Yao (2017a). "Phase 3 Trial of 177 Lu-DOTATATE for Midgut Neuroendocrine Tumors". In: *New England Journal of Medicine* 376.2, pp. 125–135.

Strosberg, J. et al. (2017b). "Phase 3 trial of 177lu-dotatate for midgut neuroendocrine tumors". In: *New England Journal of Medicine* 376.2, pp. 125–135.

Strosberg, Jonathan R. et al. (2021). "177Lu-Dotatate plus long-acting octreotide versus high-dose long-acting octreotide in patients with midgut neuroendocrine tumours (NETTER-1): final overall survival and long-term safety results from an open-label, randomised, controlled, phase 3 trial". In: *The Lancet Oncology* 22.12, pp. 1752–1763.

Cette thèse est accessible à l'adresse : https://theses.insa-lyon.fr/publication/2023ISAL0068/these.pdf
© [L. Vergnaud], [2023], INSA Lyon, tous droits réservés

Sundlöv, A et al. (2017). "Individualised 177Lu-DOTATATE treatment of neuroendocrine tumours based on kidney dosimetry". In: *European Journal of Nuclear Medicine and Molecular Imaging* 44.9, pp. 1480–1489.

Sundlöv, A et al. (2018). "Feasibility of simplifying renal dosimetry in 177Lu peptide receptor radionuclide therapy". In: *EJNMMI Physics* 5.1, pp. 1–19.

Sundlöv, Anna et al. (2022). "Phase II trial demonstrates the efficacy and safety of individualized, dosimetry-based 177Lu-DOTATATE treatment of NET patients". In: *European Journal of Nuclear Medicine and Molecular Imaging* 49.11, pp. 3830–3840.

Sweeney, D. C. and G. S. Johnston (1995). "Radioiodine therapy for thyroid cancer". In: *Endocrinology and Metabolism Clinics of North America* 24.4, pp. 803–839.

Swiha, Mina M. et al. (2022). "Survival predictors of 177Lu-Dotatate peptide receptor radionuclide therapy (PRRT) in patients with progressive well-differentiated neuroendocrine tumors (NETS)". In: *Journal of Cancer Research and Clinical Oncology* 148.1, pp. 225–236.

Szeles, Csaba (2004). "CdZnTe and CdTe materials for X-ray and gamma ray radiation detector applications". In: *Physica Status Solidi (B) Basic Research* 241.3, pp. 783–790.

Takahashi, Yasuyuki, Masao Miyagawa, Yoshiko Nishiyama, Hayato Ishimura, and Teruhito Mochizuki (Jan. 2013). "Performance of a semiconductor SPECT system: comparison with a conventional Anger-type SPECT instrument". en. In: *Ann Nucl Med* 27.1, pp. 11–16. ISSN: 0914-7187, 1864-6433.

Tamborino, Giulia et al. (2022). "Dosimetric Evaluation of the Effect of Receptor Heterogeneity on the Therapeutic Efficacy of Peptide Receptor Radionuclide Therapy: Correlation with DNA Damage Induction and in Vivo Survival". In: *Journal of Nuclear Medicine* 63.1, pp. 100–107.

Tanderup, Kari et al. (2017). "Advancements in brachytherapy". In: *Advanced Drug Delivery Reviews* 109, pp. 15–25.

Taprogge, J, J Wadsley, E Miles, and G D Flux (2021). "Recommendations for Multicentre Clinical Trials Involving Dosimetry for Molecular Radiotherapy". In: *Clinical Oncology* 33.2, pp. 131–136.

Thapa, Pradeep et al. (2016). "Performance of 177Lu-DOTATATE-based peptide receptor radionuclide therapy in metastatic gastroenteropancreatic neuroendocrine tumor: A multiparametric response evaluation correlating with primary tumor site, tumor proliferation index, and dual tracer imaging characteristics". In: *Nuclear Medicine Communications* 37.10, pp. 1030–1037.

The Anatomy of Bone Marrow (2023). https://www.verywellhealth.com/bone-marrow-anatomy-5076272.

Thomas, M. Allan, Armeen Mahvash, Mohamed Abdelsalam, Ahmed O. Kaseb, and S. Cheenu Kappadath (2020). "Planning dosimetry for 90Y radioembolization with glass microspheres: Evaluating the fidelity of 99mTc-MAA and partition model predictions". In: *Medical Physics* 47.10, pp. 5333–5342.

Tomographic Reconstruction (2023). http://irene.guillemet.org/coursem/DESMNRecon_2006bis.pdf.

Tran-Gia, Johannes and Michael Lassmann (2019). "Characterization of noise and resolution for quantitative 177 Lu SPECT/CT with XSPECT quant". In: *Journal of Nuclear Medicine* 60.1, pp. 50–59.

Tran-Gia, Johannes et al. (2021). "A multicentre and multi-national evaluation of the accuracy of quantitative Lu-177 SPECT/CT imaging performed within the MRT-Dosimetry project." In: *EJNMMI physics* 8.1.

Cette thèse est accessible à l'adresse : https://theses.insa-lyon.fr/publication/2023ISAL0068/these.pdf
© [L. Vergnaud], [2023], INSA Lyon, tous droits réservés

Tuncel, Murat, Tuğçe Telli, Meltem Çağlar Tuncal, and Erdem Karabulut (2021). "Predictive factors of tumor sink effect: Insights from 177Lu-Prostate-specific membrane antigen therapy". In: *Annals of Nuclear Medicine* 35.5, pp. 529–539.

Turpin, L et al. (2019). "Radiothérapie interne vectorisée par 177Lu-PSMA-617 de l'adénocarcinome prostatique métastatique résistant à la castration : à propos d'un cas et revue de la littérature". In: *Médecine Nucléaire* 43.3, pp. 298–303.

Uribe, Carlos F. et al. (2017). "Accuracy of 177Lu activity quantification in SPECT imaging: a phantom study". In: *EJNMMI Physics* 4.1.

Usman, S and A Patil (2018). "Radiation detector deadtime and pile up: A review of the status of science". In: *Nuclear Engineering and Technology* 50.7, pp. 1006–1016.

Vaz, Sofia C., Francisco Oliveira, Ken Herrmann, and Patrick Veit-Haibach (2020). "Nuclear medicine and molecular imaging advances in the 21st century". eng. In: *The British Journal of Radiology* 93.1110, p. 20200095. ISSN: 1748-880X.

Velikyan, Irina et al. (2014). "Quantitative and qualitative intrapatient comparison of 68Ga-DOTATOC and 68Ga-DOTATATE: Net uptake rate for accurate quantification". In: *Journal of Nuclear Medicine* 55.2, pp. 204–210.

Vergnaud, Laure et al. (2022). "Patient-specific dosimetry adapted to variable number of SPECT/CT time-points per cycle for 177Lu-DOTATATE therapy". In: *EJNMMI Physics* 9.1.

Vergnaud, Laure et al. (2023). "Dosimetric impact of 3D motion-compensated SPECT reconstruction for SIRT planning". In: *EJNMMI Physics* 10.8.

Vilgrain, V et al. (2017). "Efficacy and safety of selective internal radiotherapy with yttrium-90 resin microspheres compared with sorafenib in locally advanced and inoperable". In: *The lancet Oncology* 18.12, pp. 1624–1636.

Violet, John et al. (2019). "Dosimetry of 177Lu-PSMA-617 in metastatic castration-resistant prostate cancer: Correlations between pretherapeutic imaging and whole-body tumor dosimetry with treatment outcomes". In: *Journal of Nuclear Medicine* 60.4, pp. 517–523.

Violet, John et al. (2020). "Long-Term Follow-up and Outcomes of Retreatment in an Expanded 50-Patient Single-Center Phase II Prospective Trial of 177Lu-PSMA-617 Theranostics in Metastatic Castration-Resistant Prostate Cancer". In: *Journal of nuclear medicine : official publication, Society of Nuclear Medicine* 61.6, pp. 857–865.

Visvikis, Dimitris et al. (2022). "Application of artificial intelligence in nuclear medicine and molecular imaging: a review of current status and future perspectives for clinical translation". In: *European Journal of Nuclear Medicine and Molecular Imaging* 49.13, pp. 4452–4463.

Völter, Friederike et al. (2021). "Correlation of an index-lesion-based SPECT dosimetry method with mean tumor dose and clinical outcome after 177Lu-PSMA-617 radioligand therapy". In: *Diagnostics* 11.3, p. 428.

Wang, Ge, Jong Chul Ye, and Bruno De Man (2020). "Deep learning for tomographic image reconstruction". In: *Nature Machine Intelligence* 2.12, pp. 737–748.

Wang, Jingnan et al. (2019). "Pretherapeutic 68Ga-PSMA-617 PET may indicate the dosimetry of 177 Lu-PSMA-617 and 177 Lu-EB-PSMA-617 in main organs and tumor lesions". In: *Clinical Nuclear medicine* 44.6, pp. 431–438.

Weber, M. et al. (2022). "EANM procedure guideline for the treatment of liver cancer and liver metastases with intra-arterial radioactive compounds". In: *European Journal of Nuclear Medicine and Molecular Imaging* 49.5, pp. 1682–1699.

Webster Stayman, J. and Jeffrey A. Fessler (2000). "Regularization for uniform spatial resolution properties in penalized-likelihood image reconstruction". In: *IEEE Transactions on Medical Imaging* 19.6, pp. 601–615.

Cette thèse est accessible à l'adresse : https://theses.insa-lyon.fr/publication/2023ISAL0068/these.pdf
© [L. Vergnaud], [2023], INSA Lyon, tous droits réservés

Wehrmann, Christiane, Stefan Senftleben, Carolin Zachert, Dirk Müller, and Richard P. Baum (2007). "Results of individual patient dosimetry in peptide receptor radionuclide therapy with 177Lu DOTA-TATE and 177Lu DOTA-NOC". In: *Cancer Biotherapy and Radiopharmaceuticals* 22.3, pp. 406–416.

Wernick, Miles and John Aarsvold (2004). *Emission Tomography The Fundamentals of PET and SPECT*. California: ELSEVIER academic press.

Willowson, K P et al. (2018a). "Feasibility and accuracy of single time point imaging for renal dosimetry following 177 Lu-DOTATATE ('Lutate') therapy". In: *EJNMMI Physics* 5.1.

Willowson, Kathy P et al. (2018b). "A Comparison of 2D and 3D Kidney Absorbed Dose Measures in Patients Receiving 177Lu-DOTATATE." In: *Asia Oceania journal of nuclear medicine & biology* 6.2, pp. 113–119.

Wong, Ka Kit et al. (2022). "Differences in tumor-to-normal organ SUV ratios measured with 68Ga-DOTATATE PET compared with 177Lu-DOTATATE SPECT in patients with neuroendocrine tumors". In: *Nuclear Medicine Communications* 43.8, pp. 892–900.

Wright, Chadwick L. et al. (2012). "Radiation pneumonitis following yttrium-90 radioembolization: Case report and literature review". In: *Journal of Vascular and Interventional Radiology* 23.5, pp. 669–674.

Xiang, Haowei, Hongki Lim, Jeffrey A. Fessler, and Yuni K. Dewaraja (2020). "A deep neural network for fast and accurate scatter estimation in quantitative SPECT/CT under challenging scatter conditions". In: *European Journal of Nuclear Medicine and Molecular Imaging* 47.13, pp. 2956–2967.

Xin, Lin, Weihai Zhuo, and Tianwu Xie (2023). "Development of a voxel S-value database for patient internal radiation dosimetry". In: *Physica Medica* 106, p. 102519.

Xue, Song et al. (2022). "Application of machine learning to pretherapeutically estimate dosimetry in men with advanced prostate cancer treated with 177Lu-PSMA I&T therapy". In: *European Journal of Nuclear Medicine and Molecular Imaging* 49.12, pp. 4064–4072.

Yadav, Madhav P. et al. (2017). "Post-therapeutic dosimetry of 177Lu-DKFZ-PSMA-617 in the treatment of patients with metastatic castration-resistant prostate cancer". In: *Nuclear Medicine Communications* 38.1, pp. 91–98.

Yadav, Madhav Prasad et al. (2020). "Efficacy and Safety of 177Lu-PSMA-617 Radioligand Therapy in Metastatic Castration-Resistant Prostate Cancer Patients". In: *Clinical Nuclear Medicine* 45.1, pp. 19–31.

Yilmaz, Burcak et al. (2019). "Effect of external cooling on 177Lu-PSMA uptake by the parotid glands". In: *Journal of Nuclear Medicine* 60.10, pp. 1388–1393.

Yorke, Ellen, Daphna Gelblum, and Eric Ford (2011). "Patient safety in external beam radiation therapy". In: *American Journal of Roentgenology* 196.4, pp. 768–772.

Yousaf, M, T Akyurek, and S Usman (2015). "A comparison of traditional and hybrid radiation detector dead-time models and detector behavior". In: *Progress in Nuclear Energy* 83, pp. 177–185.

Zaidi, Habib and Bruce Hasegawa (2003). "Determination of the attenuation map in emission tomography." In: *Journal of nuclear medicine : official publication, Society of Nuclear Medicine* 44.2, pp. 291–315.

Zeintl, Johannes, Alexander Hans Vija, Amos Yahil, Joachim Hornegger, and Torsten Kuwert (2010). "Quantitative accuracy of clinical 99mTc SPECT/CT using ordered-subset expectation maximization with 3-dimensional resolution recovery, attenuation, and scatter correction". In: *Journal of Nuclear Medicine* 51.6, pp. 921–928.

Cette thèse est accessible à l'adresse : https://theses.insa-lyon.fr/publication/2023ISAL0068/these.pdf
© [L. Vergnaud], [2023], INSA Lyon, tous droits réservés

Zhang, Jingjing et al. (2018). "Safety, pharmacokinetics, and dosimetry of a long-acting radiolabeled somatostatin analog 177Lu-DOTA-EB-TATE in patients with advanced metastatic neuroendocrine tumors". In: *Journal of Nuclear Medicine* 59.11, pp. 1699–1705.

Zhang, Jingjing et al. (2019). "177Lu-PSMA-617 radioligand therapy in metastatic castration-resistant prostate cancer patients with a single functioning kidney". In: *Journal of Nuclear Medicine* 60.11, pp. 1579–1586.

Zhao, W et al. (2019). "Accuracy of kidney dosimetry performed using simplified time activity curve modelling methods: A 177Lu-DOTATATE patient study". In: *Physics in Medicine and Biology* 64.17.

Zhao, Wei et al. (2018). "Determination of gamma camera calibration factors for quantitation of therapeutic radioisotopes". In: *EJNMMI Physics* 5.1.

Özkan, Ahu et al. (2020). "Posttherapeutic Critical Organ Dosimetry of Extensive 177Lu-PSMA Inhibitor Therapy with Metastatic Castration-Resistant Prostate Cancer: One Center Results". In: *Clinical Nuclear Medicine* 45.4, pp. 288–291.

Cette thèse est accessible à l'adresse : https://theses.insa-lyon.fr/publication/2023ISAL0068/these.pdf
© [L. Vergnaud], [2023], INSA Lyon, tous droits réservés

FOLIO ADMINISTRATIF

THESE DE L'INSA LYON, MEMBRE DE L'UNIVERSITE DE LYON

NOM : VERGNAUD DATE de SOUTENANCE : 06/10/2023

Prénoms : Laure, Michelle

TITRE : Dosimetry for ^{177}Lu and ^{90}Y radionuclide therapies through imaging and Monte Carlo simulations

NATURE : Doctorat Numéro d'ordre : 2023ISAL0068

Ecole doctorale : Electronique, Electrotechnique, Automatique

Spécialité : Traitement du Signal et de l'Image

RESUME :

En médecine nucléaire, la radiothérapie interne vectorisée (RIV) consiste à injecter par intraveineuse un radiopharmaceutique (médicament radioactif) qui va venir se fixer aux cellules tumorales grâce à un vecteur sélectionné selon le type de récepteurs sur-exprimés par ces dernières, être internalisé et les détruire. Ce traitement a démontré son efficacité pour les tumeurs neuroendocrines (TNE) et pour les cancers de la prostate métastatiques résistants à la castration (PC). Cependant, les plans de traitement sont standardisés alors que des études ont montrées que les doses absorbées (énergie absorbée par unité de masse) par les organes à risque et les tumeurs diffèrent d'un patient à un autre. Afin de pouvoir les personnaliser, il est donc nécessaire d'estimer les doses absorbées et de les mettre en regard avec les toxicités et l'efficacité du traitement.
Lors de la désintégration radioactive de certains radioisotopes tels que le ^{177}Lu, des photons gamma sont émis et peuvent être détectés à l'aide d'une gamma caméra. Une acquisition TEMP (Tomographie d'Emission MonoPhotonique) est généralement réalisée afin de connaître la biodistribution 3D du radiopharmaceutique à un instant donné qui est nécessaire pour l'estimation des doses absorbées par les régions d'intérêt. Dans cette thèse, nous nous sommes intéressés aux aspects quantitatifs et dosimétriques des thérapies au ^{177}Lu et à l'^{90}Y à partir des images SPECT acquises.
En RIV, la dosimétrie au ^{177}Lu requière un suivi de la biodistribution du radiopharmaceutique au cours du temps et donc, des acquisitions TEMP post-injection multiples. Cependant, les contraintes cliniques ne permettent pas toujours de disposer des temps et du nombre d'acquisitions que l'on souhaiterait. C'est pourquoi, la première contribution a eu pour objectif de fournir un workflow dosimétrique s'adaptant au nombre d'acquisitions disponibles pour les thérapies au ^{177}Lu-DOTATATE (TNE). Plusieurs méthodes de dosimétrie simplifiées ont été proposées et évaluées par rapport à une méthode de référence s'appuyant sur trois acquisitions post-injection.
La radiothérapie interne sélective (RIS) est un traitement local des lésions hépatiques dans lequel des microsphères d'^{90}Y sont injectées dans l'artère intra-hépatique, vont venir se bloquer dans les vaisseaux irrigant les tumeurs et les détruire. Ce traitement est simulé à l'aide d'une injection de ^{99m}Tc associé à des macroaggrégats d'albumine. Une acquisition TEMP est ensuite réalisée puis l'image est reconstruite afin de prédire les doses absorbées et d'adapter l'activité à injecter pour la thérapie. Pendant l'acquisition TEMP, les mouvements respiratoires peuvent impacter l'acquisition mais ne sont pas forcément corrigés au cours de la reconstruction. La seconde contribution a permis d'évaluer l'impact dosimétrique de la correction du mouvement respiratoire en comparant les estimations de doses et d'activité à injecter avec et sans correction du mouvement dans la reconstruction.
Enfin, plus récemment, les gamma caméras CZT ont permis de réduire les durées d'acquisition tout en conservant la qualité de l'image. Cependant, elles ne permettent pas toujours d'acquérir les photons de hautes énergies (>200 keV) et donc, le pic énergétique recommadé pour la dosimétrie au ^{177}Lu. Dans une troisième contribution, une étude de faisabilité de la quantification au ^{177}Lu (pic énergétique à 113 keV) a été réalisée à l'aide de fantômes et des paramètres de reconstruction optimaux ont été fournis. Ces paramètres ont ensuite été utilisés lors d'une étude dosimétrique préliminaire sur patients traités au ^{177}Lu-PSMA.

MOTS-CLÉS : Dosimétrie / ^{177}Lu-DOTATATE / ^{177}Lu-PSMA / TEMP/CT / Simulations Monte Carlo / Radiothérapie interne vectorisée

Laboratoire (s) de recherche : CREATIS

Directeur de thèse: David Sarrut (Co-directeur : Jean-Nöel Badel)

Président de jury : Florent Cachin

Composition du jury : Yuni Dewaraja (Rapporteure), John Dickson (Rapporteur), Lidia Strigari (Examinatrice), Florent Cachin (Examinateur), David Sarrut (Directeur de thèse), Jean-Noël Badel (Co-directeur de thèse), Anne-Laure Giraudet (Invitée)

Cette thèse est accessible à l'adresse : https://theses.insa-lyon.fr/publication/2023ISAL0068/these.pdf
© [L. Vergnaud], [2023], INSA Lyon, tous droits réservés